Design and characterization of widely tunable semiconductor lasers based on etched slots

Thesis

By

Marta Nawrocka

A thesis submitted to the

University of Dublin

for the degree of

Doctor of Philosophy.

School of Physics,

University of Dublin,

Trinity College Dublin,

Dublin.

March, 2015.

Declaration

This thesis has not been submitted as an exercise for a degree in this or any other university. The work described in this thesis is entirely my own, with exception of assistance recognised in the acknowledgements and the collaborative work noted in the publications. I agree to deposit this thesis in the University's open access institutional repository or allow the library to do so on my behalf, subject to Irish Copyright Legislation and Trinity College Library conditions of use and acknowledgement.

Marta Nawrocka

Summary

Tunable semiconductor lasers play an important role in numerous technologies for optical communication and sensing systems. They are widely used in dense wavelength division multiplexed (DWDM) systems and in other important markets such as trace gas detection for environmental emission motoring. Tunable lasers are also becoming a key component in optical packet and burst switching systems to reduce the latency and increase the capacity of current optical transmission networks. These systems require tunable lasers with wide wavelength tuning range >30 nm, a high side- mode suppression ratio (SMSR) >30dB, a fast wavelength switching time, and a high output power >10dBm. Tunable lasers have been used in optical networks for some years now, starting with devices with small tuning range but moving toward devices with full- band coverage. So far, a number of wavelength tunable lasers have been developed, however they are conventionally fabricated with a grating that requires at least one re- growth step, complicating the device fabrication and therefore increasing the device cost. Another issue related to the laser operation is an optical feedback which is provided by cleaving the ends of the laser to form two semi-reflecting facets. Due to the cleaving, it is difficult to integrate these lasers with other optical components. The objective of this thesis is to show widely wavelength tunable lasers, based on etched slots that are re- growth free, can be fabricated by standard photolithography and are suitable for photonics integration. This kind of slotted laser platform has several advantages: a significant reduction of cost, it enables use of AlGaInAs materials for high temperature operation and also it is integrated with a semiconductor optical amplifier (SOA) on a single chip to control the output power.

A group of slots provide the necessary reflectivity for the laser operation which is completely independent of the cleaved facet. The loss introduced by the series of slots is compensated by the gain in the laser. Also the laser mirrors are active. As there is no cleaving needed, this laser can be easily integrated with semiconductor optical amplifiers (SOA) or Mach- Zehnder modulators (MZI) and therefore significantly reduce the chip cost and complexity. In this thesis multi-section tunable lasers integrated with semiconductor optical amplifier (SOA) are described. The lasers have tuning range of ~ 50 nm with a good SMSR> 30dB.

In this thesis a design and fabrication process of slotted tunable laser is presented. Different slot periods were chosen to show how tuning parameters such as tuning range, number of super- modes, free spectral range (FSR) and SMSR are influenced by this parameter. We also presented various types of the slotted lasers: five-, six-, and nine section lasers. The full tuning characterization of these lasers is presented here as well as an investigation of the phase tuning of the six section laser. A further characterization of the slotted tunable lasers is introduced in this thesis by determining the continuous tuning, the temperature tuning and the linewidth measurements using the delayed self-heterodyne method. The lasers have the linewidth in the range of MHz. Finally the tunable lasers with short slot periods were characterized here showing very good performance. The shortest slot period is 52μm for the front mirror and 57 μm for the back mirror.

Acknowledgments

Firstly I would like to thank my supervisor Prof. John Donegan for giving me the opportunity to join his group and work on this project, and also his great supervision and support throughout the last four years.

I would also like to thank Dr. Qiaoyin Lu for teaching me everything she knew about working in the lab and also for her help in theoretical and simulation aspects of this project. Thanks also the past members of Photonics Group for familiarizing me with the lab, offices and Dublin. A big thanks to the present members of the group, especially Xia Zhang for being a great friend and all 'outside PhD' fun stuff we've been doing together. Thanks to Azat for being my lab partner during the first two years in Trinity, for all scientific and less scientific conversations. Michael- thank you for all your help in the lab during the last few months and plotting endless data!

A massive thanks to my friends outside of Trinity, Adam and Paweł, for their stimulating friendship, support and all fun we always have together.

A massive thanks to my family, especially to my amazing parents for their constant love, support, encouragement through all my years in school, college and PhD. They taught me to always look at the bright sides and never give up. Without them and their wisdom, I wouldn't have gone so far in my life. Nie mogłabym mieć lepszych rodziców od Was! To, że zaszlam tak daleko w życiu, zawdzięczam właśnie Wam, waszej miłości i wsparciu przez te wszystkie lata. Thanks to Anne and Philip for their love and support especially during the last year. Thomas, my 'sun and stars'- you know how I feel about you. Without you my life would've been very empty, thank you!

'Serenity now!'- Frank Costanza

List of Publications

M. Nawrocka, Q. Lu, W.H. Guo, A. Abdullaev, F. Bello, J. O'Callaghan, T. Cathcart, and J. F. Donegan, "Widely tunable six-section semiconductor laser based on etched slots." *Optics Express* 22(16), pp.18949-18957, 2014.

A. Abdullaev, Q. Lu, W.H. Guo, M. Nawrocka, F. Bello, J. O'Callaghan, J. Donegan, "Linewidth characterization of integrable slotted single mode lasers. ", IEEE Photonics Technology Letters, 2014

W. H. Guo, Q. Lu, M. Nawrocka, A. Abdullaev, J. O'Callaghan, J. F. Donegan, "Nine-channel wavelength tunable single mode laser array based on slots. ", *Optics express*, *21*(8), pp. 10215-1022, 2013.

F. Bello, Q.Y. Lu, A. Abdullaev, M. Nawrocka, J.F. Donegan, "Linewidth and noise characterization for a partially- slotted single mode laser.", IEEE Journal of Quantum Electronics 50(9), pp 755-759, 2014.

W. H. Guo, , Q. Lu, M. Nawrocka, A. Abdullaev, J. O'Callaghan, M. Lynch, J. F. Donegan, "Integrable slotted single-mode lasers", *Photonics Technology Letters, IEEE*, *24*(8), 634-636, 2012.

Lu, Qiaoyin, Weihua Guo, Marta Nawrocka, Azat Abdullaev, Chris Daunt, James O'Callaghan, Michael Lynch, Vincent Weldon, Frank Peters, and John F. Donegan. "Single mode lasers based on slots suitable for photonic integration." *Optics express* 19, no. 26 (2011): B140-B145.

Lu, Qiaoyin, Weihua Guo, A. Abdullaev, M. Nawrocka, T. N. Huynh, J. O'Callaghan, M. Lynch, V. Weldon, L. P. Barry, and J. F. Donegan. "Two-section single mode lasers

based on slots suitable for photonic integration (Photonics)." *Electronics letters* 48, no. 15 (2012): 945-946.

Lu, Qiaoyin, Wei-Hua Guo, Azat Abdullaev, Marta Nawrocka, James O'Callaghan, Michael Lynch, Vincent Weldon, and John F. Donegan. "Tunable Single Mode Laser Array Based on Slots." In *Optical Fiber Communication Conference*, pp. OTh3I-5. Optical Society of America, 2013.

Lu, Qiaoyin, Weihua Guo, Azat Abdullaev, Marta Nawrocka, James O'Callaghan, and John F. Donegan. "31nm Quasi-Continuous Tuning Single Mode Laser Array Based on Slots." In *CLEO: Applications and Technology*, pp. JW2A-77. Optical Society of America, 2014.

Lu, Qiaoyin, Weihua Guo, Azat Abdullaev, Marta Nawrocka, James O'Callaghan, Michael Lynch, Vincent Weldon, and John F. Donegan. "High-yield two-section single mode lasers based on a 37th order surface grating." In*Lasers and Electro-Optics (CLEO), 2012 Conference on*, pp. 1-2. IEEE, 2012.

Lu, Qiaoyin, Azat Abdullaev, Marta Nawrocka, Wei-Hua Guo, James O'Callaghan, and John F. Donegan. "Slotted Single Mode Lasers Integrated With a Semiconductor Optical Amplifier." *IEEE Photonics Technology Letters*25 (2013): 564-567.

Table of contents

Abbreviations

AR- Anti- reflection
ASE- Amplified spontaneous emission
DBR- Distributed Bragg reflector
DFB- Distributed feedback
DS- DBR- Digital Supermode Distributed Bragg Reflector
DS- H- Delayed self- heterodyne
DWDM- Dense- Wavelength division multiplexing
ESA- Electrical spectrum analyser
FMCW- Frequency- modulated continuous wave
FP- Fabry- Perot
FSE- Fourier series expansion
FSR- Free Spectral Range
FWHM- Full width half maximum
ICP- Indutively coupled plasma
ITU- The International telecommunication union
MQW- multi- quantum well
OSA- Optical Spectrum Analyser
PA- Polarization controller
PD- Photodetector
QCSE- Quantum- confined Stark effect
SEM- Scanning electron microscope
SG-DBR – Sampled Grating Distributed Bragg Reflector
SMM- Scattering matrix method
SMSR- Side mode suppression ratio
SNR- Signal- to – noise ratio
SOA- Semiconductor optical amplifier
SSG- DBR- Superstructure Grating Distributed Bragg Reflector
TEC- Thermoelectric cooler
TLA- Tunable laser array
TMM- transmission matrix method
WDM- Wavelength division multiplexing

Chapter 1. Introduction

The concept behind the laser was first proposed by Einstein who said that the light consists of wave energies called photons and their energies correspond to the frequency of the waves. The higher the frequency is, the greater is the energy carried by the waves.
The first laser action was demonstrated in microwave region in 1954 by Charles Townes and his co-workers. They produced a beam of ammonia molecules through a system of focusing electrodes. When microwave power of the desired frequency was passed through the cavity, the amplification occurred. It was called Microwave Amplification by Stimulated Emmission of Radiation or M.A.S.E.R. The term "laser" was first created in 1957 by Gordon Gould. The first practical laser, the ruby laser, was invented in 1960 by Theodore Mainman. In 1962, laser action in semiconductor material was demonstrated by Robert Hall although it took almost another decade for the first semiconductor laser diode to be developed and to be able to operate at room temperature. A high- performance AlGaAs/GaAs laser was demonstrated in 1970 and become a commercial product in the late 70s. The structure had many advantages such as size, power-conversion efficiency, direct- current pumping, reliability and wavelength flexibility. Semiconductor laser diodes are now the most common laser types, with several million devices being produced every month. They have many application in CD players, printers, gas sensing devices, spectroscopy, and optical communication systems. Tunable laser diodes have their applications mostly in optical communication systems and the research has mainly been driven by increasing demand on transmission capacity in optical telecommunication systems to increase the bandwidth and reduce latency. The networks operate with wavelength division multiplexing (WDM) techniques and coherent optical detection schemes [1] [2]. Single- mode laser diodes with electronically tunable wavelength are the key components on the transmitter and receiver side. Tunable laser diodes that can be monolithically integrated with other optical components on a single chip are the favored devices.
The required tunable laser characteristics are the tuning range, side mode suppression ratio (SMSR) of more than 30dB to consider the laser single mode operating, optical power, spectral linewidth, the continuous tunability and FM modulation bandwidth. The tuning range is the most specific parameter for a tunable laser as its width improves the

laser suitability for all practical applications. Also in many applications, the optical power being constant throughout all tuning range is necessary. In FMCW (frequency- modulated continuous wave) radar and spectrum analysis where high coherence is required, the laser linewidth is the most important issue. As experience shows, an ideal performance of a tunable laser diode cannot be obtained mainly due to the wavelength tuning mechanism affecting the optical losses so that the optical power changes during tuning. Also the optical power control by the injected currents affects the device temperature and therefore the emission wavelength. Therefore, it is desirable to have a specific application in mind to produce a tunable laser fulfilling the application's requirements. Figure 1.1 shows an overview of the tunable laser diodes applications and their specific demands.

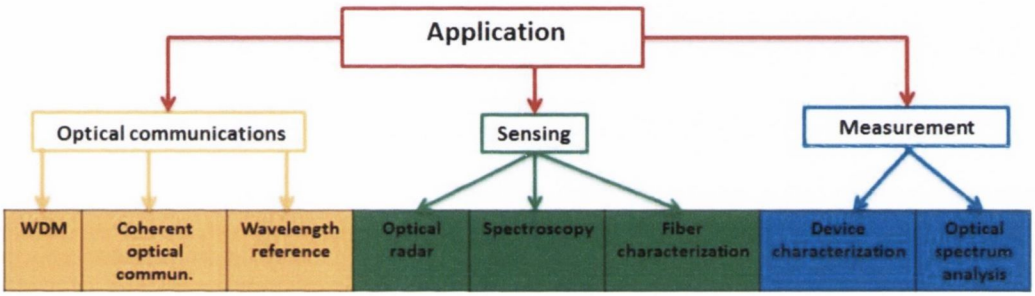

Continuous tuning		●	●	●		●	●	●
Tuning range	●	●		●	●	●	●	●
Optical power	●	●	●	●	●	●		
Linewidth		●	●	●	●			●
FM modulation bandwidth	●	●		●			●	

Figure 1.1. Major applications and specific demands on performance of tunable laser diodes from [1].

The purpose of this thesis was to understand the physics behind the slotted tunable lasers that are integrated with a semiconductor optical amplifier (SOA) on a single chip. The design process including optimization of the slot parameters and preparing of the laser mask is presented in this thesis as well as fabrication details and characterization of the slotted lasers. The thesis deals with characterization of various type of multi- section slotted tunable lasers such as tuning range, SMSR, optical power, continuous tuning, and linewidth measurements.

Chapter 2 introduces the basic concepts behind semiconductor tunable lasers. Single mode lasers like distributed Bragg reflector (DBR) laser and distributed feedback (DFB) laser are described there. Tuning mechanisms to change the wavelength position are then presented where continuous, quasi- continuous and discontinuous tunings are introduced. Then the electronic and thermal control of the output wavelength is described as well as the free carrier plasma effect as a mechanism used to achieve tuning in semiconductor lasers. The Vernier tuning effect is then introduced to expand the laser tuning range. Finally, various types of DBR tunable lasers are presented.

Chapter 3 deals with Fabry- Perot (FP) laser measurements which are important in designing tunable lasers. The FP laser characteristic shown in Chapter 3 is based on measurements of the amplified spontaneous emission spectrum (ASE) analysed using the Fourier series expansion method. The parameters such as internal loss, quasi- Fermi level separation, linewidth enhancement factor and geometric spontaneous emission factor are extracted.

Chapter 4 introduces the scattering matrix method (SMM) which is used to optimize the slotted tunable laser parameters such as slot number, slot depth, slot period. Details of the laser simulations as well as simulated tuning maps are also presented. Finally laser mask design and fabrication process is introduced.

Chapter 5 shows characteristic for five, six and nine section tunable laser and a five contact laser with nine slots on the front mirror and five slots on the back mirror. The lasers characterized in this chapter have different slot periods to show how tuning parameters such as tuning range, number of super-modes, free spectral range change with varying slot period. The output power, wavelength and SMSR maps of those lasers are presented in this chapter. Also phase tuning of six contact laser is introduced.

Chapter 6 deals with further characterization of the slotted tunable lasers. Continuous tuning for a laser with nine slots on both mirrors, a laser with nine/five slots and a laser with nine contacts are analysed. The temperature tuning is also shown in this chapter. Finally, the linewidth is measured using self- heterodyne method for the laser with the longest and the shortest slot period.

Chapter 7 shows the characterization of the slotted tunable lasers from the second fabrication run. All lasers presented in this chapter have short slot periods. The purpose of using short slot periods was to investigate its influence on the wavelength tuning range. The linewidth for the laser with the shortest slot period is also measured in this chapter.

Chapter 8 gives some conclusion and future work that can be done to improve the laser design. Also possibility of further measurements is suggested there to achieve full characterization.

References

[1] J. Buus, M. Amann and D. Blumenthal, Tunable laser diodes and related optical sources, IEEE Wiley- Interscience, 2005.

[2] L. Coldren, S. Corzine i M. Masanavic, Diode lasers and photonics integrated circuits, Wiley; 2nd edition, 2012.

Chapter 2. Introduction to tunable semiconductor lasers

In this chapter, an introduction to semiconductor tunable lasers is presented. The background of single mode laser operation and a grating concept is shown leading to the realisation of two of the most popular single mode lasers: Distributed Bragg Reflector laser (DBR) and Distributed Feedback laser (DFB). The electronic control of the laser is then examined showing how changes in the injection current density and changes of the laser temperature influence the laser wavelength output. Finally, the Vernier tuning effect is presented and its mechanism to extend the tuning range. Also various types of DBR tunable lasers are introduced employing the Vernier tuning with different types of gratings.

2.1. Wavelength propagation in periodic structures

Optical gain in semiconductors

Considering the propagation of a monochromatic plane wave in an isotropic medium characterized by the complex propagation constant (or wave number)

$$\beta = k_0 n = k_0 \left(n' + jn'' \right) \tag{2.1}$$

where k_0 is the free- space propagation constant for wavelength λ

$$k_0 = \frac{\omega}{c} = \frac{2\pi}{\lambda} \tag{2.2}$$

the optical gain (loss) for a plane wave propagating in a semiconductor in the z-direction can be approximated by [1]

$$g = -\alpha = \frac{1}{I}\frac{dI}{dz} = 2k_0 n'' \tag{2.3}$$

There are some important properties of the gain that are specific for semiconductor lasers.

The first is that the values of the gain are extremely high. The magnitude of the gain is of hundreds of cm^{-1}, which is orders of magnitude greater than in any other type of laser. Due to this fact, semiconductor lasers can be small, much less than 1 mm long. The second property is that the gain spectrum is wide, in the range of tens of nm. The reason for this is that the optical transition is between a pair of energy bands, instead of between well- defined states [2].

Side mode suppression ratio

Side mode suppression ratio (SMSR) [1] is simply the ratio of the output power in the primary laser mode to that in the next strongest mode from one end of the laser. It can be calculated by means of multimode rate equations. For the dominant mode N and the second strongest mode N+1, these equations read under stationary conditions

$$\frac{d\bar{S}_N}{dt} = 0 = R_{sp}(\lambda_N) + \bar{S}_N v_g g_c(\lambda_N) \tag{2.4}$$

$$\frac{d\bar{S}_{N+1}}{dt} = 0 = R_{sp}(\lambda_{N+1}) + \bar{S}_{N+1} v_g g_c(\lambda_{N+1}) \tag{2.5}$$

where $R_{sp}(\lambda_i)$ and $\bar{S}_i$ are the spontaneous emission rate and the average photon density of the i-th mode. The SMSR equals the photon density quotient of modes N and N+1:

$$SMSR = \frac{\bar{S}_N}{\bar{S}_{N+1}} \tag{2.6}$$

After introducing gain and side mode suppression ratio, an overview of grating used to achieve a single mode operation in semiconductor lasers over a wide tuning range will be presented. A good analysis can be found in [1]. The aim of this analysis is to show the reflection variation as the wavelength is varied about the Bragg frequency of a grating.

The refractive index varies periodically in the propagation direction according to

$$n(z) = n_{eff}^{'} + \frac{\Delta n}{2}\cos(2\beta_0 z) \tag{2.7}$$

where $\Delta n / 2 \ll n_{eff}^{'}$. The Bragg propagation constant is related to the grating period of the structure Λ by

$$\beta_0 = \frac{M\pi}{\Lambda} = \frac{2\pi}{\lambda_B} n_{eff}^{'} = k_0(\lambda_B) n_{eff}^{'} \tag{2.8}$$

where λ_B is the Bragg wavelength in free space, $k_0(\lambda_B)$ is the free space propagation constant for wavelength λ_B and M is the period order. For the first order grating we have

$$\Lambda = \frac{\lambda_B}{2n_{eff}^{'}} \tag{2.9}$$

which means that the period is equal to a half wavelength in the structure. The effect of the periodic structure is to couple forward- going (right) and backward- going (left) waves in the structure. Suppressing the time factor exp(jωt), and keeping in mind that all transverse and lateral variations are neglected, we can write the equation of the electric filed propagating with a wavelength λ as

$$\frac{d^2E}{dz^2} + [n(z)k_0]^2 E = 0 \tag{2.10}$$

If we neglect the terms containing $(\Delta n)^2$ and use $\beta = n_{eff}^{'} k_0$ we get

$$[n(z)k_0]^2 = \beta^2 + 4\beta\kappa\cos(2\beta_0 z) \tag{2.11}$$

where κ is known as the coupling coefficient given by

$$\kappa = \frac{\pi\Delta n}{2\lambda} \tag{2.12}$$

Considering only wavelengths near to the Bragg wavelength λ_B, hence $\beta = \beta_0 + \Delta\beta$ with $\Delta\beta \ll \beta$. We can write the electric field as a sum of right- and – left- propagating waves:

$$E(z) = R(z)\exp(-i\beta_0 z) + S(z)\exp(i\beta_0 z) \tag{2.13}$$

The functions $R(z)$ and $S(z)$ vary comparatively slowly with z because we have included the rapidly varying phase factor in the exponential functions. Inserting 2.11 and 2.13 into 2.10 and neglecting the second derivatives of R and S as they are much smaller than the first derivatives, a pair of coupled- mode equations are:

$$\frac{dR}{dz} + j\Delta\beta R = -j\kappa S \tag{2.14}$$

$$\frac{dS}{dz} - j\Delta\beta S = j\kappa R \tag{2.15}$$

Considering the case shown in figure 2.3 below representing a periodic grating in which the index varies in a stepwise manner between two values and where each subsection of the structure has a length of a half a period, from the Fresnel formula the reflection coefficient r from the first discontinuity is

$$r = \frac{\Delta n'}{2n'_{eff}} \tag{2.16}$$

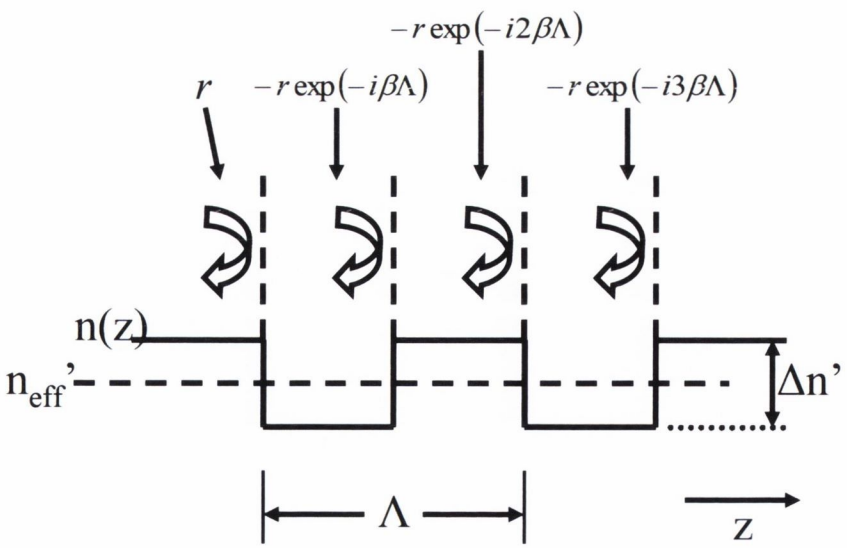

Figure 2.3. Propagation and reflection in a 'square' grating.

The field reflection of the next discontinuity is $-r$ because we are now going from a high to low refractive index. When the wavelength is equal to the Bragg wavelength, the phase change for a round- trip is a subsection is $\beta_0 \Lambda = \pi$, corresponding to a factor -1. All reflections add up in phase, and the field reflectivity per unit length (with two reflections per period) is:

$$\kappa' = \frac{2r}{\Lambda} = \frac{\Delta n'}{n'_{eff}} \frac{2n'_{eff}}{\lambda_B} = \frac{2\Delta n'}{\lambda_B} \tag{2.17}$$

Therefore the coupling coefficient can be described as the amount of reflection per unit length.

The coupled mode equations together with equation 2.13 describe the field in a structure with a periodic index variation given by equation 2.7. If we know R and S at a given point, we can now find the general solution as

$$R(z) = \left[\cosh(\gamma z) - \frac{j\Delta\beta}{\gamma} \sinh(\gamma z) \right] R(0) - \frac{j\kappa}{\gamma} \sinh(\gamma z) S(0) \tag{2.18}$$

$$S(z) = \frac{j\kappa}{\gamma} \sinh(\gamma z) R(0) + \left[\cosh(\gamma z) + \frac{j\Delta\beta}{\gamma} \sinh(\gamma z) \right] S(0) \tag{2.19}$$

where

$$\gamma^2 = \kappa^2 - \Delta\beta^2 \tag{2.20}$$

Introducing the length L for distance z

$$R(L) = \left[\cosh(\gamma L) - \frac{j\Delta\beta}{\gamma} \sinh(\gamma L) \right] R(0) - \frac{j\kappa}{\gamma} \sinh(\gamma L) S(0) \tag{2.21}$$

$$S(L) = \frac{j\kappa}{\gamma} \sinh(\gamma L) R(0) + \left[\cosh(\gamma L) + \frac{j\Delta\beta}{\gamma} \sinh(\gamma L) \right] S(0) \tag{2.22}$$

We can write the results in a matrix from:

$$\begin{bmatrix} R(L) \\ S(L) \end{bmatrix} = F_{per}(L) \begin{bmatrix} R[0] \\ S(0) \end{bmatrix} \tag{2.23}$$

where $F_{per}(L)$ can be written as

$F_{per} = \begin{pmatrix} \left[\cosh(\gamma L) - \frac{j\Delta\beta}{\gamma}\sinh(\gamma L)\right] & -\frac{j\kappa}{\gamma}\sinh(\gamma L) \\ \frac{j\kappa}{\gamma}\sinh(\gamma L) & \left[\cosh(\gamma L) + \frac{j\Delta\beta}{\gamma}\sinh(\gamma L)\right] \end{pmatrix}$. The matrix elements of $F_{per}(L)$ follow directely from 2.21 and 2.22.

This is a transfer matrix that relates the right- and left- propagating waves at one end of the structure to the right- and left- propagating waves at the other end. Using a periodic structure of length L and having $S(L) = 0$, the field reflection coefficient is

$$r_{per} = \frac{S(0)}{R(0)} = -\frac{(F_{per})_{21}}{(F_{per})_{22}} = \frac{-\frac{j\kappa}{\gamma}\sinh(\gamma L)}{\cosh(\gamma L) + \frac{j\Delta\beta}{\gamma}\sinh(\gamma L)} \tag{2.24}$$

where $(F_{per})_{21}$ and $(F_{per})_{22}$ are the components of matrix $F_{per}(L)$.

If κL is very close to $\Delta\beta L, \gamma L$ is small and we get to the first order

$$r_{per} \approx \frac{-j\kappa L}{1 + j\Delta\beta L} \tag{2.25}$$

Therefore r_{per} increases with increasing κL (a higher coupling coefficient leads to a stronger reflection), r_{per} decreases with increasing $\Delta\beta L$ (the reflection becomes smaller when the wavelength deviates from the Bragg wavelength). This is the basic of two of the most successfully manufactured single mode lasers, the distributed Bragg reflector laser DBR and the distributed feedback laser DFB.

Distributed Bragg Reflector Lasers

For wavelengths close to the Bragg wavelength, the reflections from the individual parts of the grating are in phase and the reflection coefficients are high. Its value depends on the value of the coupling coefficient κ. For wavelengths away from the Bragg wavelength, the reflections do not add up in phase and therefore the reflection will be

low. This wavelength dependence can be used to achieve a wavelength – dependent cavity gain for a laser by using a periodic structure as a reflector at one/both ends of the laser structure. This is the basic principle of the distributed Bragg- reflector DBR laser.
The 'coupling strength' can be defined as a product of the coupling coefficient κ and the laser length L, and the deviation from the Bragg wavelength by the dimensionless product $\Delta\beta L$. The deviation $\Delta\lambda$ of the wavelength λ from the Bragg wavelength λ_B is related to the deviation of the propagation constant β from the Bragg- propagation constant β_0:

$$\Delta\beta = \beta - \beta_0 = \frac{2\pi n_{eff}'(\lambda)}{\lambda} - \frac{2\pi n_{eff}'(\lambda_B)}{\lambda_B} \approx \frac{2\pi n_g}{\lambda_B^2}\Delta\lambda \qquad (2.26)$$

At the Bragg wavelength with a periodic structure of length L as a reflector for an incoming wave with an amplitude $R(0)$ at $z=0$, and no incoming wave and no reflection at $z=L$ that is $S(L)=0$, the solutions of 2.21 and 2.22 are

$$R(z) = \frac{\cosh\left[\kappa(z-L)\right]}{\cosh(\kappa L)}R(0) \qquad (2.27)$$

$$S(z) = \frac{j\sinh\left[\kappa(z-L)\right]}{\cosh(\kappa L)}R(0) \qquad (2.28)$$

At the Bragg wavelength, the magnitude of the field and power reflection coefficients only depend on κL:

$$\left|r_{per}\right| = \tanh(\kappa L) \qquad (2.29)$$

$$R_{per} = \left|r_{per}\right|^2 = \tanh^2(\kappa L) \qquad (2.30)$$

For values of κL of more than about 0.7 the reflectivities are similar to or higher than a cleaved facet. The reflection bandwidth λ_r can be found using 2.26 and approximating $\Delta\beta \approx 2\kappa$:

$$\Delta\lambda_r = \frac{\lambda_B^2}{\pi n_{g,eff}} = \frac{\lambda_B \Delta n}{2n_{g,eff}} \tag{2.31}$$

which shows that the relative bandwidth is proportional to the relative index variation. The mode spacing $\Delta\lambda_m$ for a laser of length L' is given by

$$\Delta\lambda_m = \frac{\lambda^2}{2n_{g,eff}L'} \tag{2.32}$$

The phase ϕ of the reflected wave can be found using 2.24

$$r_{per} = |r_{per}| e^{-j\phi} \tag{2.33}$$

From the phase an effective length of the Bragg reflector can be defined as

$$2L_{eff} = \frac{d\phi}{d\beta} \tag{2.34}$$

For the case of $\beta = \beta_0$, the simple result can be found

$$L_{eff} = \frac{\tanh(\kappa L)}{2\kappa} = \frac{L}{2}\frac{\tanh(\kappa L)}{\kappa L} \tag{2.35}$$

This shows that for small values of κL we have $L_{eff} = L/2$, and for large values of κL we have $L_{eff} = 1/(2\kappa)$. For high values of κL, the amplitude of the incoming wave decreases by a factor of exp(0.5) at the point $z = L_{eff}$. If we define the penetration depth as the point where the incoming power decreases by a factor e, the penetration depth is simply given by L_{eff}.

Here the grating idea is extended to include periodic grating with a variation on the refractive index also in the x and y directions. For the first order rectangular grating with equal lengths of mark and space regions (shown in figure 2.4) we have

$$\kappa = \frac{2\Delta n'_{eff}}{\lambda_B} = \frac{2\left(n'_{eff,A} - n'_{eff,B}\right)}{\lambda_B} \tag{2.36}$$

where $n'_{eff,A}$ and $n'_{eff,B}$ are the effective refractive indices corresponding to the mark and space regions, respectively.

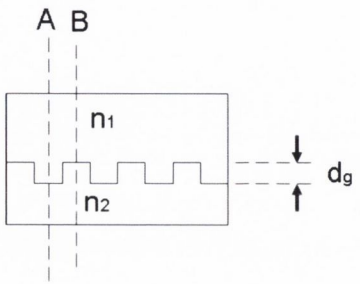

Figure 2.4. Grating structure; A and B indicate 'mark' and 'space' regions.

If we consider the presence of the grating as a perturbation, the from the wave equation

$$\Delta n'_{eff} = \Gamma_g \left(n_1 - n_2 \right) \tag{2.37}$$

where n_1 and n_2 are the refractive indices of the layers forming the grating, and Γ_g is the confinement factor for the grating region of thickness d_g. The first order grating with equal mark and space periods gives the highest coupling coefficient. For other grating shapes, the coupling coefficient is

$$\kappa = \left(\frac{2\Delta n'_{eff}}{\lambda_B} \right) f_{red} \tag{2.38}$$

where $f_{red} < 1$ is a reduction factor. For a rectangular grating with unequal length of the mark and space, the reduction factor follows from the Fourier coefficient of the grating shape:

$$f_{red} = \sin\left(\pi \frac{\Lambda_m}{\Lambda} \right) \tag{2.39}$$

This result can be extended to gratings of higher order, where M denotes the order

$$f_{red} = \frac{1}{M} \left| \sin\left(\pi \frac{\Lambda_m}{\Lambda} M \right) \right| \tag{2.40}$$

Distributed Feedback Lasers

In DBR lasers, the active region which provides the gain and the grating which provides the wavelength selectivity, are separated longitudinally. In distributed feedback lasers both the grating and the active region are distributed along the laser cavity in the longitudinal direction with the grating above the active region in an index coupled structure making these lasers easier to fabricate as there is no integration of active and passive sections required.

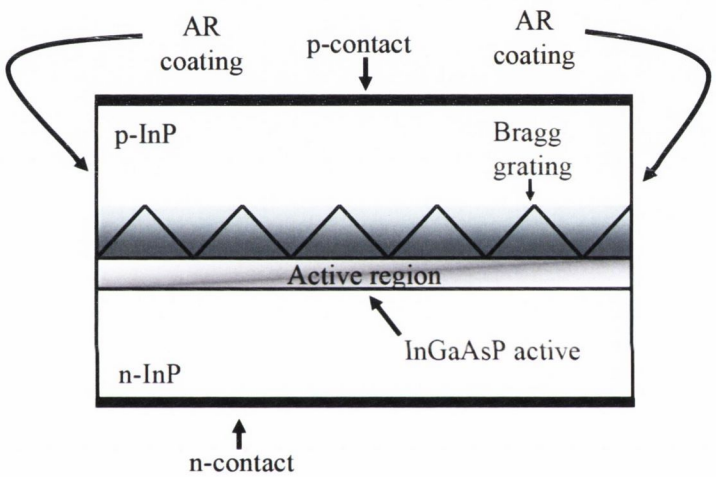

Figure 2.5. Schematic structure of DFB laser.

The analysis of a DFB laser is not as simple as for DBR laser as the gain and phase conditions cannot be separated. However, as the laser is essentially a single periodic structure the transfer matrix theory can be used as in [1]. The oscillation condition can be represented as

$$\cosh(\gamma L)+\frac{j(\Delta\beta+jg_0)}{\gamma}\sinh(\gamma L)=0 \qquad (2.41)$$

where we added jg_0 to allow for the presence of gain; g_0 represents the gain of the field. The parameter γ is given by

$$\gamma^2=\kappa^2-(\Delta\beta+jg_0)^2 \qquad (2.42)$$

where κ is the coupling coefficient. The oscillation condition 2.41 can be rewritten as

$$\gamma L \cosh(\gamma L) = -j(\Delta\beta L + j g_0 L) \tag{2.43}$$

For the mode with the lowest value of g_0 the required intensity gain $2g_0$ is equal to the net gain

$$g_{net} = (\Gamma g - \alpha_i) \tag{2.44}$$

which must be supplied to compensate for the power emitted from the ends. Therefore the quantity $2g_0$ is equivalent to the end mirror loss for a Fabry-Perot laser. Solving numerically equation 2.43 for the defined products of coupling strength κ and cavity length L gives possible values of $\Delta\beta L$ and $g_0 L$ as shown in figure 2.6. It can be seen that no DFB modes exist at $\Delta\beta L = 0$ and therefore $\Delta\beta = 0$ as the cavity length L cannot be 0. This means that there is no propagation at $\Delta\beta = 0$ which is the Bragg wavelength. This is the DFB stop band.

It is analogous to the forming of stop- bands in solid- states physics, with no propagation exactly at the Bragg wavelength.

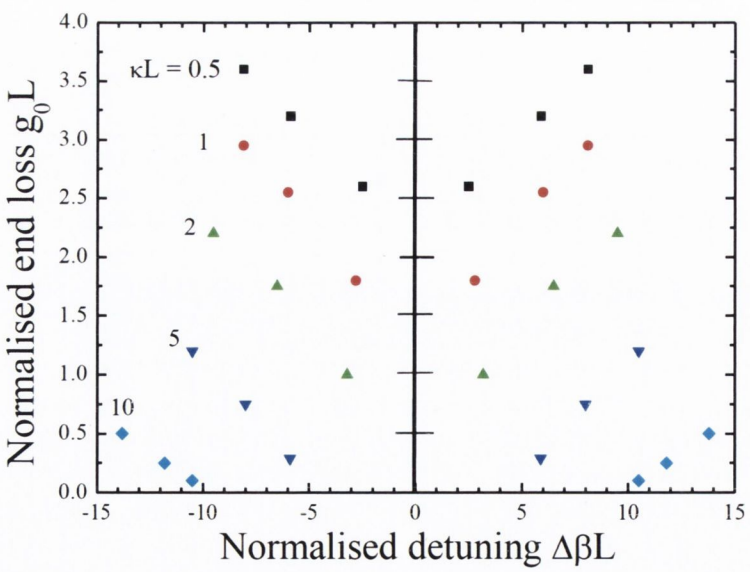

Figure 2.6. DFB modes for various values of κL.

At this exact Bragg wavelength $\Delta\beta = 0$

$$\gamma^2 = \kappa^2 + g_0^2 \tag{2.45}$$

It can be seen that there are two modes at the same distance from the Bragg wavelength and hence single mode operation in this kind of DFB laser is not possible. For better understanding let us consider a rectangular grating as shown in figure 2.7.

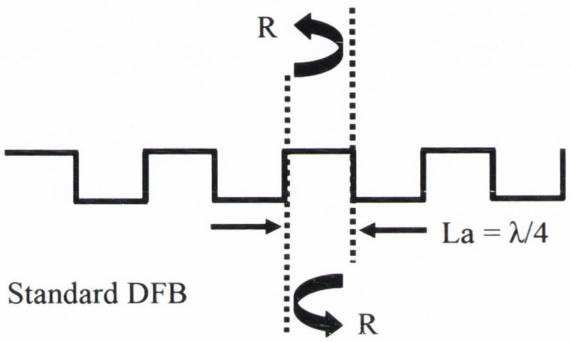

Figure 2.7. Schematic structure of standard DFB grating with reflectivity R [3].

For this grating, the cavity can be taken to anywhere inside the DFB since all periods look the same. The active length La is therefore a quarter- wavelength long taking the mirror reference planes yielding a zero grating reflection phase at the Bragg wavelength. Therefore this type of configuration is anti- resonant at the Bragg wavelength. Introducing a cavity length increase of a half- wavelength long [4] [5] the device becomes resonant at the Bragg frequency where the reflection phase is zero. It is called a quarter-wave shifted DFB as a half wavelength mirror spacing corresponds to a quarter- wave shift between the two gratings as shown in figure 2.8.

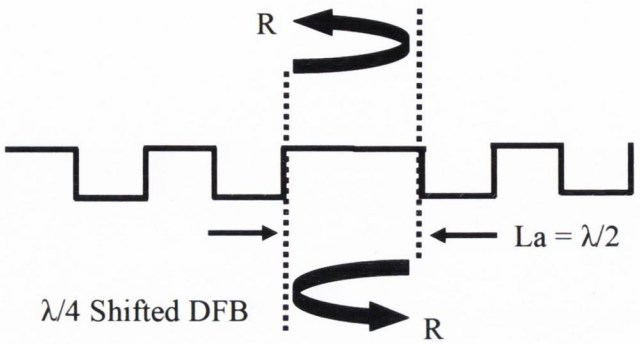

Figure 2.8. Schematic of a quarter- shifted DFB grating with reflectivity R [3].

Other methods to achieve single mode DFB lasers are to leave one or both facets cleaved rather than AR coating both faces [6]. Introducing the cleaving will destroy the degeneracy of the modes and allow one to reach threshold first as the net reflection phase from one end is shifted from that of the grating alone. This will introduce a yield problem since the reflection from the cleave will have a random relative phase and the yield depends on the required end loss differences [7].

2.2. Tuning mechanism

Current injection tuning

Depending on how the tuning is performed, and which device structure is used three basic tuning schemes can be distinguished: (i) continuous tuning, (ii) discontinuous tuning, (iii) quasi-continuous tuning. The schematic characteristics are shown in figure 2.9 below.

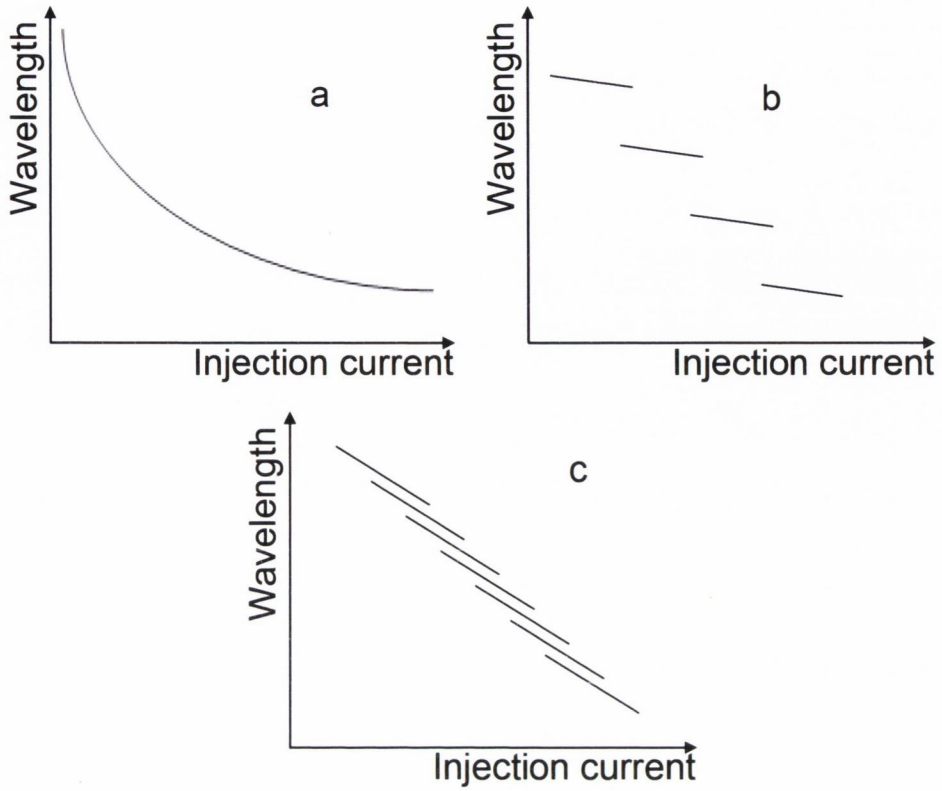

Figure 2.9. Schematic of a) continuous tuning; b) discontinuous tuning; c) quasi- continuous tuning.

For most practical applications, the ideal tuning scheme is continuous tuning [8] [9] in which the laser wavelength is tuned smoothly in arbitrarily small steps without mode changes while all other laser parameters are kept constant as far as possible.

Achieving larger tuning ranges is possible by allowing for longitudinal mode to change during tuning. Here, the tunability of the comb- mode spectrum has no limitation on the total tuning range, which is now determined by the tuning range of the cavity gain characteristics. Unfortunately, for the discontinuous tuning range it is impossible to access all wavelengths within the tuning range.

The quasi-continuous tuning is accomplished by joining overlapping small regimes. To achieve a large wavelength coverage each region is continuously tunable by a single longitudinal mode. The total tuning range is limited by tunability of the gain characteristics, while the tuning of the comb- mode spectrum occurs only over about one longitudinal mode spacing.

Tuning of the cavity gain, the comb mode and electronic control tuning.

Tuning of the cavity gain can be done by a spectral shift of the cavity gain curve $g_c(\lambda)$ from its initial state $g_c^0(\lambda)$. Tuning of the g_c characteristics means that the gain peak wavelength λ_p is shifted either by varying the wavelength dependence of the active medium gain $g_a(\lambda)$ or by using laser mirrors with a tunable wavelength- selective mirror loss $\alpha_m(\lambda)$.

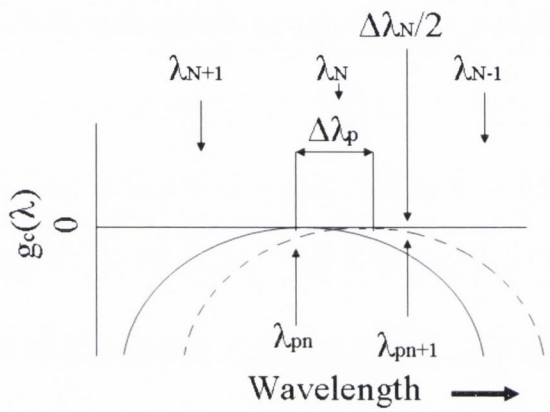

Figure 2.10. Wavelength tuning via shifting the gain peak wavelength.

When $\Delta\lambda_p$ increase above $\Delta\lambda_m / 2$ then a mode hop occurs and the mode at λ_{N-1} starts to lase. Using this method the wavelengths in between the mode hops cannot be access and so this is the discontinuous tuning scheme. From figure 2.10 λ_{pn} is the gain peak wavelength without tuning, λ_N is the laser wavelength for mode N.

Tuning of the comb- mode spectrum is done by keeping λ_p fixed and changing the optical length of the laser by adjusting which cavity mode is lasing. As shown in figure 2.11 below the difference between this method and the cavity gain method is that the mode wavelengths change linearly within each mode jump.

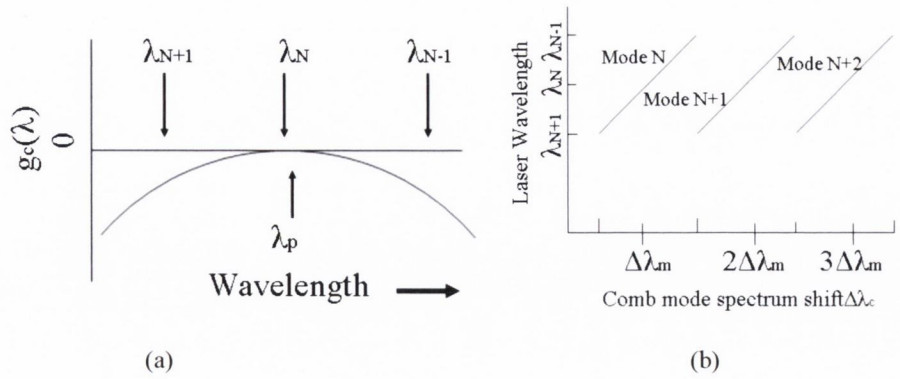

Figure 2.11. a) Wavelength tuning by shifting the comb- mode spectrum, b) laser wavelength versus comb-mode shift.

In a simple Fabry- Perot laser above threshold the gain clamping mechanism prevents significant carrier changes so that the variation of the semiconductor gain curve by changing the injection current has very little impact on the lasing wavelength.

Electronic wavelength control

To have control of the output wavelength of a tunable laser it is needed to control the position of the gain peak wavelength of the cavity round trip gain λ_p and/or the longitudinal modes λ_N. The gain peak wavelength λ_p depends on the injected carrier density and as was mentioned before, in a Fabry- Perot laser the carrier density clamps above the threshold therefore there is little wavelength tuning in Fabry- Perot lasers. Widely tunable laser diodes rely on this mechanism for large wavelength tuning if there are un- clamped carrier density regions such as passive gratings.

In order to shift the output wavelength it is needed to change the position of the longitudinal modes λ_N by changing the real part of the effective refractive index as shown in the phase condition

$$\lambda_i = \frac{2n'_{eff}(\lambda_i)L}{m} \tag{2.46}$$

where $n_{eff}^{'}$ is the effective refractive index, L is the cavity length and m is the mode number. Therefore to control the output wavelength a waveguide with an electronically controllable effective refractive index is needed, where the amount of tuning is proportional to the product of the cavity length and the effective refractive index. In DBR and DFB lasers the tuning of the cavity round- trip gain may be accomplished by tuning the Bragg reflector and therefore changing the position of the comb modes. Looking at the equation

$$\Lambda = \frac{\lambda_B}{2n_{eff}^{'}} \tag{2.47}$$

it can be seen that the only element that can be changed is the effective refractive index as the grating element is fixed during the fabrication of the Bragg mirror. As the effective index is determined by confinement factor and the refractive index of the layers of the laser and changes in the refractive index in any of these layers can change the effective refractive index and therefore the end mirror loss $\alpha_m(\lambda)$. This type of tuning is used commonly in many tunable lasers [10] [11].

The extent of the lasers continuous tuning when the same cavity mode lases across the wavelength span can be determined from

$$\frac{\Delta\lambda}{\lambda_0} = \frac{\left|\Delta n_{eff}^{'}\right|}{n_{g,eff}} \tag{2.48}$$

where $\Delta\lambda$ is the wavelength tuning, λ_0 is the Bragg wavelength, $\Delta n_{eff}^{'}$ is the change in the real part of the effective refractive index and $n_{g,eff}$ is the group effective refractive index. From this analysis it can be seen that the electronic control the wavelength of the tunable laser depends on the ability to control the effective refractive index of the laser. In practice the effective refractive index can be controlled by three different methods either carrier induced effects- free carrier plasma effect, by applying an electric across the device- quantum confined Stark effect, or by varying the temperature of the device- thermal tuning.

Free- Carrier Plasma Effect

The free- carrier plasma effect is the most popular and widely used mechanism for tuning semiconductor lasers. It also achieves the largest tuning range [1]. The free carrier plasma effect works by changing the refractive index caused by the injection of electron- hole plasma into a semiconductor. This electron- hole plasma polarizes the free carriers and spectrally shifts the absorption edge of the semiconductor [12] [13]. The effect of the carrier polarization is much larger than the absorption edge shift in the case of a passive wavelength control waveguide section when the bandgap energy is larger than the photon energy. The refractive index change due to a change for a carrier injection is given by

$$\Delta n' = -\frac{e^2\lambda^2}{8\pi^2 c^2 n\varepsilon_0}\left(\frac{1}{m_e}-\frac{1}{m_h}\right)N \qquad (2.49)$$

where c is the speed of light, n is the refractive index, ε_0 is the free space permittivity, m_e is the electron effective mass, m_h is the hole effective mass and N is the injected carrier density. This implies a negative refractive index change and therefore a negative wavelength change- a blue shift. There is also a change in the optical gain due to the change in the imaginary part of the refractive index given by

$$2k_0\Delta n'' = -\frac{e^3\lambda^2}{4\pi^2 c^3 n\varepsilon_0}\left(\frac{1}{m_e^2\mu_e}+\frac{1}{m_h^2\mu_h}\right)N \qquad (2.50)$$

where μ_e is the electron mobility and μ_h is the hole mobility. The injection of carriers also causes band filling and band gap shrinkage which have a refractive index change of the same sign as the polarization effect and therefore increase the index change with injected carriers. These are the main effects by which the tunable lasers described in this thesis are tuned.

Quantum- confined Stark effect

While the electro-optic effect is rather weak in the usual III/V semiconductors [14], enhanced refractive index changes can be achieved in multi-quantum well MQW structures exploiting the quantum- confined Stark effect QCSE [15]. This effect is observed by placing the quantum wells in an electric field that reduces the band gap energy by effectively making the band edges inclined relative to each other and thereby

reducing the energy between the lowest order wavefunction of the conduction band and the lowest order wavefunction in the valence band as shown in figure 2.12.

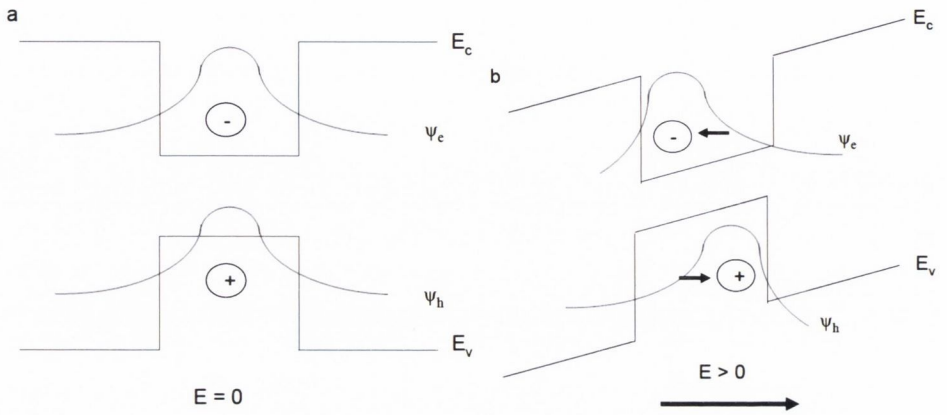

Figure 2.12. The quantum- confined Stark effect, a) the band edges become inclined and the wavefunctions are displaced with respect to each other and their energy difference is slightly reduced b).

The significant effects on the refractive index are achieved only for photon energies near the bandgap energy, where absorption also occurs. The refractive index changes are still very small typically of the order 10^{-3} to 10^{-2} even in multiple quantum well lasers where the quantum well used in the tuning section matches the laser wavelength [10] [16]. However with asymmetric quantum wells the refractive change can be increased to ~0.01 [17] [18].

Thermal Tuning

Temperature changes may also control the emission wavelength of the laser diode as the bandgap energy and the Fermi distribution are sensitive to temperature changes. Therefore both the gain peak wavelength of the active medium as well as the refractive index show a temperature dependence. For the laser with an emission peak at 1550nm a change of 0.5nm/K for Fabry- Perot lasers and 0.1nm/K for DFB and DBR lasers are observed [1] [19]. The Fabry- Perot lasers exhibit mode jumps while the temperature is changing. Although the temperature dependence is quite weak for each longitudinal mode, the Fabry- Perot laser on average show the same high temperature shift of around 0.5 nm/K of the gain peak wavelength. The wavelength of single- mode lasers changes only by 0.1 nm/K over the whole temperature range. This is due to the fact that the wavelength of Fabry- Perot and single- mode lasers are functions of the refractive index and do not depend on the gain curve and also the gain peak of Fabry- Perot laser consists

of several modes and each of those modes depends on refractive index. The wavelength increases with temperature. The carrier injection and recombination processes in case of the plasma effect is associated with a parasitic thermal tuning. Any heating of the laser cavity will also increase the threshold current and decrease the differential efficiency of the laser. This can limit the tunability of the laser diode by temperature tuning. In wavelength tunable lasers diodes, an increase of the driving current will increase the temperature which causes an increase of the refractive index. However the carriers effects will decrease the refractive index and this leads to a limitation in refractive index wavelength tuning.

Vernier Effect Tuning

DBR and DFB lasers can be tuned by either changing the injected current or changing the temperature, however there is a limitation to these methods due to a limit in how much the refractive index can be changed. The total tuning range using these methods is 5nm-10nm. There is a large amount of research in how to extend the tuning range of the laser diode beyond the refractive index limits [20] [21] [22] [23] [24] [25] [26] [27] [28] [29]. In order to increase the tunability further, a technique that allows us to use a change in the refractive index difference instead of the refractive index itself and therefore allowing a relative wavelength change to be used which can be much larger than the wavelength change due to a refractive index change. One method that exploits this refractive index difference of semiconductor lasers is the Vernier tuning effect. This effect requires two differing wavelength dependent mirror reflectivities to produce two spectrally different comb mode reflection spectra. The comb mode reflection peaks will overlap at certain wavelengths where the lasing will occur as the gain will overcome loss since the round-trip loss is inversely proportional to the product of two reflectivities. Both mirror reflection can be directly and independently controlled by controlling the effective refractive index in those mirror sections. Any change in the effective refractive index in the mirror sections will produce a shift in the comb mode reflection spectrum and allow different reflection peaks to overlap and shift the wavelength accordingly. Using the Vernier tuning effect greatly increases the tuning range and lasers such as Sampled Grating Distributed Bragg Reflector SG-DBR laser have shown tuning ranges of up to 60 nm [30]. There some practical limitations to this effect in tunable lasers:

- The coincidence spacing must be comparable to the width of the gain spectrum or modes at the neighbour coincidences must be suppressed to keep high SMSR.
- The difference in the reflection periods should be comparable with the width of the individual reflection maxima.
- The cavity gain difference must be sufficient to supress other modes.
- The phase condition must be satisfied so that the round- trip phase of the desired mode must be multiple of 2π .

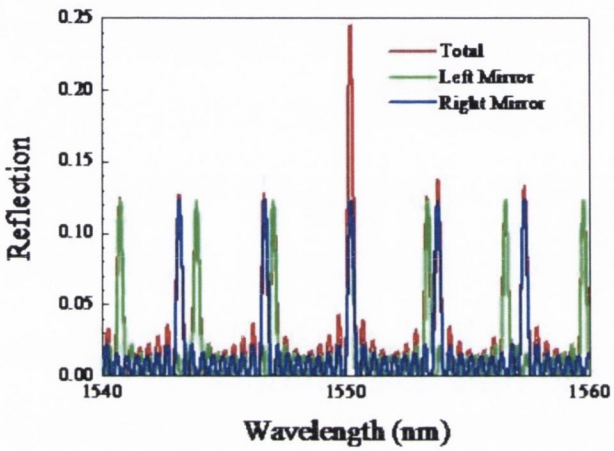

Figure 2.13. Vernier tuning effect showing an overlap of two comb- mode spectrums at 1550nm.

2.4. DBR-Type Laser Structures

In the previous section it was shown how a comb- like reflection spectrum can be achieved by using a cavity as a reflector, and how it could be used to achieve an external tuning range. However the Vernier tuning is not suitable for implementation in a practical laser structure as sufficiently high values of the reflectivity cannot be easily achieved in a monolithic structure. Instead it is possible to use a structure with multiple cavities and to use a short grating as reflector for each cavity. There are different ways to do so.

Sampled grating DBR laser

A comb- like reflection spectrum can be achieved by using a sampled grating [31] [32] [33]. The sampled grating consists of several sections of interrupted grating and each sampling period of the length L_s acts like a short cavity with the discrete reflector replaced by a grating. The reflection peaks are separated by

$$\Delta\lambda_s = \frac{\lambda^2}{2n_g L_s} \tag{2.51}$$

where n_g is the group index of the structure [1]. By controlling the refractive index of both mirrors separately and having differing sampling lengths in each mirror section the wavelength output can be controlled by the Vernier mechanism as was described in the previous section. To take advantage of the Vernier tuning, a laser with sampled gratings at both front and back mirrors, with the sampling periods $L_{s,f}$ and $L_{s,b}$ being different, can be fabricated. By increasing the refractive index of the front section which has a long sampling period, a discontinuous tuning toward longer wavelength is achieved. By increasing the refractive index of the back mirror which has a short sampling period, a discontinuous tuning toward shorter wavelength is achieved. When the front section is tuned, the width of the wavelength jumps is determined by the reflection peak spacing of the back section and vice versa. In order to get a higher fraction of the total emitted power from the front, it is advantageous to use a design with a lower number of sampling periods at the front than at the back.

A schematic structure of an SG-DBR laser is shown in figure 2.14.

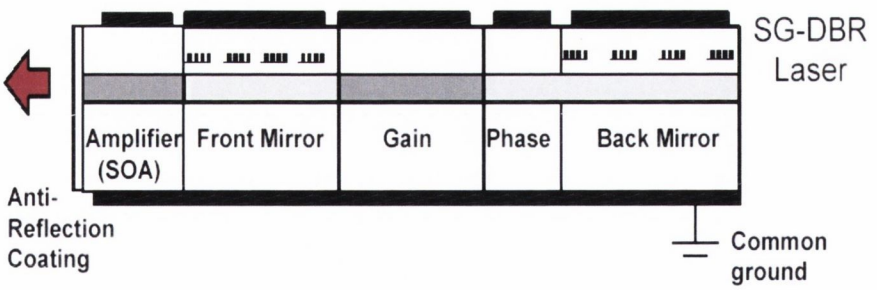

Figure 2.14. A schematic structure of an SG-DBR laser.

The device consists of five independent sections, a semiconductor optical amplifier, a front mirror, an active gain section, a phase section and the back mirror. For a comparison of the performance of the slotted lasers described later in this thesis, we checked the tuning behavior of a commercial packaged sampled grating distributed Bragg reflector (SG-DBR) semiconductor laser. The current injected to the gain section was kept constant with a value of 150 mA. Current injected to the front and back mirrors

were scanned between 0-100 mA and 0-150 mA respectively. The phase section was left unbiased. The temperature during the measurements was kept constant at 20°C. The wavelength tuning map is shown in figure 2.15 below. Seven super-modes are clearly visible over the tuning range of about 50 nm. The super- mode islands are found to change from the small ones toward the big ones as the currents injected into the mirror sections are increasing.

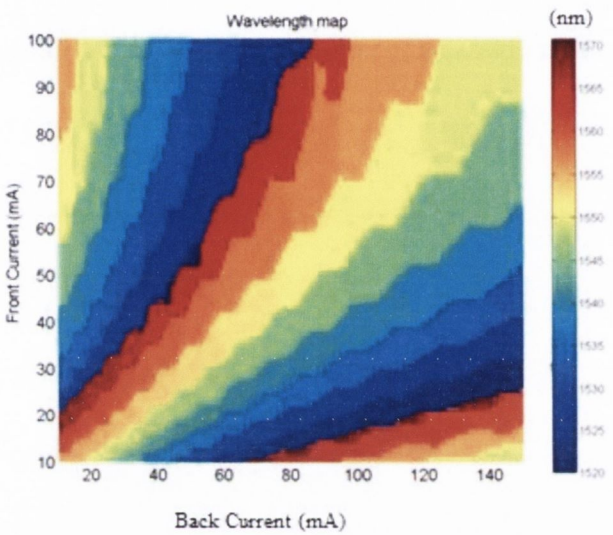

Fig 2.15. SG-DBR laser wavelength tuning map versus the current injected to the front and back mirrors.

The SMSR map is shown in figure 2.16. It can be seen that the tuning islands have a hexagonal shape and the highest SMSR value is placed in the center of each tuning island.

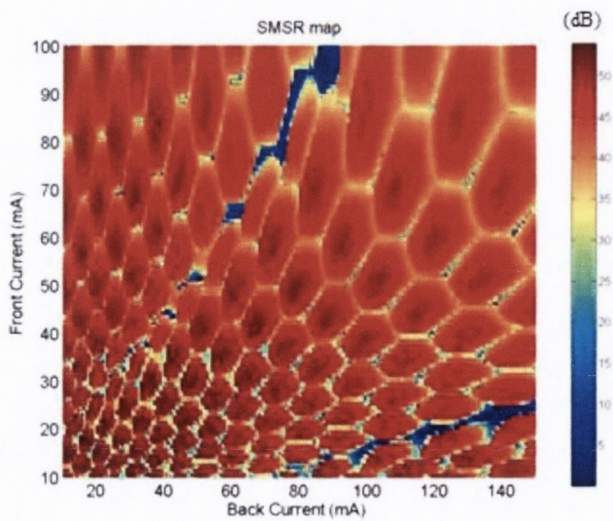

Fig 2.16. SG-DBR laser SMSR tuning map versus the current injected to the front and back mirrors.

SMSR and output power versus wavelength are shown in figure 2.17 below. Seven distinct super-modes can be clearly visible over the tuning range of 50 nm from 1520nm to 1570nm. All modes exhibit an SMSR of up to 50dB. The output power versus peak wavelength shown in figure 2.17 (b) is uniform, with variation within 2dBm.

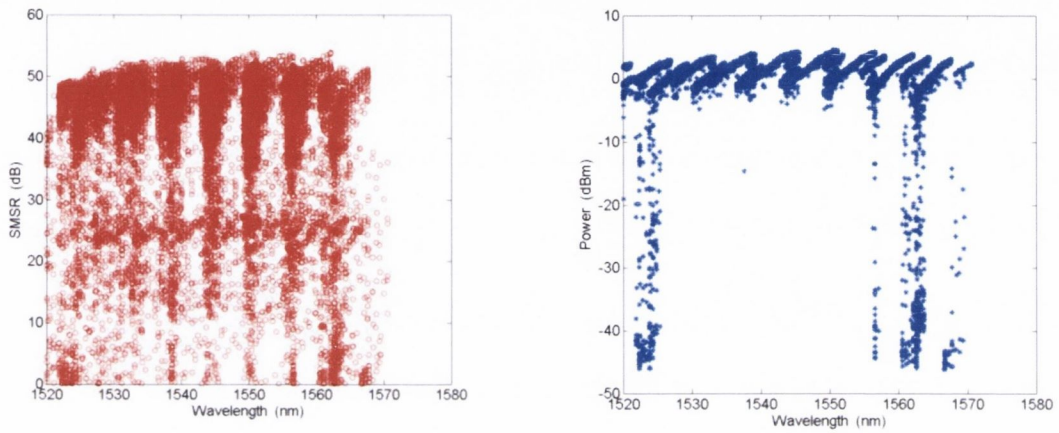

(a) (b)

Fig. 2.17. (a) SMSR vs. peak wavelength; (b) output power vs. peak wavelength for SG-DBR laser

Superstructure- Grating (SSG) DBR Laser

Another design of widely tunable laser is the SSG structure. The SSG structure is based on linear chirping in the grating pitches with a large period [34] [35] [36]. The linear chirping results in a high- reflection band over a wide wavelength range. The grating pitch in the SSG chirps continuously from Λ_a to Λ_b as one unit with a large period of Λ_s . The periodicity of the modulated grating pitch results in a spectrum with high reflection peaks in the wavelength range from $\lambda_a = 2n_g\Lambda_a$ to $\lambda_b = 2n_g\Lambda_b$, where n_g is the refractive index of the waveguide. The two SSG reflectors have comb-shaped reflection spectra, with slightly different peak spacing. For stable single-mode operation, a peak of each reflection comb and a longitudinal mode have to be aligned. The SSG reflectors can be tuned by current injection. A typical tuning characteristic is shown in figure 2.19. If one of the reflectors is tuned, different pairs of reflector peaks will successively overlap and the lasing frequency will jump by approximately the peak spacing [37].

A schematic structure of a SSG-DBR laser is shown in figure 2.18.

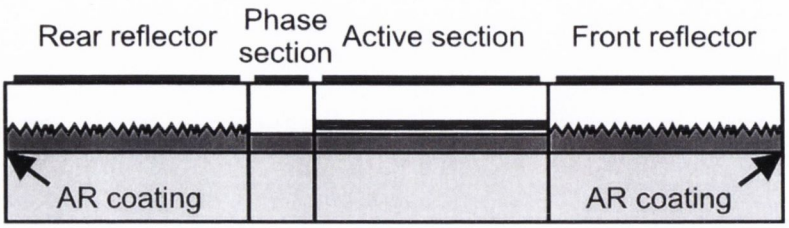

Figure 2.18. Schematic structure of SSG-DBR laser [37]

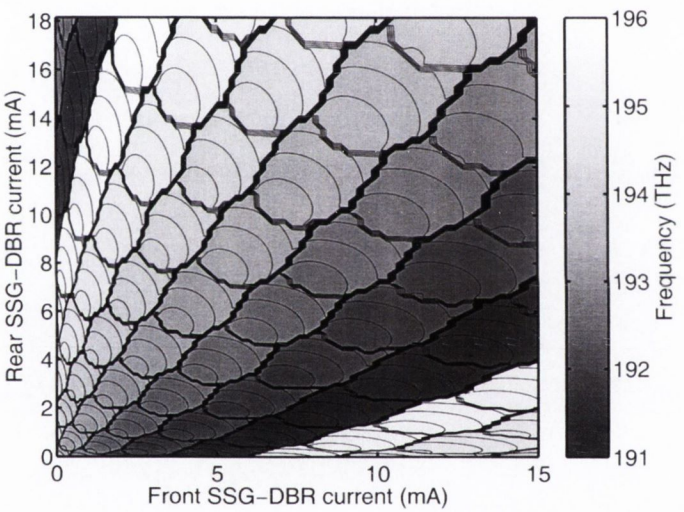

Figure 2.19. An example of a typical tuning map for SSG-DBR laser [37].

Digital Supermode DBR lasers (DS-DBR)

Instead of using a sampled or superstructure grating as a front mirror, it is possible to use a set of gratings having a relatively low reflection and a relatively broad bandwidth. The reflection maxima for the gratings occur at different wavelengths [38] [39]. The laser structure is shown schematically in figure 2.20 below. If current is supplied to one of the front sections, the corresponding reflection maximum moves to a shorter wavelength. This gives rise to an increased reflection over a certain wavelength range. A particular wavelength in that range can then be picked out by tuning reflection comb provided by

the back mirror. As the selection mechanism is partly digital – switching on a given current, the laser structure is called digital super-mode DS DBR [40].

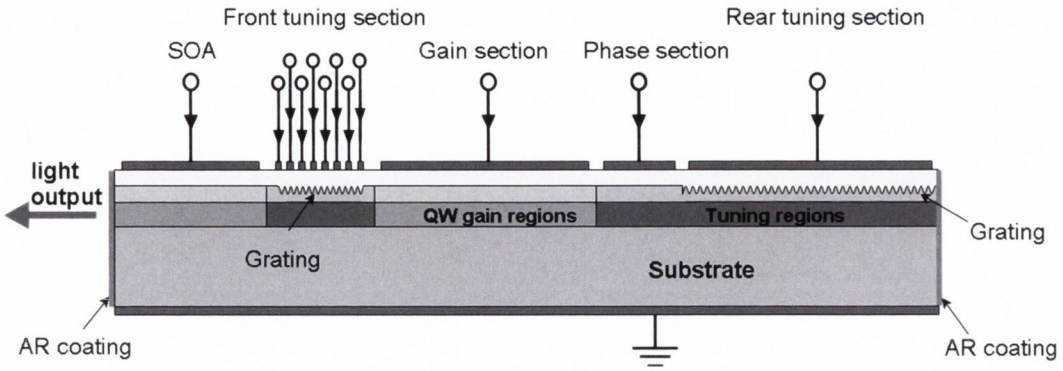

Figure 2.20. Schematic structure of DS- DBR laser [41].

An example of the wavelength tuning map of a DS-DBR laser is shown in figure 2.21.

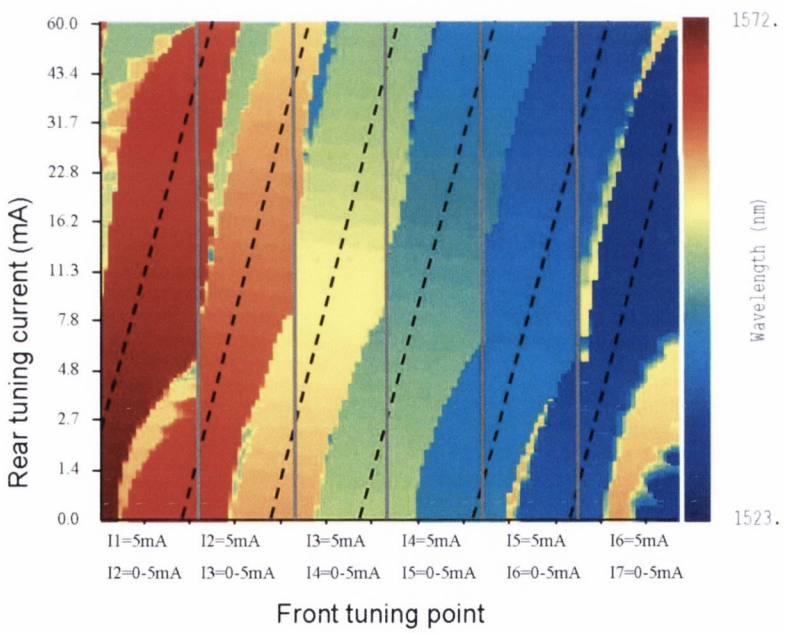

Figure 2.21. An example of a wavelength tuning map for a DS- DBR laser [42].

Conclusion

In this chapter an introduction to tunable lasers was presented. First a typical single mode lasers: distributed Bragg reflector (DBR) and distributed feedback (DFB) lasers were described as an introduction to grating structures. Then various tuning mechanism were introduced as well as the Vernier tuning effect to extend the laser tuning range. Finally, various types of DBR tunable are described to give an idea how the slotted lasers fit in the general tunable laser field.

References

[1] J. Buus, M. Amann and D. Blumenthal, Tunable laser diodes and related optical sources, IEEE Wiley- Interscience, 2005.

[2] J. Buss, "Single frequency semiconductor lasers, ISBN 0-8194-0535-3, 1991.

[3] L. Coldren, S. Corzine and M. Masanavic, Diode lasers and photonics integrated circuits, Wiley; 2nd edition, 2012.

[4] H. Haus and C. Shank, „Antisymmetric taper of distributed feedback lasers," *IEEE Jornal of Quantum Electronics,* vol 12, pp. 532-539, 1976.

[5] K. Utaka, S. Akiba, K.Sakai and Y. Matsushima, „Analysis of quarter- wave- shifted DFB laser," *Electronics Letters,* vol 20, pp. 326-327, 1984.

[6] S. Chinn, „Effects of mirror reflectivity in a distributed- feedback laser," *IEEE Journal of Quantum Electronics,* vol 20, pp. 574-580, 1973.

[7] J. Buus, „Dynamic single- mode operation of DFB lasers with phase shifter gratings and reflecting mirrors," *IEE Proceedings J (Optoelectronics)* , vol 133, no 2, pp. 163-163, 1986.

[8] K. Kobayashi and I. Mito, „Single frequency and tunable laser diodes," *IEEE Journal of Lightwave Technology,* vol 6, pp. 1623-1633, 1988.

[9] T. Koch and U. Koren, „Semiconductor lasers for coherent optical fiber communications," *IEEE Journal of Lightwave Technology,* vol 8, pp. 274-293, 1990.

[10] H. Yamamoto, M. Asada and Y. Suematsu, „Electric- field- induced refractive index variation in quantum- well structure," *Electronics Letters,* vol 21, pp. 579- 580, 1985.

[11] N. Susa and T. Nakahara, „Enhancement of change in the refractive index in an asymmetric quantum well," *Applied Physics Letters,* vol 60, pp. 245-2459, 1992.

[12] R. Soref and J. Lorenzo, „All- silicon active and passive guided- wave components for λ=1.3 and 1.6 micorns," *IEEE Journal of Quantum Electronics,* vol 22, pp. 873-879, 1986.

[13] J. Weber, „Optimization of the carrier- induced effective index change in InGaAsP waveguides- Application of tunable Bragg filters," *IEEE Journal of Quantum Electronics,* vol 1, pp. 116-120, 1994.

[14] S. Chuang, Physics of Optoelectronic Devices, Chichester U.K.: Wiley, 1995.

[15] H. Yamamoto, M. Asada and Y. Suematsu, „Electric- field induced refractive index variation in quantum- well structure," *Electronics Letters,* vol 21, pp. 579-580, 1985.

[16] J. Zucker, I. B.-. Joseph, B. Miller, U. Koren and D. Chemla, „Quaternary quantum wells for electro-optic intensity and phase modulation at 1.3 and 1.55 micorns," *Applied Physics Ltters,* vol 54, pp. 10-12, 1988.

[17] N. Susa and T. Nakahara, „Enhancement of change in the refractive index in an asymmetric quantum well," *Aplied Physics Letters,* vol 60, pp. 2457-2459, 1992.

[18] N. Susa, „Electric- field- induced index change in InGaAs-InAlAs asymmetric coupled quantum wells," *IEEE Journal of Quantum Electronics,* vol 31, pp. 92-100, 1995.

[19] K. Chinen, K. Gen-Ei, H. Suhara, A. Tanaka, M. T, K. Konno and Y. Muto, „Low-threshold 1.55 micorns InGaAsP/InP buried heterostructure distributed feedback lasers," *Applied Physics Letters,* vol 51, pp. 273-275, 1987.

[20] V. Jayaraman, Z. Chuang and L. Coldren, „Theory, design and performance of extended tuning range semiconductor lasers with sampled gratings," *IEEE Journal of Quantum Electronics,* vol 29, pp. 1824-1834, 1993.

[21] Y. Tohmori, Y. Yoshikuni, H. Ishii, F. Kano, T. Tamamura, Y. Kondo and M. Yamamotot, „Broad- range wavelength - tunable supersturucture gratin (SSG) DBR lasers," *IEEE Journal of Quantum Electronics,* vol 29, pp. 1817-1823, 1993.

[22] J. Wesstrom, S. hammerfeldt, J. Buus, R. Siljian, R. Laroy and H. d. Vries, „Design of a widely tunable modulated grating Y- branch laser using the additive Vernier effect for improved super- mode selection," *IEEE 18th International Coference in Semiconductor Lasers,* pp. 99-100, 2002.

[23] P. Rigole, S. Nilsson, L. Backbom, T. Klinga, J. Wallin, B. Stanacke, E. Berglind and B. Stoltz, „114-nm wavelenth tuning range of a vertical grating assisted codirectional coupler laser with a super structure grating distributed Bragg reflector," *IEEE Photonics Technology Letters,* vol 7, pp. 687-699, 1995.

[24] A. Ward, D. Robbins, G. Busico, N. Whitbread, P. Williams, D. Reid and J. Rawsthorne, „Modelling of phase grating based wideband tunable lasers with simplified quasi- digital wavelength selection," *IEEE Optoelectronics Proceedings,* vol 150, pp. 199-204, 2003.

[25] G. Morthier, B. Moeyersoon and R. Beats, „A sampled of superstructure grating

tunable twin- guide laser for wide tunability with 2 tuning currents," *in Optical Fiber Communication Conference and Exhibit,* vol 2, pp. TuB2-1-TuB2-3, 2001.

[26] C. Chang-Hasnain, „Tunable VCSEL," *IEEE Journal of Selected Topics in Quantum Electronics,* vol 6, pp. 978-987, 2000.

[27] F. Riemenschneider, M. Maute, H. Halbritter, G. Boehm, M. Amann and P. Meissner, „Continuously tunable long- wavelength MEMS-VCSEL with over 40-nm tuning range," *Phototnics Technology Letters,* vol 16, pp. 1429-1432, 2004.

[28] P. Signoret, M. Myara, J. Tourrenc, B. Orsal, M. Monier, J. Jacquet, P. Leboudec and F. Marin, „Bragg section effects on linewidth and lineshape in 1.55 micron DBR tunable laser diodes," *Phototnics Technology Letters,* vol 16, pp. 1429-1431, 2004.

[29] A. Syrbu, V. Iakovlev, G. Suruceanu, A. Caliman, A. Rudra, A. Mircea, A. Mereuta, S. Tadeoni, C. Berseth, M. Achtenhagen, J. Boucart and E. Kapon, „1.55 micron optically pumped wafer- fused tunable VCSELs with 32-nm tuning range," *Photonics Technology Letters,* vol 16, pp. 1991-1993, 2004.

[30] B. Mason, G. Fish, J. Barton, L. Coldren and S. DenBaars, „Characteristics of sampled grating DBR lasers with integrated semiconductor optical amplifiers," *in Optical Fiber Communication Conference* , vol 1, pp. 193-195, 2000.

[31] L. Coldren, G. Fish, Y. Akulova, J. Barton, L. Johansson and C. Coldren, „Tunable semiconductor lasers: a tutorial," *Journal of Lightwave Technology,* vol 22, no 1, p. 193, 2004.

[32] T. Liijeberg, R. Tohmon, E. Hall, P. Abraham, M. Focht, G. A. Fish, M. C. Larson and L. A. Coldren, „High-power, widely-tunable sampled grating DBR laser integrated with a semiconductor optical amplifier," *IEEE in 18th International Semiconductor Laser Conference,* pp. 45-46, 2002.

[33] H. Wang, J. Zhao and Y. Yu, „A novel tunable semiconductor laser based on a sampled grating reflector and an interleaved sampled grating reflector," *In Asia Communications and Photonics Conference and Exhibition, Optical Society of America,* p. 83080J, 2011.

[34] Y. Tohmori, Y. Yoshikuni, H. Ishii, F. Kano, T. Tamamura, Y. Kondo and M. Yamamoto, „Broad-range wavelength-tunable superstructure grating (SSG) DBR lasers," *IEEE Journal of Quantum Electronics,* vol 29, no 6, pp. 1817- 1823, 1993.

[35] Y. Tohmori, Y. Yoshikuni, H. Ishii, F. Kano, T. Tamamura and Y. Kondo, „Over 1100 nm wavelength tuning in superstructure grating (SSG) DBR lasers," *Electronics letters,* vol 29, no 4, pp. 352-354, 1993.

[36] H. Ishii, H. Tanobe, F. Kano, Y. Tohmori, Y. Kondo and Y. Yoshikuni, „Quasicontinuous wavelength tuning in super-structure-grating (SSG) DBR lasers," *IEEE Journal of Quantum Electronics,* vol 32, no 3, pp. 433-441, 1996.

[37] G. Sarlet, G. Morthier and R. Baets, „Control of Widely Tunable SSG-DBR Lasers for Dense Wavelength Division Multiplexing," *journal of Lightwave Technology,* vol 18, no 8, pp. 1128-1138, 2000.

[38] A. Ward, D. Robbins, G. Busico, E. Barton, L. Ponnampalam, J. Duck, N. Whitbread, P. Williams, D. Reid, A. Carter and M. Wale, „ Widely tunable DS-DBR laser with monolithically integrated SOA: design and performance.," *IEEE Journal of Selected Topics of Quantum Electronics,* vol 11, no 1, pp. 149-156, 2005.

[39] A. J. Ward, G. Busico, N. D. Whitbread, L. Ponnampalam, J. P. Duck and D. J. Robbins, „Linewidth in widely tunable digital supermode distributed Bragg reflector lasers: Comparison between theory and measurement," *IEEE Journal of Quantum Electronics,* vol 42, no 11, pp. 1122-1127, 2006.

[40] L. Ponnampalam, D. J. Robbins, A. J. Ward, N. D. Whitbread, J. P. Duck, G. Busico and D. J. Bazley, „Equivalent performance in C-and L-bands of digital supermode distributed bragg reflector lasers," *IEEE Jurnal of Quantum Electronics,* vol 43, no 9, pp. 798-803, 2007.

[41] L. Ponnampalam, D. J. Robbins, A. J. Ward, N. D. Whitbread, J. P. Duck, G. Busico and D. J. Bazley, „Equivalent Performance in C- and L-Bands of Digital Supermode Distributed Bragg Reflector Lasers," *IEEE Journal of Quantum Electronics,* vol 43, no 9, pp. 798-803, 2007.

[42] A. J. Ward, G. Busico, N. D. Whitbread, L. Ponnampalam, J. P. Duck and D. J. Robbins, „Linewidth in Widely Tunable Digital Supermode Distributed Bragg Reflector Lasers: Comparison Between Theory and Measurement," *IEEE Journal of Quantum Electronics,* vol 42, no 11, pp. 1122-1127, 2006.

Chapter 3. Fabry- Perot laser characterization.

Introduction

The Fabry- Perot laser is the simplest kind of semiconductor laser. It is very easy to fabricate and widely used in laboratories and industry. As it is a multimode laser it is not suitable for many applications such as optical communication systems, where the single mode operation is desirable. Fabry- Perot laser are preferable in cases where the cost of fabrication is crucial and when the bandwidth of the emission spectrum does not play a very important role. The Fabry- Perot laser can be used as a cheap wavelength- division-multiplexing sources in fiber- to the- home applications [1]. Also in laboratories FP lasers are very useful to obtain the material and device information such as the modal gain, internal loss, injection efficiency, linewidth enhancement factor. Various methods were developed to extract those parameters from the fabricated FP laser. One of them is the cutback method [2] which requires FP lasers with different cavity lengths. The internal loss and injection efficiency can be estimated by measuring the relationship between the output slope efficiency and the cavity length. To obtain the net modal gain the amplified spontaneous emission spectrum of the FP laser operating below the threshold needs to be recorded. There are various methods to extract the net modal gain, such as the Hakki-Paoli method [3], the Fourier transform method [4] [5], the method proposed by Cassidy [6], and the Fourier series expansion FSE method [7].

In this chapter a Fabry- Perot laser will be characterized based on its amplified spontaneous emission spectrum and Fourier series expansion method as it was described in [8]. The internal loss and quasi- Fermi level separation will be obtained and also geometric spontaneous emission factor as well as injection efficiency and linewidth enhancement factor will be calculated. The Fabry- Perot laser used for those measurements has a length of 650μm with a threshold of 19mA. All measurements were carried out for the laser operating below the threshold current.

3.1. Characterization method

Theoretical description of the ASE spectrum

A schematic of a Fabry- Perot laser is shown in figure 3.1. The theoretical ASE spectrum output from the facet at zero can be obtained by integrating the small ASE contributions from small sections along the whole cavity. From a section of unit length located at x, we can separate the ASE contribution into two parts: (i) part initially propagating toward the facet at zero F^-, (ii) part initially propagating toward the facet at L, F^+. Then it is possible to express those two parts as:

$$F^- = \frac{\sqrt{S}\exp\left(-jkn_{eff}x\right)\sqrt{1-R_l}\exp\left((g/2)x\right)}{1-b\exp\left(-j2kn_{eff}L\right)} \qquad (3.1)$$

$$F^+ = \frac{\sqrt{S}\exp\left(-jkn_{eff}\left(2L-x\right)\right)\sqrt{\left(1=R_l\right)R_r}\exp\left(g/2\left(2L-x\right)\right)}{1-b\exp\left(-j2kn_{eff}L\right)} \qquad (3.2)$$

where S is the spontaneous emission from the active region that is coupled into the waveguide mode per unit length and has a unit of mW/(nm*cm), $k=\frac{2\pi}{\lambda}$ is the wavelength number in vacuum, n_{eff} is the effective index of the laser waveguide, R_l is the left facet reflectivity and R_r is the right facet power reflectivity. R_l and R_r are equal to each other for a Fabry- Perot cavity with uncoated cleaved facets, $b=\exp(gL)\left(R_lR_r\right)^{1/2}$ is the round- trip gain, g is the net modal gain, L is the cavity length.

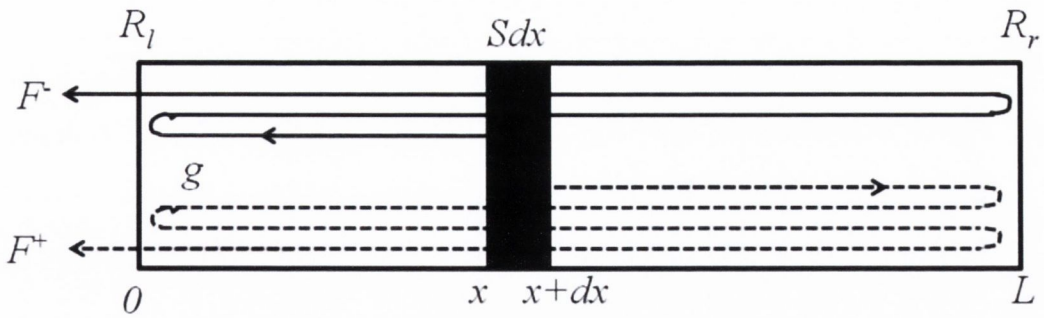

Figure 3.1. Schematic structure of a Fabry- Perot laser [8].

Summing those two parts, calculating the ASE contribution from the section is possible. There are two ways to do the summation: first is the amplitude summation and the second one is the power summation. Here we use an amplitude summation [9]. After neglecting a small term the result is the same as it would be using the power summation. The ASE contribution from this small section is obtained as follows

$$\begin{aligned}\left|F^- + F^+\right|^2 &= \frac{S(1-R_l)\exp(gL)}{1+b^2-2b\cos(2kn_{eff}L)} \\ &\times\left[\exp(g(x-L)) + R_r\exp(g(L-x)) + 2\sqrt{R_r}\cos(2kn_{eff}(L-x))\right]\end{aligned} \tag{3.3}$$

By integrating the contributions from the whole laser cavity, the ASE emission from the total laser cavity can be expressed as

$$\begin{aligned}I &= \frac{S(1-R_l)\exp(gL)}{1+b^2-2b\cos(2kn_{eff}L)} \\ &\times\left[\frac{(1+R_r\exp(gL))(1-\exp(-gL))}{g} + \frac{\sin(2kn_{eff}L)}{kn_{eff}}\right] \\ &\approx \frac{S(1-R_l)(1+R_r\exp(gL))(\exp(gL)-1)}{g} \\ &\times\frac{1}{1+b^2-2b\cos(2kn_{eff}L)}\end{aligned} \tag{3.4}$$

where kn_{eff} is around $1.3*10^5 cm^{-1}$. Because g has a maximum value of 40 cm^{-1} for a Fabry- Perot laser with a cavity length of 300μm, therefore a good approximation is to

neglect the latter term in the square bracket in equation 3.4 along with assuming that S and g are uniform along the cavity. This assumption can be made if the Fabry- Perot laser is biased under threshold as then the stimulated emission causing the carried density to vary along the laser cavity, is negligible. The spontaneous emission S can be written as

$$S = \frac{hc}{\lambda} r_{sp} A \beta_g \tag{3.5}$$

where h is the Plank constant, c is the speed of light, A is the cross- section area of the quantum wells in the active region, β_g is the geometrical spontaneous emission factor describing the ratio of the spontaneous emission from the quantum wells into the waveguide mode in a single propagation direction, r_{sp} in the total spontaneous emission rate that has a unit of $1/(s*nm*cm^3)$. β_g described in [10] is defined as the fraction of the spontaneous emission with the same polarization as the waveguide mode is coupled into the waveguide mode. Equation 3.4 is describing the intrinsic ASE spectrum output from the left facet of the laser. In practice, the ASE spectrum needs to be coupled with a lensed fiber into the Optical Spectrum Analyser OSA and then measured. The measured spectrum can be expressed as

$$I' = \int I(\lambda') f(\lambda - \lambda') d\lambda' \tag{3.6}$$

where $f(x)$ is the OSA response function with x of an unit of nanometer. By using the OSA to measure a spectral line having a bandwidth narrower that the resolution bandwidth of the OSA itself, the response function can be extracted. In this case the spectral line can be written as $P_1 \delta(\lambda - \lambda_0)$, where P_1 is the total power of the spectral line and λ_0 is the central wavelength of the spectral line. The Dirac function has a unit of nm^{-1}. The spectrum measured by the OSA can be written as

$$\begin{aligned} P_2(\lambda) &= \int P_1 \delta(\lambda' - \lambda_0) f(\lambda - \lambda') d\lambda' \\ &= P_1 f(\lambda - \lambda_0) \end{aligned} \tag{3.7}$$

And therefore the response function of the OSA can be expressed as

$$f(x)=\frac{P_2(\lambda-\lambda_0)}{P_1} \tag{3.8}$$

Fourier series expansion method

More details about the Fourier series expansion method can be found in [7]. The Fourier series expansion FSE method forks on individual modes of the amplified spontaneous emission ASE spectrum. A schematic of a single longitudinal mode is shown in figure 3.2.

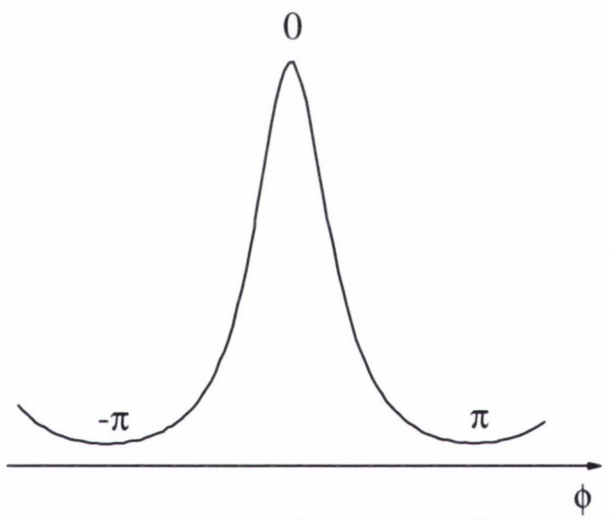

Figure 3.2. Schematic diagram of a single longitudinal mode [8].

The round trip phase $\phi = 2kn_{eff}L$ of a single longitudinal mode is varying from $-\pi$ to π where the mode peak has a phase of 0. The two adjustment valleys have phases of $-\pi$ and π, respectively. Carrying out the FSE operation, the following harmonics can be obtained

$$\tilde{I}_m=\frac{1}{2\pi}\int_{-\pi}^{\pi} I(\phi)\exp(-jm\beta\phi)d\phi \tag{3.9}$$

which can be calculated as

$$\tilde{I}_0 = \frac{S(1-R_l)(1+R_r \exp(gL))(\exp(gL)-1)}{g} \frac{1}{1-b^2} \tag{3.10}$$

$$\tilde{I}_m = \tilde{I}_0 b^{|m|} \tag{3.11}$$

where m is an integer. The approximation that the net modal gain and the round- trip gain are constant over the longitudinal mode range have to made to obtain those equations. This approximation can be made because the gain varies slowly over tens of nanometers while the longitudinal modes cover around 1 nm. The ratio between the first harmonic and the zeroth harmonic results in the round- trip gain b. In general, only the zeroth and first harmonics are used because they have better signal- to- noise ratio (SNR) [7]. By using the OSA, the ASE spectrum dependent on wavelength is always achieved. The wavelength can be related to the phase ϕ in a small wavelength range covered as

$$\phi = -2\pi \frac{\lambda - \lambda_l}{\Delta\lambda} \tag{3.12}$$

where $\Delta\lambda$ is the longitudinal mode spacing expressed as: $\Delta\lambda = \lambda_r - \lambda_l$. λ_r, λ_l are the wavelength at the right and left valley of the longitudinal mode peak, respectively. Based on equation 3.12, equation 3.9 can be re- written as

$$\tilde{I}_m = \frac{1}{\Delta\lambda} \int_{\lambda_l}^{\lambda_r} I(\lambda) \exp\left(j \frac{2m\pi(\lambda - \lambda_l)}{\Delta\lambda} \right) d\lambda \tag{3.13}$$

The obtained harmonics and the round- trip gain are defined as being at the peak wavelength of the longitudinal mode and this process can be repeated over the entire ASE spectrum to get the round- trip gain spectrum. Using the convolution theorem, the influence from the OSA response function can be solved resulting in

$$\tilde{I}'_m = \tilde{I}_m \tilde{f}_m \tag{3.14}$$

where

$$\tilde{f}_m = \int f(x)\exp\left(j2m\pi\frac{x}{\Delta\lambda}\right)dx \tag{3.15}$$

The zeroth harmonic of the longitudinal mode of the intrinsic ASE spectrum can be obtained by summarizing equation 3.15

$$\tilde{I}_0 = \frac{\tilde{I}_0'}{\tilde{f}_0} \tag{3.16}$$

and the round- trip gain of the same longitudinal mode can be written as

$$b = \frac{\tilde{I}_1'}{\tilde{I}_0'}\frac{\tilde{f}_0}{\tilde{f}_1} \tag{3.17}$$

Therefore the net modal gain can be calculated as

$$g = \frac{\log(b) - \log\left(\sqrt{R_l R_r}\right)}{L} \tag{3.18}$$

Method to obtain the internal loss and the quasi- Fermi level separation

To obtain the internal loss and the quasi- Fermi level separation an assumption is made that the Fabry- Perot cavity is formed simply by two identical cleaved facets without any coating so that $R_l = R_r \equiv R$. Having this the zeroth harmonic of the intrinsic ASE longitudinal mode can be simplified and therefore the spontaneous emission coupled into the waveguide mode can be calculated as

$$S = \frac{\tilde{I}_0 g(1-b)}{(1-R)(\exp(gL)-1)} \tag{3.19}$$

From equation 3.5, S includes the factor of the spontaneous emission rate r_{sp} that is related to the material gain g_m through the relationship [11]

$$g_m = \frac{\lambda^4}{8\pi c n^2} r_{sp} \left[1 - \exp\left(\frac{hc/\lambda - \Delta F}{k_B T} \right) \right] \tag{3.20}$$

where ΔF is the quasi- Fermi level separation, k_B is the Boltzmann constant, T is the carrier temperature, and n is the refractive index in the active region. The material gain is related to the net mode gain as

$$g = \Gamma g_m - \alpha_{in} \tag{3.21}$$

where Γ is the optical confinement factor and α_{in} is the internal loss. Combining equations 3.20 and 3.21 we get:

$$\begin{aligned} g(\lambda) &= C' \left(S \cdot \lambda^5 \cdot \left(1 - \exp\left(\frac{hc/\lambda - \Delta F}{k_B T} \right) \right) \right) - \alpha_{in} \\ &\equiv C' q(\lambda, \Delta F) - \alpha_{in} \end{aligned} \tag{3.22}$$

where

$$C' = \frac{\Gamma}{8\pi h A \beta_g c^2 n^2 C} \tag{3.23}$$

An extra constant C was added into equation 3.23 to include the coupling loss caused by the mode mismatch between the lensed fiber and the laser waveguide. The relationship between $g(\lambda)$ and $q(\lambda, \Delta F)$ is linear over different wavelengths [12] [13] , where g is measured and q is calculated based on S which is also measured and therefore the quasi- Fermi level separation ΔF can be determined. In practice ΔF is treated as a variable and is varying through a suitable range. For each of the variation a curve $g(\lambda) - q(\lambda)$ is fitted, where $g(\lambda)$ is treated as y and $q(\lambda)$ is treated as x, with a line $y = ax + d$. The standard deviation D between the vector y and the vector from the linear fitting y' is calculated for each variation of ΔF as

$$D = \frac{\sum_i \left(y_i - y_i^{'}\right)^2}{\sqrt{\sum_i y_i^2}\sqrt{\sum_i y_i^{'2}}} \tag{3.24}$$

The minimum value of D states corresponds to the quasi- Fermi level separation. When the quasi- Fermi level separation is obtained, the same fitting is used again and the interception d gives the internal loss α_{in} from 3.22 and the slope a yields $C^{'}$ as it was defined in 3.23. In practice, the OSA influence is removed by the procedures in eq. 3.16 and 3.17.

Calculation of spontaneous emission factor

It was shown above that another product from the fitting in the coefficient $C^{'}$ which includes the geometrical spontaneous emission factor β_g. This factor can be calculated as

$$\beta_g = \frac{\Gamma}{8\pi h A C^{'} c^2 n^2 C} \tag{3.25}$$

The optical confinement factor Γ can be calculated through simulation. To calculate the coupling coefficient C first a large area detector needs to be put very close to the laser output facet to measure the total power P-I curve of the laser. Then another P-I curve is measured by coupling the light using the lensed fiber. The coupling efficiency is the ratio of the coupled power to the total power when the laser is biased highly above the threshold.

Calculation of injection efficiency

The way to measure the internal loss was introduced in the third section and the injection efficiency can be obtained from the slope efficiency of the laser. Having the total power P-I curve, the slope efficiency can be calculated as 'dP/dI' which has units of mW/mA. The injection efficiency is describing the fraction of the injected carriers contributing to the stimulated emission above the threshold can be calculated as [14]

$$\eta = \frac{2\lambda e}{hc}\frac{dP}{dI}\left(1 - \frac{\alpha L}{\log(R)}\right) \tag{3.26}$$

where e is the electron charge. The factor 2 stands for the laser being measured from only one uncoated facet.

Calculation of linewidth enhancement factor.

The ratio between the real index change and the imaginary index change is called the linewidth enhancement factor. The imaginary index change is due to the change of the gain or loss of the quantum wells change by the current injection. In Fabry- Perot laser case the linewidth enhancement factor can be measured by measuring the ASE spectrum at two slightly different injection current [15]. The real index change can be extracted from the longitudinal mode wavelength change and the imaginary index change can be extracted from the net modal gain change. The formula to calculate the linewidth enhancement factor is

$$\alpha_{LWEF} = -\frac{\lambda_2 - \lambda_1}{\log(b_2) - \log(b_1)}\frac{2\pi}{\Delta\lambda} \tag{3.27}$$

where $\lambda_{1,2}$ are the longitudinal mode wavelengths at two different current injections, $b_{1,2}$ are the round- trip gain at those two injection currents for the same longitudinal modes, $\Delta\lambda$ is the longitudinal mode spacing. Various methods can be used to measure the round-trip gain and the best one is the FSE method (3.17) as the OSA response function is just giving the extracted round- trip gain a ratio correction that does not influence the linewidth enhancement factor [16].

3.2. Practical measurements

The measured Fabry- Perot laser has a cavity length of 650μm and a waveguide ridge has a width of 2.5 μm. An active layer consists of five AlGaInAs quantum wells that have an emission peak around 1550nm. During the measurements the laser was placed on a thermoelectric cooler that kept constant temperature of 20°C. Figure 3.3 shows the power-current P-I curve, from which the threshold current is 19mA with the slope efficiency of 0.35 mW/mA. The ASE spectrum was measured using an anti- reflection AR coated fiber. The spectrum was recorded using an Agilent Optical Spectrum Analyser (OSA) which has the lowest resolution of 0.06 nm. First, the measured ASE spectrum for OSA resolutions of 0.06nm, 0.1nm, 0.2nm and 0.5nm for the injection current of 18mA. The spectrum for different OSA resolution settings is shown in figure 3.4 below, where a 4nm range around the emission peak is shown. When the resolution of the OSA is decreased from 0.06nm to 0.5 nm, the longitudinal mode peak power increases by about 5dB while the valley power increases of about 12dB. The modes are about 0.85 nm apart.

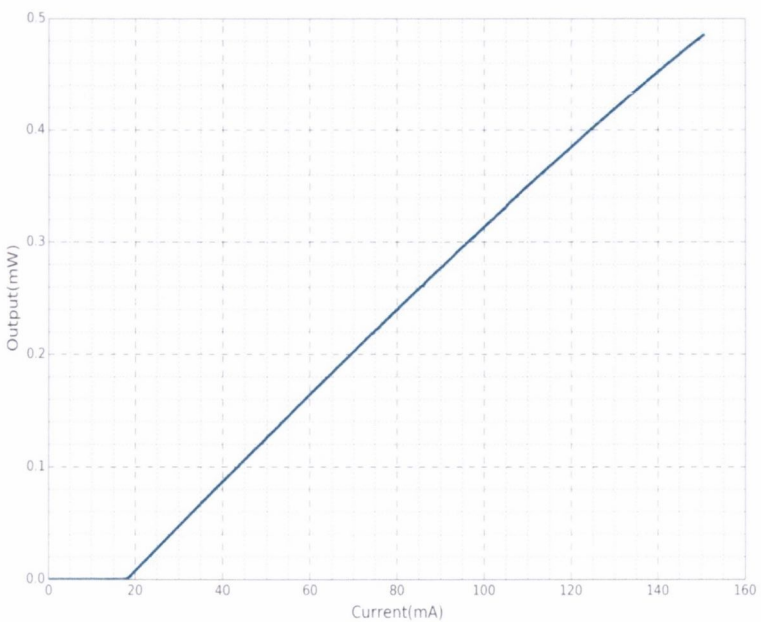

Figure 3.3. Power- current curve for the Fabry- Perot laser showing the threshold current.

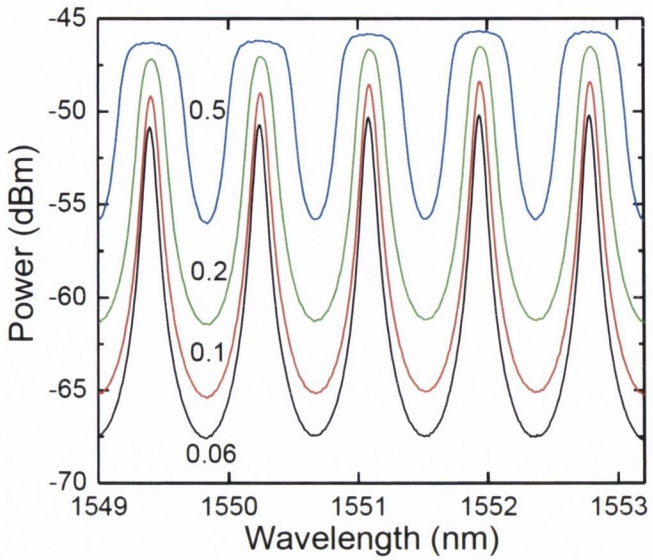

Figure 3.4. ASE spectrum measured with the OSA resolutions of 0.06, 0.1, 0.2, 0.5nm.

The response function of the OSA is shown in figure 3.5 below. The response function was found by measuring the emission spectrum of an external tunable laser with an emission wavelength of 1550nm. The linewidth of the emission line of the external laser was 150kHz while the resolution of the OSA is around 7.5GHz at the highest resolution of 0.06nm.

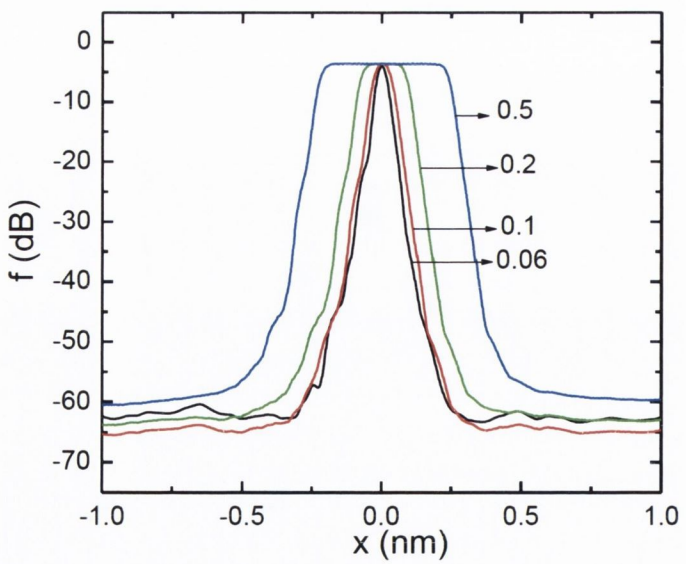

Figure 3.5. Response function of the OSA for resolution of 0.06, 0.1, 0.2, 0.5 nm.

To calculate the round- trip gain spectrum, first the ASE spectrum of the Fabry- Perot laser was measured for different injection current from 15mA to 18mA with a step of

0.5nm. The OSA resolution was set to 0.1nm. The step of 0.5 nm was chosen during the measurements because then the wavelength shift due to the current injection is lower than the mode spacing. The measured ASE spectrum of the Fabry- Perot laser for an injection current of 18mA is shown in figure 3.6 below. The emission peak of the laser is around 1550nm. From these measured ASE spectra, the round- trip gain was calculated for different injection currents from 15mA to 18mA as shown in figure 3.7.

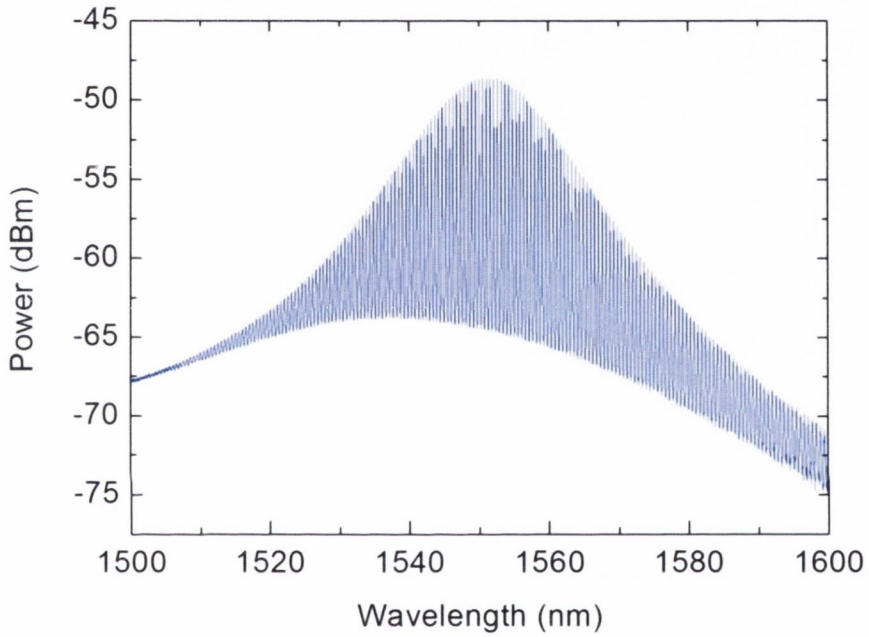

Figure 3.6. Measured ASE spectrum of Fabry- Perot laser for the wavelength of 1550nm and the resolution bandwidth of the OSA of 0.1nm.

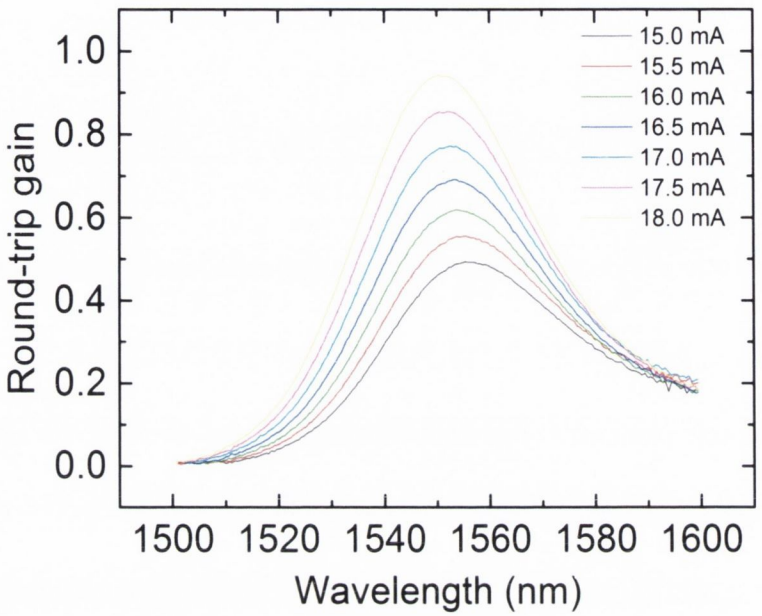

Figure 3.7. Extracted round- trip gain.

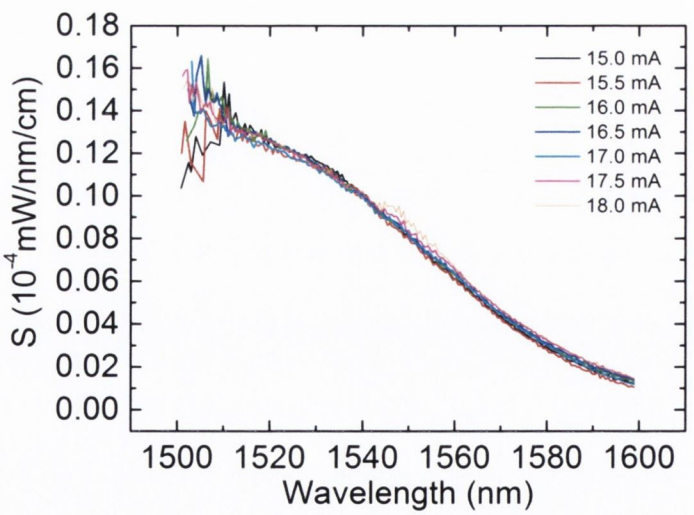

Figure 3.8. Extracted spontaneous emission coupled into the waveguide mode. Currents vary from 15 mA to 18mA with the step of 0.5 mA.

Next, the spontaneous emission coupled into the waveguide mode was calculated using eq. 3.19. The results are shown in figure 3.8. From 3.8 it is seen that the spontaneous emission spectrum is obtained only for the long wavelengths.

Based on the obtained spontaneous emission spectrum S, the spectrum of $q(\lambda, \Delta F)$ at different values of ΔF can be calculated and then the $g(\lambda)$-$q(\lambda)$ curve is fitted. The fitting effect is evaluated by the standard deviation calculated from eq. 3.24. The standard deviation versus different values of ΔF is shown in figure 3.9 for the current of 16mA. The estimated quasi- Fermi level separation for this particular current corresponds to the minimum value of the standard deviation. For the current of 18mA the estimated quasi-Fermi level separation is 0.8183 eV. At this value of ΔF , the g-q curve and the linear fit are shown in figure 3.10 below. It is seen that a very good linear fit is achieved. The intercept of the linear fit leads to the estimated internal loss which in this case is 18.72cm^{-1}.

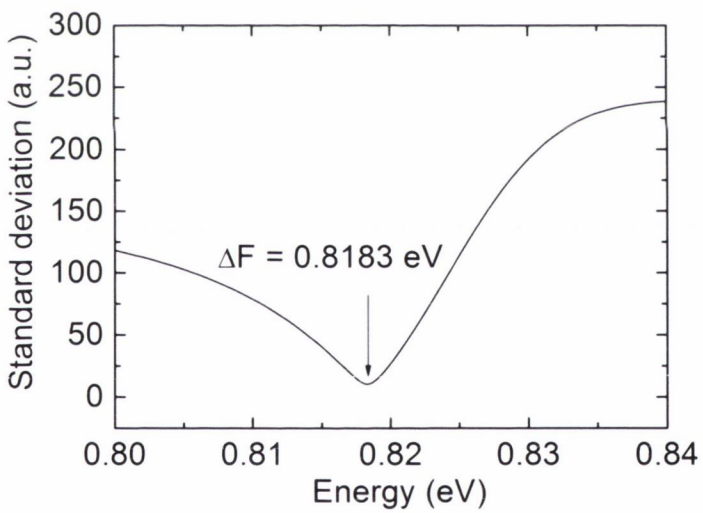

Figure 3.9. Standard deviation between the linear fit and the original g-q curve versus different values of ΔF.

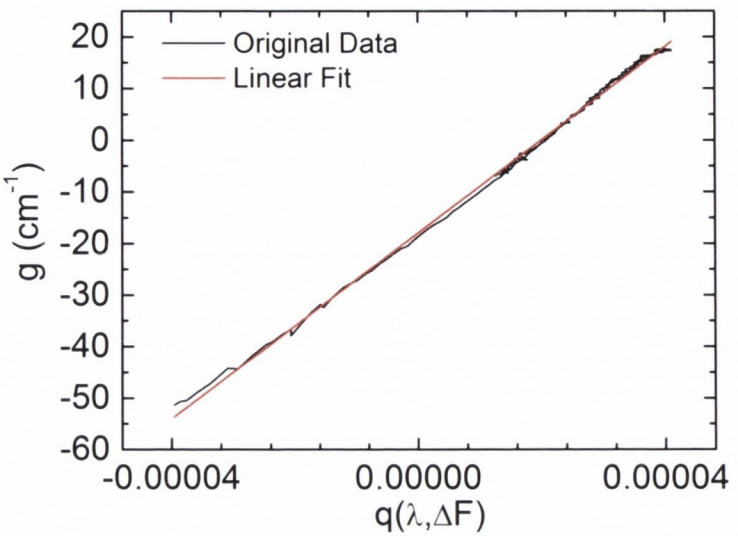

Figure 3.10. g-q curve and the linear fit when ΔF equals the estimated quasi- Fermi level separation.

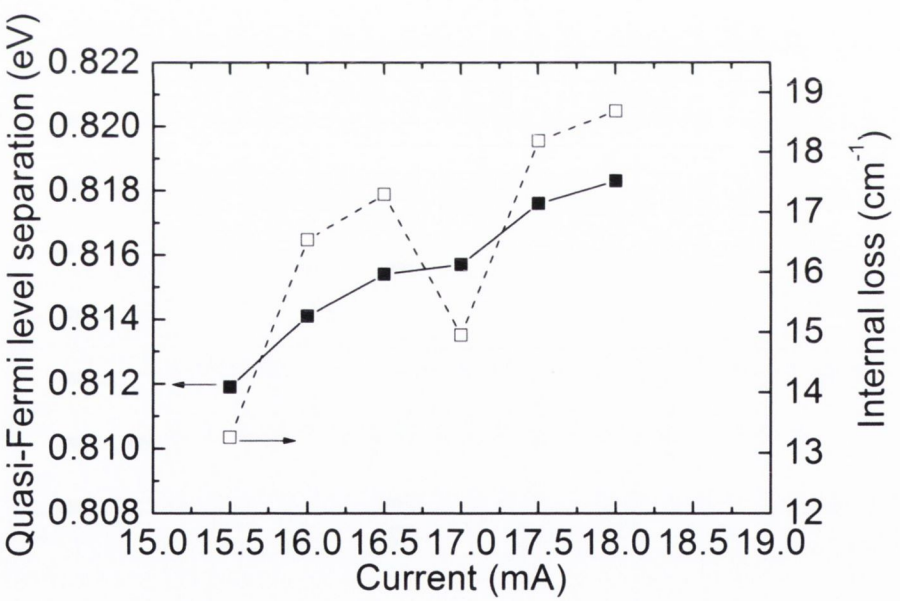

Figure 3.11. Extracted quasi- Fermi level separations and internal loss versus injected current.

The measurements from above were then repeated to find the quasi- Fermi level separation and internal loss for different injection currents as shown in figure 3.11 below. The quasi- Fermi level separation increases with the injection current up to 18mA. The internal loss varies from 13cm^{-1} to around 19cm^{-1} for different current injections.

The extracted quasi- Fermi has a standard deviation of 0.1 meV which is independent of the injected currents. On the extracted net modal gain curve, the value corresponding to the quasi- Fermi level separation is the internal loss as the gain at the position of the quasi- Fermi level separation is zero. From 3.12 the slope of the curve at the position of the quasi- Fermi level separation is -2.12 cm^{-1}/meV for the current of 18mA. It means that the deviation of the quasi- Fermi level separation by 0.1 meV will cause the estimated internal loss to deviate by 0.21 cm^{-1}.

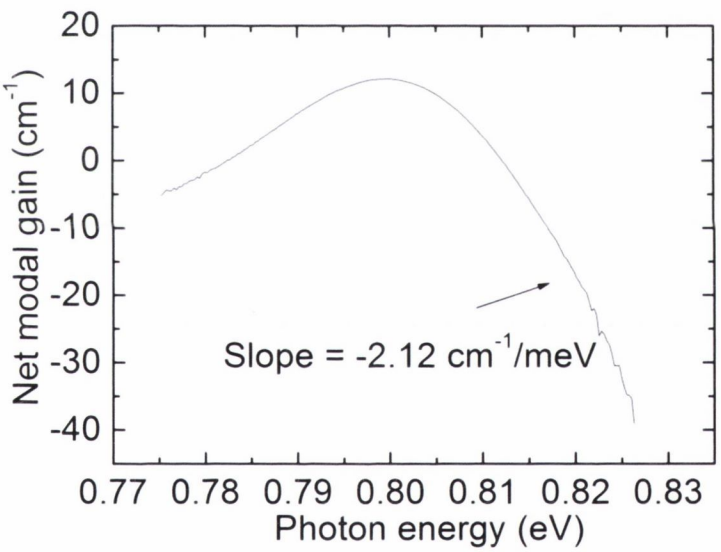

Figure 3.12. Net modal gain versus photon energy for current of 18mA.

From the linear fit the coefficient $\dot{C}$ is also extracted. It is close to 600 mW^{-1}μm^{-1}. Based on this coefficient the geometrical spontaneous emission factor can be calculated using equation 3.24. The optical confinement factor Γ is calculated to be around 5% and therefore each quantum well possessing 1%. The cross- section area of the quantum wells in the active region is $2.5\times0.006\times5=0.075\mu m^2$. The geometrical spontaneous emission factor is shown in figure 3.13 below. The value of the geometrical spontaneous emission is dimensionless and is around 0.00014 for the injected currents.

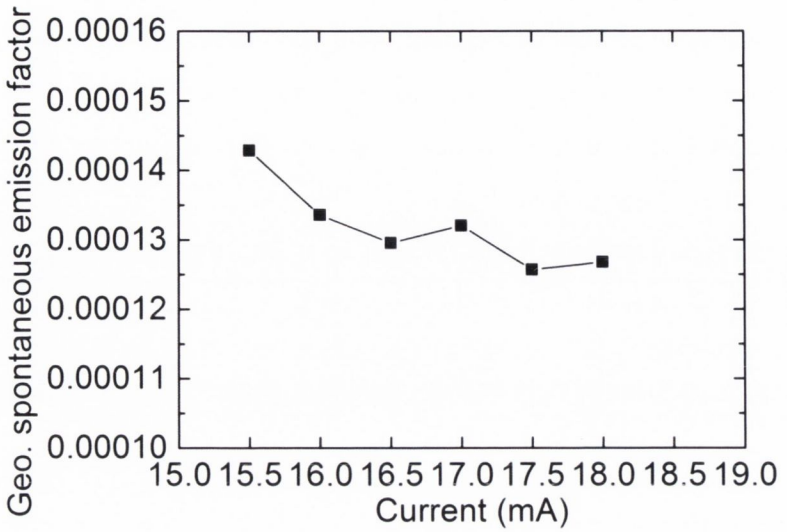

Figure 3.13. Calculated geometrical spontaneous emission factor versus injected current.

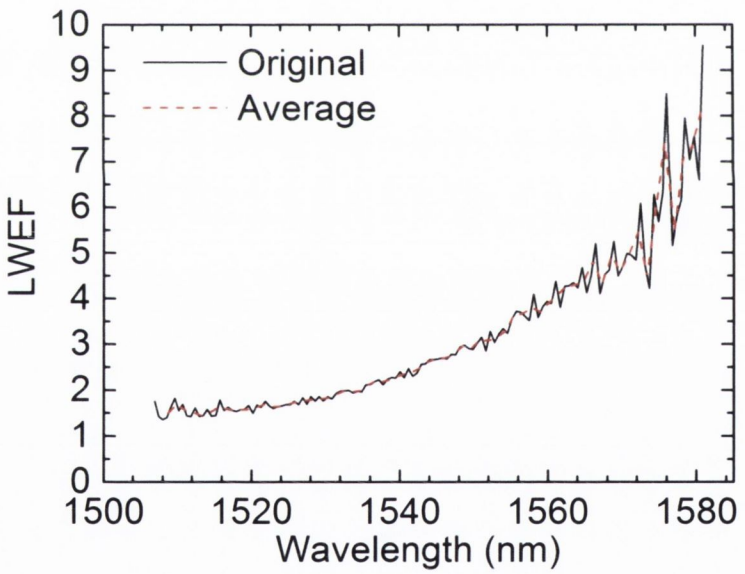

Figure 3.14. Linewidth enhancement factor versus wavelength calculated between 17.5 mA and 18mA.

The linewidth enhancement factor for different wavelengths is calculated from the ASE spectra using equation 3.27. The dashed line represents the average results. For this InAlGaAs quantum well system, the gain peak is around 3.0.

Conclusion

In this chapter a Fabry-Perot laser was characterized based on the ASE spectrum measurements below the threshold current. The laser has a cavity length of 650μm and the threshold is around 19mA with the slope efficiency of 0.35mW/mA. Various parameters were extracted such as the internal loss, quasi- Fermi level separation, spontaneous emission, round- trip gain, linewidth enhancement factor. From the measurement the internal loss of $18cm^{-1}$ was obtained with the linewidth enhancement factor of 3 for the wavelength of 1550nm.

References

[1] H. Kim, S. Kang and C. Lee, „A low cost WDM source with an ASE injected Fabry-Perot semiconductor laser," *IEEE Photonics Technology Letters,* vol 12, no 8, pp. 1067-1069, 2000.

[2] L. Coldren and S. Corzine, Diode lasers and photonics integrated circuits, Wiley, 1995.

[3] B. Hakki and T. Paoli, „Gain spectra in GaAs double- heterostructure injection lasers," *Journal of Applied Physics,* vol 46, no 3, pp. 1299-1305, 1975.

[4] D. Hofstetter and J. Faist, „Measurement of semiconductor laser gain and dispersion curves utilizing Fourier transforms of the emission spectra," *IEEE Photonics Technology Letters* , vol 11, no 11, pp. 1372-1374, 1999.

[5] W. Guo, Q. Lu, C. Han and L. Yu, „Measurement of gain for Fabry- Perot laser by the Fourier transfoerm method with deconvolution process," *IEEE Journal of Quantum Electronics,* vol 39, no 6, pp. 716-721, 2003.

[6] D. Cassidy, „Technique for measurement of the gain spectra of semiconductor diode lasers," *Journal of Applied physics,* vol 56, no 11, pp. 3096-3099, 1984.

[7] W. Guo, Q. Lu, Y. Huang and L. Yu, „Fourier series expanssion method for gain measurement from amplified spontaneous emission spectra of Fabry- Perot semiconductor lasers," *IEEE Journal of Quantum Electronics* , vol 40, no 2, pp. 123-129, 2004.

[8] W. Guo, D. Byrne, Q. Lu, B. Corbett and J. Donegan, „Fabry- Perot laser characterization based on the amplified spontaneous emission spectrum and the Fourier series expansion method," *IEEE Journal of selected topics in quantum electronics,* vol 17, no 5, pp. 1356-1363, 2011.

[9] G. Morrison and D. Cassidy, „A probablity- amplitude tranfer matrix model for distributed- feedback laser structures," *IEEE Journal of Quantum Technology Letters,* vol 36, no 6, pp. 633-640, 2000.

[10] D. Cassidy, „Spontaneous emission factor of semiconductor diode lasers," *Journal of Optical Society of America B,* vol 8, no 4, pp. 747-752, 1991.

[11] J.Minch, S. Park, T. Keating and S. Chaung, „Theory and experiment of In 1-x Ga x As y P 1-y and In 1-xy Ga x Al y As long-wavelength strained quantum-well lasers," *IEEE Journal of Quantum Electronics,* vol 35, no 5, pp. 771-782, 1999.

[12] L. Fu, L. Wu and H. Schweizer, „The extension of gain spectra and accurate determination of the quasi- Fermi level separation from measured amplified spontaneous emission spectra," *Applied Physics letters,* vol 75, no 20, pp. 3069-3071, 1999.

[13] W. Guo, D. Byrne, Q. Lu, R. Phelan, J. Donegan and B. Corbett, „Determination of internal loss and quasi- Fermi level separation from the amplified spontaneous emission spectrum of Fabry- Perot semiconductor lasers," *IEEE Photonics Technology Letters,* vol 18, no 18, pp. 1910-1912, 2006.

[14] L. Coldren and S. Corzine, Diode lasers and photonics integrated circuits, Wiley, 2012.

[15] C. Green, N. Dutta and W. Watson, „Linewidth enhancement factor in InGaAsP/InP multiple quantum well lasers," *Aplied Physics Letters,* vol 50, no 20, pp. 1409-1410, 1987.

[16] D. Byrne, W. Guo, R. Phelan, Q. Lu, J. Donegan and B. Corbett, „Measurement of linewidth enhancement factor for InGaAlAs laser diode by Fourier series expansion method," *Electronics letters,* vol 43, no 21, pp. 1145-1146, 2007.

Chapter 4. Slotted tunable laser design and fabrication.

Introduction

Widely tunable semiconductor laser play an important role in optical communication systems and other applications and have already demonstrated their potential to be integrated with other optical components on a single chip [1] [2] [3] [4] [5]. It is a key technology in the development of optoelectronic systems.

The strong interaction between electronic, optical and thermal effects makes the design of the photonic integrated devices particularly challenging. With the help of numerical models and various software for calculation and optimization, preparing the tunable laser mask and simulating the laser performance, the time and cost of designing the laser can be significantly reduced [6] [7] [8].

In this chapter, a slotted tunable laser design and its fabrication process is introduced step by step. Also the scattering matrix method (SMM) is introduced here as we use it to optimize the laser parameters. The simulated laser performance is also presented here to give an idea about the future fabricated laser performance. For the optimization of slots parameters and extracting modelled tuning maps, MatLab software was used. The tunable laser mask design was completed using CleWin 4.

4.1. Optimization of parameters

The key in designing a tunable laser is the optimization of the parameters such as slot width, slot depth, slot period and slot number. To do so we use the Scattering Matrix Method (SMM) is described below.

Detailed analysis of SMM used to characterize a slotted laser can be found in [11]. From [11] we assume that 2- D slotted waveguide can be separated into N uniform sections including input and output regions. The 2-D scattering matrix model is used to compute the field reflected and coupled into the input waveguide and also the field transmitted and coupled into the output waveguide, which are defined as the reflection and transmission from the group of slots. A schematic structure of 2-D waveguide with slots is shown in figure 4.1.1 below, where d_s is slot width, d_w is slot spacing and d_p is slot period.

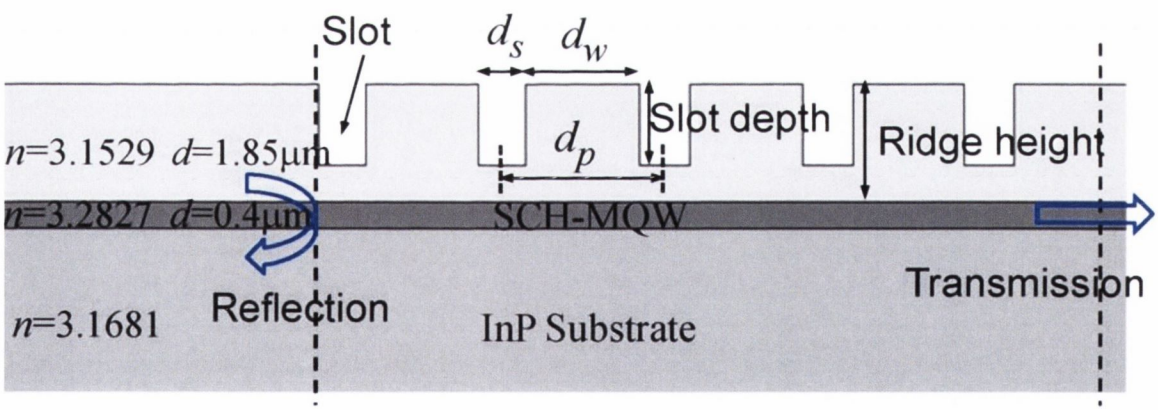

Figure 4.1.1. 2-D waveguide structure with slots [13]

A normalized amplitude a_j having a magnitude equal to the square root of the power flow is used to work with complex laser cavities. Then we can refer to the phase of the electric field as

$$E(x,y,z,t) = \hat{e}E_0 U(x,y) e^{j(\omega t - \tilde{\beta} z)} \tag{4.1}$$

where $\hat{e}$ is the unit vector, E_0 is the field magnitude, $U(x,y)$ is the normalized electric field profile, ω is the angular frequency, t is time, $\tilde{\beta}$ is the complex propagation constant and z is the propagation distance . The normalized amplitude can be defined as

$$a_j = \frac{E_0}{\sqrt{2\eta_j}} e^{-j\tilde{\beta} z} \tag{4.2}$$

where $\eta_j = \frac{377\Omega}{\bar{n}_j}$ is the mode impedance which is the ratio of the transverse electric to transverse magnetic field magnitudes of the mode. Thus if $\int |U|^2 dxdy = 1$ then $a_j a_j^* = P_j^+$, the power is flowing in the positive z- direction in the mode. For some waveguides, there are incident (inputs) and reflected (output) powers. The inputs can be defined as having normalized amplitudes a_j, and the outputs as having normalized amplitudes b_j. Therefore at port j, the net power flowing into the port is

$$P_j = a_j a_j^* - b_j b_j^* \tag{4.3}$$

If the outputs can be linearly related to the inputs, a matrix formalism can be expressed as a weighted combination of the inputs as

$$b_i = \sum_j S_{ij} a_j \tag{4.4}$$

where S_{ij} are called scattering coefficients. To determine a particular S_{ij}, all inputs except a_j must be set to zero

$$S_{ij} = \left. \frac{b_i}{a_j} \right|_{a_k = 0, k \neq j} \tag{4.5}$$

In a more general view $b = Sa$, where a and b are column vectors and S is a matrix. The two port scattering junction is shown in figure 4.1.2 below and is given as an example in 4.6.

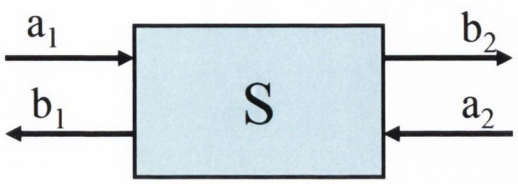

Figure 4.1.2. Scattering matrix representation of a two port network.

$$\begin{bmatrix} b_1 \\ b_2 \end{bmatrix} = \begin{bmatrix} S_{11} & S_{12} \\ S_{21} & S_{22} \end{bmatrix} \begin{bmatrix} a_1 \\ a_2 \end{bmatrix} \tag{4.6}$$

the S values are called scattering coefficients. They are useful because they have direct physical significance as they represent the ratio of a normalized output amplitude to a normalized input amplitude. For example in the two ports shown above S_{11} and S_{22} are simply r_1 and r_2 which are the amplitude reflectivities at junction 1 and 2. The power reflection coefficients are in this case $|S_{11}|^2$ and $|S_{22}|^2$. The off- diagonal terms represent the complex (amplitude to phase) output at one port due to the input at another. The magnitude squared of a scattering coefficient $|S_{ij}|^2$ is the fraction of power appearing at the port i due to the power entering port j. For a lossless two port network, power conservation yields $|S_{11}|^2 + |S_{21}|^2 = 1$ and $|S_{22}|^2 + |S_{12}|^2 = 1$. Loss can be included by making these equalities less than 1.

Another important matrix that relates the normalized amplitudes is the transmission matrix method. The transmission matrix method TMM is used for cascading networks together as simple matrix multiplication can be used. The transmission matrix expresses the inputs and outputs at a given port in terms of those and the others. The transmission of two ports is defined as

$$\begin{bmatrix} A_1 \\ B_1 \end{bmatrix} = \begin{bmatrix} T_{11} & T_{12} \\ T_{21} & T_{22} \end{bmatrix} \begin{bmatrix} A_2 \\ B_2 \end{bmatrix} \tag{4.7}$$

where instead of using the input and output amplitudes a_i and b_i, the forward- going and backward- going waves A_i and B_i will be used.

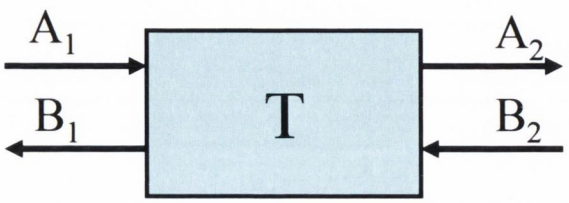

Figure 4.1.3. Transmission matric representation of two port network.

The correspondence between the transfer matrix and scattering matrix amplitudes is as follows: $A_1 = a_1$, $B_1 = b_1$, $A_2 = b_2$, $B_2 = a_2$. Therefore using TMM a series of two port junctions can be multiplied together using matrix multiplication as illustrated in figure 4.1.4 below.

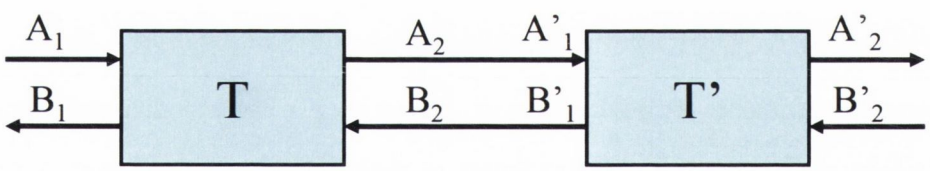

Figure 4.1.4. TM representation of two networks cascaded together.

By putting $A_2 = A_1^{'}$ and $B_2 = B_1^{'}$ the fields on the left side can be related to the fields on the right side as

$$\begin{bmatrix} A_1 \\ B_1 \end{bmatrix} = \begin{bmatrix} T_{11} & T_{12} \\ T_{21} & T_{22} \end{bmatrix} \begin{bmatrix} A_2 \\ B_2 \end{bmatrix} = \begin{bmatrix} T_{11} & T_{12} \\ T_{21} & T_{22} \end{bmatrix} \begin{bmatrix} T_{11}^{'} & T_{12}^{'} \\ T_{21}^{'} & T_{22}^{'} \end{bmatrix} \begin{bmatrix} A_2^{'} \\ B_2^{'} \end{bmatrix} \tag{4.8}$$

The dielectric interface

A dielectric interface can be characterised by having different refractive indices n_1 and n_2 on each side of the interface as illustrated in figure 4.1.5.

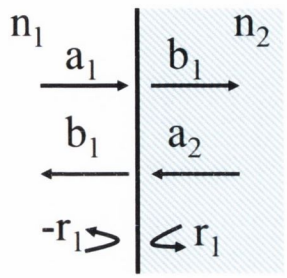

Figure 4.1.5. Dielectric interface.

The reference planes at the physical interface between the two dielectrics and the scattering junction length is zero. Using 4.5

$$S_{11} = \left.\frac{b_1}{a_1}\right|_{a_2=0} = -r_1 = \frac{n_1 - n_2}{n_1 + n_2} \tag{4.9}$$

the reflection is positive if $n_2 > n_1$. The second port S_{22} can be found as

$$S_{22} = \left.\frac{b_2}{a_2}\right|_{a_1=0} = r_2 = -\left(-r_1\right) \tag{4.10}$$

and

$$S_{12} = S_{21} = t = \sqrt{1 - r_1^2} \tag{4.11}$$

The waves are assumed to be plane waves and have no loss at the interface as the interface has a length of zero. For the waveguide modes power conservation suggests that the mode profile are continuous across the dielectric interface. For the normally incident plane wave case $t = 2\left(n_1 n_2\right)^{1/2} / \left(n_1 + n_2\right)$. The scattering matrix for the dielectric interface is

$$S = \begin{bmatrix} -r_1 & t \\ t & r_1 \end{bmatrix} \tag{4.12}$$

The corresponding transfer matrix is

$$T = \frac{1}{t}\begin{bmatrix} 1 & -r_1 \\ -r_1 & 1 \end{bmatrix} \tag{4.13}$$

Waveguide with no discontinuities

A network that is a length of waveguide L with no discontinuities is shown in figure 4.1.6. The network consists of two reference planes on a waveguide.

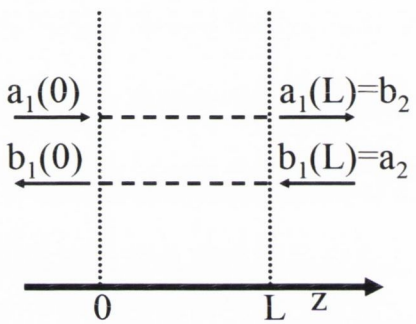

Figure 4.1.6. Waveguide with no discontinuities.

Because there is no coupling between the waves propagating in the forward and backward directions $S_{11} = S_{22} = 0$ and therefore

$$b_2 = a_1(L) = a_1(0)e^{-j\tilde{\beta}L} = a_1 e^{-j\tilde{\beta}L} \tag{4.14}$$

and

$$a_2 = b_1(L) = b_1(0)e^{j\tilde{\beta}L} = b_1 e^{j\tilde{\beta}L} \tag{4.15}$$

To employ the Vernier tuning [9], a set of the same number of slots with different periods are etched on the front and back mirrors. It is also possible to introduce slightly different number of slots on both reflectors as will be shown in Chapter 5 where this kind of laser is characterized.

The reflection from a single slot is relatively weak [11] so a series of slots in both mirrors is needed to provide sufficient feedback for lasing. The reflection from the group of slots will saturate and they will introduce some loss, therefore both mirror sections are active to provide optical gain in order to compensate any loss introduced by the slots. The reflection from N equally spaced slots can be described by

$$r_t = r_s \frac{1 - t_s^{2N} \exp(gNl) \exp(-j2kn_{eff}Nl)}{1 - t_s^2 \exp(gl) \exp(-j2kn_{eff}l)} \tag{4.16}$$

where r_s and t_s are the reflection and transmission of a single slot, r_t is the total reflection from the group of slots, g is the net modal gain of the active waveguide between the slots, l is the slot spacing, $k = \frac{2\pi}{\lambda}$ is the wave number in vacuum, and n_{eff} is the effective index of the active waveguide. Equally spaced slots will produce a periodic reflection spectrum with the free spectral range (FSR) determined by the slot spacing

$$\Delta\lambda = \frac{\lambda^2}{2n_g l} \tag{4.17}$$

where

$$n_g = n_{eff} - \frac{\lambda dn_{eff}}{d\lambda} \tag{4.18}$$

is the group index of the active waveguide.

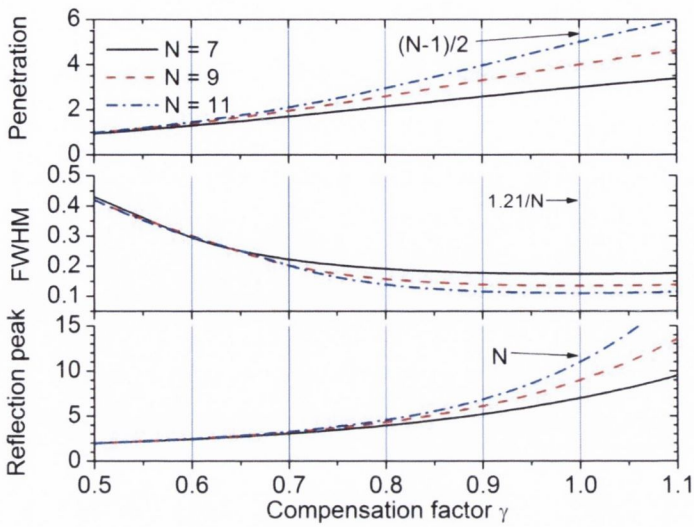

(a)

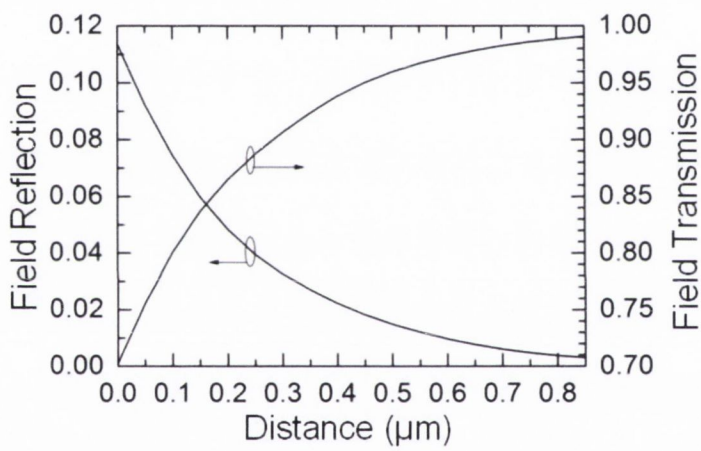

(b)

Figure 4.1.7. (a) Penetration depth into the mirror section normalized to the slot period, FWHM of the reflection peak normalized to the FSR, and maximum values of the reflection peak normalized to the single slot reflection versus slot loss compensation factor for different number of equally spaced slots; (b) field reflection and transmission of the single slot versus slot depth represented by the distance between the bottom of the slot and the top of the waveguide core. N is the number of slots [10].

The maximum width and value of each reflection peak in the reflection spectrum is determined by the number of slots and the slot compensation level. The slot compensation level is determined as

$$\gamma = t_s^2 e^{gl} \tag{4.19}$$

For γ=1 we have a full slot loss compensation when all loss introduced by the slot is compensated by the gain in the region between the slots, resulting in the narrowest reflection peak.

The penetration depth of the field into the slot region normalized by slot spacing in shown in figure 4.1.7 (a) with the full-width at half maximum (FWHM of the reflection peak normalized by FSR, and the maximum value of the reflection peak normalized by the individual slot reflection versus slot loss compensation factor γ for different number of slots. It can be seen that when the slot loss in strongly undercompensated i.e. γ<0.6 , an increasing number of slots results in little difference in the reflection. The field decays quickly into the slot region. In case of the full compensation, the reflection peak has a minimum normalized FWHM and the field penetrates halfway into the slot region. The calculated reflection and transmission from a single slot changing with etch depth is shown in figure 4.1.7 (b) [11] [12]. Using the results shown in figure 4.1.7 we chose nine slots in both mirrors as a compromise between maximizing the reflectivity and minimizing the width of the reflection peaks. We also want to keep the laser length to a minimum. As it can be seen a laser with 11 slots in each mirror would provide narrower bandwidth of reflection peak and a larger section reflection; however it would result in having the mirror section over 1mm long [10].

For a laser with the slot period of 97μm for the front mirror and 108μm for the back mirror the penetration depth of both mirrors can be calculated as [13]:

$$d_{penetr} = \frac{(N-1)dp}{2} \tag{4.20}$$

where N is the number of slots on the mirror and dp is the slot period in the mirror. The slot period of 97μm/108μm was chosen to obtain a 300 GHz spacing between the channels. Having nine slots on the front mirror with the slot period of 97μm, the penetration depth of the front mirror is 388μm. Similarly, having nine slots on the back mirror with the slot period of 108μm, the penetration depth of the back mirror is 432μm. Therefore having the gain section with the length of 500μm, the effective cavity length L_{eff} will be 1320μm(=500+432+388). The mode spacing can be calculated as [13]:

$$\Delta\lambda = \frac{\lambda^2}{2 * n_g * L_{eff}} \tag{4.21}$$

For λ= 1550nm, n_g = 3.5 and L_{eff} =1320μm, the calculated mode spacing $\Delta\lambda$ is ~0.26nm. For this design we set the slot width of 1μm as then the laser can be fabricated by standard photolithography. This parameter was not changed during the optimization and simulation processes. The slot depth was chosen to be 1.85μm as for this value the lowestamplitude transmission was obtained (figure 4.1.8)

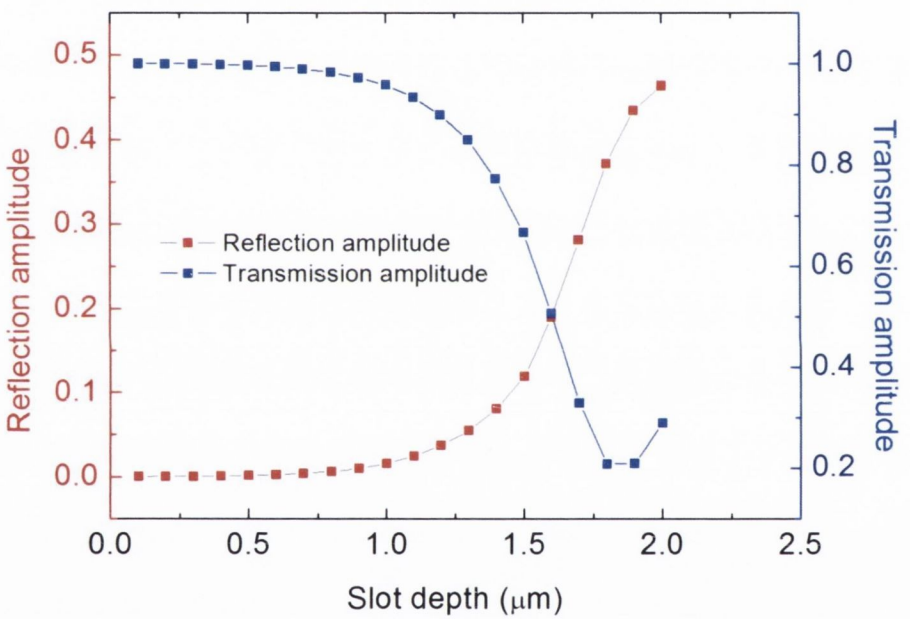

Figure 4.1.8. Reflection and transmission versus slot depth from SMM.

4.2. Tuning modelling

In this section, the simulated tuning behaviour for the tunable laser with different slot period is presented. For the simulation a MatLab programme was used. The programme was written previously and was modified to simulate the lasers performance presented in this chapter. The model of the laser used in this simulation is simpler than the real fabricated laser structure. Nevertheless it gives an idea about how the tuning behaviour depends on the slot parameters. The main focus of those simulation is to show how tuning of the laser is altered while changing the slot period. The following conditions have to be taken into account:

1. A three section laser is used in the simulations. The sections are: the front mirror, central gain section, the back mirror.
2. To reduce complexity of the calculations, both mirrors are considered as passive structures, the active region is only underneath the gain section, which makes the simulated laser similar to the industry standard SG-DBR laser.
3. The length of the gain section is 500μm.
4. The reflection and transmission used in the simulations are set to 0.1 and 0.8, respectively for each slot.
5. Temperature effects are not included.
6. The slot width and slot depth are set to 1μm and 1.85μm, respectively. As explained in the previous section, the sloth width of 1μm was chosen to ease the fabrication process, as then the laser can be fabricated using standard photolithography. Having deep slots etched to just above the active region makes the reflection arising from the slots stronger.
7. Since the mirrors experience a high level gain especially at high injection currents and the reflectivity from the mirrors is high, therefore the current range set for the simulation needs to be low.
8. There are nine slots in the front and the back mirrors.

The scattering matrix method was used to set up the modelling programme [4-5] [14] [9]. To run the modelling programme first, the input parameters need to be chosen. The slot number on both reflectors is set to nine. Then the different slot periods are

implemented in the mirrors, for example 97 μm in the front mirror and 108 μm in the back mirror. For the modelling work presented here, the only parameter varying was the slot period. The slot width and slot depth were set to 1 μm and 1.85 μm, respectively, and were not altered during the calculations. The length of the gain section was kept constant at 500 μm with the simulated injected current of 100mA. The gain data used in this programme were obtained experimentally in Tyndall National Institute for the wavelength from 1535nm to 1565nm, with the central wavelength peak of 1550nm.

The first laser structure considered has nine slots in the front and back mirror with the slot period of 97μm and 108 μm, respectively to employ the Vernier tuning. The central peak wavelength is set to 1550 nm and the gain section is 500 μm long. The current injected into the gain section in this simulation is set to 100mA. The injection currents are changing from 70mA to 10mA with a step of 1mA.

Figure 4.2.1. below shows the simulated output power. The best values of the power are achieved for high current injected into the back mirror section. The simulated wavelength and SMSR maps are shown in figures 4.2.2. and 4.2.3 below. Ten distinct super-modes are present over the tuning range of 30nm for the wavelength from 1535nm to 1565nm. Good SMSR values are achieved for almost the whole map as seen in figure 4.2.3. The smaller SMSR values occur at the boundaries of the super-mode hops.

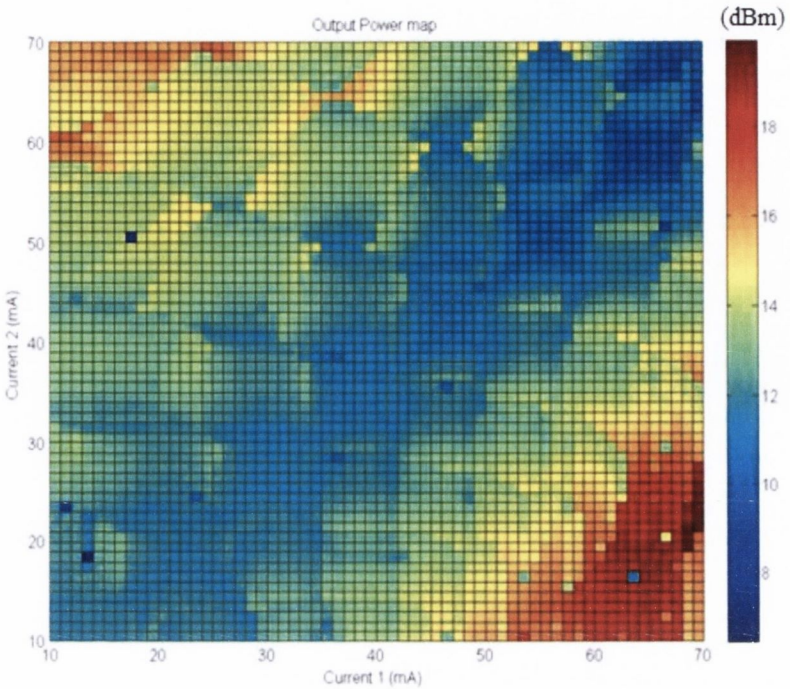

Figure 4.2.1. Simulated output power map for the laser with the slot periods of 97μm in the front mirror and 108 μm in the back mirror.

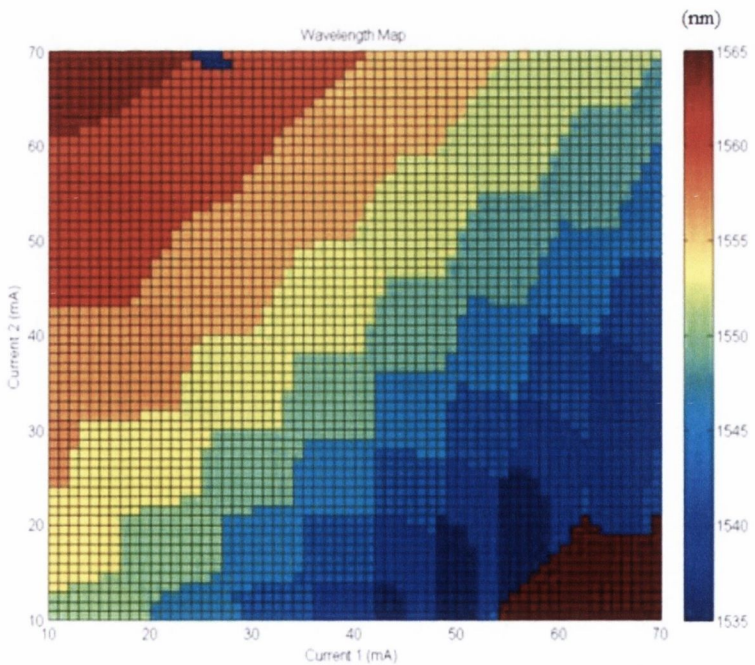

Figure 4.2.2. Simulated wavelength map for the laser with the slot period of 97μm in the front mirror and 108 μm in the back mirror.

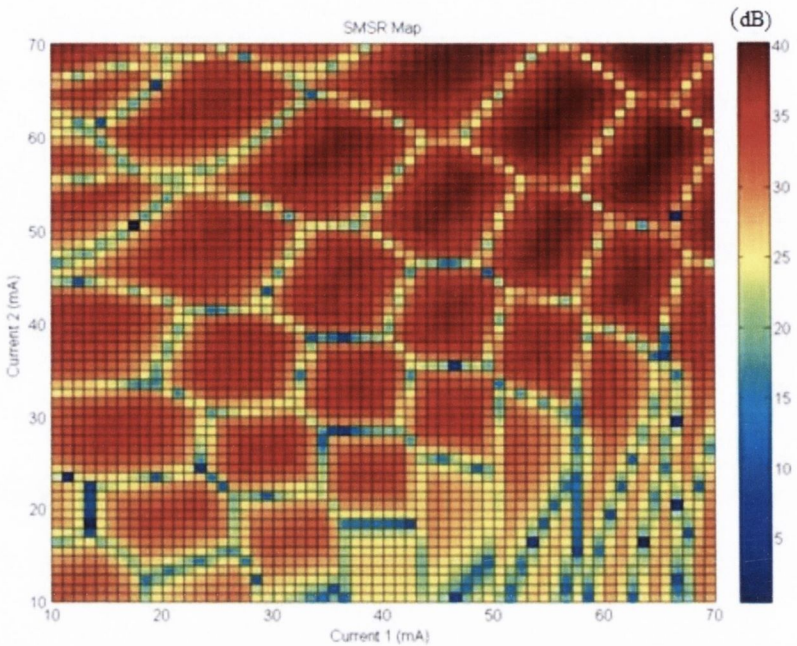

Figure 4.2.3. Simulated SMSR map for the laser with the slot period of 97μm in the front mirror and 108 μm in the back mirror.

Combining figures 4.2.2 and 4.2.3 SMSR versus peak wavelength can be plotted as seen in figure 4.2.4. Ten super-modes are present, nine of them with SMSR values more than 30dB. The modes on the edge of the gain spectrum exhibit lower SMSR.

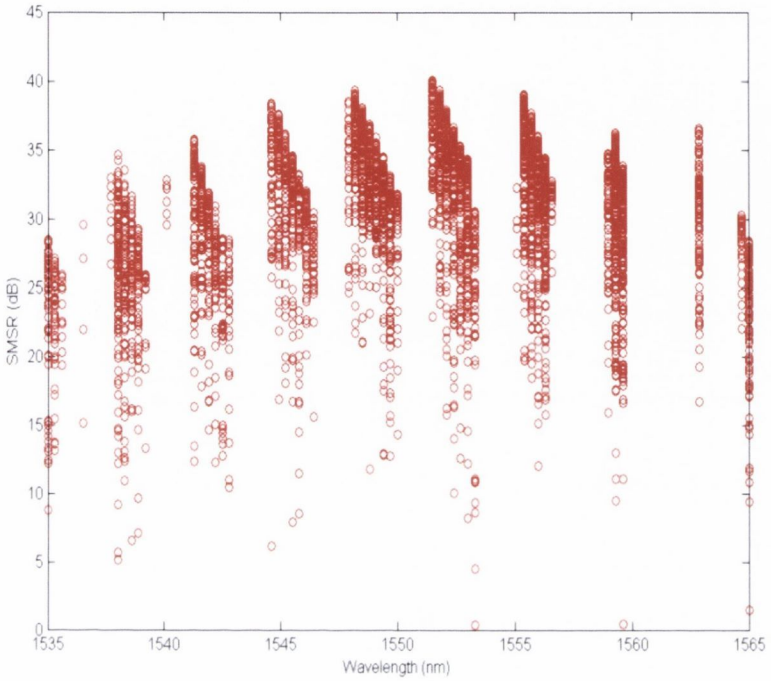

Figure 4.2.4. SMSR versus peak wavelength for the laser with the slot period of 97μm in the front mirror and 108 μm in the back mirror.

The second simulated laser structure has nine slots in both reflectors with the slot period of 70μm in the front mirror and 76μm in the back mirror. The central peak wavelength is 1550nm. The currents injected into the mirror sections are changing between 70mA and 10mA with a step of 1mA. The current injected into the 500μm long central gain section is set to 100mA.

As seen from figure 4.2.5, the output power reaches the best values for high current injected into the back mirror section. From the wavelength and SMSR maps it can be seen that for this region the laser tuning does not work well. No further super-mode hops occur in the regions where one on the injected current is low. Clear super-mode bands and islands can be observed from the wavelength tuning map. As seen from figure 4.2.7 lower SMSR occur as the boundaries of the super-mode hops.

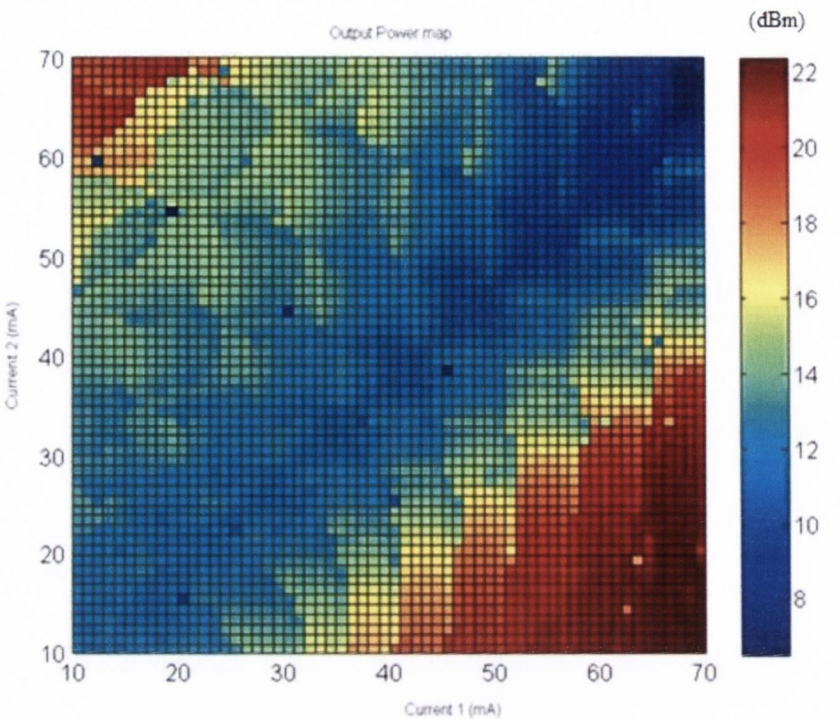

Figure 4.2.5. Simulated output power map for the laser with the slot period of 70μm in the front mirror and 76 μm.

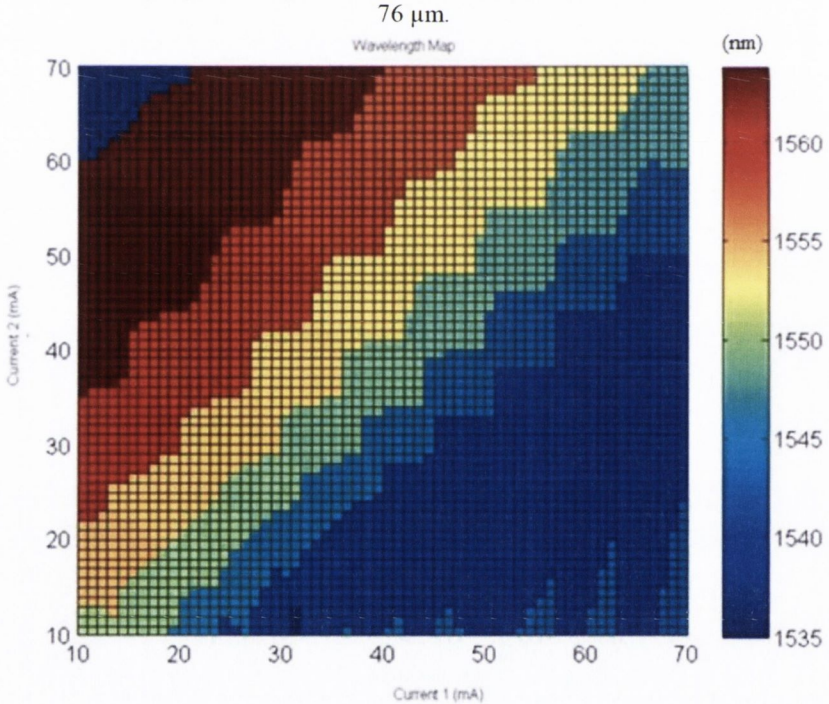

Figure 4.2.6. Simulated wavelength map for the laser with the slot period of 70μm in the front mirror and 76 μm.

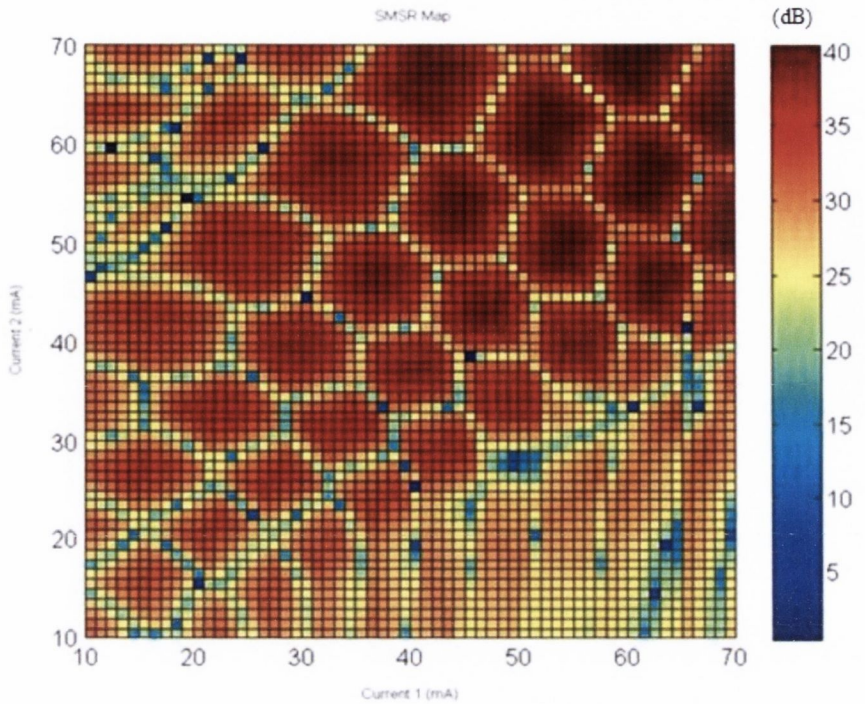

Figure 4.2.7. Simulated SMSR map for the laser with the slot period of 70μm in the front mirror and 76 μm.

From figure 4.2.8 six distinct super-modes can be observed over the tuning range of about 27nm for the wavelength of 1537nm to 1564nm. All modes have SMSR more than 30dB.

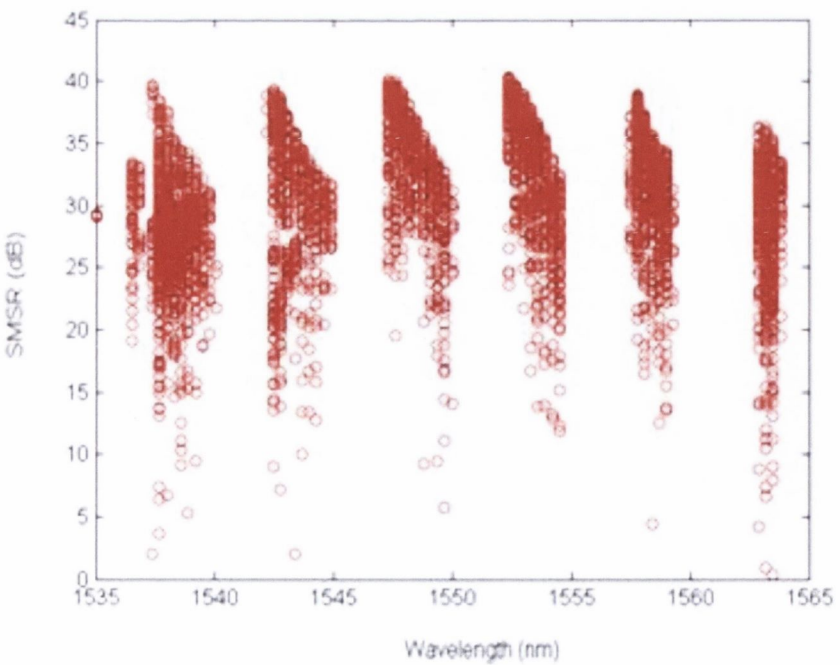

Figure 4.2.8. SMSR versus peak wavelength for the laser with the slot period of 70μm in the front mirror and 76 μm.

The third simulated laser structure is a laser with the slot period of 52μm in the front mirror and 57 μm in the back mirror. Again the laser has nine slots in both reflectors. The currents injected into the mirror section vary from 70mA to 10mA. The current injected into the central gain section is set to 100mA.

The simulated output power, wavelength and SMSR maps are shown in figures 4.2.9, 4.2.10, 4.2.11, respectively. Again, the laser exhibit the best output power for the high current injected into the back mirror section and the low current injected into the front mirror section. From the wavelength map in figure 4.2.10 clear wavelength bands are visible except the region where the back current is high. No mode jumps occur in this region. As seen from the SMSR tuning map in figure 4.2.11, the tuning islands are clearly visible with good SMSR values above 30dB. Low SMSR occur at the boundaries of the super-mode hops.

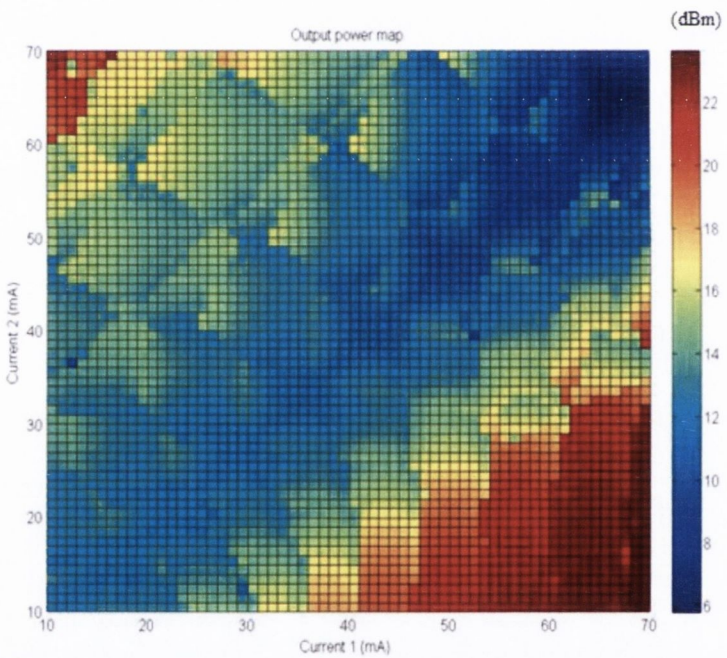

Figure 4.2.9. The simulated power map for the laser with the slot period of 52μm in the front mirror and 57μm in the back mirror.

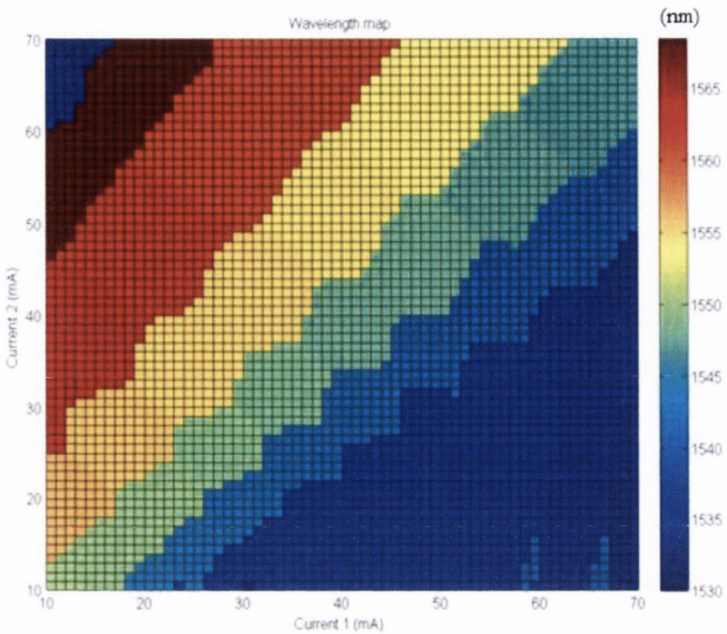

Figure 4.2.10. The simulated wavelength map for the laser with the slot period of 52μm in the front mirror and 57μm in the back mirror.

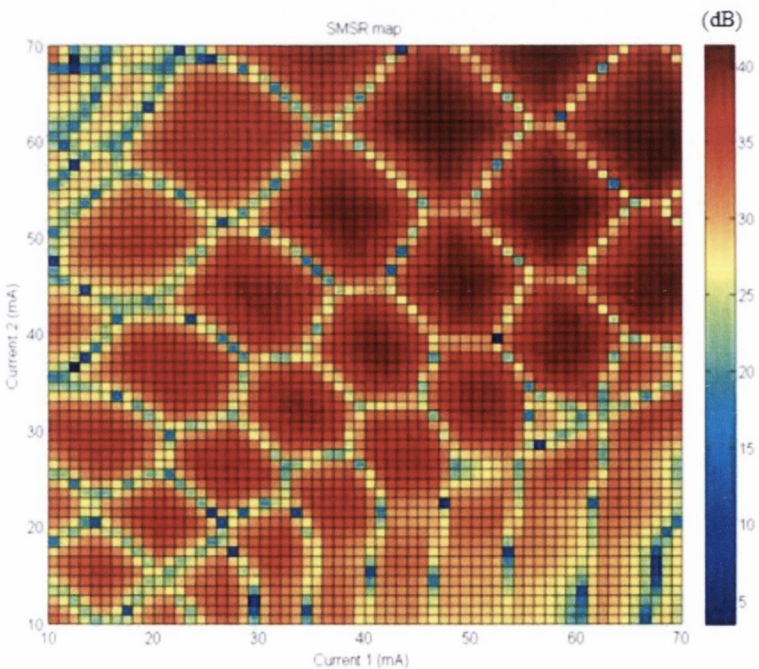

Figure 4.2.11. The simulated SMSR map for the laser with the slot period of 52μm in the front mirror and 57μm in the back mirror.

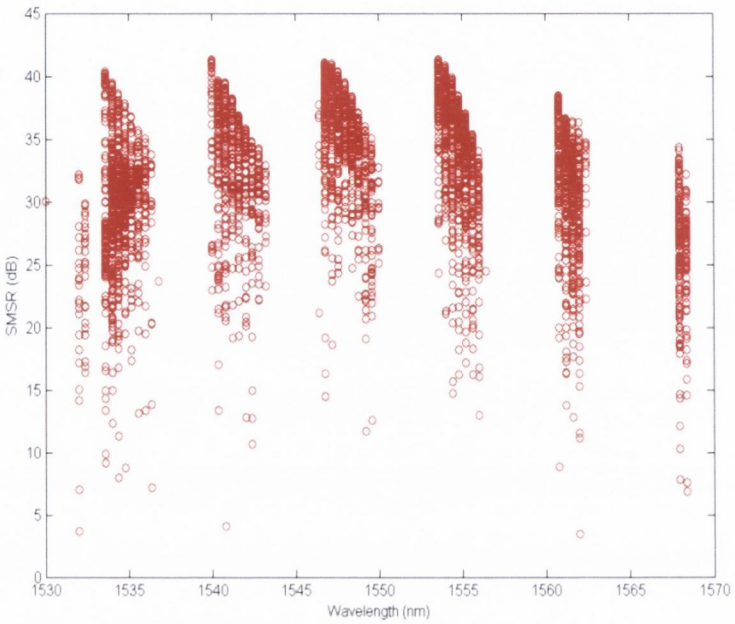

Figure 4.2.12. SMSR versus peak wavelength for the laser with the slot period of 52μm in the front mirror and 57μm in the back mirror.

As seen from figure 4.2.12 above, six distinct super-modes are present over the tuning range of about 37nm for the wavelength from 1532nm to 1569nm. All modes have good SMSR more than 30dB.

From the simulated results it can be seen that the region with poor laser tuning where the back injection current is high grows bigger as the slot period is decreasing. The number of the super-modes is decreasing with decreasing slot period. The longest laser with the slot period of 97μm/108μm has ten distinct modes while the laser with the shortest slot period of 52 μm/57 μm has only six modes. Also as expected, the tuning range and the mode separation are getting wider as the slot period is decreasing due to the larger mode separation. From the simulation shown above, lasers with short slot periods were chosen for the second fabrication run as they have wider tuning range as well as good SMSR values for all super-modes. The results from those particular lasers are presented in chapter 7.

Slot period	97μm/108μm	70μm/76μm	52μm/57μm
FSR	3.36nm/3.02nm	4.9nm/4.5nm	6.6nm/6.02nm
Tuning range	30nm	27nm	37nm
Number of super-modes	10	6	6
Number of super-modes with SMSR > 30dB	9	6	6

Table 4.1. Tuning parameters for the laser with the slot periods of 97μm/108μm, 70μm/76μm, 52μm/57μm.

4.3. Mask design

In this section, the tunable mask design process is presented. For the mask design CleWin 4 software was used. The first step is to set the mask size which in our case is 5 inches by 5 inches. The mask layout consists of 6 different layers: (i) the e-beam alignment marks are required to control the correct position of the wafer during the e-beam lithography process, (ii) the slots positions, (iii) the waveguide layer and also the number of the lasers on the bar, (iv) the window layer, (v) marks for scribing marks, (vi) waveguide cover and contacts, cleaving marks.

All the lasers on the bars have the same length ~3110 μm to ease the fabrication process. Layer 1 of the mask with e-beam marks is shown in figure 4.3.1. The squares inside the mask layout are the e-beam lithography marks.

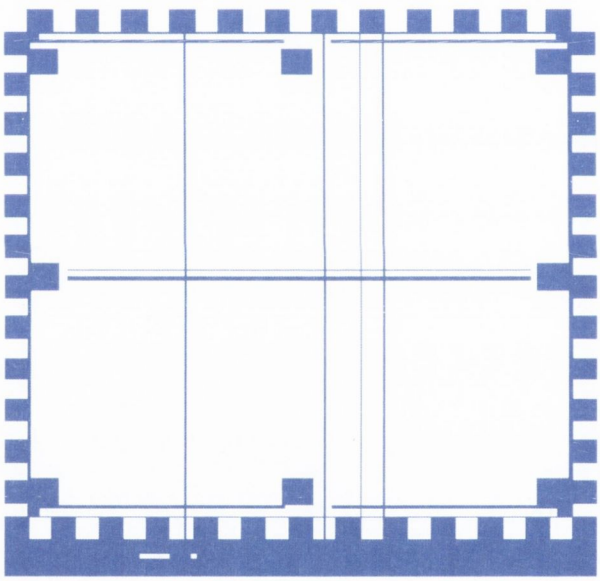

Figure 4.3.1. The schematic structure of the tunable laser mask layout. The squares inside represents the e-beam lithography marks The outer squares, vertical and horizontal lines represent the alignment marks for placing the mask on the right position during the fabrication process.

The next step is to mark the slots on the mask. As was mentioned before, each laser has nine slots with different periods on the front and the back mirror. The two mirror sets of slots are separated by the 500μm gain section. In the design described here, three multi section type lasers are present: five contact, six contact and nine contact lasers. The six section lasers have an extra angled slot to separate the phase and the gain section from one another. The nine section lasers have four extra angled slots placed in front and at the back of the mirror sections, to separate different laser sections from one another and to

prevent the current leakage between different sections. Nine slots on the front and back mirror act like reflection centres as was explained before. The mask layout with marked slots positions and the slots for different multisection lasers are shown in figures 4.3.2 and 4.3.3, respectively.

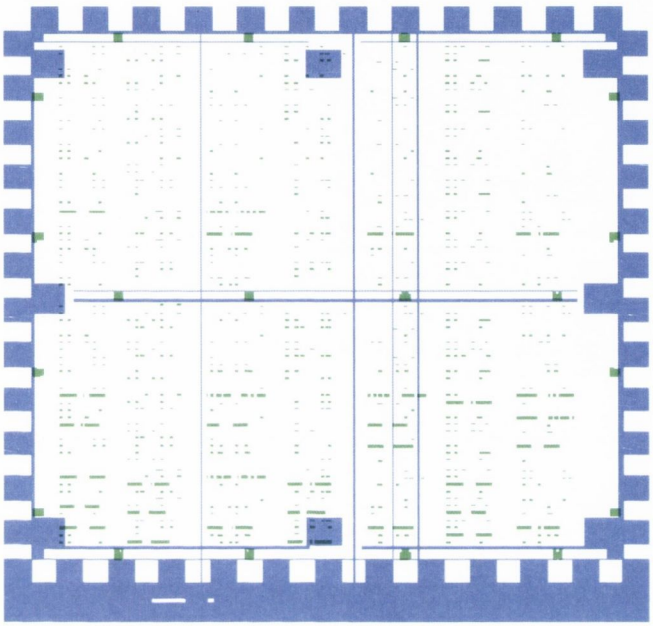

Figure 4.3.2. The mask layout with marked slots positions- green colour.

Figure 4.3.3. Slots for five, six and nine contact lasers, respectively. All slots presented here have the same width of 1 μm but due to the small scale on the mask some of them look thicker than the others.

Once the slot positions are chosen on the mask, the laser waveguides can be placed. The ends of the waveguides (marked in dark green colour) are angled at 7°. The waveguide ridge is designed to be 2.5 μm wide. The last layer is the metal cover (green colour).

Each laser on the bar has a number from one to eleven and each laser bar has its own number by which it can be identified. Figure 4.3.4. shows a fragment of the ready mask for a bar with five contact lasers. The blue numbers are the number of each laser on the bar. The bar number is indicated by the green colour. It can be seen that each section of the laser is naturally separated by the slots. Looking from the left hand side we have the SOA section without the slots, the front mirror section with the slots, the gain section, the back section and the photodetector (PD) section. All lasers on the bar have the same length to ease the cleaving.

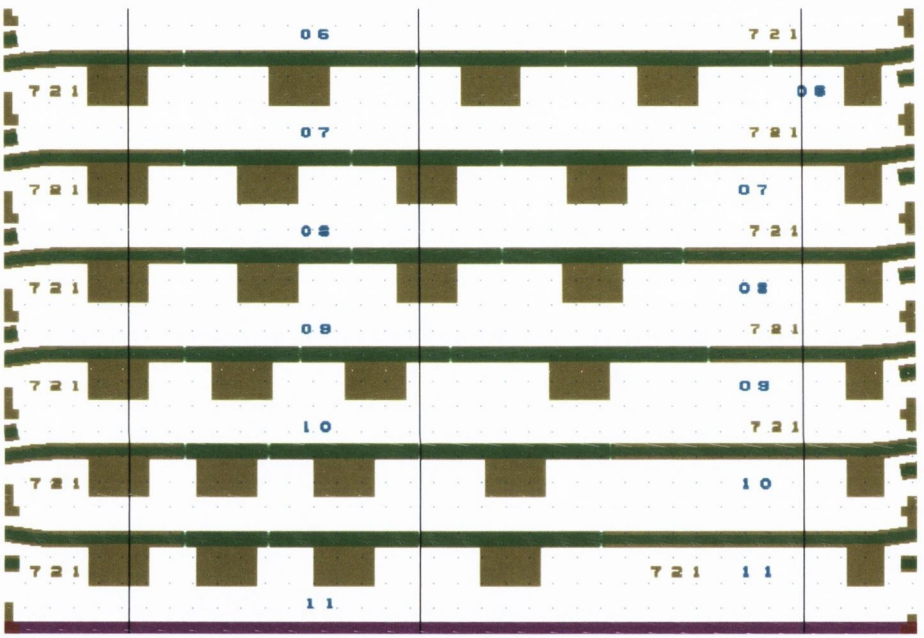

Figure 4.3.4. Fragment of the laser mask for the bar with five contact lasers of different periods.

Figure 4.3.5. shows a fragment of a ready mask for a bar with a six contact laser. Again as it was explained before, each laser on the bar has a number from one to eleven marked in blue colour. The laser bar number is again marked by the green colour. Looking from the left hand side we have the SOA section, the front section, the gain section, short phase section, the back mirror section, and the PD section. The gain section in this case is 400 μm long and the phase section is 100 μm long.

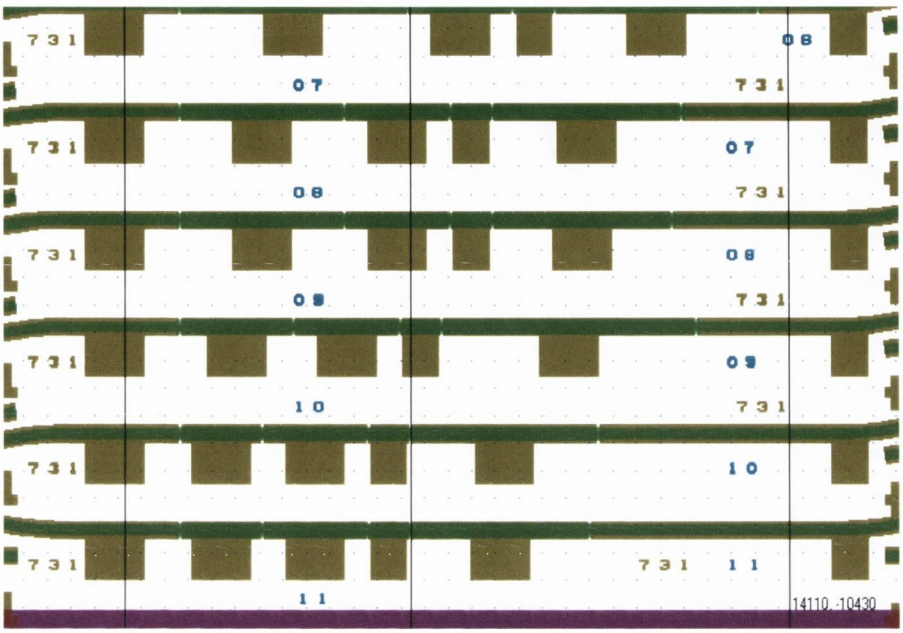

Figure 4.3.5. Fragment of the laser mask for the bar with six contact lasers.

Figure 4.3.6. shows a fragment of a bar with nine contact lasers. Small isolation contacts are placed between the SOA and the front mirror, the front mirror and the gain section, the gain section and the back mirror, and the back mirror and PD section.

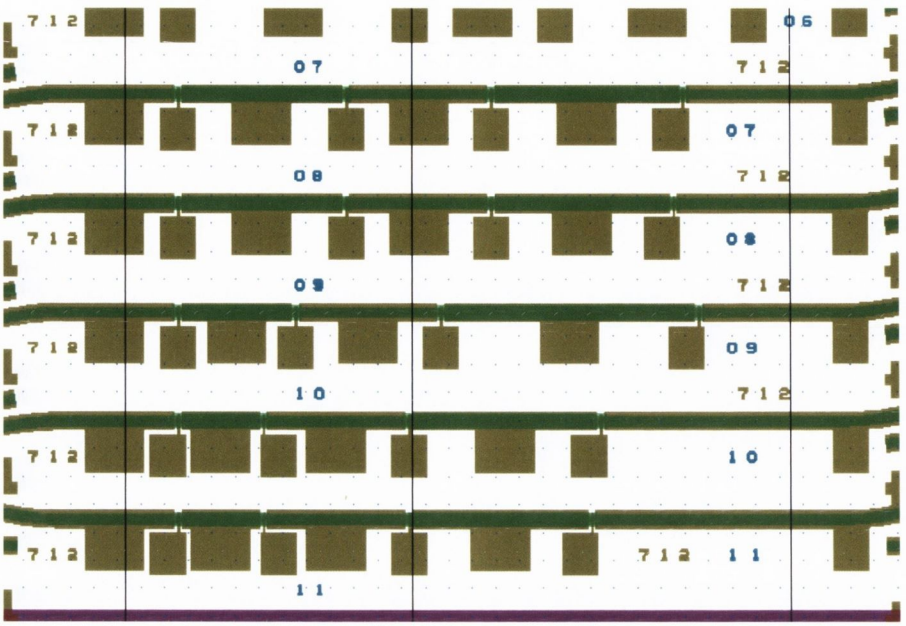

Figure 4.3.6. Fragment of the laser mask for the bar with nine contact lasers.

The ready mask is shown in figure 4.3.7. This shows the coverage of the mask with varying designs. We move various designs around to maximize the number of different designs we can accommodate on the mask.

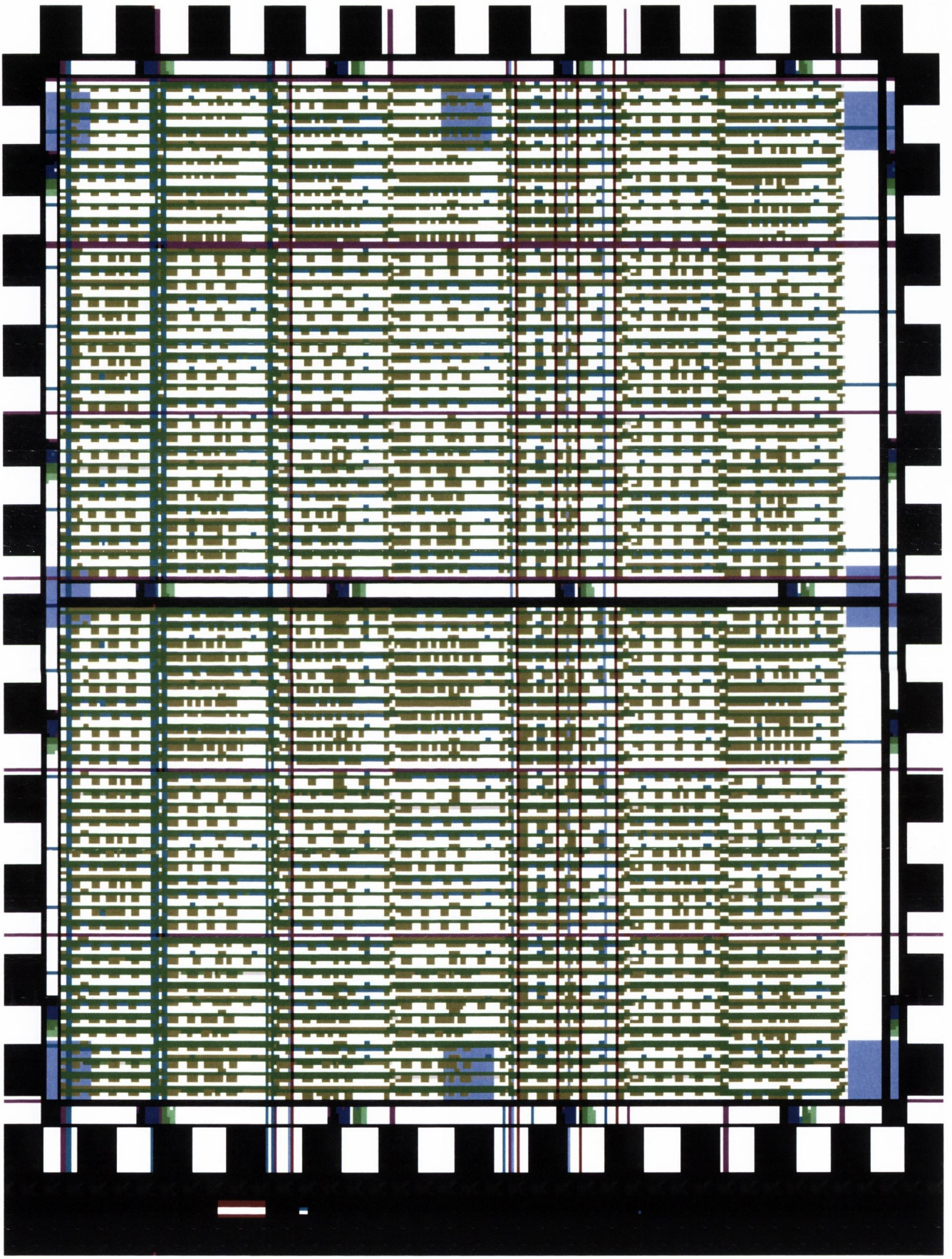

Figure 4.3.7. Final tunable laser mask with 462 devices.

4.4. Fabrication process

The laser structure consists of five AlGaInAs quantum wells that have a emission peak around 1550nm. The active region is surrounded by n and p doped InP cladding layers. The waveguide ridge is 2.5 μm wide and was formed by inductively coupled plasma (ICP) dry etching using Cl_2/N_2 gas. The slots are etched simultaneously with the ridge to a depth just above the active layer. First a 0.5 μm high shallow ridge was formed with the slot area being protected by SiO_2 during the dry etching. Afterward the protection layer was removed and a second dry etching was used to form the slots and to etch the ridge to a depth of 1.85 μm. The slots in the tunable lasers are about 0.5μm shallower than the ridge as was determined by this dry etching process. The ridge then was passivated and metal contacted to finish the laser structure. The etched slot is sufficient to isolate different sections of the laser allowing independent current injection. The devices are cleaved to a desired lengths and an antireflection (AR) coating is applied to the facets. The whole laser cavity is about 3 mm long, of which the gain section is set to 500 μm long to provide enough gain for the laser operation. The standard IQE wafer structure for laser fabrication is shown in table 4.2. The wafer consists of 16 layers. Layers from 4 to 13 form waveguide core with 5 AlGaInAs quantum wells.

	Layer	Material	Group	Repeat	Mole Fraction (x)	Mole Fraction (y)	Strain (ppm)	PL (nm)	Thickness (μm)
	16	GaIn(x)As			0.530		0		0.2000
	15	GaIn(x)As(y)P			0.710	0.620	0	1300 +/-50	0.0500
	14	InP							0.1000
	13	InP							1.5000
	12	GaIn(x)As(y)P			0.850	0.330	0	1100 +/-20	0.0200
	11	InP							0.0500
	10	[Al(x)Ga]In(y)As			0.900	0.530	0		0.0600
	9	[Al(x)Ga]In(y)As			0.720 to 0.900	0.530	0		0.0600
	8	[Al(x)Ga]In(y)As			0.440	0.490	-3000	1100 +/-20	0.0100
Waveguide Core 5-AlGaInAs QWs	7	[Al(x)Ga]In(y)As	1	5	0.240	0.710	12000	1530	0.0060
	6	[Al(x)Ga]In(y)As	1	5	0.440	0.490	-3000	1100 +/-20	0.0100
	5	[Al(x)Ga]In(y)As			0.900 to 0.720	0.530	0		0.0600
	4	[Al(x)Ga]In(y)As			0.900	0.530	0		0.0600
	3	[Al(x)Ga]In(y)As			0.860 to 0.900	0.530	0		0.0100
	2	InP							1.2000
	1	InP							0.3000
							SUBSTRATE		

Table 4.2. IQE wafer structure used to fabricate tunable lasers.

The fabrication details shown in this section were provided by Thomas Slight from Compound Semiconductor Technologies.

The detailed fabrication process is described as follows: (i) a 300nm layer of Silicone nitride is deposited on the top of the wafer

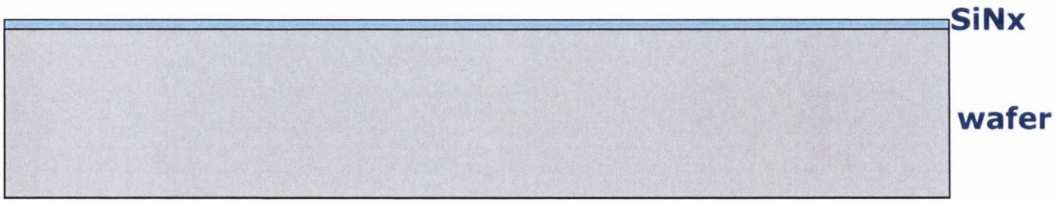

(ii) then the spin resist layer is applied and positions of the slots are marked by e- beam lithography. Here we show the etching process used for both shallow and deep slots. The deep slots are those used in our Vernier lasers.

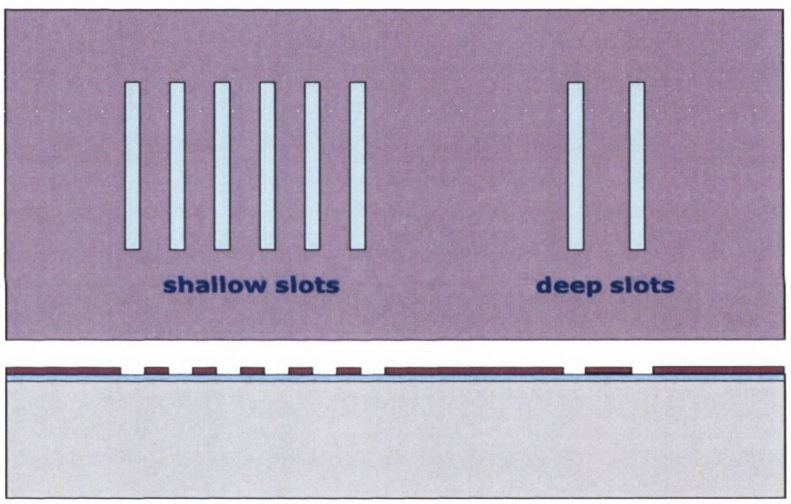

(iii) the third step is the dry etching of the nitride. The slots are etched through the nitride layer.

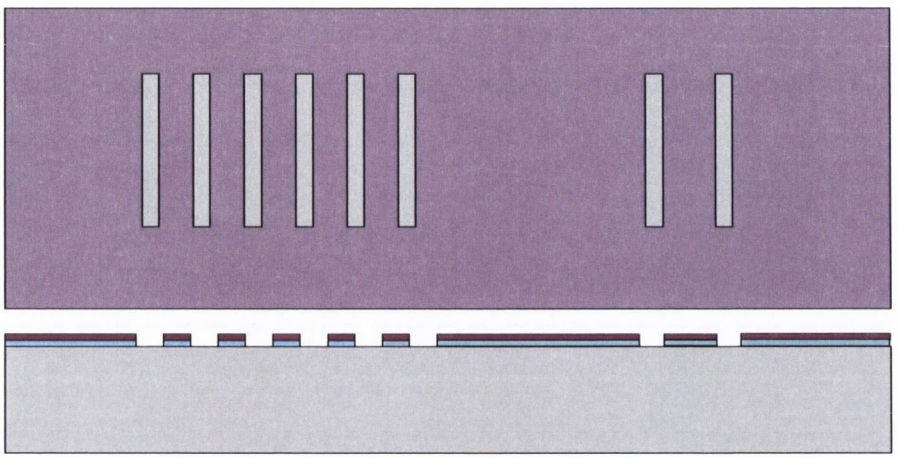

(iv) the next step is to apply the strip resist and oxide layer (marked in blue colour)

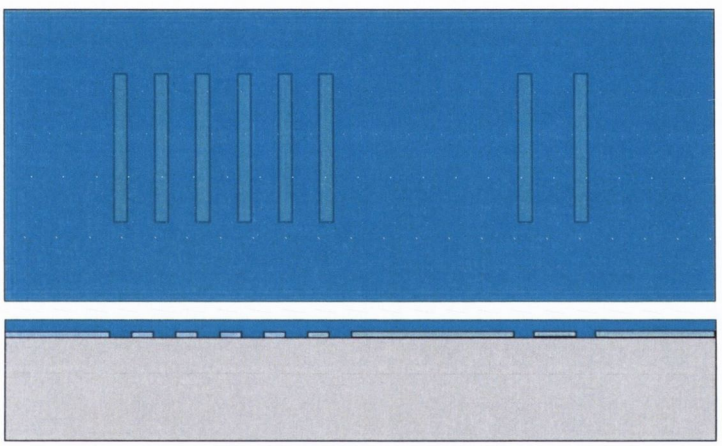

(v) the patterned oxide layer is left to protect the shallow slots pattern and another spin resist layer is applied to form the ridge of the laser

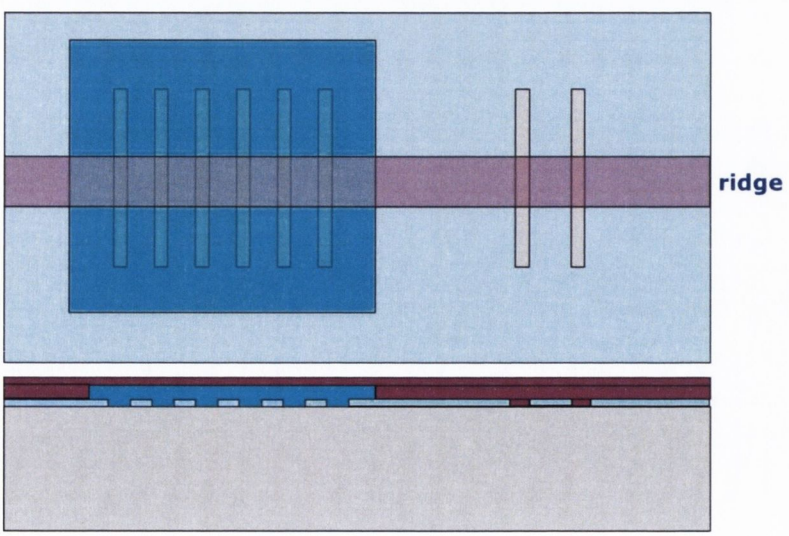

(vi) the next step is to dry etch the dielectric and another strip resist is applied to start forming the deep slots and 0.5μm high ridge. On the right hand side an end view of the waveguide is depicted.

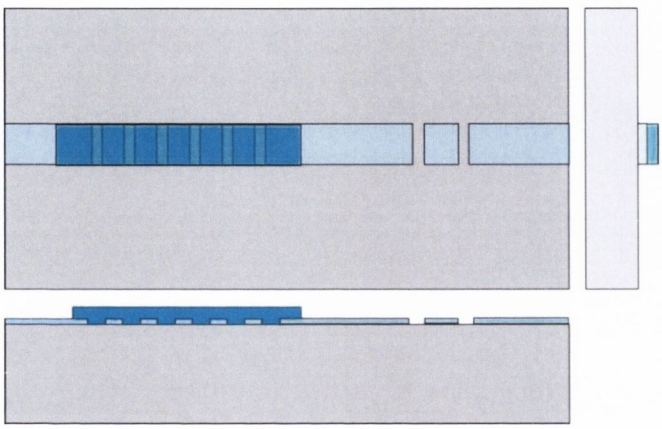

(vii) the first inductively coupled plasma dry etching (ICP) using Cl_2/N_2 gas is used here to form the deep slots

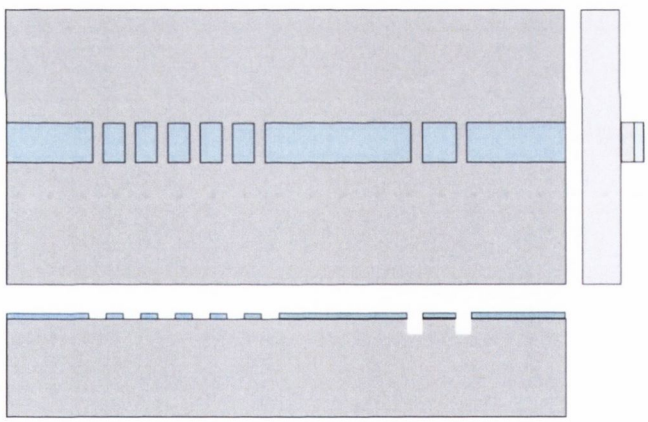

(viii) the oxide layer is selectively removed. On the right hand side an end view of the waveguide is depicted.

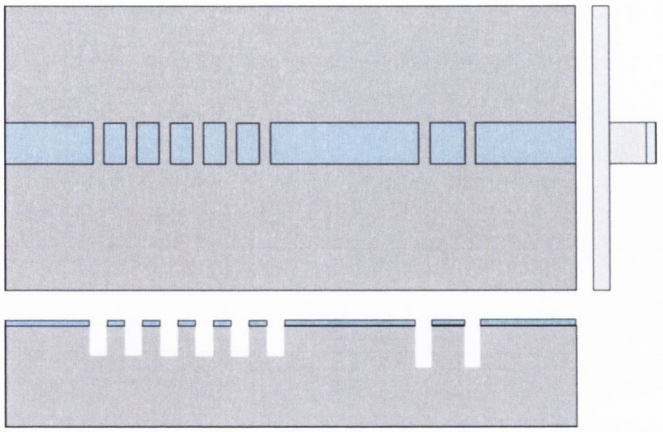

(ix) the second dry of inductively coupled plasma etching is used to form the shallow slots and the ridge to a depth of 1.85μm. On the right hand side an end view of the waveguide is depicted.

After forming the slots and the ridge, the p-metal is deposited on the structure and the p contacts are formed by lift-off lithography. It is a method for patterning deposited films and films which are difficult to dry etch. A pattern is defined on a substrate using photoresist and standard photolithography. A film is blanket- deposited all over the substrate, covering the photoresist and areas where the photoresist has been cleared. During the actual lifting-off, the photoresist under the film is removed with solvent, taking the film with it, and leaving only the film which was deposited directly on the substrate.

To ease the fabrication process, the slot width is set to 1 μm, which makes it suitable for the standard photolithography although in this case e-beam lithography was used to set the slot positions. The slot depth is 1.85 μm. Figure 4.4.1. shows SEM pictures of slots and ridge, precisely. The slot are uniform and have vertical walls. All slots have rectangular shape.

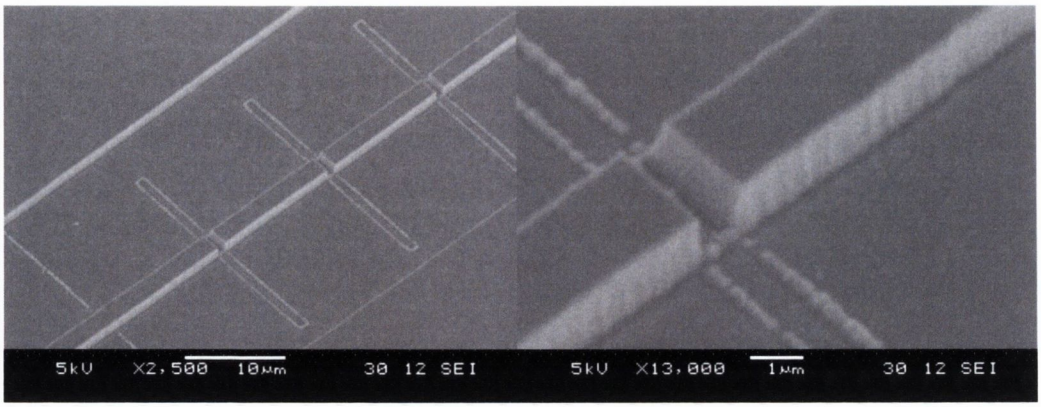

Figure 4.4.1. SEM picture of slots and ridge.

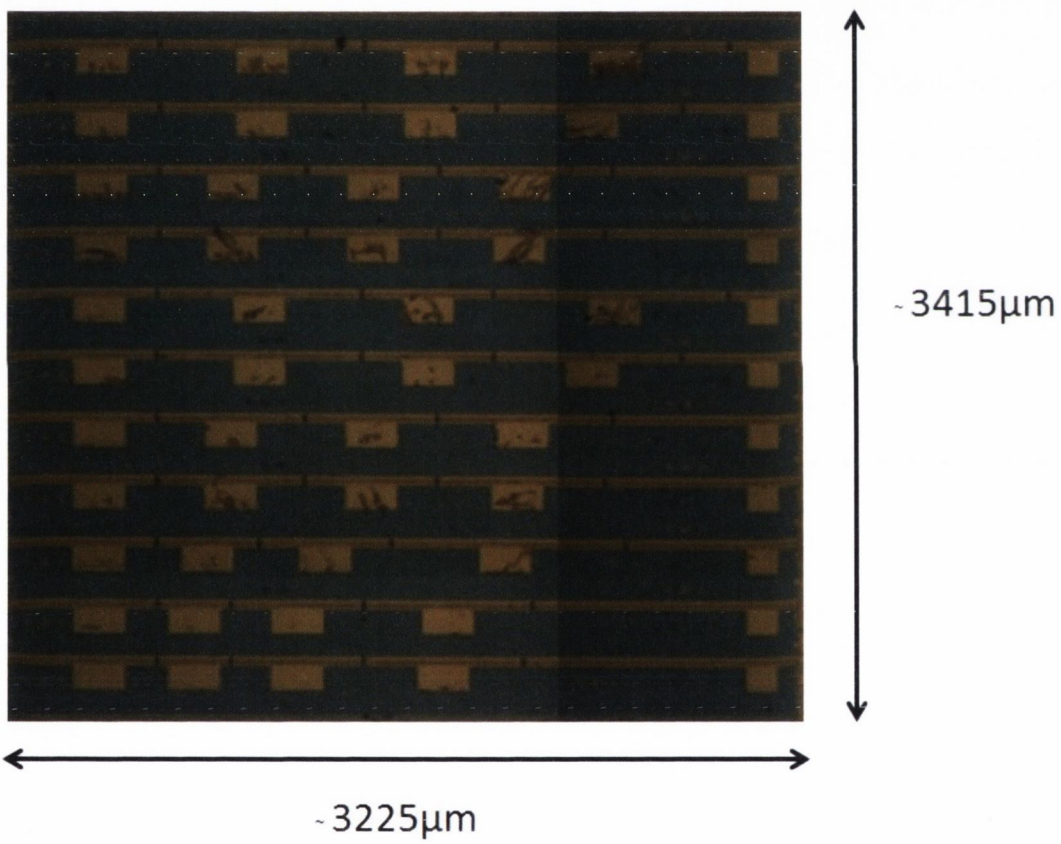

Figure 4.4.2. A picture of a ready submount of 5 contact lasers. Eleven laser are placed on a single laser chip. From left hand side: Semiconductor Optical Amplifier-SOA section, front mirror, gain section, back mirror, photo detector-PD section.

Conclusion

The designing method and the fabrication process of a multi-section tunable laser were presented in this chapter. Using MatLab software it was possible to complete the slot optimization and to extract modelling tuning maps of the lasers. For the first fabrication run detailed later, the laser with the shorter slot period was chosen as they show the widest tuning range and good SMSR values for all super-modes. The tunable laser mask design process was also described in this chapter. Three types of tunable laser were placed on the mask: five contact laser, six contact lasers and nine contact lasers. Finally the full fabrication process was described. From the first fabrication run we got four submounts with eleven laser placed on each of them: one submount with five contact lasers, one submount with six contact lasers and two submounts with nine contact lasers, in total forty- four lasers. From the second fabrication run we got fourteen submounts with eleven lasers on each of them: six submounts with five contact lasers, five submounts with six contact lasers and three submounts with nine contact lasers. In total 154 lasers. The complete tunable lasers characterization is presented in chapter 5,6,7.

References

[1] M. Masanovic, V. Lal, J. Summers, J. Barton, E. Skogen, L. Coldren and D. Blumenthal, "Design and performance of a monolithically integrated widely tunable all-optical wavelength converter with independent phase control," *IEEE Photonics Technology Letters,* vol. 16, no. 10, pp. 2299-2301, 2004.

[2] M. Sysak, J. Barton, L. Johansson, J. Raring, E. Skogen, D. Blumenthal, M. Masanovic and L. Coldren, "Single-chip wavelength conversion using a photocurrent-driven EAM integrated with widely tunable samped grating DBR laser," *IEEE Photonics Technology Letters 16(9),* vol. 16, pp. 2093-2095, 2004.

[3] B. Mason, G. Fish, J. Barton, L. Coldren and S. DenBaas, "Characteristics of sampled grating DBR lasers with integrated semiconductor optical amplifiers," *Proc. Opt. Fiber. Commun. Conf.,* vol. 1, pp. 193-195, 2000.

[4] J.P. Engelstaetder, B. Roycroft and B. Corbett, "Laser and detector using integrated reflector for photonics integration," *Electronic Letters,* vol. 44, pp. 1017-1019, 2008.

[5] A. Ward, D. Robbins, G. Busico, E.Barton, L. Ponnampalam, J. Duck, N. Whitbread, P. Williams, D. Reid, A. Carter and M. Wale, "Widely tunable DS-DBR laser with monolithically integrated SOA: design and performance," *IEEE J. Sel. Topics Quantum Electron.,* vol. 11, no. 1, pp. 149-156, 2005.

[6] R. E. Bank, D. J. Rose and W. Fichtner, "Numerical methods for semiconductor device simulations," *IEEE Transations on Electronic Devices,* vol. 30, no. 9, pp. 1031- 1041, 183.

[7] H. Wenzel, "Green's function based simulations of the optical spectrum of multisection lasers," *IEEE J.Sel. Topics Quantum Electron.,* vol. 18, no. 6, pp. 865-871, 2003.

[8] M. Pfeiffer, A. Witzig and W. Fichtner, "Coupled electro-thermo-optical 3D simulations of edge- emitting lasers," in *NUSOD*, 2001.

[9] J. Buus and M. C. Amann, Tunable laser diodes and Related Optical Sources, Wiley-IEEE Press, 2005.

[10] D. C. Byrne, J. P. Engelstaedter, W.-H. Guo, Q. Y. Lu, B. Corbett, B. Roycroft, J. O'Callaghan, F. H. Peters and J. F. Donegan, "Discretely tunable semiconductor lasers suitable for photonic integration," *IEEE Journal of Selected Topics in Quantum Elecronics 15(3),* vol. 15, no. 3, pp. 482-487, 2009.

[11] Q. Lu, W. Guo, R.Phelan, D.Byrne, J. Donegan, P. Lambkin and B.Corbett, "Analysis of slot characteristic in slotted single mode semiconductor laser using the 2-D Scattering Matrix Method," *IEEE Photonics Technology Letters,* pp. 2605-2607, 2006.

[12] L. Coldren and S. Corzine, Diode lasers and photonics integrated circuits, 1995.

[13] Q. Lu, W.-H. Guo, D. Byrne and D. J. F., "Design of Slotted Single-Mode Lasers Suitable for Photonics Integration," *IEEE Photonics Technology Letters,* vol. 22, no. 11, pp. 787-789, 2010.

[14] N. Cotter, T. Preist and J. Sambles, "Scattering- matrix approach to multilayer diffraction," *Journal of the Optical Society of America A,* vol. 12, pp. 1097-1103, 1995.

Chapter 5. Tunable lasers characteristics

Introduction

Widely tunable semiconductor laser are the key components in dense – wavelength division multiplexed (DWDM) telecommunication systems [1] [2] [3]. Tunable lasers are also needed in other important markets such as trace gas detection for environmental emission monitoring [4] [5] . Semiconductor tunable lasers also play an important role in wavelength converters [6] [7] and wavelength routing [8] where optical- electronic-optical converters detect any input channel and convert it to any output channel. They can also be used for phased array radar systems that use true- time delay beam steering [9].

So far, a number of monolithic wavelength-tunable lasers have been developed such as the sampled-grating distributed Bragg reflector (SG-DBR) lasers [10] [11] [12], the super-structure grating distributed Bragg reflector (SSG-DBR) lasers [13] [14] [15], the digital supermode distributed Bragg reflector (DS-DBR) lasers [16] [17] [18] and tunable DFB [19] [20] [21] and slotted laser arrays (TLAs) [22]. However, such structures apart from that in [22] are conventionally fabricated with an embedded grating, which requires at least one re-growth step complicating the device fabrication and therefore increasing the device cost. To reduce the cost, complexity and to increase the wafer yield, our group has recently demonstrated single mode lasers and wavelength tunable lasers based on slots [22] [23]. The merit of this laser platform is that it is re-growth free, can be fabricated by standard photolithography and is inherently suitable for photonic integration due to the high reflectivity of the mirror sections. Such a laser platform has several advantages: a significant reduction of cost, it enables the use of AlGaInAs materials for high temperature operation and also enables the integration with other optical components i.e. semiconductor optical amplifiers (SOA) to control the output power and with electro-absorption and Mach-Zehnder modulators [24].

In this chapter, five- section, six- section and nine- section widely tunable lasers are presented and charcterized. The design of six- section laser includes a phase section for fine tuning. A nine- section laser has extra contacts between the main laser sections to improve the laser performance. A short section semiconductor optical amplifer (SOA) is integrated with all lasers. The fabricated lasers has a very wide tuning range from ~40nm to ~ 55 nm with 9 to12 supermodes with side mode suppression ratio over 30dB.

5.1. Five contact laser

Nine slots front mirror with the slot period of 97μm, nine slots back mirror with the slot period of 108 μm

The five section lasers presented in this chapter have the same epitaxial structure. The only difference is in the slot periods varying from the long one for both mirrors, 97/108 μm, towards the short one, 70/76 μm, to extend the Vernier tuning range. As mentioned in the previous chapter the tuning range depends on the slot period [25]

$$\Delta\lambda' = \frac{\lambda_f \lambda_b + 1}{\lambda_b - \lambda_f} \tag{5.1}$$

where λ_f, λ_b are free spectral ranges FSRs for the front and back mirrors respectively. The free spectral range (FSR) is determined as

$$FSR = \frac{\lambda^2}{2 * n_g * dp_{f,b}} \tag{5.2}$$

where λ is the central wavelength, in this case is set to 1550nm, n_g is the group index of the active waveguide set to 3.5, and dp_f, dp_b are the slot periods in the front and back mirror, respectively. Therefore shorter slot period results in bigger FSR and larger tuning range.

In order to get a higher fraction of the total emitted power from the front, it is advantageous to use a design with a shorter slot period at the front than at the back [26].

The schematic structure of the laser is shown in figure 5.1.1 below.

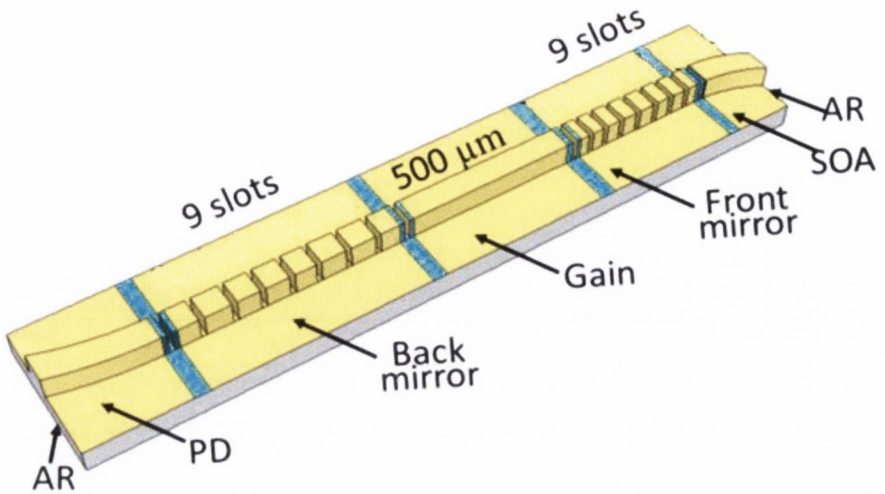

Figure 5.1.1. Five section tunable laser schematic structure.

For the laser characterisation, four current sources were used independently to inject current to the SOA, gain and two mirror sections. The device was mounted on heat sink which was held to a constant temperature of 20°C using a thermoelectric cooling device. The currents injected into the SOA and the gain sections were kept constant and set to 20 and 100 mA, respectively with the PD section left unbiased. The currents injected into the two mirror sections were scanned from 0 to 300 mA with a step of 2 mA. The photodiode and picoammeter were used to record the coupled output power to determine if the coupling efficiency is stable. The output spectra, peak wavelength and side mode suppression ratio (SMSR) were recorded using an optical spectrum analyser with a resolution bandwidth of 0.01 nm and a sensitivity of -75dB.

The experimental set-up to measure the performance of the lasers is shown schematically in figure 5.1.2. The same set-up is used for characterisation of all lasers described in this chapter.

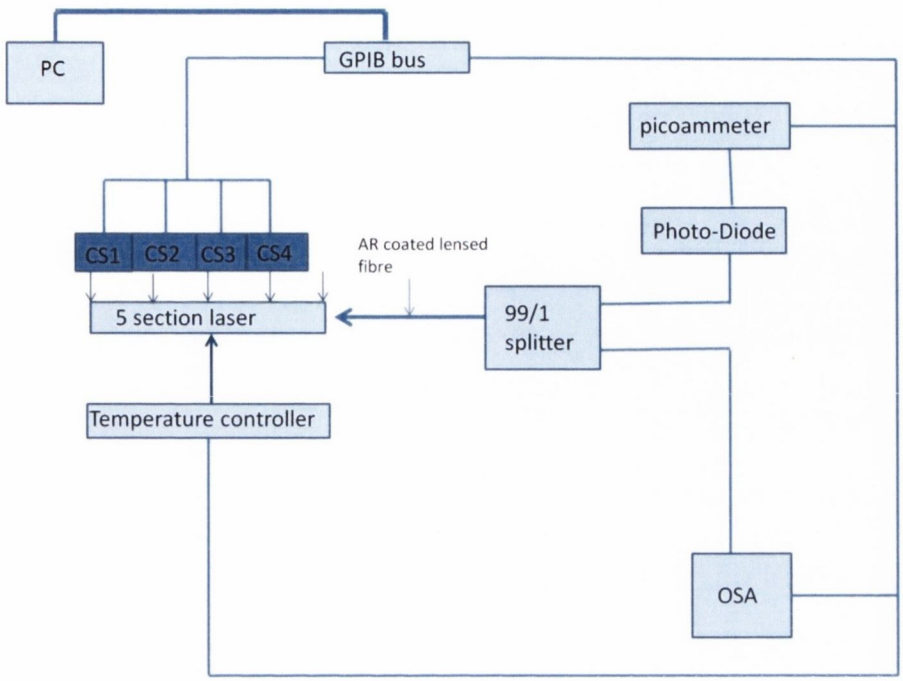

Figure 5.1.2. An experimental set-up to characterize five section tunable laser.

First we characterised the laser with the slot periods of 97 μm and 108 μm for the front and back mirror, respectively. With a group index of 3.5 this yields a FSR in both mirrors of 3.36 and 3.02 nm, respectively. Using the formula to calculate the frequency:

$$f = \frac{c}{\lambda}$$

where f is freguency, c is speed of light and λ is wavelength. Substituting $c=3*10^8$ m/s and $\lambda_1=1.55*10^{-6}$m we get the frequency f_1=465GHz. The next channel is 3.5 nm apart therefore the wavelength is $\lambda_2=1.5535*10^{-6}$m. Substituting again $c=3*10^8$ m/s and $\lambda_2=1.5535*10^{-6}$m into equation we get f_2=465.9GHz. the difference between the channel frequencies is equal to

$$f_{diff} = f_2 - f_1$$

we get the channel spacing of about 400GHz.

The front and back reflectors length are 873 μm and 972 μm, respectively.

The output power map versus currents injected into the front and back mirror is shown in Figure 5.1.3 below. It can be seen that the output power is dependent on the currents injected to the mirror sections and it is increasing with increasing current injected to the front mirror. The back mirror does not strongly affect the output power although as we will see, tuning can still be achieved through adapting the back current. In this case the higher power, marked in red colour on the map, is obtained for the front current from 270 to 300 mA. The scales for all tuning maps go from small values of output power, SMSR, wavelength low values marked in blue toward high values marked in red.

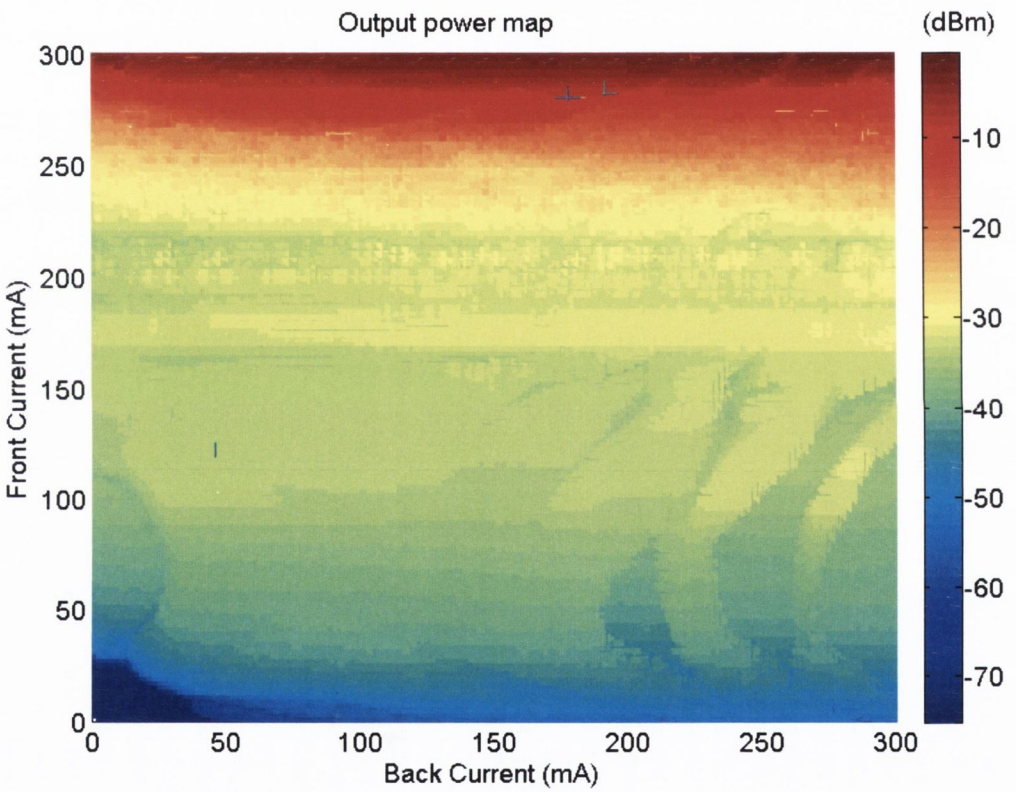

Figure 5.1.3. Output power map versus currents injected into the mirror sections for a laser with the slot periods of 97μm for the front mirror and 108μm for the back mirror.

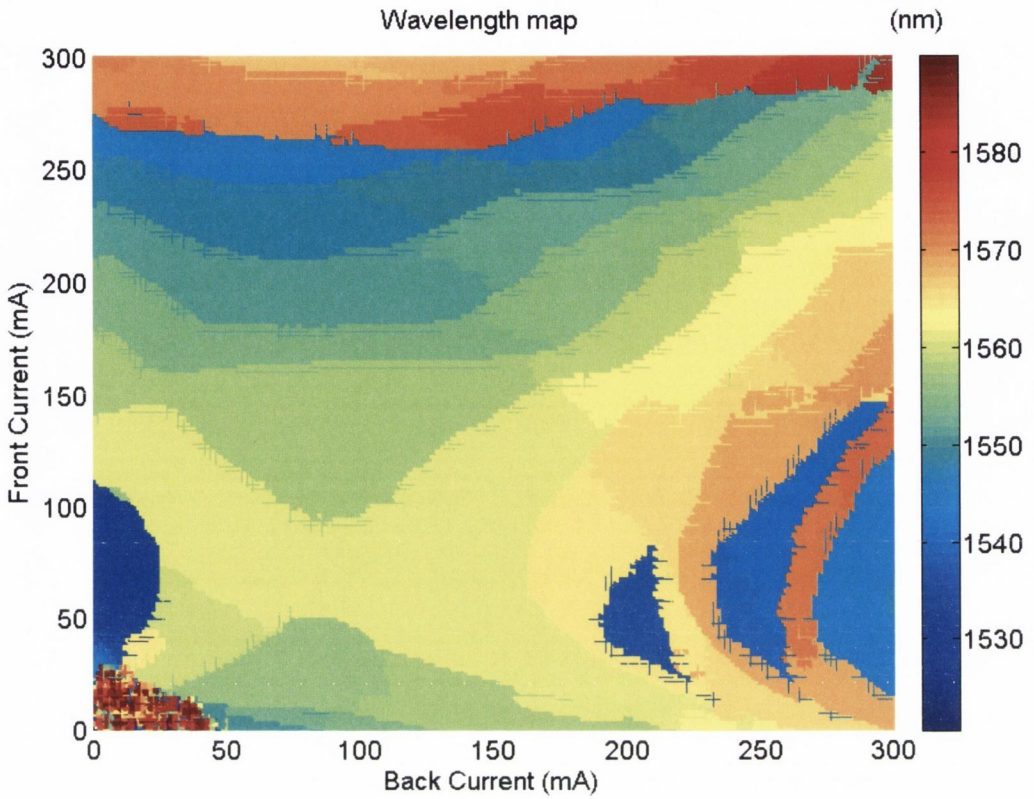

Figure 5.1.4. Wavelength map versus currents injected into mirror sections for a laser with the slot period of 97μm for the front mirror and 108μm for the back mirror.

As mentioned before the currents injected into the front and back mirror sections are scanned between 0 and 300 mA with the step of 2 mA. For each pair of the front and back currents, the wavelength, SMSR and output power is recorded using an optical spectrum analyzer OSA. The recorded values of wavelength, SMSR and power are then plotted against the injected currents resulting in tuning maps to clearly see how these parameters are changing with current changes.

As can be seen in figure 5.1.4 super-mode hopping occurs at the boundaries of each colour within this map. SMSR at least over 30 dB is required for the lasing to be designated as single mode output. As can be seen form figures 5.1.4 and 5.1.5, there are very large regions indicated in red colour, where the SMSR is very high but there are also some small region where the SMSR has a low value. The effect occurs due to the mode competition, usually when one of the currents injected to the mirror sections is high.

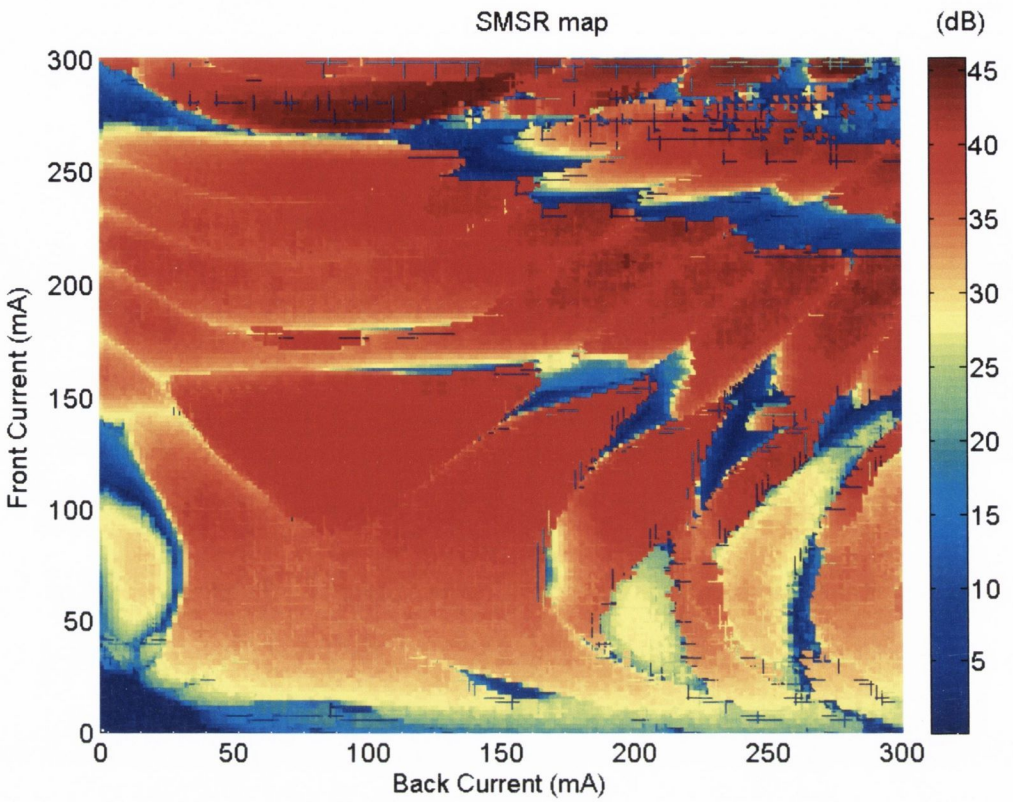

Figure 5.1.5. SMSR map versus currents injected into the mirror sections for a laser with the slot periods of 97μm for the front mirror and 108μm for the back mirror.

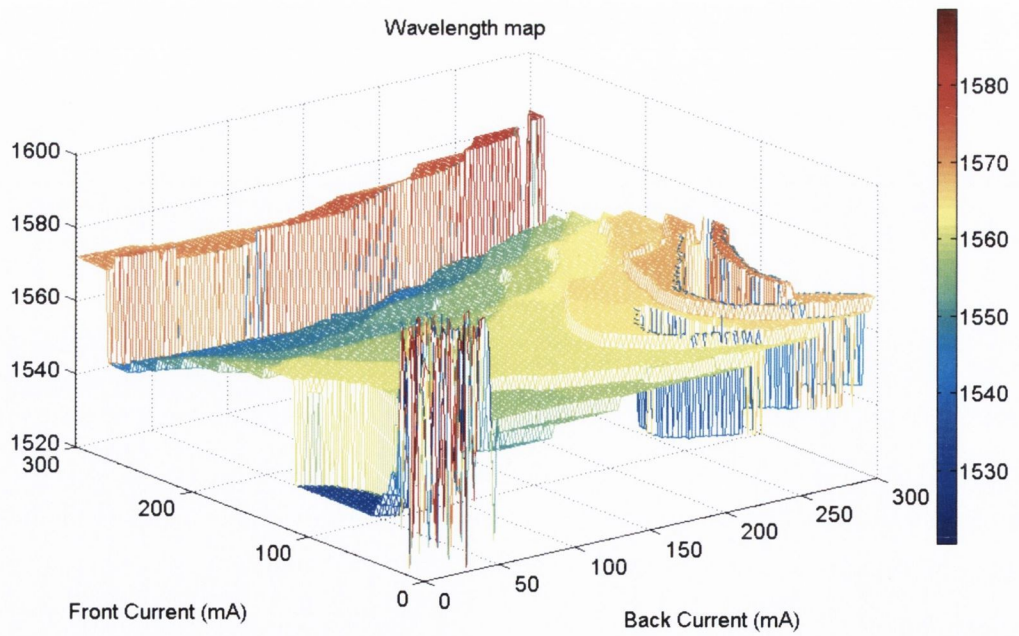

Figure 5.1.6. Wavelength 3D mesh map versus currents injected into the mirror sections for a laser with the slot period of 97μm for the front mirror and 108μm for the back mirror.

Figure 5.1.6. shows the mesh map in which it is easier to see the transitions from one wavelength to another. It shows the wavelength plotted versus currents injected into the front and back mirrors in the 3D view. The steps of colour on the map correspond to different wavelengths.

Combining figures 5.1.4 and 5.1.5 the SMSR versus wavelength over all injected currents can be found. To obtain the precise tuning range as well as the number of supermodes the SMSR against peak wavelength is plotted. For each pair of scanned front and back current from figures 5.1.4 and 5.1.5, the values for the peak wavelength as well as the SMSR were extracted. Then the SMSR against peak wavelength for each front and back current combination is plotted as shown in figure 5.1.7. A discrete tuning behaviour for 14 supermodes can be found over the tuning range of 50 nm from 1532 nm to 1580nm. The first 3 modes on the blue side of the spectrum suffer from a low SMSR less than 30 dB. For the wavelength range from 1545nm to 1580 nm all modes exhibit SMSR values higher than 40 dB.

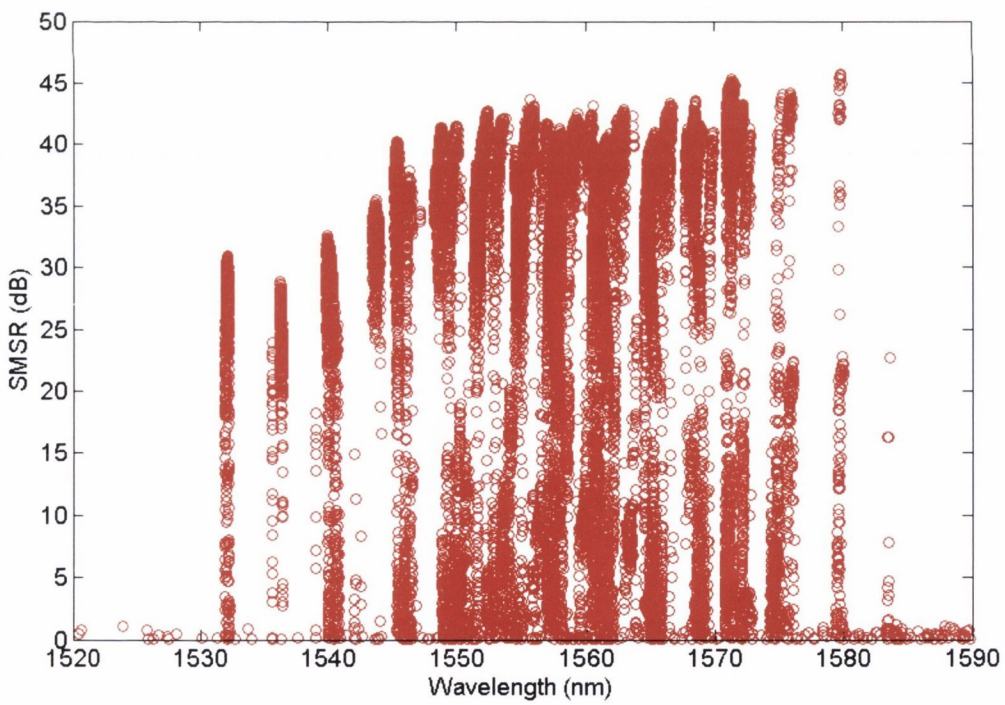

Figure 5.1.7. SMSR versus peak wavelength for a laser with the slot period of 97μm for the front mirror and 108μm for the back mirror.

Again combining figures 5.1.3 and 5.1.4 the output power versus wavelength over all injected currents is shown in figure 5.1.8. The output power is not uniform for all super-

modes. The modes on the red side of the spectrum exhibit higher output power. Where the SMSR is large the power is also large showing that there is good single mode lasing at these wavelengths with a particular current injection combination.

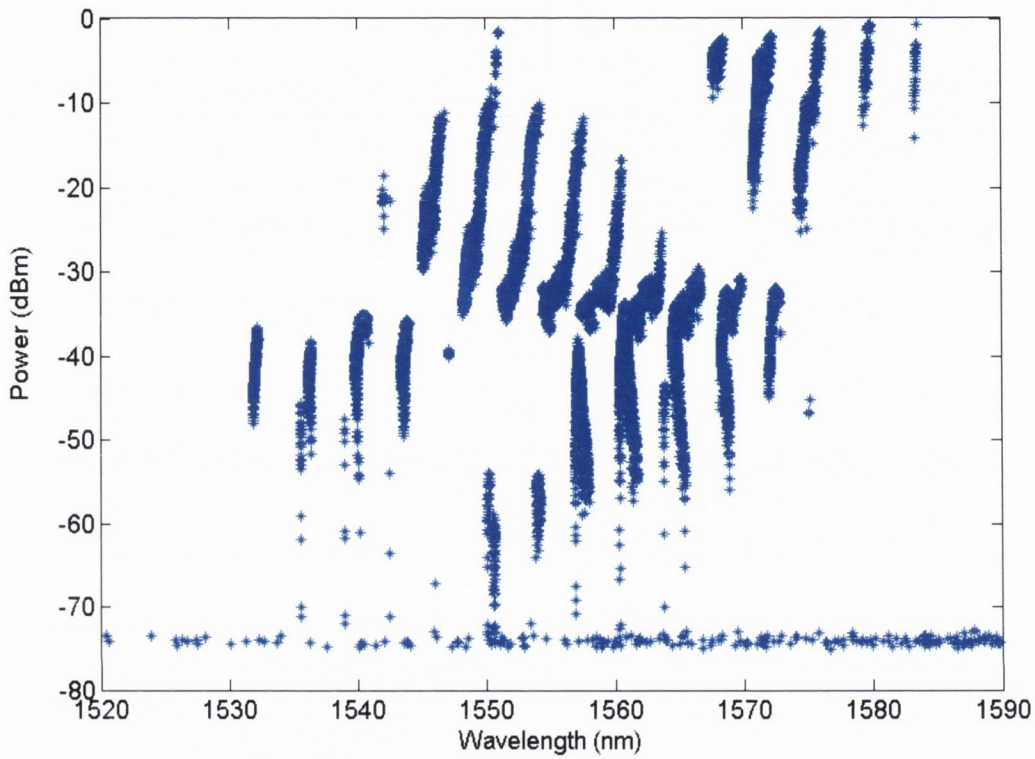

Figure 5.1.8. Output power versus peak wavelength for a laser with the slot period of 97μm for the front mirror and 108μm for the back mirror.

Nine slots front mirror with the slot period of 86μm, nine slots back mirror with the slot period of 97 μm

The next laser characterised here has the slot periods of 86 μm in the front mirror and 97 μm in the back mirror, which leads to FSR of 3.8nm and 3.36 nm, respectively. The mirror lengths are 774 μm and 873 μm for the front and back, respectively.

The output power map is shown in the figure 5.1.9 below. As can be seen there are two regions where the output power is in high: the first one for the front current from 280mA to 300mA and the second one for the front current from 150mA to 200mA.

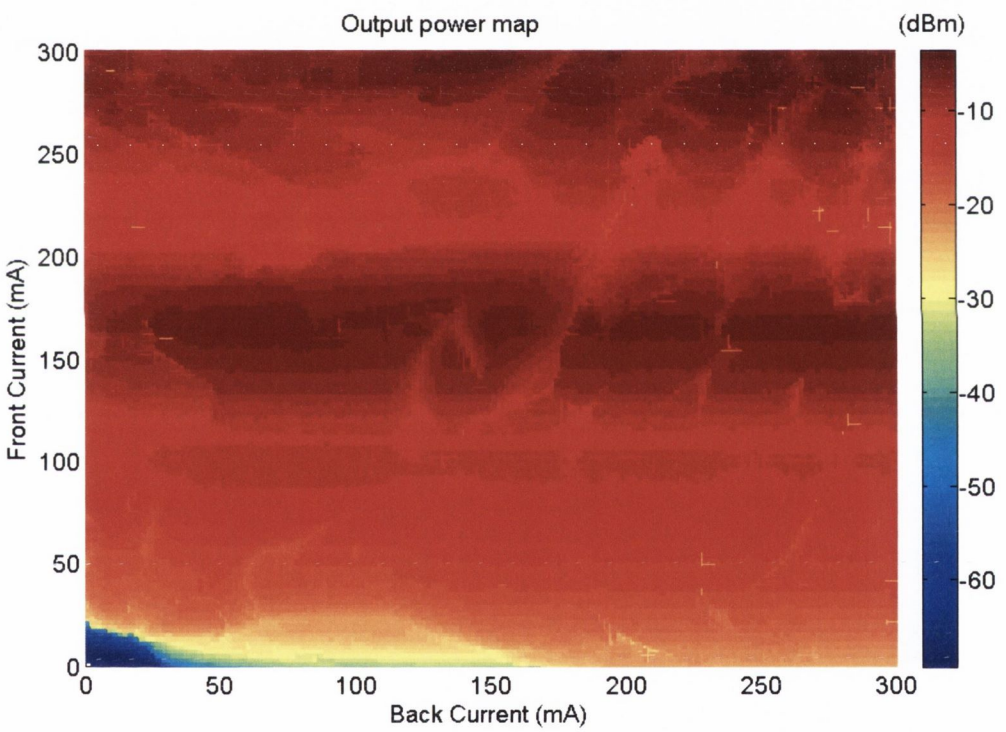

Figure 5.1.9. Output power map versus currents injected into the mirror sections for a laser with the slot period of 86μm for the front mirror and 97μm for the back mirror.

The wavelength and the SMSR maps are shown in the figures 5.1.10 and 5.1.11, respectively. As seen in the figure 5.1.10, the wavelength is not changing smoothly with the injected currents. Also as can be seen in the SMSR map in figure 5.1.11, the laser suffers from the mode competition showing big regions with low SMSR.

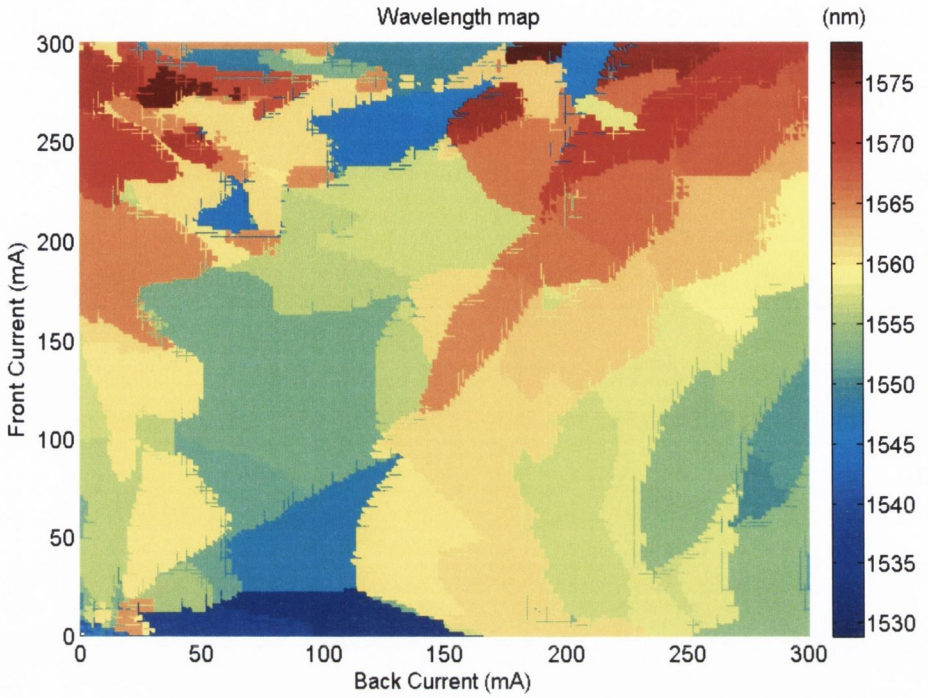

Figure 5.1.10. Wavelength tuning map versus currents injected into the mirror sections for a laser with the slot period of 86μm for the front mirror and 97μ for the back mirror.

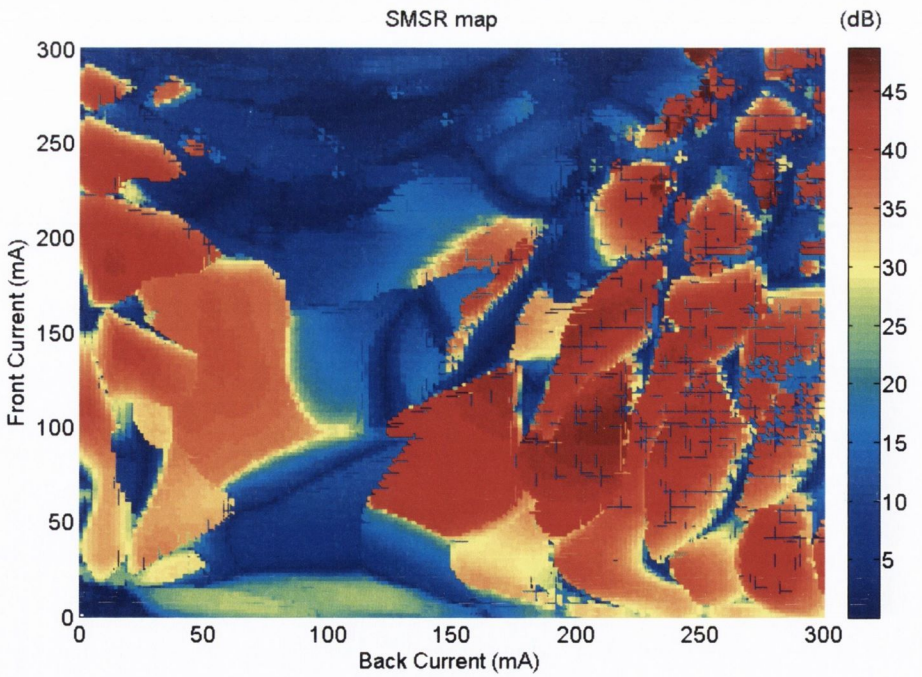

Figure 5.1.11. SMSR map versus currents injected into the mirror sections for a laser with the slot period of 86μ for the front mirror and 97μm for the back mirror.

Figure 5.1.12 shown below shows the extracted SMSR versus corresponding peak wavelength for all injected currents. A discrete tuning range can be obtained for the wavelength of 1535nm to 1580 nm. Modes for the wavelength from 1550nm to 1580 nm show a good SMSR values over 40 dB therefore the tuning range is 30nm. The output power versus peak wavelength is shown in figure 5.1.13. Where the SMSR is high the power is also high showing that there is good singe mode lasing at these wavelengths with a particular current injection combination.

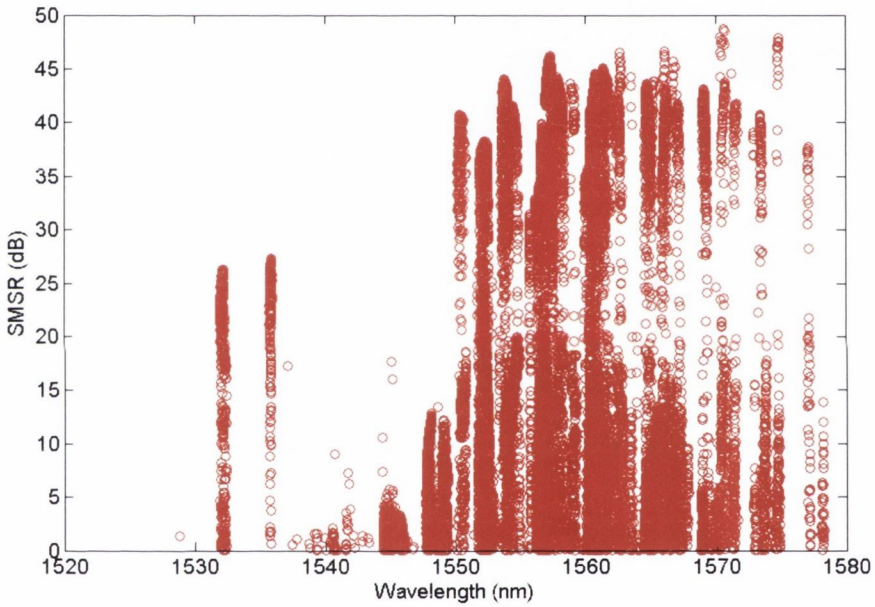

Figure 5.1.12. SMSR versus peak wavelength for a laser with the slot period of 86μm for the front mirror and 97μm for the back mirror.

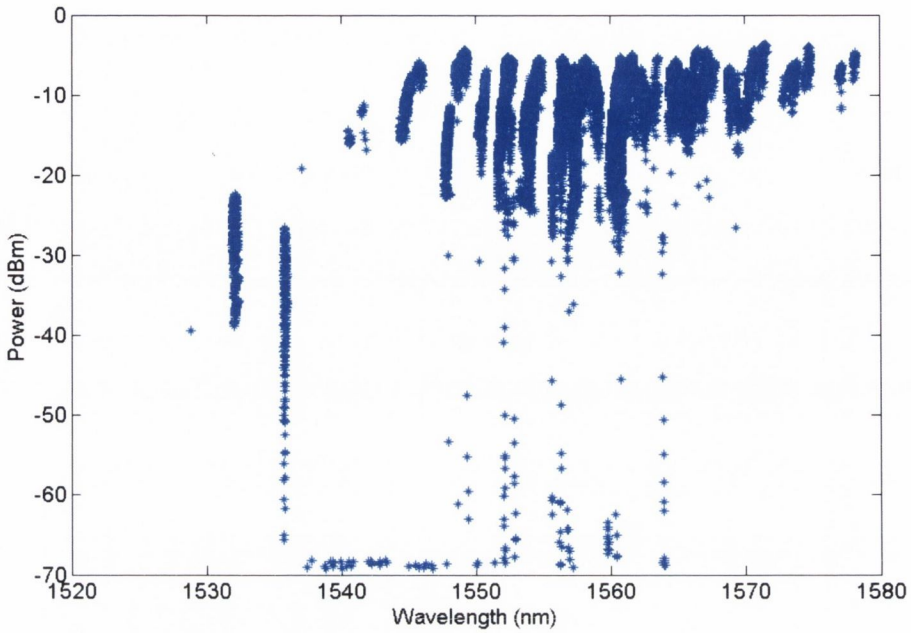

Figure 5.1.13. Output power versus peak wavelength for a laser with the slot period of 86μm for the back mirror and 97μm for the back mirror.

Figure 5.1.14 below shows a mesh wavelength map in which it is easier to see the transitions from one mode to another.

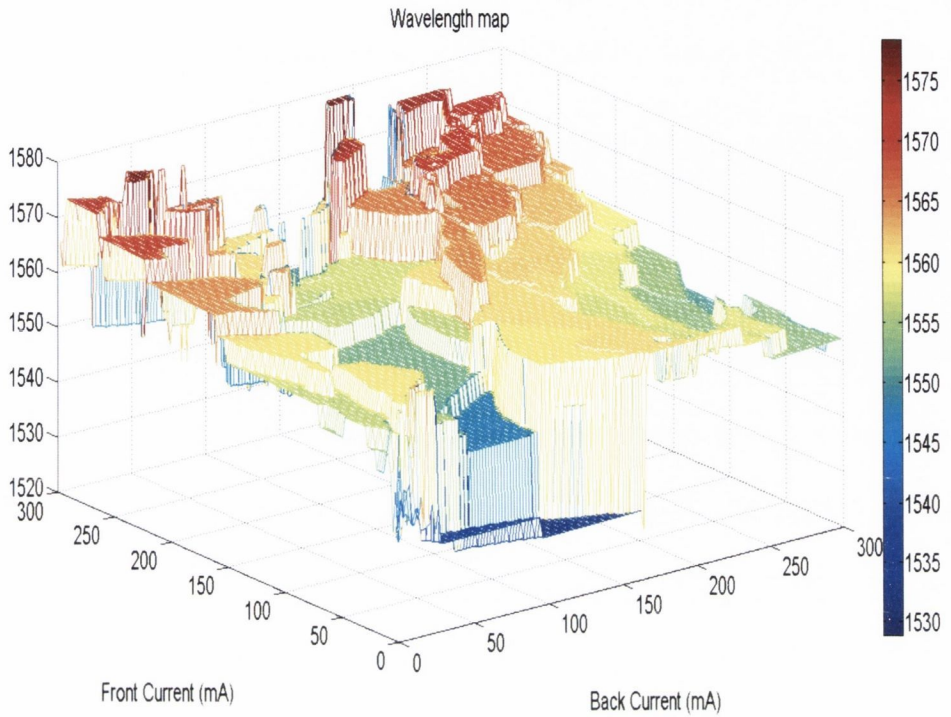

Figure 5.1.14. Wavelength mesh map versus currents injected into the mirror sections for a laser with the slot period of 86μm for the front mirror and 97μm for the back mirror.

For a comparison we checked the device with the same slot periods of 86 μm and 97 μm as the one described above, but placed further down on a laser submount.

The output power is shown in figure 5.1.15 below. As it can be seen the output has a high value for high front injection current.

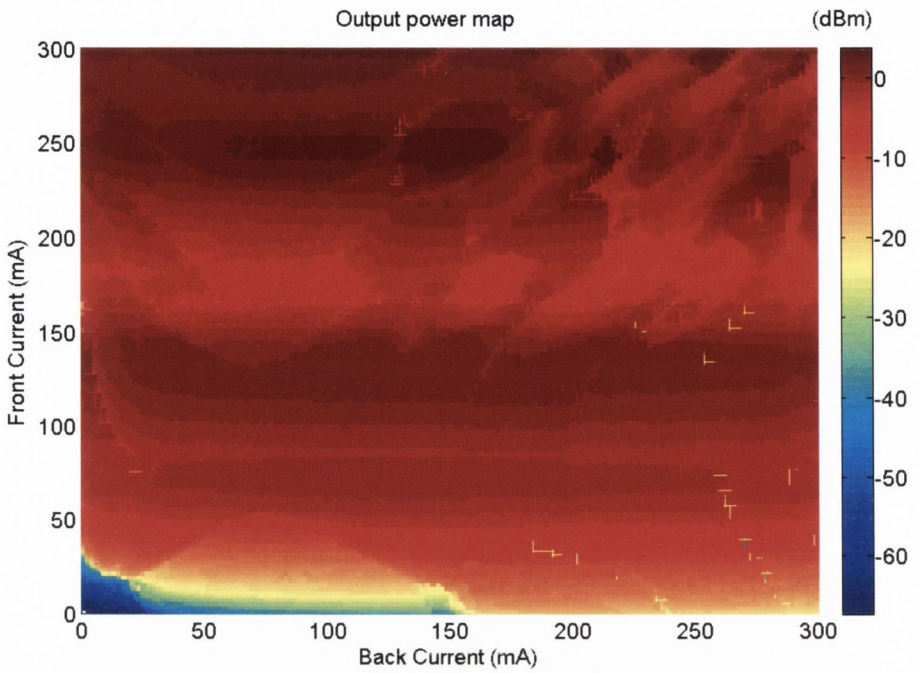

Figure 5.1.15. The output power map versus currents injected into the mirror sections for a laser with the slot period of 86μm for the front mirror and 97μm for the back mirror.

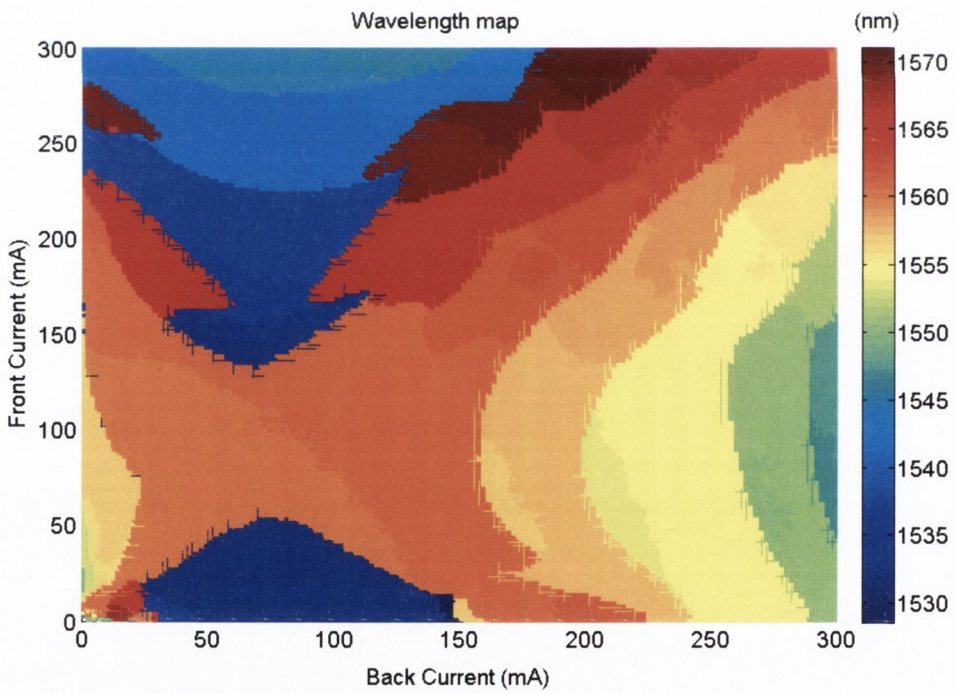

Figure 5.1.16. Wavelength map versus currents injected into both mirror sections for a laser with the slot period of 86μ for the front mirror and 97μm for the back mirror.

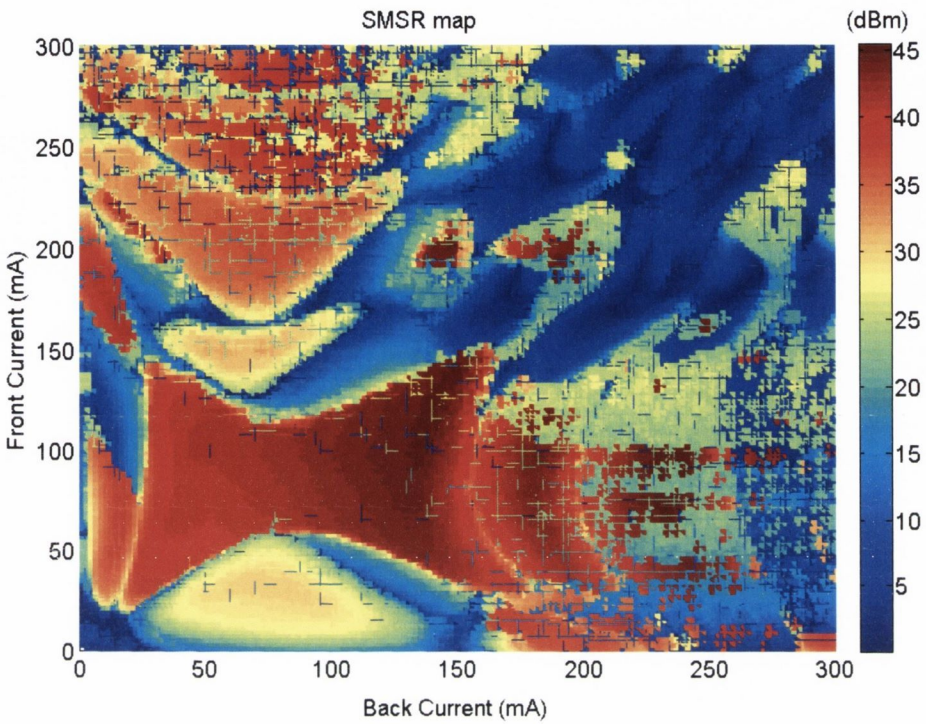

Figure 5.1.17. SMSR map versus currents injected into both mirror sections for a laser with the sot period of 86μm for the front mirror and 97μm for the back mirror.

The wavelength and SMSR maps are shown in the figures 5.1.16 and 5.1.17 above. The wavelength bands in this case are smooth and clearly visible. It can be seen that there is still some mode competition resulting in some low SMSR values. This effect here occurs for high currents injected into the mirror sections which may be due to the heating problem in the laser. Figure 5.1.18 shows mesh wavelength map.

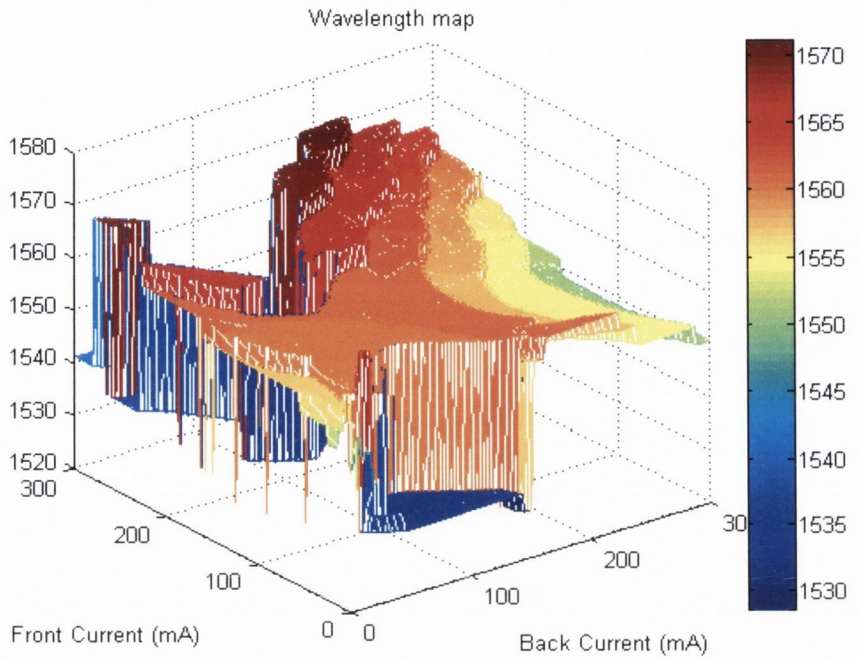

Figure 5.1.18. Wavelength mesh map versus currents injected into the both mirror sections for a laser with the slot periods of 86μm and 97μm for the back mirror.

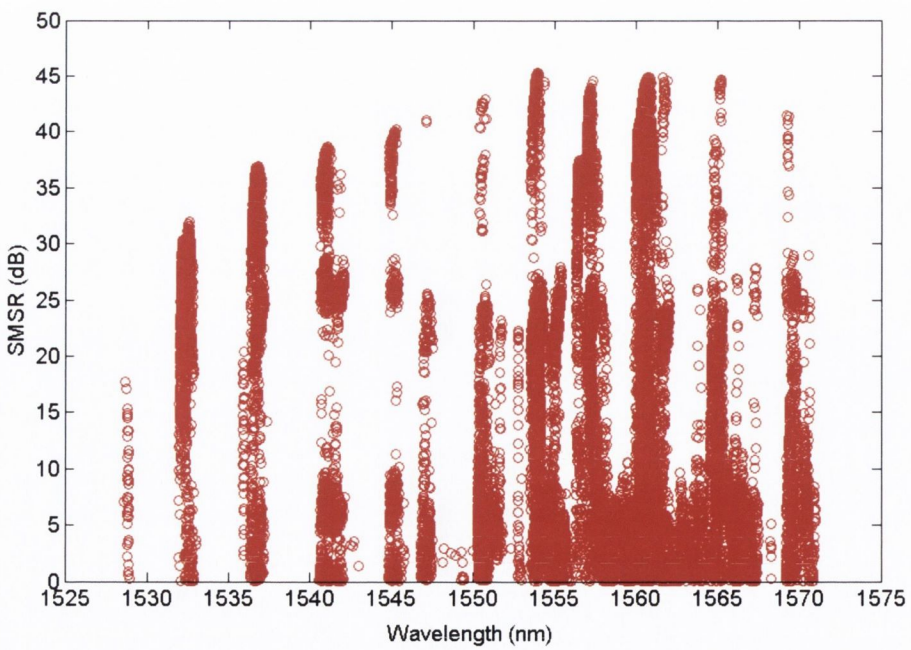

Figure 5.1.19. SMSR versus peak wavelength for a laser with the slot period of 86μm for the front mirror and 97μm for back mirror.

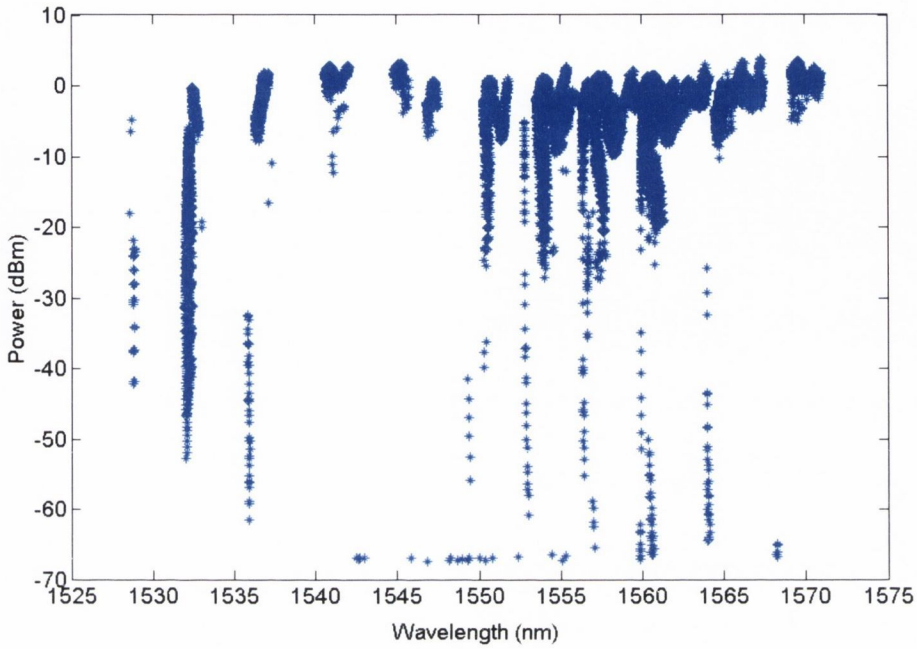

Figure 5.1.20. Output power versus peak wavelength for a laser with the slot period of 86μm for the front mirror and 97μm for the back mirror.

Figures 5.1.19 and 5.1.20 show plotted SMSR and power versus wavelength for all injected currents, respectively. As can be seen in figure 5.1.19, 12 super-modes are accessible for wavelength from 1528 nm to 1579 nm. 11 of the super-modes have the SMSR greater than 30 dB for the wavelength from 1532nm to 1570nm. The tuning range for DBR type lasers exceeds the longitudinal mode spacing, a continuous change in tuning current will lead to a stepwise change in lasing frequency known as discrete tuning [27]. Overall the discrete tuning range is 42 nm long. The output power versus wavelength plotted in figure 5.1.20 is uniform with a variation within 2dBm. It is clearly seen that the performance of the laser with the same structure but placed further down on the laser bar is much better. The reason for that is that the lasers placed on the edge of the bar are more likely to be damaged during the fabrication process.

Nine slots, front mirror with the slot period of 70μm, nine slots back mirror with the slot period of 80 μm

The laser described in this section has slots periods of 70 μm for the front mirror and 80 μm for the back mirror. The FSRs are 4.9 nm and 4.3 nm for the front and back mirror, respectively. The front mirror length is 630 μm and the back mirror length is 720 μm.

The output power map is shown in figure 5.1.21 below. The power reaches higher values with increasing front and back current. The best output power is achieved for the current combination of 150 mA for the front current and the back current for 50 mA to 300 mA.

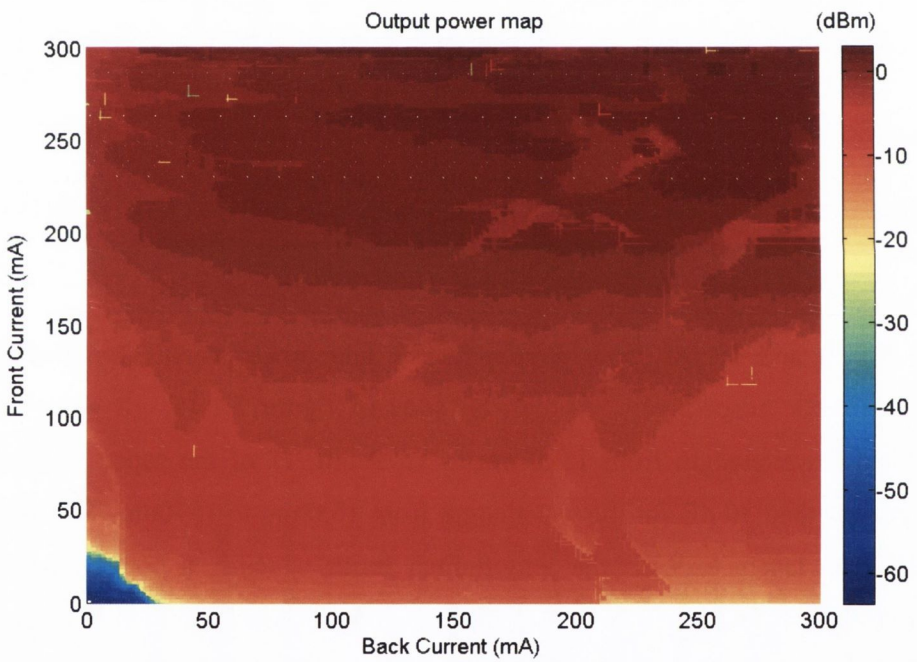

Figure 5.1.21. Output power versus currents injected into the mirror section for a laser with the slot period of 70μm for the front mirror and 80μm for the back mirror.

The wavelength and SMSR tuning maps versus currents injected into the front and back mirror are shown in figures 5.1.22 and 5.1.23, respectively. In figure 5.1.22 the super-modes islands are clearly visible for all currents injected into the front and back mirror sections. The SMSR map in figure 5.1.23 shows some regions with low SMSR for increasing front and back currents. This effect occurs due to the temperature problem in

the laser. Lower SMSR also occurs at the boundary of super-mode hopping. Figure 5.1.24. shows mesh 3 D wavelength map.

The SMSR and power versus wavelength for are shown in figures 5.1.25 and 5.1.26, respectively. In this case, in figure 5.1.27, the discrete tuning range is 45 nm for the wavelength range from 1530 nm to 1575 nm. This figure shows that ~ 13 distinct super-mode positions are visible. Some of these are very broad (>1 nm) and it is difficult to determine if this is one mode or two. The modes at the end of the range show low SMSR values < 25 dB.

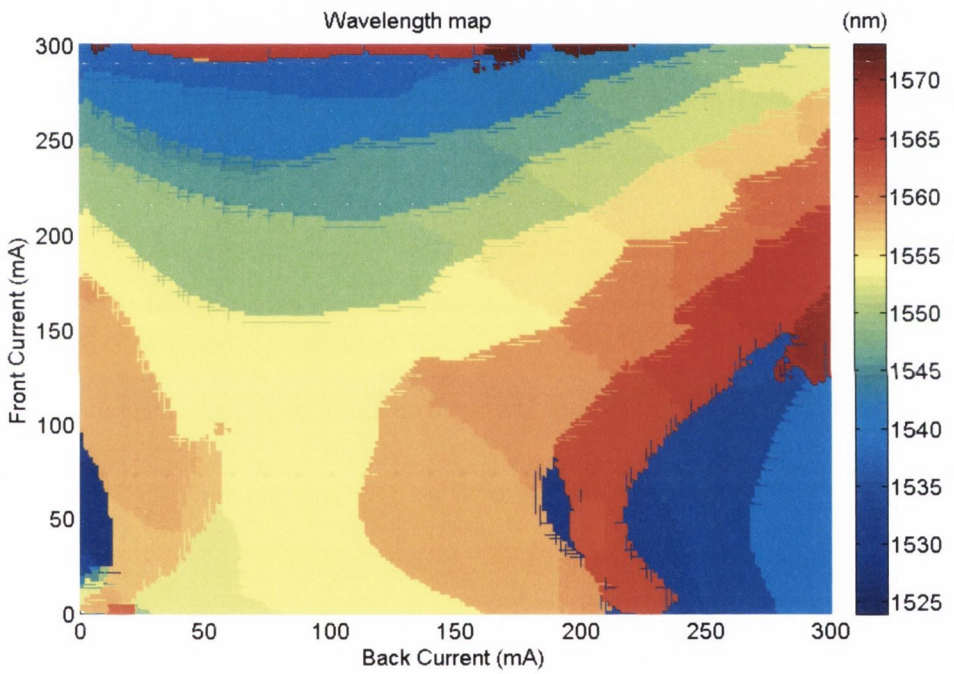

Figure 5.1.22. Wavelength map versus currents injected into the both mirror section for a laser with the slot period of 70μm for the front mirror and 80μm for the back mirror.

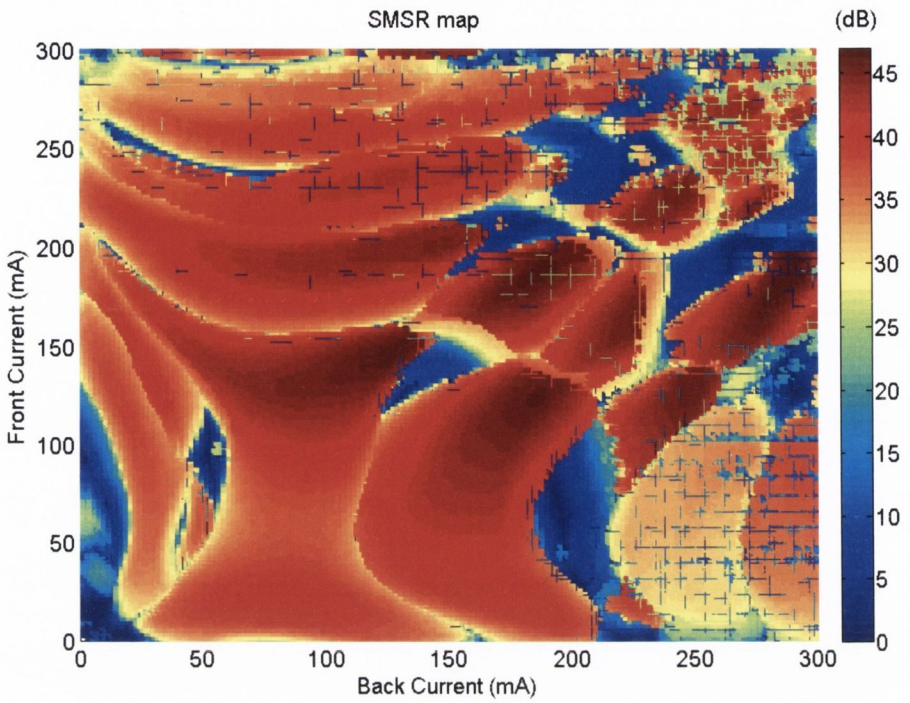

Figure 5.1.23. SMSR map versus currents injected into the both mirror sections for a laser with the slot period of 70μm for the front mirror and 80μm for the back mirror.

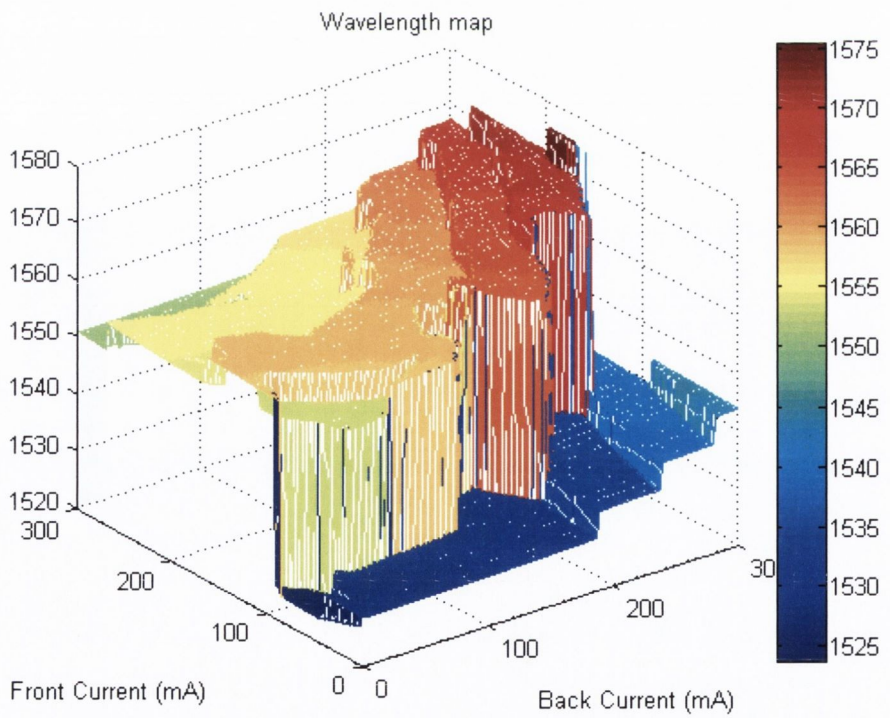

Figure 5.1.24. Wavelength mesh map versus currents injected into the both mirror sections for a laser with the slot period of 70μm for the front mirror and 80μm for the back mirror.

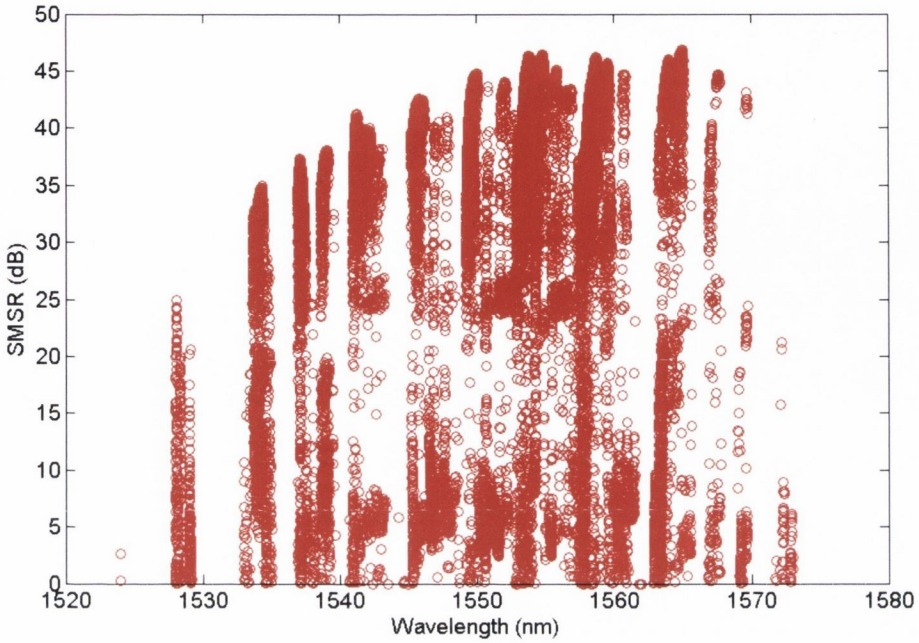

Figure 5.1.25. SMSR versus peak wavelength for a laser with the slot period of 70μm for the front mirror and 80μm for the back mirror.

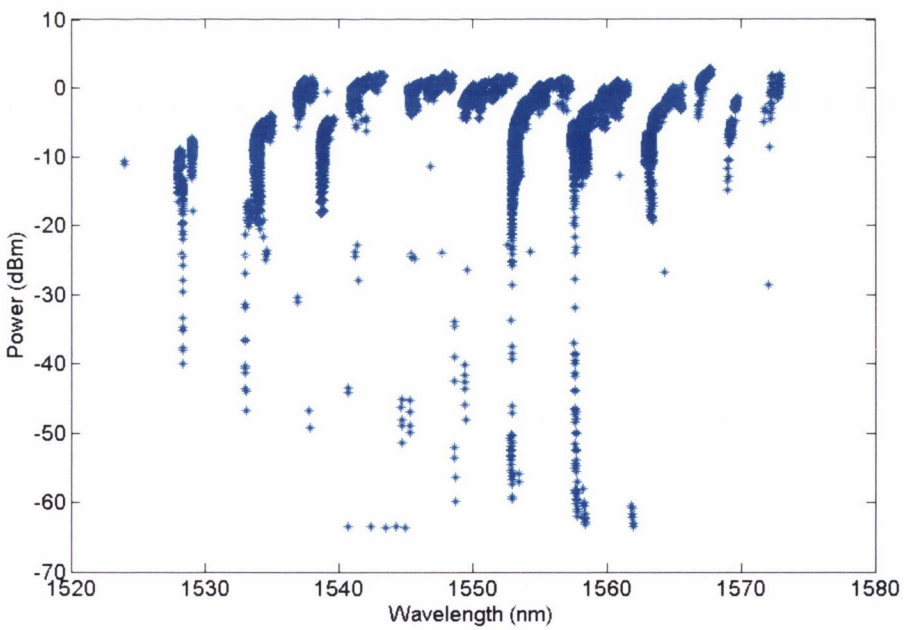

Figure 5.1.26. Output power versus peak wavelength for a laser with the slot period of 70μm for the front mirror and 80μm for the back mirror.

In figure 5.1.25 modes on the blue side of the spectrum show lower SMSR. Generally tunable lasers suffer from a lower SMSR on the blue side and the red side of gain

spectrum due to their large gain differences [26]. Therefore the super modes on the red side experience a higher gain comparing with those in blue side, which results in lower SMSRs on the blue side compare with the red side. To increase the SMSR on the blue side of the spectrum we increased the current injected to the gain section to 150 mA. Figure 5.1.27 shows SMSR for the gain current of 100 mA- marked in red and SMSR for the gain current of 150 mA- marked in blue. It can be seen in the figure that increasing the current injected into the gain section significant improved the SMSR values on the blue and red side of the spectrum. SMSR for the first mode for the wavelength of 1530 nm increased now from 25dB to 45dB. All super-modes now exhibit an SMSR over 40 dB. Figure 5.1.28 shows the output power versus wavelength peak for the current injected into the gain section of 100mA-blue and 150mA-red. The best SMSR value is about 48dB. The output power also increases with increasing gain current.

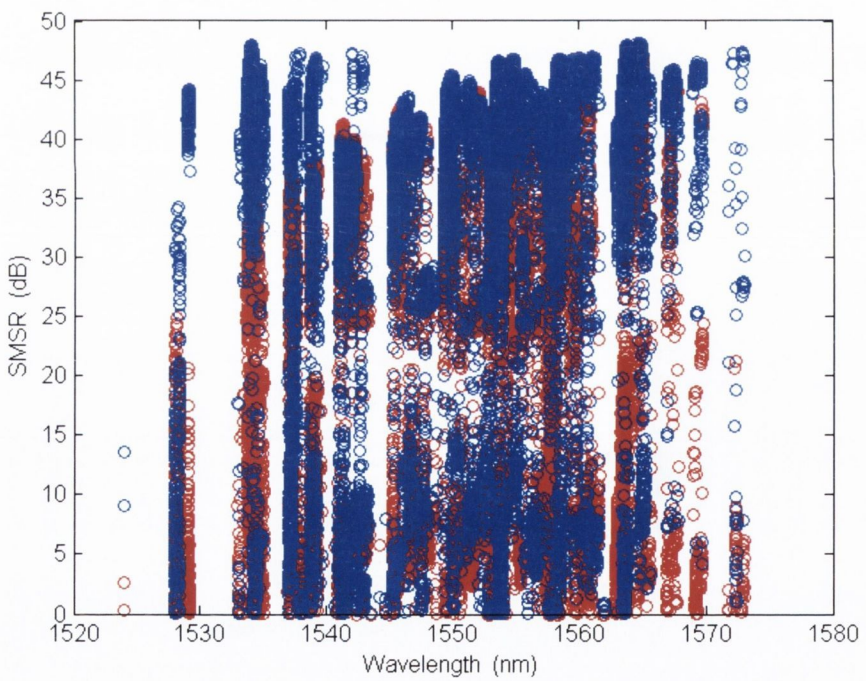

Figure 5.1.27. SMSR versus peak wavelength for the current injected into the gain section of: 100mA- red, 150mA- blue.

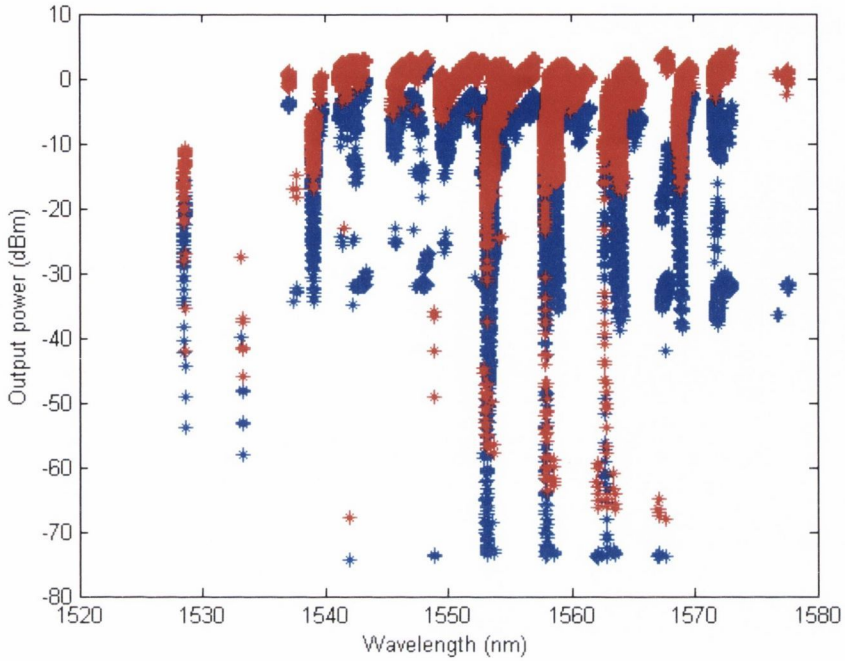

Figure 5.1.28. Output power versus peak wavelength for the current injected into the gain section of: 100mA-blue, 150mA-red.

Nine slots front mirror with the slot period of 70μm, nine slots back mirror with the slot period of 76 μm

The laser presented in this section has a slot period of 70 μm for the front mirror and 76 μm for the back mirror, which lead to FSR of 4.9nm and 4.5nm, respectively. The mirror lengths are 630 μm and 684 μm for the front and back, respectively.

The output power is shown in figure 5.1.29. When the currents injected into the mirror sections increase, the output power also increases.

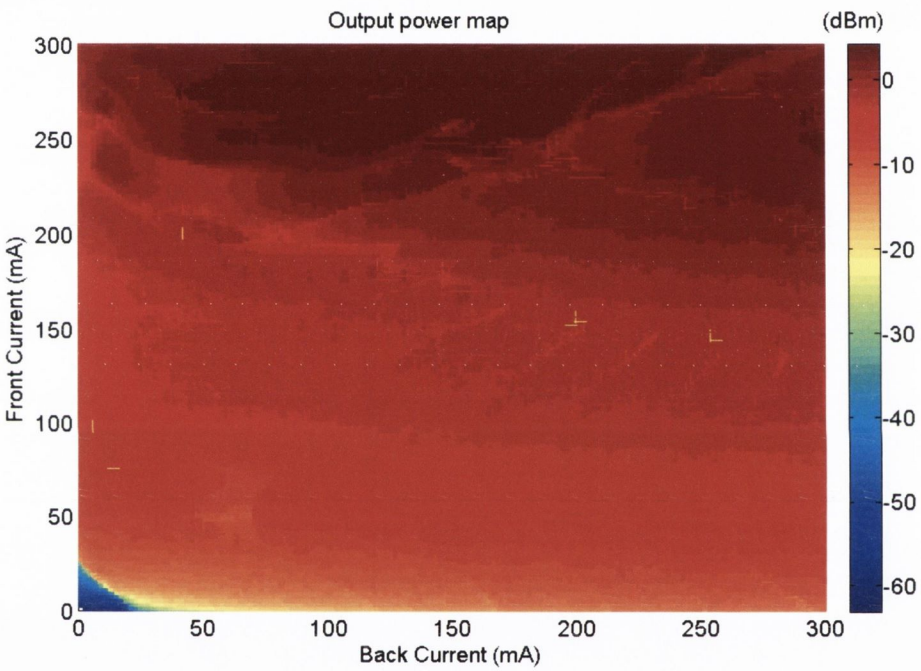

Figure 5.1.29. Output power versus currents injected into the both mirror sections for a laser with the slot period of 70μm for the front mirror and 76μm for the back mirror.

Figures 5.1.30 and 5.1.31 show the wavelength and SMSR maps, respectively. From these figures clear super mode positions with high SMSR are observed over a discrete discontinuous tuning range of 55 nm. The wavelength bands are smooth and the wavelength islands are clearly visible. The SMSR map shows big islands with high SMSR values. Figure 5.1.32 shows a mesh wavelength map. Plotting the data as SMSR and coupled output power versus wavelength shows the regions of high SMSR and power at particular wavelengths as in figures 5.1.33 and 5.1.34 below. From figure 5.1.33 ~ 15 distinct super- modes are visible over a wide discontinuous tuning range from 1525 nm to

1580nm. Fourteen of them show the SMSR greater than 30 dB. The highest SMSR value is around 45 dB. The output power shown in figure 5.1.34 is uniform for all super-modes with the variation between them within 2dBm.

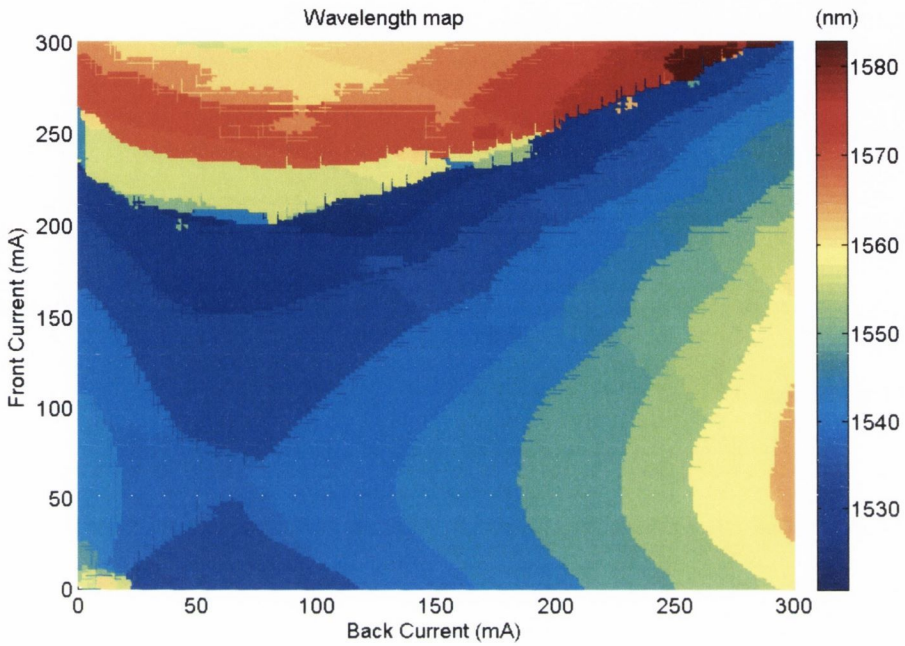

Figure 5.1.30. Wavelength map versus currents injected into the both mirror sections for laser with the slot periods of 70μm for the front mirror and 76μm for the back mirror.

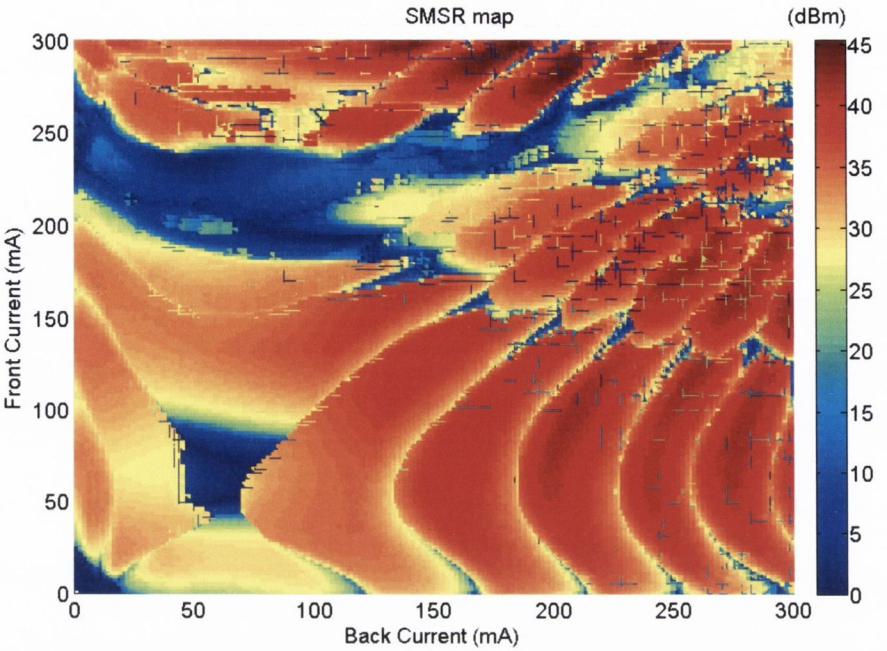

Figure 5.1.31. SMSR map versus currents injected into the both mirror sections for a laser with the slot period of 70μm for the front mirror and 76μm for the back mirror.

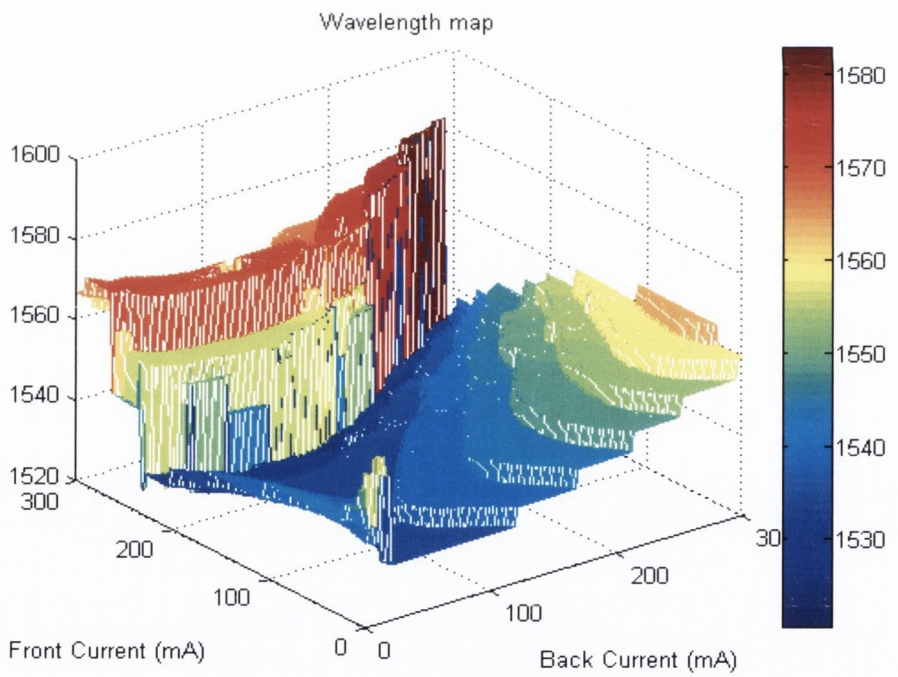

Figure 5.1.32. Wavelength mesh map versus currents injected into the both mirror sections for a laser with the slot periods of 70μm for the front mirror and 76μm for the back mirror.

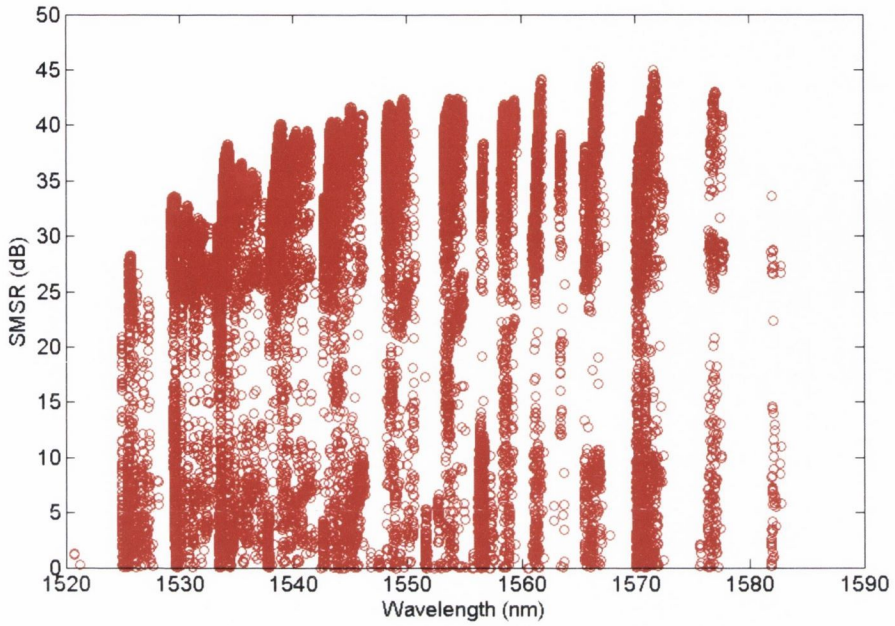

Figure 5.1.33. SMSR versus peak wavelength for a laser with the slot period of 70μm for the front mirror and 76μm for the back mirror.

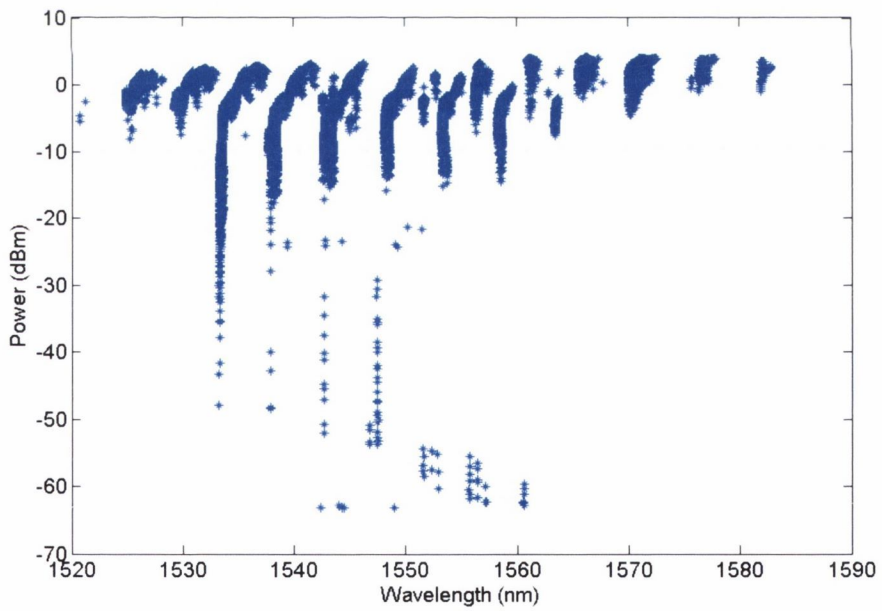

Figure 5.1.34. Power versus peak wavelength for a laser with the slot period of 70μm for the front mirror and 76μm for the back mirror.

Nine slots on the front mirror with the slot period of 97μm, five slots on the back mirror with the slot period of 108 μm.

The laser presented here has nine slots on the front mirror with slot period of 97μm and five slots on the back mirror with slot period of 108 μm. The mirror lengths are 873 μm and 540 μm for the front and back mirror, respectively. The output power map is shown in figure 5.1.35 below. The super-mode structure is visible on the map. The output power increases with increasing currents injected into the front and back mirror.

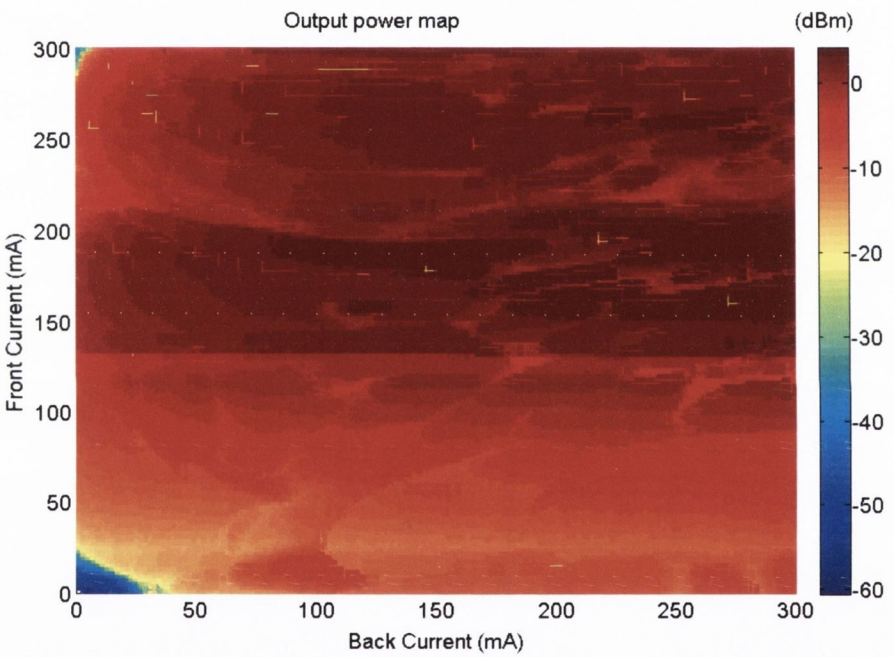

Figure 5.1.35. The output power map for the laser with nine slots on the front mirror and five slots on the back mirror.

Figures 5.1.36 and 5.1.37 show the wavelength tuning map and the SMSR map, respectively. The wavelength map does not have clear wavelength bands as the maps for the lasers with nine slots on both mirrors. From figure 5.1.36 the wavelength tuning range can be estimated as 40nm. Maps appear squashed compared with nine-nine slots case.

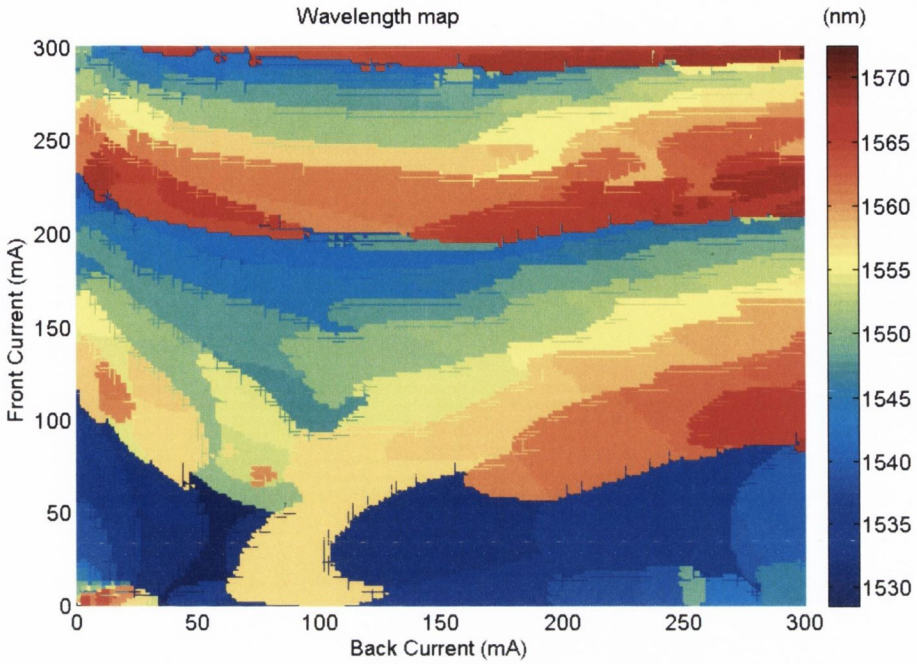

Figure 5.1.36. The Wavelength tuning map for the laser with nine slots on the front mirror and five slots on the back mirror.

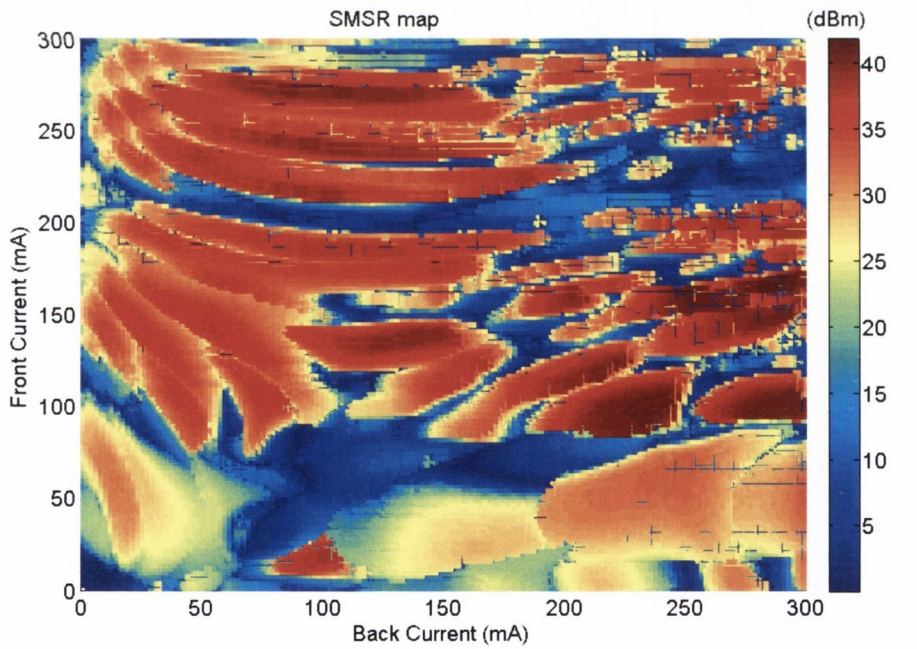

Figure 5.1.37. SMSR map for the laser with nine slots on the front mirror and five slots on the back mirror.

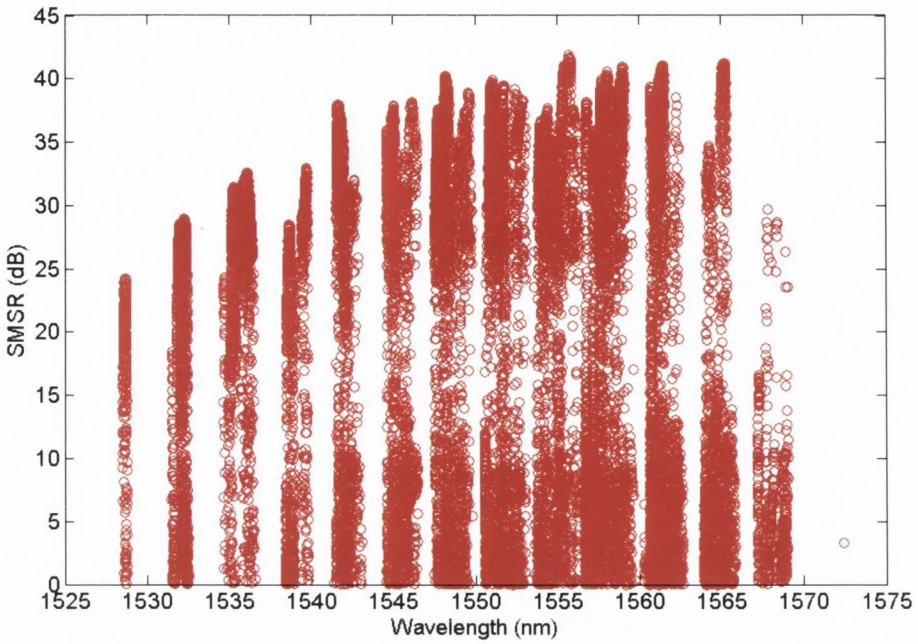

Figure 5.1.38. SMSR versus peak wavelength for the laser with nine slots on the front mirror and five slots on the back mirror.

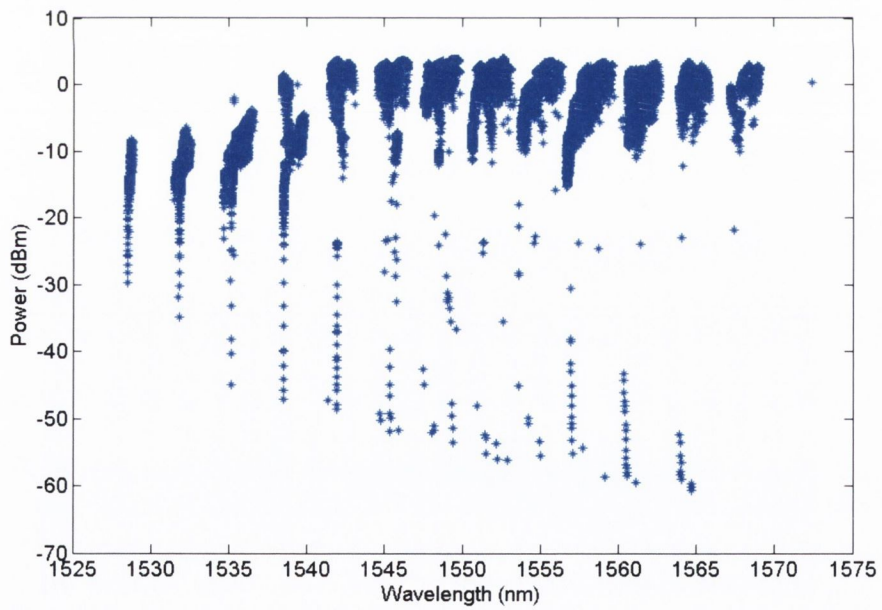

Figure 5.1.39. Output power versus peak wavelength for the laser with nine slots on the front mirror and five slots on the back mirror.

Figures 5.1.38 and 5.1.39 above show SMSR plotted versus peak wavelength and the output power plotted versus peak wavelength, respectively. Thirteen super-modes are present over the tuning range of about 40nm for the wavelength from 1528nm to 1568nm.

Eleven super-modes exhibit the SMSR greater than 30dB for the wavelength from 1535nm to 1568nm. The first two modes placed on the edge of the gain spectrum have SMSR lower than 30dB. From figure 5.1.39 the output power is observed not to be uniform for all super-modes. The first three modes have lower output power. A wavelength map in 3D is shown in figure 5.1.40 below.

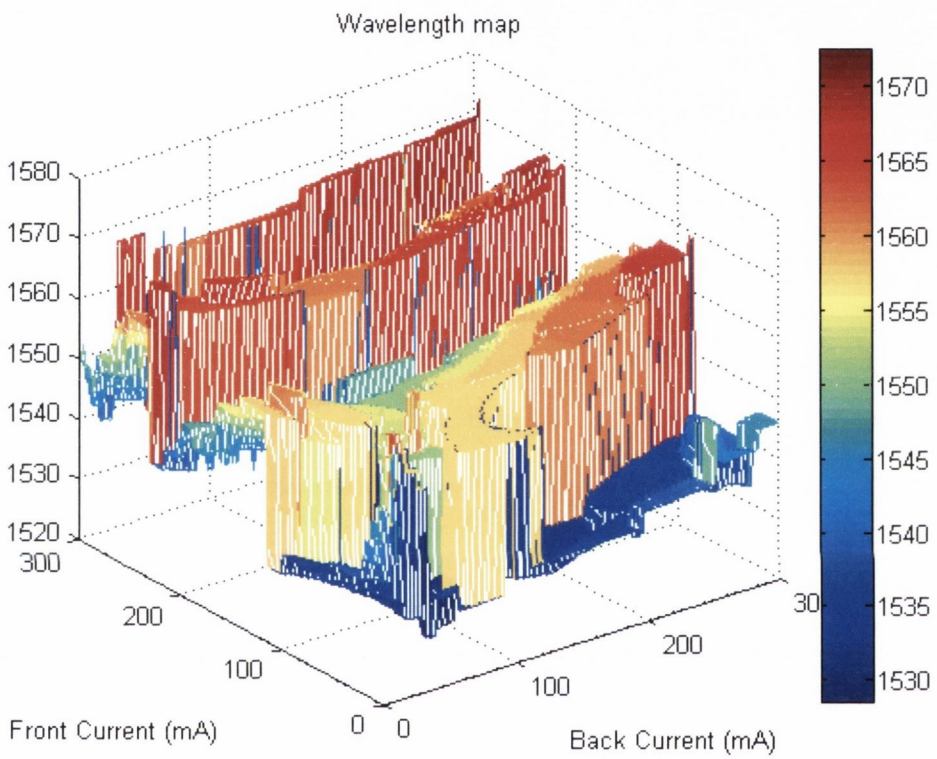

Figure 5.1.40. Wavelength tuning map in 3D for the laser with the slot period of 97μm and 108μm, and nine slots in the front mirror and five slots in the back mirror.

Conclusion

Lasers with different slot periods from long to short were presented in this section. Also a laser with nine slots on the front mirror and five slots on the back mirror was characterized here. All tuning maps for the laser with nine slots on the both mirrors show similar trends: (i) two symmetry lines: one horizontal for a low current injected into the front mirror, and one vertical for a low current injected into the back mirror, for SG-DBR type lasers show a diagonal symmetry line (ii) the tuning islands go from big toward small as the currents injected into the both mirror sections are increasing, where for SG-DBR laser the tuning islands go from small toward big as the mirror currents are increasing, (iii) the widest tuning range of around 55nm was obtained for a laser with the shortest slot period of 70μm in the front mirror and 76μm in the back mirror (figures 5.1.29-5.1.34). The biggest number of 15 super-modes is from a laser with the slot period of 70/76μm. The laser with slot period of 97/108μm has 14 super- modes, the laser with slot period of 70/80μm has 13 super- modes and the laser with slot period of 86/97μm has 12 super-modes. We want to have a big number of super-modes to get wide tuning range and also to cover as many wavelengths as possible. The super-mode spacing is controlled by the distance between the slots etched on the laser waveguide. To boost the output power and SMSR of the modes at the edge of the spectrum, we can increase the current injected into the central gain section. The best laser of all presented in this chapter is the laser with the slot period of 70/76μm. It exhibits the widest tuning range of 55 nm with the biggest number of super- modes. Only the first super- mode has a SMSR slightly lower than 30 dB but it can be easily improved by increasing the current injected into the gain. Also it has a good output power for almost all currents injected into the front and back mirror as shown in figure 5.1.29. The wavelength and SMSR maps show clear tuning islands and symmetry lines.

The laser with nine/five slots does not perform as well as the laser with nine slots on both mirrors. The tuning maps do not show clear trends: there are no symmetry lines and no order in placing the tuning islands. The laser has a tuning range of 40 nm which is about 10 nm shorter than the tuning range of the lasers with equal slot number. In future designs this type of laser will not be considered due to its poor performance. Instead to make the laser cavity shorter a laser with smaller number of slots on each mirror, for example eight/eight, seven/seven will be considered.

5.2. Six section tunable laser

Nine slots on the front mirror with the slot period of 70μm, nine slots on the back mirror with the slot period of 76 μm.

Including another section between the gain section and one of the mirror sections can improve the quasi-continuous tuning of the laser diode. From Chapter 2 the quasi-continuous tuning is accomplished by joining overlapping small regimes which are continuously tunable by a single longitudinal mode to achieve a large wavelength coverage [26] . This is achieved as this addictional section can act like a phase section in an SG-DBR laser [28] [29] [30] [31]. By changing the current injected into the phase section of the laser, it is possible to re-tune the lasing peak to a new position with a high SMSR value and therefore to improve that laser performance.

The laser consists of six independent sections: first the SOA- semiconductor optical amplifier, the front mirror, the gain section, the phase section, the back mirror and the PD-photodiode section. All sections are electrically isolated from each other by the slots between them. The gain section in this case is 400 μm long, and the phase section is 100 μm long. For the experiment with the phase tuning we chose a device with the shortest slot period of 70 μm in the front mirror and 76 μm in the back mirror as it shows the best performance from the results above.

The first part of the experiment and experimental set up were the same as it was for the five section lasers described in the previous section. In this case an extra current source is added to inject the current into the phase section during the second part of the experiment. The six section laser was mounted on an AlN carrier and placed on a copper heat sink which was mounted on a thermoelectric cooler (TEC) to control the chip temperature. The temperature was set constant to 20°C. Five independent current sources were used to inject the current into the gain, phase, SOA, and both mirrors. For the first set of measurements, the phase section was connected to the gain section. The currents injected into the gain and SOA sections were set at 100mA and 20mA with the PD left unbiased. The currents injected into the front and back mirror sections were both scanned between 0 and 300mA with a step of 2mA. The output spectra were recorded using an optical spectrum analyzer with a resolution bandwidth of 0.1 nm and a sensitivity of -75dB. The schematic structure of a six section laser is shown if figure 5.2.1 below.

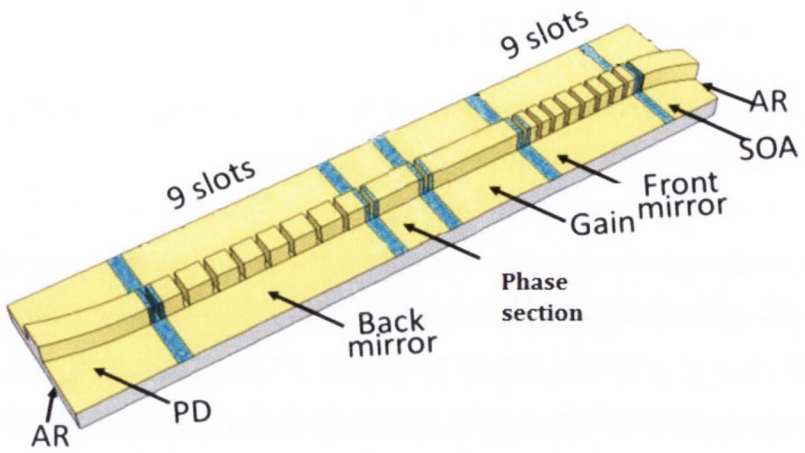

Figure 5.2.1. Schematic structure of six section tunable laser.

The output power map is shown in figure 5.2.2 below. As is can be seen the output power increases when the current injected into the front mirror increases. The wavelength and SMSR tuning maps are shown in figures 5.2.3 and 5.2.4, respectively. The super-mode hoping islands are clearly visible for all modes over the discrete tuning range. Figure 5.2.4 shows that there are large regions of red colour indicating a very high SMSR. The blue regions corresponding to low SMSR values can be eliminated by using the phase tuning.

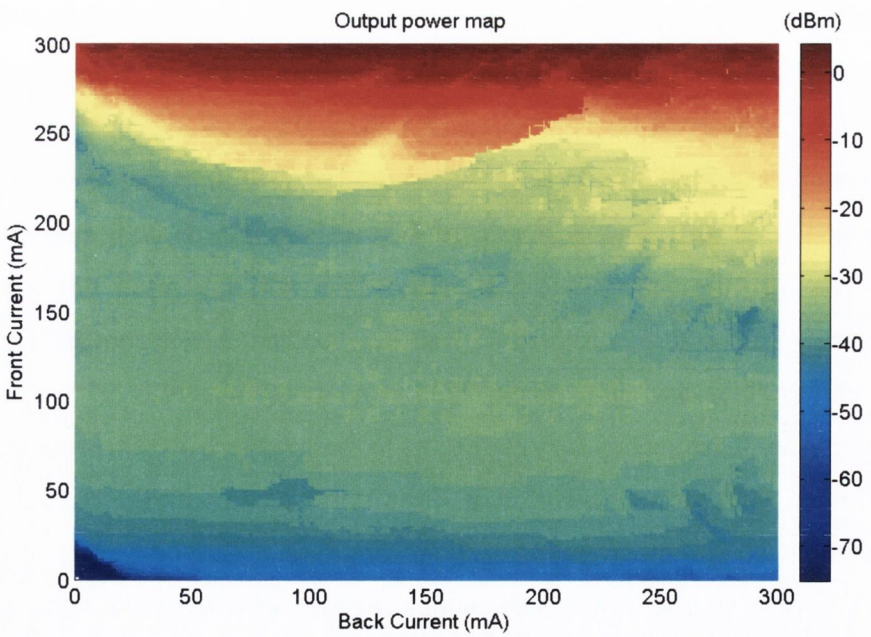

Figure 5.2.2. Output power versus currents injected into the both mirror sections for a six section laser with the slot period of 70μm for the front mirror and 76μm for the back mirror.

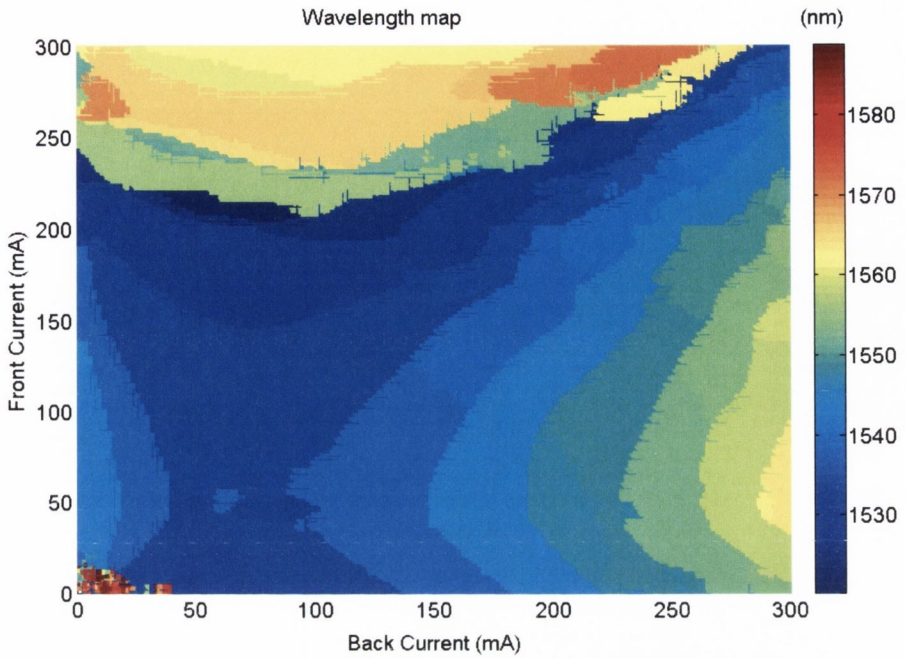

Figure 5.2.3. The wavelength tuning map versus currents injected into the both mirrors sections for a six section laser with the slot period of 70μm for the front mirror and 76μ for the back mirror.

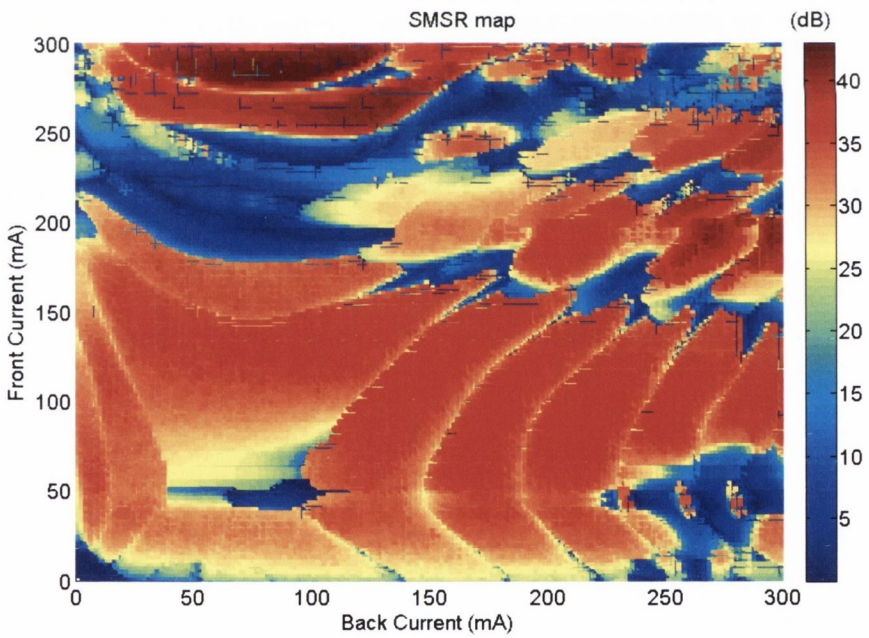

Figure 5.2.4. The SMSR tuning map versus currents injected into both mirror sections for a six section laser with the slot period of 70μm for the front mirror and 76μm for the back mirror.

The extracted SMSR and output power are shown in figures 5.2.5 and 5.2.6, respectively. Twelve super-modes around 1525-1570nm show good SMSR greater than 30dB. The higher SMSR value is around 45 dB for the wavelength of 1560nm. From figure 5.2.6 it can be seen that the output power is not uniform for all super-modes. Super-modes for the

wavelength from 1540-1555nm exhibit lower output power. Comparing with the wavelength tuning maps in figure 5.2.3 it can be seen that these are the modes with a particular combination of high currents injected to the both mirrors. The output power may be lower due to the heating dissipation problems. Figure 5.2.7. shows mesh wavelength tuning map.

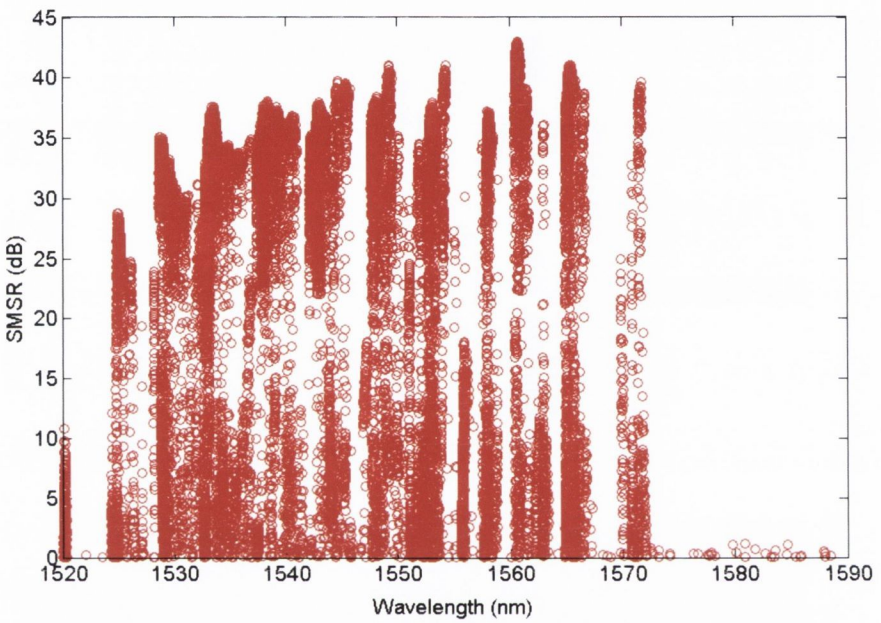

Figure 5.2.5. SMSR versus peak wavelength for a six section laser with the slot period of 70μm for the front mirror and 76μm for the back mirror.

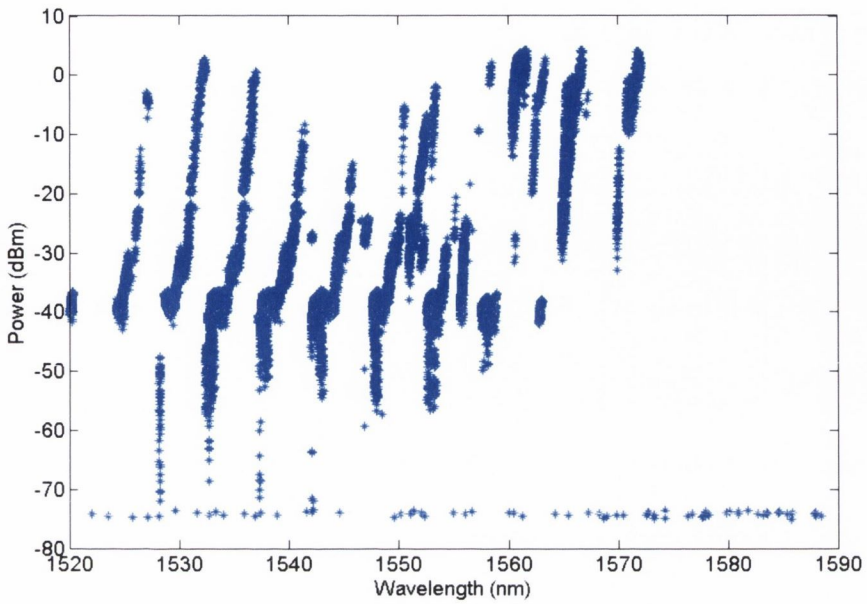

Figure 5.2.6. Output power versus peak wavelength for a six section laser with the slot period of 70μ for the front mirror and 76μm for the back mirror.

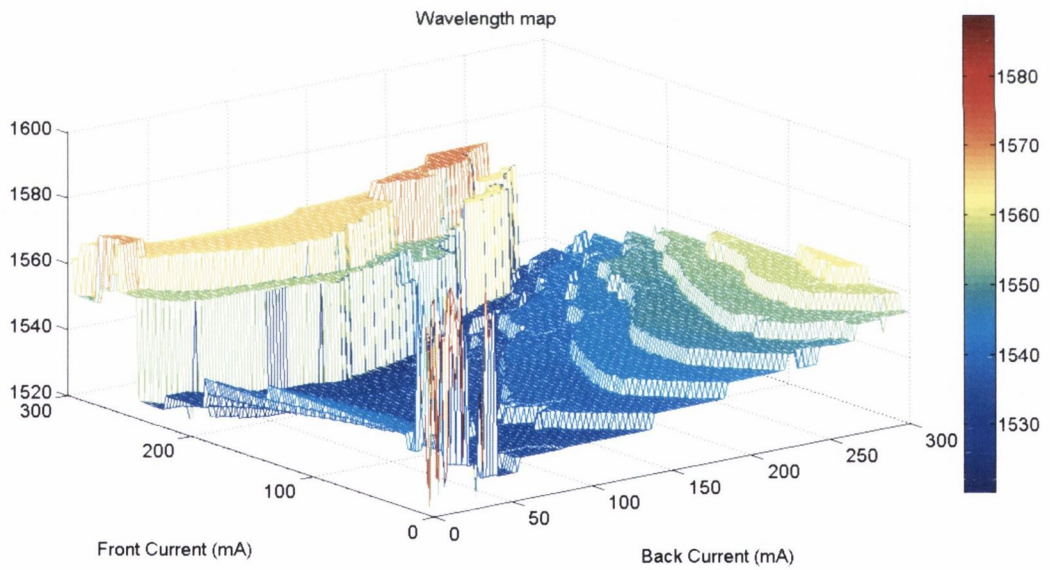

Figure 5.2.7. Mesh wavelength tuning map versus currents injected into the both mirrors for a six section laser with the slot period of 70μm for the front mirror and 76μ for the back mirror.

Phase tuning

Due to the mode competition, there are regions marked in blue in the SMSR maps corresponding to low SMSR. To improve the laser performance and to get only single mode operation we use the phase tuning. During the first part of the experiment the tuning maps were taken and the gain and phase section were connected together. For the second part of the experiment, the gain and phase sections were disconnected from one another. The currents injected now to the gain and phase section were 80mA and 20mA, respectively.

Figures 5.2.8-5.2.10 show examples of recorded output spectrum for three different super-modes before and after changing the current injected into the phase section. Figure 5.2.8 shows the output spectrum for the super-mode with injected currents of 150mA for the front mirror and 220mA for the back mirror. The spectrum before the phase tuning is marked in blue colour. It can be seen that for this particular currents combination there is strong mode competition: four strong modes are visible for the wavelength of around 1543nm, 1547nm, 1562nm, 1568nm, the strongest super-mode is for the wavelength of 1547nm. By changing the phase current from 20mA to 60mA, mode competition is eliminated and a good single mode lasing is achieved for the wavelength of 1547nm.

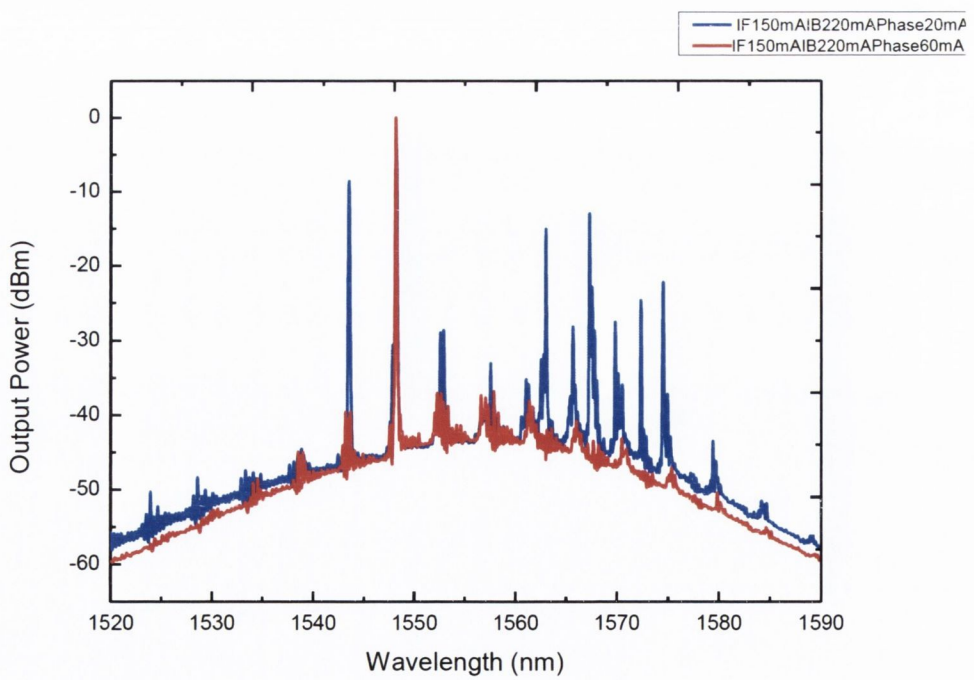

Figure 5.2.8. Output spectrum for the front current of 150mA and the back current of 220mA, with injected phase current of: 20mA- blue, 60mA- red.

Figure 5.2.9 shows the output spectrum for the mode with the injection current of 200mA for the front mirror and 80mA for the back mirror. Three strong modes competing are clearly visible for the wavelength of 1560nm, 1565nm, 1570nm. Decreasing the phase current pushes the spectrum toward the blue side and now a mode for the wavelength of 1555nm is dominating, although the mode competition is not fully eliminated in this case giving the SMSR value of about 20dB.

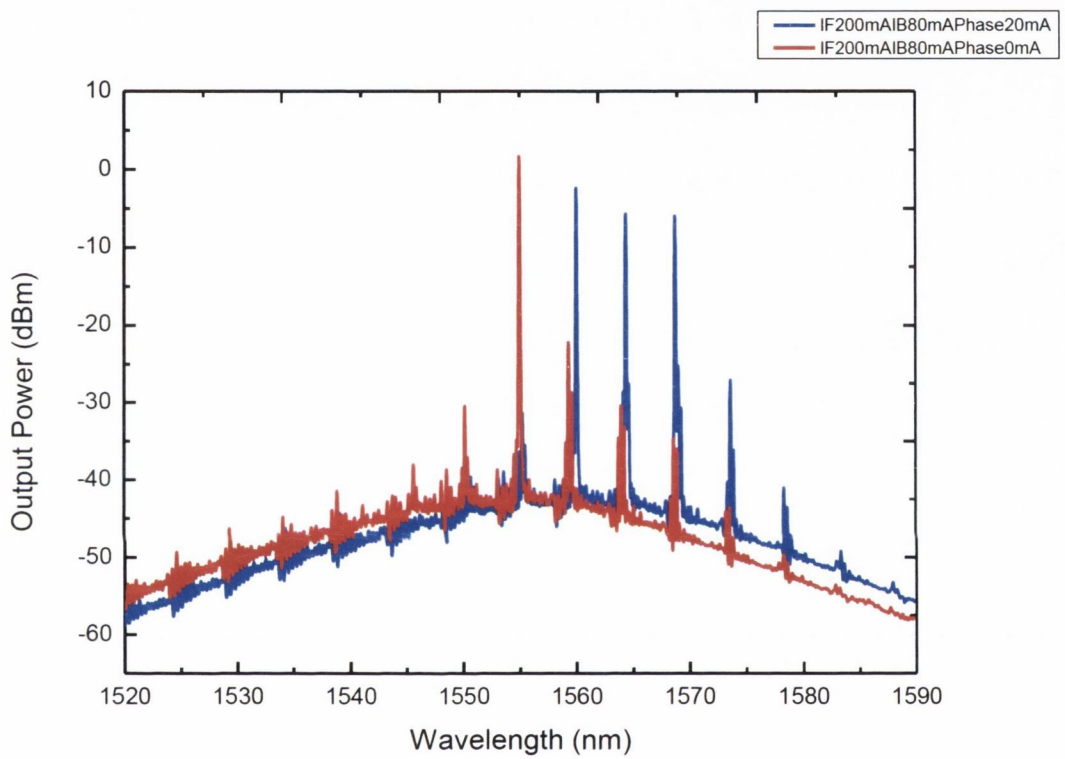

Figure 5.2.9. Output spectrum for the injected currents of 200mA for the front mirror and 80mA for the back mirror, with phase current of 0mA- red, 20mA- blue.

Figure 5.2.10 shows the output spectrum for the current set of 220mA for the front mirror and 220mA for the back mirror, with gain and phase currents of 80mA and 20mA, respectively marked in blue colour. There are two strong modes for the wavelength of 1565nm and 1570nm, where the mode for 1570nm is dominating. Decreasing the phase and gain currents to 0mA and 48mA, respectively, pushes the spectrum toward the blue side. The mode competition is fully eliminated and the lasing mode is now for the wavelength of 1565nm.

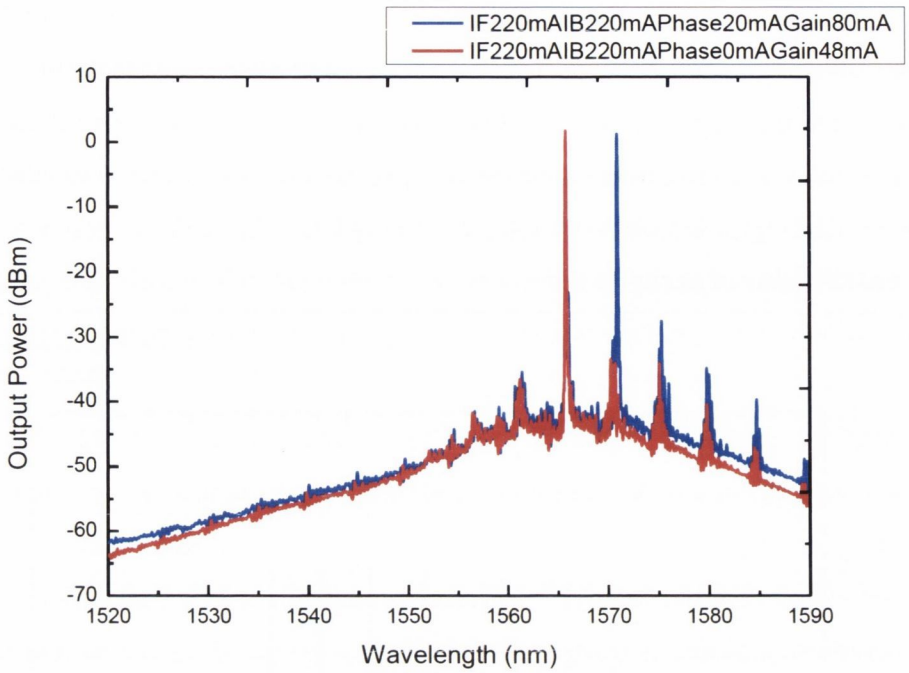

Figure 5.2.10. Output spectrum for the injected currents of 220mA for the front mirror and 220mA for the back mirror, with phase current of 20mA and the gain current of 80mA-blue, and phase current of 0mA and the gain current of 48mA-red.

The next step was to run a scan for regions with low SMSR for the currents of:(i) front current from 170 mA to 270 mA and back current from 50mA to 150 mA, (ii) front current from 230mA to 300mA and back current 150mA to 230mA, and (iii) for front current from 280 mA to 300 mA and back current from 230mA to 300 mA. The SOA and the gain currents were kept constant again with values of 20mA and 80mA, respectively. The phase current was scanned between 0-50mA with the step of 1mA for every pair of the front and back currents. Figures 5.2.11-5.2.13 show an example data taken from the phase scan for the front current of 230mA and back current of 220mA. This current set corresponds to a peak wavelength of 1535nm. Figure 5.2.11 shows how the peak wavelength is tuned with injected phase current. As can be seen in this case the wavelength is tuned by about 0.3 nm from 1535.4 to 1535.7 nm. Figure 5.2.12 show SMSR plotted versus phase current. For the initial set of the phase current of 20mA, the SMSR has a low value less than 10dB. It can be observed that the SMSR changes with scanned phase current. For small current injected in to the phase section from 0 to 10mA, the SMSR increases to 20 dB. For phase current from 32 to 50mA, the value of SMSR is high, about 35dB. Figure 5.2.13 shows peak wavelength versus SMSR. The SMSR has good values more than 30dB for the wavelength of about 1535.48nm, 1534.5nm,

1335.53nm, 1535.54nm, 15.35.58nm, 1535.6nm, 1535.61nm, 1535.62nm, 1535.64nm, 1535.66nm.

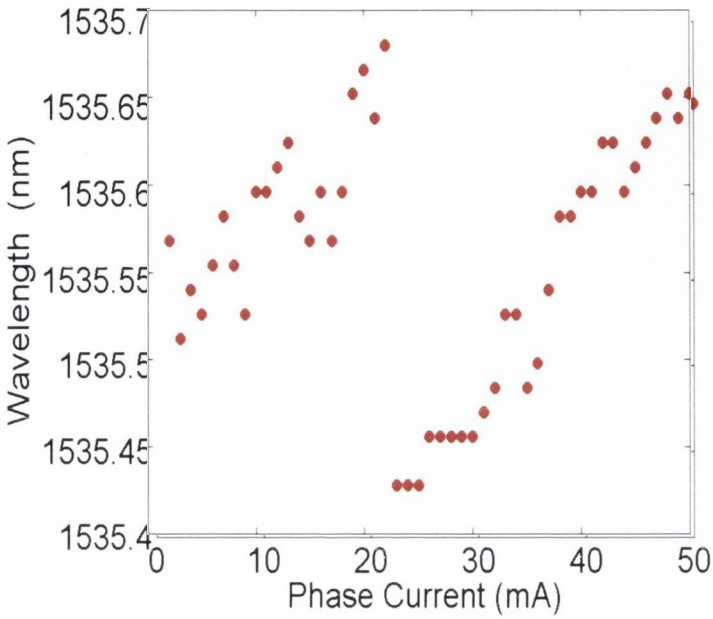

Figure 5.2.11. Phase Current versus peak wavelength of 1535nm for the fron current of 230mA and back current of 220mA.

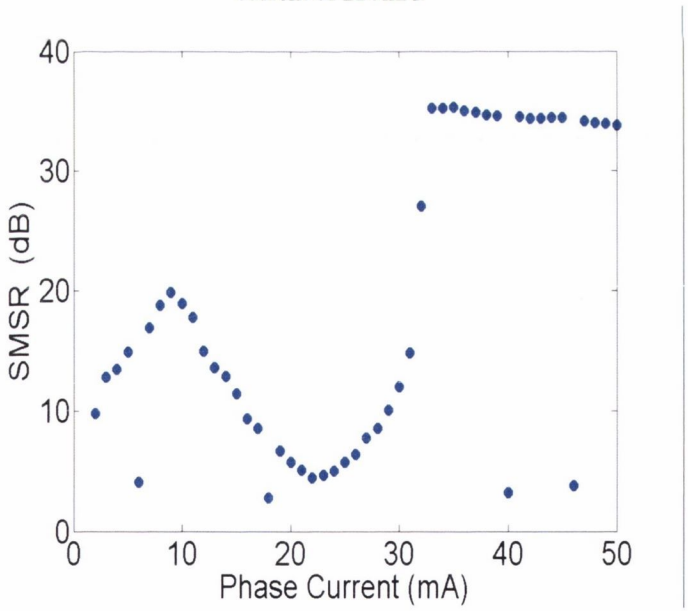

Figure 5.2.12. Phase Current versus SMSR for the front current of 230mA and back current of 220mA.

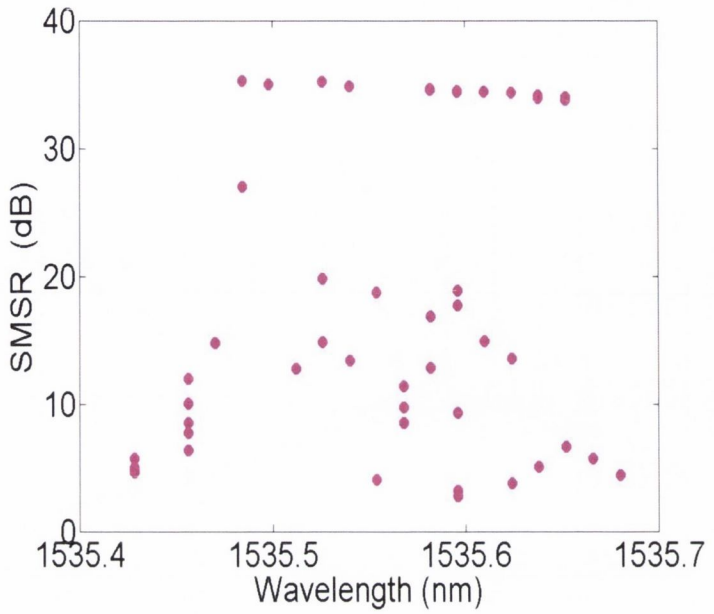

Figure 5.2.13. Wavelength versus SMSR for the front current of 230mA, back current of 220mA and the phase current scanned from 0mA to50mA.

The original SMSR map and new data taken from the phase scan are shown in figure 5.2.14. We chose the maximum SMSR values obtained from scanning the phase current and plotted them against front and back current corresponding to a particular current value and getting a new tuning map as shown in figure 5.2.14. It can be seen that the phase tuning works well and it is possible to re-tune the lasing peak to get high SMSR for almost all the scanned regions.

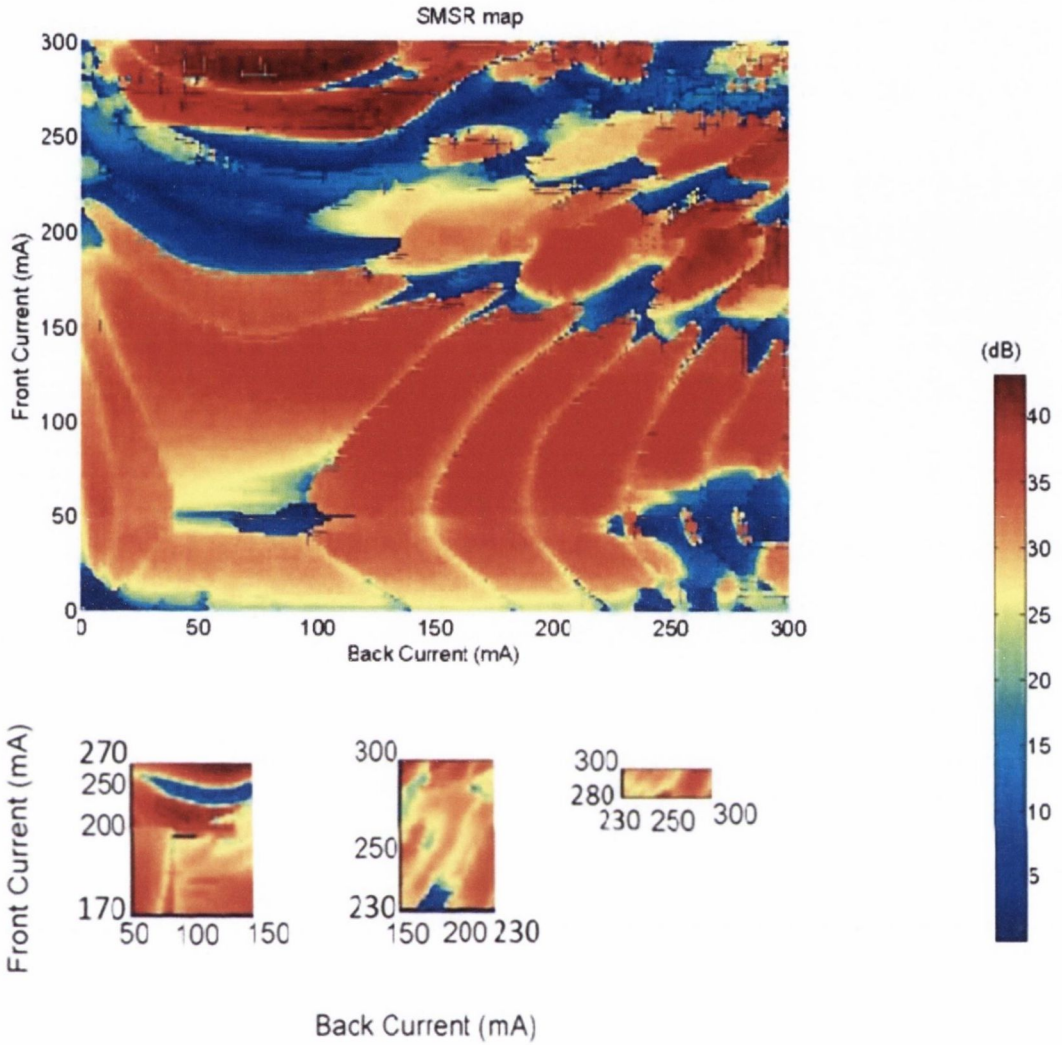

Figure 5.2.14. SMSR map with phase scanned region.

Conclusion

In this section, the performance and phase tuning of a six section laser was presented. The regions with poor SMSR values can be improved by the phase tuning. By changing the current injected into the phase section from 0mA to 50mA is it possible to re-tune the lasing peak to a position where it has a good SMSR value (>30dB). As seen from results presented in this section the phase tuning works well for almost all scanned region. Very small regions with low SMSR occurred due to the two-mode competition where two modes are separated from each other by a super- period set from the Vernier effect. In the future design we will solve this problem by adjusting the super period to place these low SMSR regions on the edge of the tuning map. For now the solution is to further increase the current injected into the phase and gain section. The temperature tuning can also be used to shift the wavelength peak.

5.3. Nine contact laser.

The laser presented in this section has the same structure as the lasers described in the section 5.1. and 5.2. In this case an extra isolation contacts are introduced between the SOA section and the front mirror, the front mirror and the gain section, the gain section and the back mirror, and the back mirror and PD section. The purpose of the isolation contact is to prevent the carrier leakage between different sections of the laser and therefore to improve its performance.

The results presented in this section were taken for unbiased isolation contact. Biasing the extra contact caused loss of the output power and therefore no laser action was observed. The laser presented in this section has the slot period of 70μm for the front mirror and 76 μm for the back mirror. The output power is shown in figure 5.3.1 below.

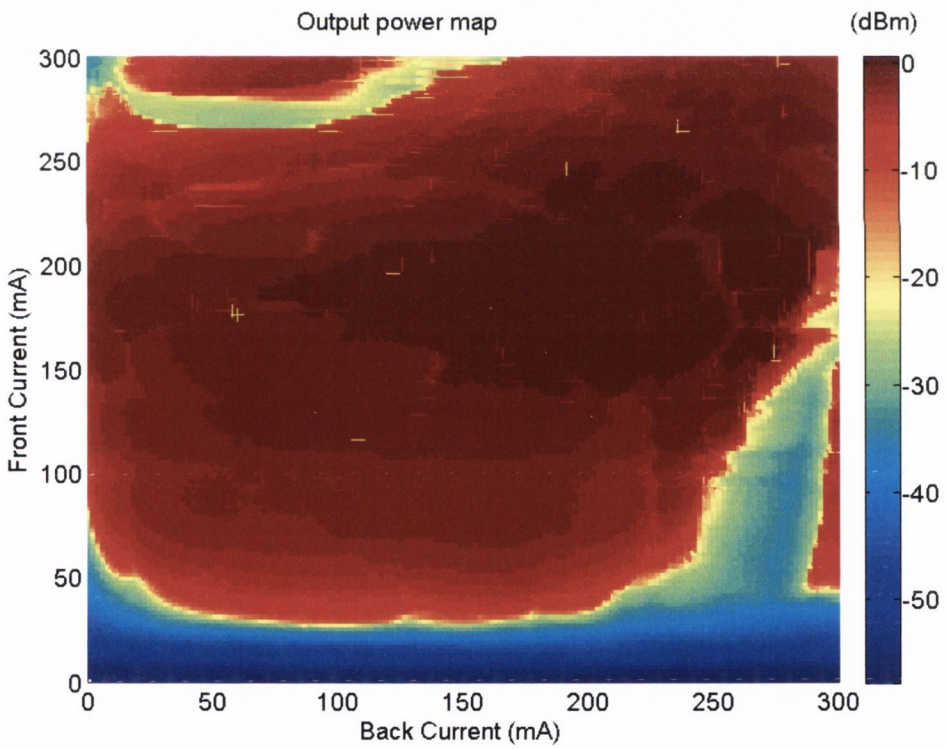

Figure 5.3.1. The output power for the laser with nine contacts with the slot period of 70/76μm. The isolation contacts were unbiased.

A very low output power is observed for low values of the current injected into the front mirror. This suggests that the back mirror has a very little influence on the tuning effect. The drop of the power appears also for the high front current.

The wavelength and SMSR tuning maps are shown in figures 5.3.2 and 5.3.3, respectively.

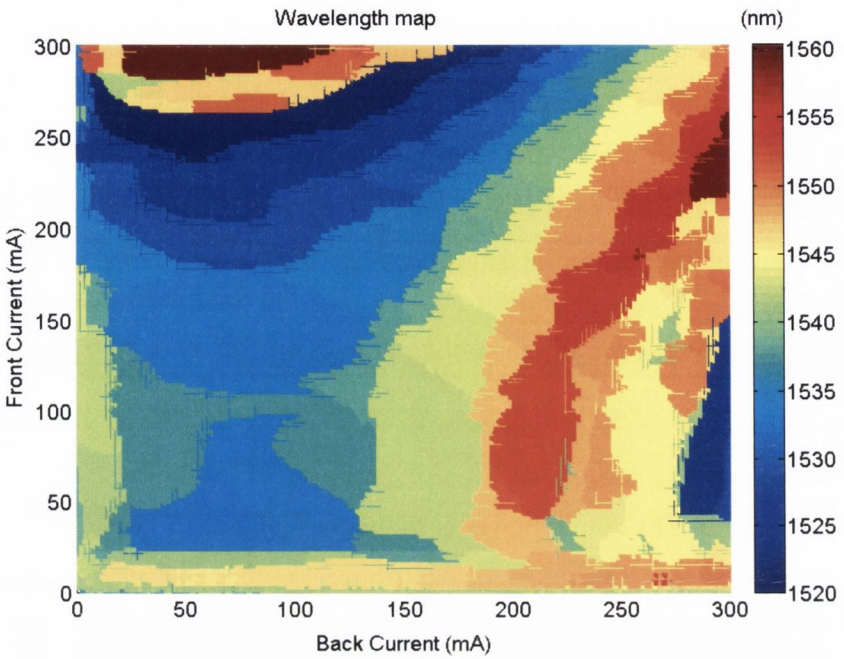

Figure 5.3.2. The wavelength tuning map for the laser with nine contacts. The isolation contact were left unbiased.

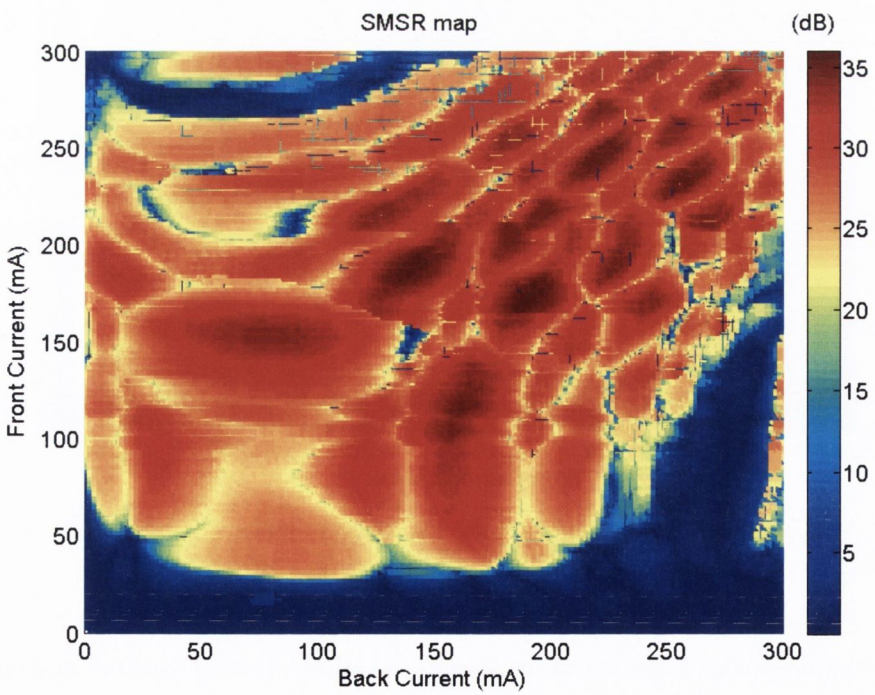

Figure 5.3.3. SMSR tuning map for the laser with nine contacts. The isolation contacts were left unbiased.

The wavelength band structure and wavelength islands are visible on the wavelength tuning map in figure 5.3.2. It can be seen that for the low values of the current injected into the front mirror there is no tuning effect even though the back current is increasing. This results in a very poor SMSR values in this region, as shown in the SMSR map. From figure 5.3.3 clear SMSR islands are present with the highest SMSR placed in the centre of each island. The overall structure of the SMSR maps looks more like the tuning maps taken for the SG-DBR laser [26] [32] [33] [34]. It suggests that the extra slots etched between the different laser sections provide themselves enough isolation to improve the laser performance without biasing the isolation contacts.

The SMSR plotted versus peak wavelength is shown in figure 5.3.4 below. Nine super-modes are clearly visible over the tuning of 40 nm for the wavelength from 1520nm to 1560nm. Eight modes have SMSR values over 30dB. The number of super-modes is lower than for the lasers with five and six contact. Also the tuning range is about 10nm shorter than for five and six contact tunable lasers.

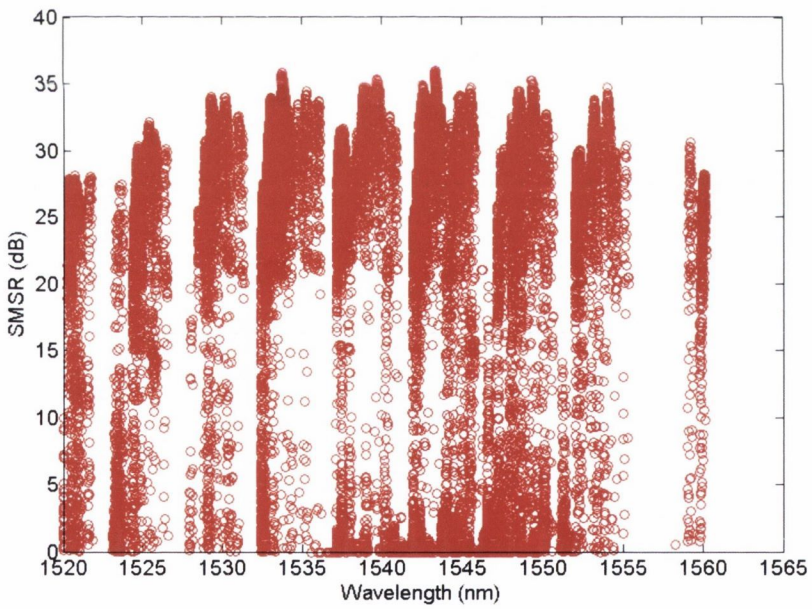

Figure 5.3.4. SMSR versus peak wavelength for the laser with nine contacts. The isolation contacts were left unbiased.

The output power plotted versus peak wavelength is shown in figure 5.3.5 below. The output power is uniform for all super-modes with a variation within 2dBm. The wavelength 3D tuning map is shown in figure 5.3.5 below.

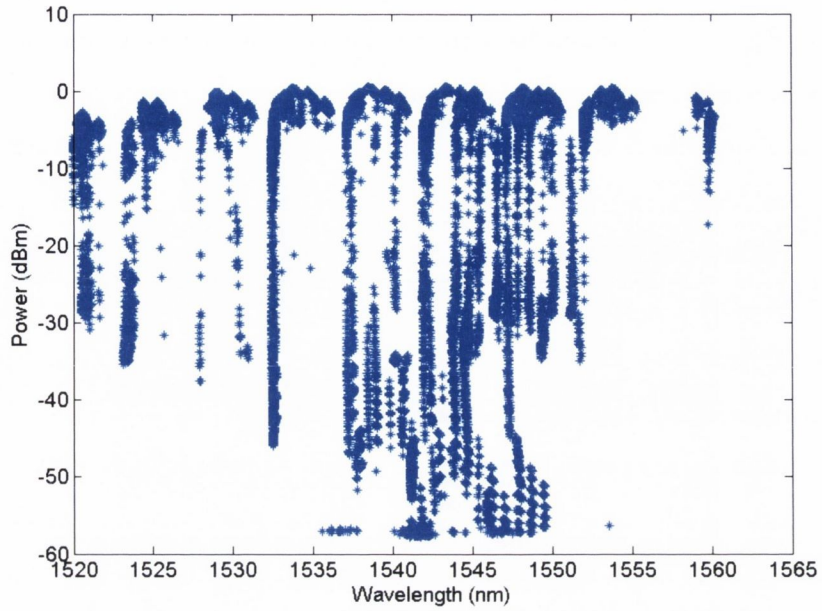

Figure 5.3.5. The output power versus peak wavelength for the laser with nine contacts. The isolation contacts were left unbiased.

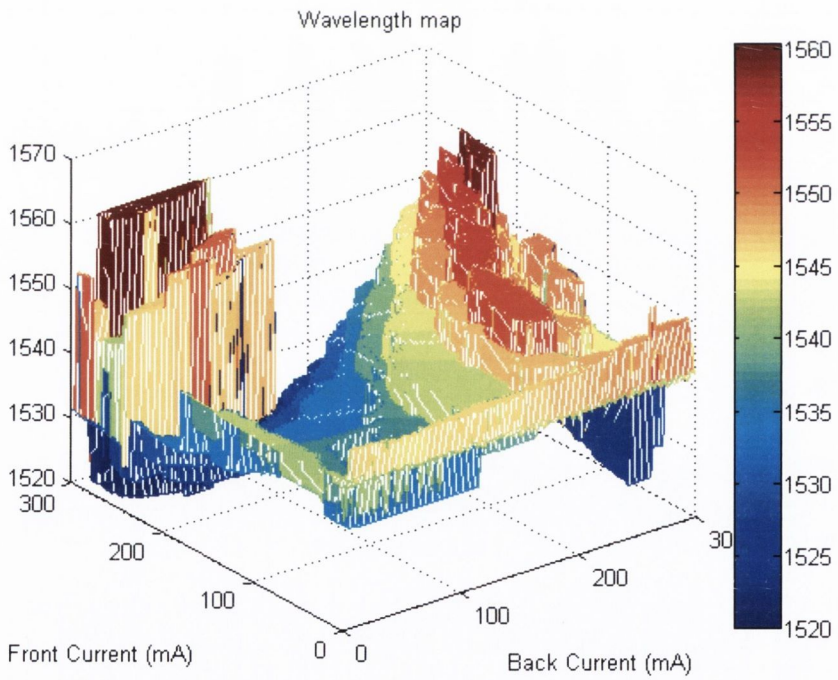

Figure 5.3.6. The wavelength 3D tuning map for the laser with nine contacts. The isolation contact were left unbiased.

Conclusion

In this section the performance of nine contact tunable laser was presented. During the experiment the isolation contact were unbiased. The laser has a tuning range of 40nm which is shorter by about 10nm than a tuning range for the laser with five and six contacts. The laser does not tune well for small currents injected into the front section. The wavelength map has a similar structure to the lasers presented in sections 5.1 and 5.2 although the tuning islands are not as clear and sharp as for the laser with five and six contacts. Also the number of super-modes is lower. The laser has 9 super- modes. The SMSR tuning map has a structure similar to an SG-DBR case in which the tuning island have hexagonal shape with the highest SMSR values placed in the centre of the islands. In our case the islands do not have a clear hexagonal shape but still the highest SMSR is placed in the centre of each tuning island. This suggests that even though the isolation contacts were left unbiased, the extra slots themselves were enough to provide an isolation between different sections of the laser.

Table 5.1 below shows all tuning parameters for the laser presented in this chapter: five contact lasers, six contact laser and nine contact laser.

	Five contact lasers				Five contact laser- nine slots on the front mirror, five slots on the back mirror	Six contact laser	Nine contact laser
Slot period	97μm/108μm	86μm/97μm	70μm/80μm	70μm/76μm	97μm/108μm	70μm/76μm	70μm/76μm
FSR	3.36nm/3.02nm	3.8nm/3.36nm	4.9nm/4.3nm	4.9nm/4.5nm	3.36nm/3.02nm	4.9nm/4.5nm	4.9nm/4.5nm
Tuning range	50nm	47nm	45nm	55nm	40nm	50nm	40nm
Number of super- modes	15	12	13	15	13	14	9
Number of super- modes with SMSR>30dB	12	11	11	14	11	12	8

Table 5.1. Tuning parameters for five, six, nine contact lasers.

References

[1] C. A. Brackett, "Dense wavelength division multiplexing networks: Principles and applications," *IEEE Journal on Selected Areas in Communications,* vol. 8, no. 6, pp. 948- 964, 1990.

[2] G. Sarlet, G. Morthier and R. Baets, "Control of widely tunable SSG-DBR lasers for dense wavelength division multiplexing," *Journal of lightwave technology,* vol. 18, no. 8, p. 1128, 2000.

[3] E. B. Basch, R. Egorov, S. Gringeri and S. Elby, " Architectural tradeoffs for reconfigurable dense wavelength-division multiplexing systems," *IEEE Journal of Selected Topics in Quantum Electronics,* vol. 12, no. 4, pp. 615-626, 2006.

[4] A. Vicet, D. A. Yarekha, A. Perona, Y. Rouillard, S. Gaillard and A. N. Baranov, " Trace gas detection with antimonide-based quantum-well diode lasers," *Spectrochimica Acta Part A: Molecular and Biomolecular Spectroscopy,* vol. 58, no. 11, pp. 2405-2412, 2002.

[5] R. Phelan, M.Lynch, J. Donegan and V. Weldon, "Simultaneous multi- spacies gas sensing by use of a sampled grating distributed Bragg reflector and modulated grating Y laser diode," *Applied Optics,* vol. 44, no. 27, pp. 5824- 5931, 2005.

[6] M. L. Masanovic, V. Lal, J. S. Barton, E. J. Skogen, L. A. Coldren and D. J. Blumenthal, " Monolithically integrated Mach-Zehnder interferometer wavelength converter and widely tunable laser in InP," *Photonics Technology Letters,* vol. 15, no. 8, pp. 1117-1119, 2003.

[7] S. B. Yoo, "Wavelength conversion technologies for WDM network applications," *Journal of Lightwave Technology* , vol. 14, no. 6, pp. 955-966, 1996.

[8] P. P. Iannone, K. C. Reichmann and a. N. J. Frigo, " High-speed point-to-point and multiple broadcast services delivered over a WDM passive optical network," *Photonics Technology Letters,* vol. 10, no. 9, pp. 1328-1330, 1998.

[9] P. J. Matthews, M. Y. Frankel and a. R. D. Esman, " A wide-band fiber-optic true-time-steered array receiver capable of multiple independent simultaneous beams," *Photonics Technology Letters,* vol. 10, no. 5, pp. 722-724, 1998.

[10] L. Coldren, G. Fish, Y. Akulova, J. Barton, L. Johansson and C. Coldren, "Tunable semiconductor lasers: a tutorial," *Journal of Lightwave Technology,* vol. 22, no. 1, p.

193, 2004.

[11] T. Liijeberg, R. Tohmon, E. Hall, P. Abraham, M. Focht, G. A. Fish, M. C. Larson and a. L. A. Coldren, " High-power, widely-tunable sampled grating DBR laser integrated with a semiconductor optical amplifier," *IEEE in 18th International Semiconductor Laser Conference,* pp. 45-46, 2002.

[12] H. Wang, J. Zhao and a. Y. Yu, " A novel tunable semiconductor laser based on a sampled grating reflector and an interleaved sampled grating reflector," *In Asia Communications and Photonics Conference and Exhibition, Optical Society of America,* p. 83080J, 2011.

[13] Y. Tohmori, Y. Yoshikuni, H. Ishii, F. Kano, T. Tamamura, Y. Kondo and M. Yamamoto, "Broad-range wavelength-tunable superstructure grating (SSG) DBR lasers," *IEEE Journal of Quantum Electronics,* vol. 29, no. 6, pp. 1817- 1823, 1993.

[14] Y. Tohmori, Y. Yoshikuni, H. Ishii, F. Kano, T. Tamamura and a. Y. Kondo, "Over 1100 nm wavelength tuning in superstructure grating (SSG) DBR lasers," *Electronics letters,* vol. 29, no. 4, pp. 352-354, 1993.

[15] H. Ishii, H. Tanobe, F. Kano, Y. Tohmori, Y. Kondo and a. Y. Yoshikuni, " Quasicontinuous wavelength tuning in super-structure-grating (SSG) DBR lasers," *IEEE Journal of Quantum Electronics* , vol. 32, no. 3, pp. 433-441, 1996.

[16] A. Ward, D. Robbins, G. Busico, E. Barton, L. Ponnampalam, J. Duck, N. Whitbread, P. Williams, D. Reid, A. Carter and M. Wale,"Widely tunable DS-DBR laser with monolithically integrated SOA: design and performance." *IEEE Journal of Selected Topics of Quantum Electronics,* vol. 11, no. 1, pp. 149-156, 2005.

[17] A. J. Ward, G. Busico, N. D. Whitbread, L. Ponnampalam, J. P. Duck and a. D. J. Robbins, "Linewidth in widely tunable digital supermode distributed Bragg reflector lasers: Comparison between theory and measurement," *IEEE Journal of Quantum Electronics,* vol. 42, no. 11, pp. 1122-1127, 2006.

[18] L. Ponnampalam, D. J. Robbins, A. J. Ward, N. D. Whitbread, J. P. Duck, G. Busico and a. D. J. Bazley, "Equivalent performance in C-and L-bands of digital supermode distributed bragg reflector lasers," *IEEE Jurnal of Quantum Electronics,* vol. 43, no. 9, pp. 798-803, 2007.

[19] H. Ishii, K. Kasaya and H. Oohashi., "Narrow spectral linewidth operation (< 160 kHz) in widely tunable distributed feedback laser array," *Electronics Letters,* vol. 46, no. 10, pp. 714-715, 2010.

[20] K. Tsuzuki, Y. Shibata, N. Kikuchi, M. Ishikawa, T. Yasui, H. Ishii and a. H. Yasaka, "Full C-Band Tunable DFB Laser Array Copackaged With InP Mach–Zehnder Modulator for DWDM Optical Communication Systems," *Selected Topics in Quantum Electronics, IEEE Journal of,* vol. 15, no. 3, pp. 521-527, 2009.

[21] M. Müller, M. Kamp, A. Forchel and a. J.-L. Gentner, "Wide-range-tunable laterally coupled distributed feedback lasers based on InGaAsP–InP," *Applied Physics Letters,* vol. 79, no. 17, pp. 2684-2686, 2001.

[22] W. Guo, Q. Lu, M. Nawrocka, A. Abdullaev, J. O. Callaghan and J. Donegan, "Nine- channel wavelength tunable laser array based on slots," *Optical Express,* vol. 21, no. 8, pp. 10215-10221, 2013.

[23] D. Byrne, Q. Lu, W.-H. Guo, J. Donegan, B. Corbett, B. Roycroft, P. Lambkin, J.-P. Engelstaedter and F. Peters, "A facetless laser suitable for monolithic integration," *OFC,* pp. 1-3, 2008.

[24] Q. Lu, W.-H. Guo, M. Nawrocka, A. Abdullaev, M. Lynch, V. Weldon and J. F. Donegan, "Single mode lasers based on slots suitable for photonic integration," *Optical Express* , vol. 19, no. 26, pp. B140-B145, 2012.

[25] H.Ishii, H. Tanobe, F. Kano, Y. Tohmori, Y. Kondo and Y. Yoshikuni, "Quasicontinuous wavelength tuning in super- structure- grating (SSG) DBR lasers," *IEEE Journal of Quantum Electronics,* vol. 32, no. 3, pp. 433- 441, 1996.

[26] J. Buus and M. Amann, Tunable laser diodes and related optical sources, Wiley-IEEE Press, 2005.

[27] "Report on Tunable Lasers," Information Gatekeepers Inc, 2002.

[28] V. Jayaraman and Z.-M. C. L. Coldren, " Theory, design, and performance of extended tuning range semiconductor lasers with sampled gratings," *IEEE Journal of Quantum Electronics,* vol. 29, no. 6, pp. 1824-1834, 1993.

[29] B. Mason, S. DenBaars and L. Coldren, " Tunable sampled-grating DBR lasers with integrated wavelength monitors," *IEEE Photonics Technology Letters,* vol. 10, no. 8, pp. 1085- 1087, 1998.

[30] A. S. Diba, F. Xie, C. Caneau, H. LeBlanc, S. Coleman and a. C.-e. Zah, "Diba, Abdou S., Feng Xie, Catherine Caneau, HeWavelength Tuning of Sampled-Grating DBR Quantum Cascade Lasers," in *In CLEO: Science and Innovations, pp. CF3K-3. Optical Society of America*, 2012.

[31] J. Mountjoy, B. Cardiff and a. A. D. Fagan, "Frequency tracking of a Sampled Grating Distributed Bragg Reflector (SG-DBR) laser after a switching event," in *In Signals and Systems Conference (ISSC 2012), IET Irish*, 2012.

[32] G. Sarlet, G. Morthier and a. R. Baets, " Control of widely tunable SSG-DBR lasers for dense wavelength division multiplexing," *Journal of lightwave technology,* vol. 18, no. 8, p. 1128, 2000.

[33] K. Shi, F. Smyth, P. M. Anandarajah, D. Reid, Y. Yu and L. P. Barry, " Linewidth of SG-DBR laser and its effect on DPSK transmission," *Optics Communications,* vol. 283, no. 24, pp. 5040-5045, 2010.

[34] K. Shi, Y. Yu, R. Zhang, W. Liu and L. P. Barry, " Static and dynamic analysis of side-mode suppression of widely tunable sampled grating DBR (SG-DBR) lasers," *optics communications,* vol. 282, no. 1, pp. 81-86, 2009.

Chapter 6. Tunable lasers – advanced characteristics

Introduction

In Chapter 4 a design, fabrication process and simulated results of tunable laser diodes with etched slots were presented. In Chapter 5 the tunable lasers were characterized exhibiting a wide tuning range of up to 55nm with good SMSR values over 30dB. A laser with the slot period of 97μm for the front mirror and 108μm for the back mirror exhibits a 400 GHz channel spacing which is useful in implementing wavelength division multiplexing- WDM- a standard technique used in optical communication systems [1]. The international telecommunication union (ITU) standardised the channel frequencies of WDM systems on a 100GHz (0.8 nm) grid in the frequency range of 186 to 196 THz (1530-1612nm in the C and L bands). In this chapter, the tunable laser based on etched slots will be further characterized. A continuous tuning of the laser over a short wavelength range as well as the thermal tuning will be presented. A continuous tuning range allows accessing all wavelengths in ~+/- 50GHz wavelength range around a super-mode position. For the temperature tuning, a tuning of 3 nm (375 GHz) for a single super-mode is observed while changing the temperature between 15°C and 40°C. Finally, the linewidth of the laser will also be presented in this chapter.

6.1. Continuous tuning

As was outlined in Chapter 2, in the continuous tuning scheme, the laser wavelength is tuned smoothly in arbitrarily small steps and the cavity mode is lasing throughout the entire tuning range. In the discontinuous tuning scheme, the tuning range is solely determined by the cavity gain which means that longitudinal mode hops are allowed and this provides a larger tuning range. Although it is impossible to access certain wavelengths inside the tuning range because of the super-mode spacing [2].

From the wavelength tuning maps in Chapter 5 it can be seen that the tuning of the laser shows small changes in the wavelength before the onset of a super-mode. These small regions are the areas of the continuous tuning accessible for the laser as shown in figure 6.1 below. Here the continuous tuning for the lasers with the slot period of 70μm/76μm will be investigated.

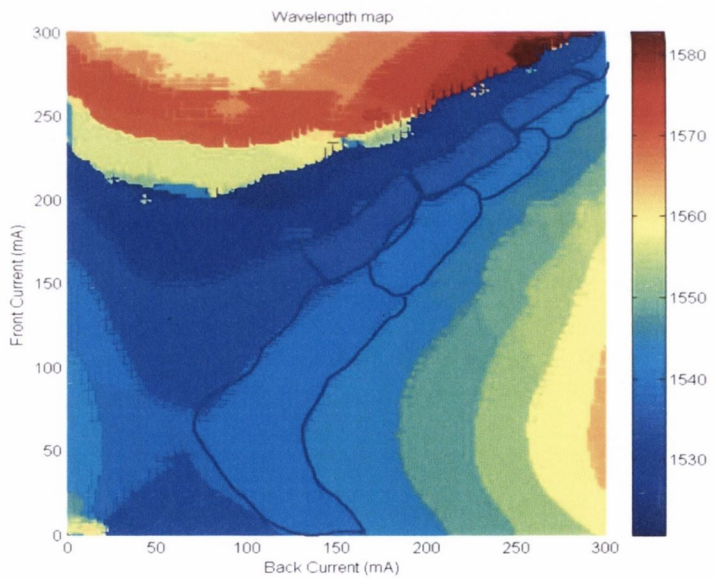

Figure 6.1. Wavelength tuning map for the laser with the slot period of 70μm for the front mirror and 76μm for the back mirror. Marked regions are an example of regions where the continuous tuning is accessible.

From the wavelength and the SMSR tuning maps shown in figures 5.32 and 5.33 four modes with good SMSR more than 30dB were selected. The regions are: (i) for the front current from 250 mA to 300mA and the back current from 140mA to 190mA, the

operating wavelength is around 1566nm; (ii) for the front current from 100mA to 150mA and the back current from 120mA to 170mA, the operating wavelength is around 1538nm; (iii) for the front current from 100mA to 150mA and the back current from 170mA to 220mA, the operating wavelength is around 1543nm; (iv) for the front current from 90mA to 140mA and the back current from 240 mA to 290mA, the operating wavelength is around 1553nm.

Figure 6.2 shows the super-modes versus wavelength. Concentrating on the super-mode operating at the wavelength of around 1566nm, two different tuning schemes can be observed. Figure 6.3 shows the selected super-mode; the green line represents one current tuning and the blue line represents two current tuning.

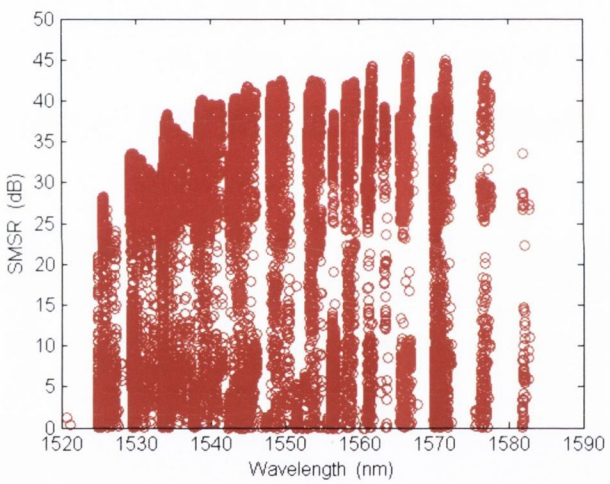

Figure 6.2 SMSR versus wavelength for the laser with slot period of 70μm on the front mirror and 76μm on the back mirror.

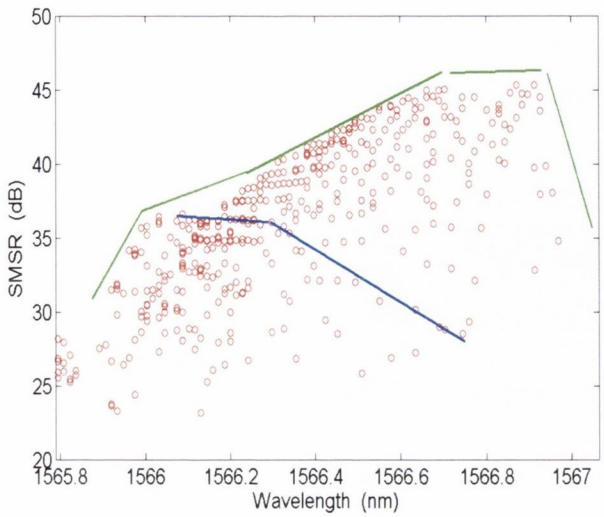

Figure 6.3 SMSR versus wavelength of 1566nm. The red dots represents the SMSR points for a different front and back currents combinations.

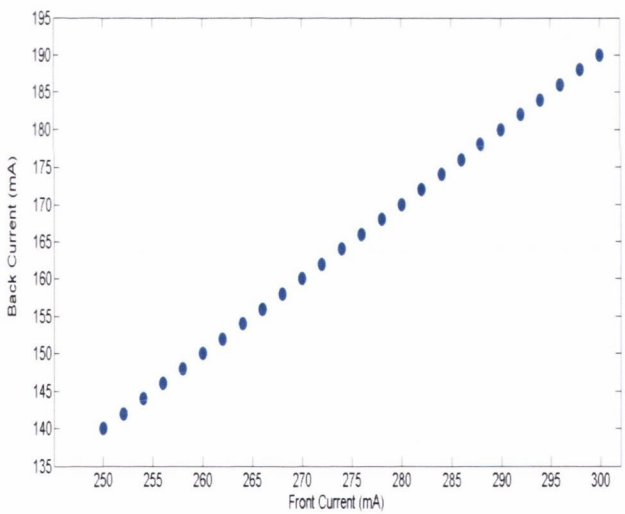

Figure 6.4 Linear injection currents for the wavelength of ~1566nm.

To tune along the green line one mirror section current is constant and the other mirror section current is scanned over a particular current range that corresponds in turn to a wavelength range. To tune along the blue line, both mirror section currents are scanned simultaneously. For the continuous tuning both injected currents need to be increased or decreased linearly as the wavelength is recorded. The mirror section injection current dependence for the first selected super-mode is shown in figure 6.4 below.

The SMSR versus wavelength is shown in figure 6.5 below.

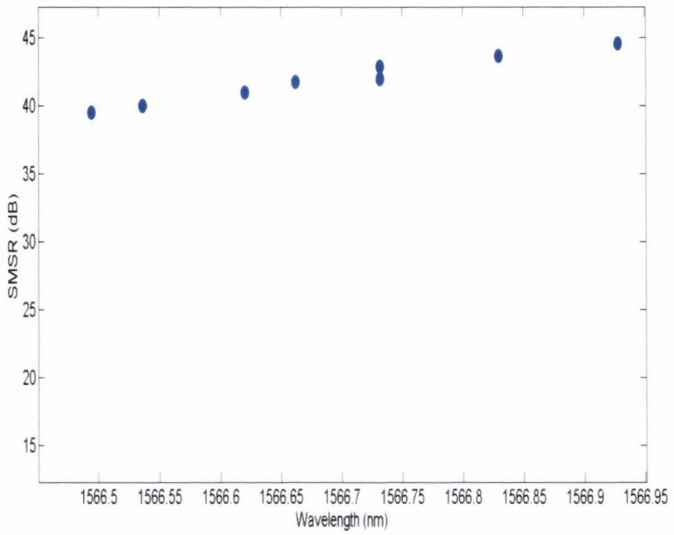

Figure 6.5. SMSR versus wavelength for the front current from 250mA to 300mA and the back current from 140mA to 190mA.

From figure 6.5 the mode shows continuous tuning of 0.4 nm (~50GHz). The rate for changing the wavelength with the current for this mode is 0.008nm/mA .

The mirror section injection current dependence for the first selected super-mode is shown in figure 6.6 below.

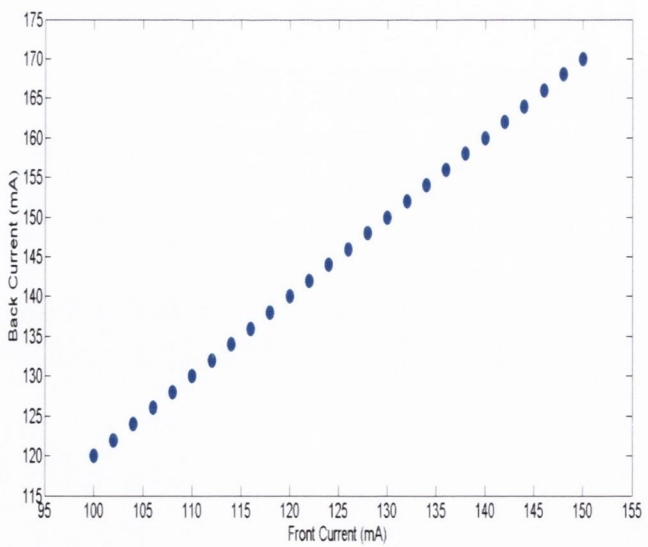

Figure 6.6. Linear injection currents for the wavelength of ~1538nm.

The SMSR versus wavelength is shown in figure 6.7 below.

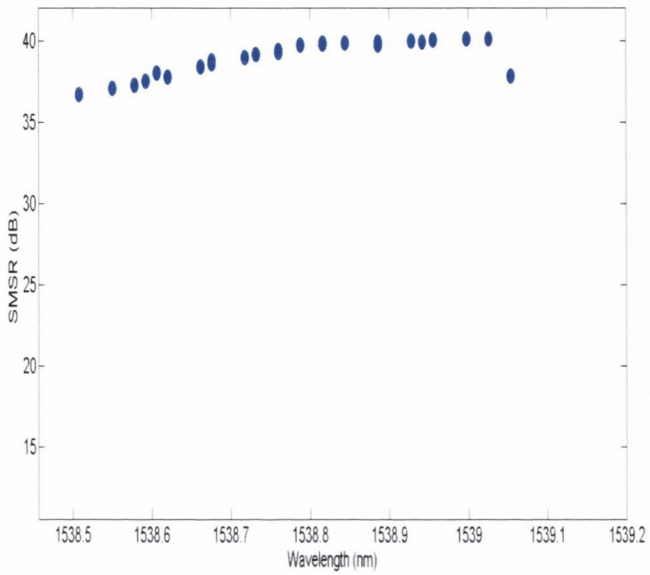

Figure 6.7. SMSR versus wavelength for the front current from 100mA to 150mA and the back current from 120mA to 170mA.

From figure 6.7 that the continuous tuning for this mode is 0.6 nm (~75 GHz). The rate for changing the wavelength with the current is again 0.012nm/mA.

The mirror section injection current dependence for the third selected super-mode is shown in figure 6.8 below.

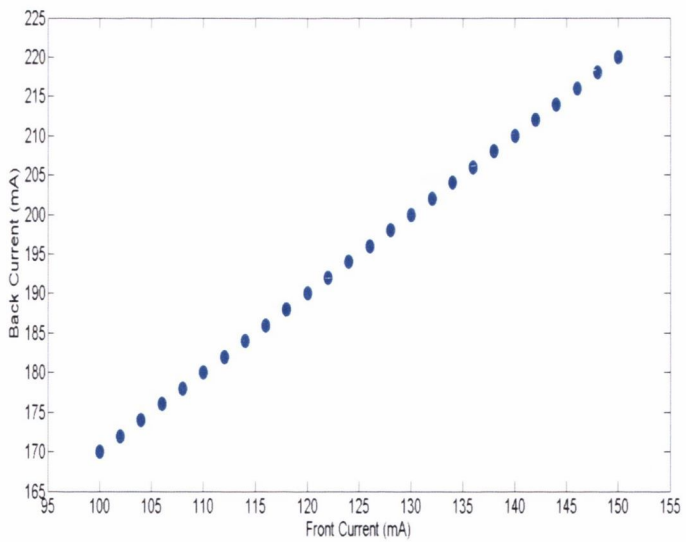

Figure 6.8. Linear injection current for the wavelength of ~1543nm.

The SMSR versus wavelength is shown in figure 6.9 below.

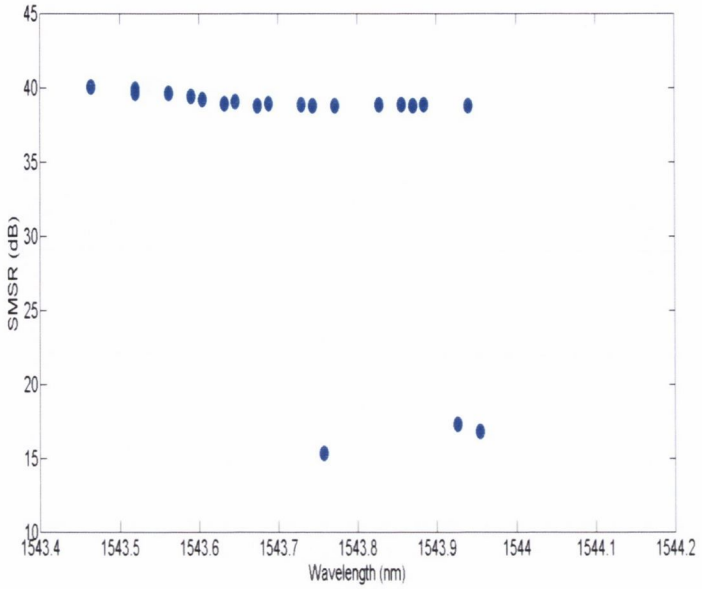

Figure 6.9. SMSR versus wavelength for the front current from 100mA to 150mA and the back current from 170mA to 220mA.

From figure 6.9 the continuous tuning for this mode is 0.6 nm (~75GHz). The rate for changing the wavelength with the current is 0.012nm/mA.

The mirror section injection current dependence for the third selected super-mode is shown in figure 6.10 below. The SMSR versus wavelength is shown in figure 6.11.

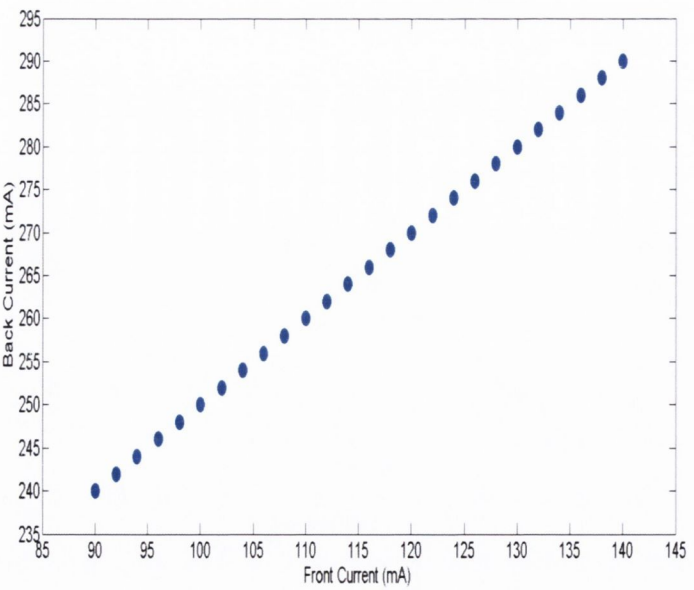

Figure 6.10. Linear injection currents for the wavelength of ~1553nm.

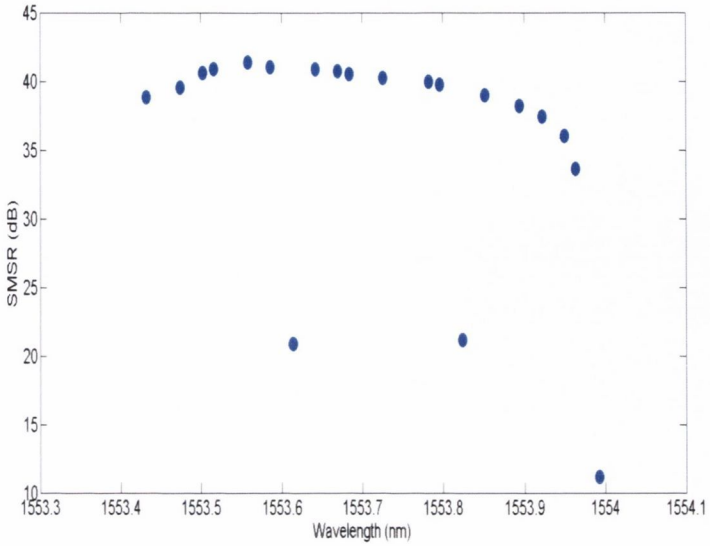

Figure 6.11. SMSR versus wavelength for the front current from 90mA to 140mA and the back current from 250mA to 290mA.

Figure 6.11 shows the continuous tuning range of 0.6nm (~75GHz). The rate for changing the wavelength with the current is 0.012nm/mA.

The modes exhibit continuous tuning of 0.4nm (~50GHz) for the first mode and 0.6nm (~75GHz) for the next three modes.This allows us to accurately set the laser to precise optical frequencies with high SMSR such as required within the C-band [3]. The continuous tuning of these modes by current injection suggests that full carrier clamping does not take place in the mirror sections of this laser. In comparison, SG-DBR laser has a continuous tuning range of <0.4nm for all discrete modes [4] [5]. In SG-DBR lasers the continuous tuning range is limited by the available index change induced by pure current injection [6]. In the device demonstrated here, both current variations and the temperature change have contributed to the continuous tuning. The temperature may be the main contribution factor in our devices considering the current variations in the mirror sections are quite large and the device is unpackaged. This is the reason why a relatively large continuously tuning range has been shown.

Continuous tuning of nine contact laser

The continuous tuning of the laser with nine contacts was also investigated. As described in Chapter 6, the isolation contact were left unbiased. The selected mode has a wavelength of

~1537nm with a good SMSR of 30dB. The selected region is for the currents of 50mA to 100mA for the front mirror and 100mA to 150mA for the back mirror. The mirror section injection current dependence for selected super-mode is shown in figure 6.12 below. From figure 6.13, the continuous tuning of this mode is now only 0.2 nm (~25GHz). The rate for changing the wavelength with the current is 0.004nm/mA.

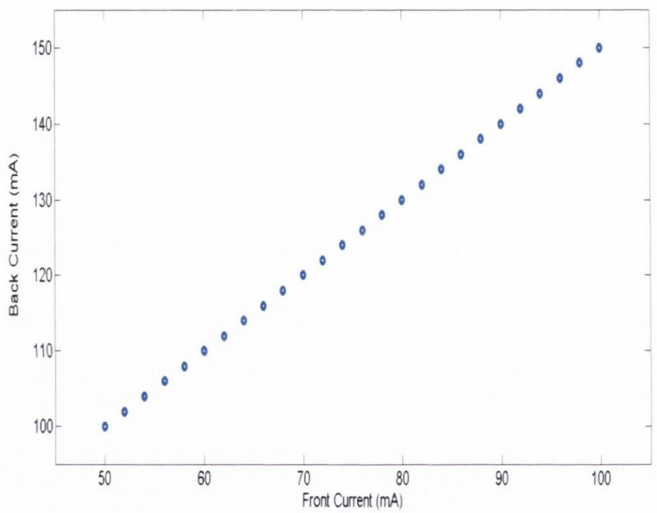

Figure 6.12. Linear injection currents for the wavelength of ~1537nm

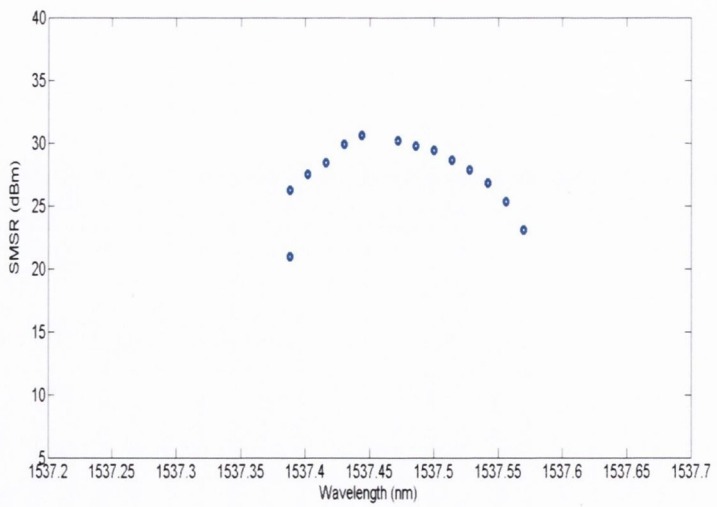

Figure 6.13. SMSR versus wavelength for the front current from 50mA to 100mA and the back current from 100mA to 150mA.

Continuous tuning of the laser with nine slots on the front mirror and five slots on the back mirror.

The continuous tuning of the laser with nine slots on the front mirror and five slots on the back mirror is shown here. The selected mode has a wavelength of ~1561nm with a good SMSR of 40dB. The selected region is for the currents of 80mA to 120mA for the front mirror and 200mA to 240mA for the back mirror. The mirror section injection current dependence for a selected super-mode is shown in figure 6.14 below. As seen from figure 6.15 the continuous tuning of this mode is 0.3 nm (~37.5GHz). The rate for changing the wavelength with the current is 0.0075nm/mA.

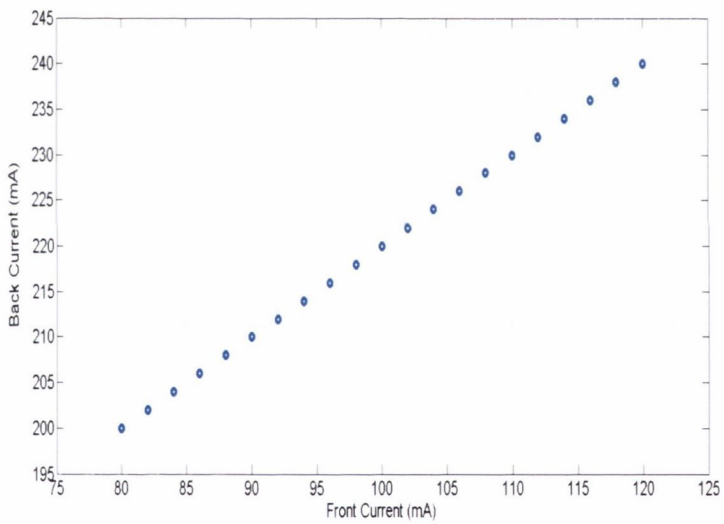

Figure 6.14. Linear injection currents for the wavelength of ~1561nm.

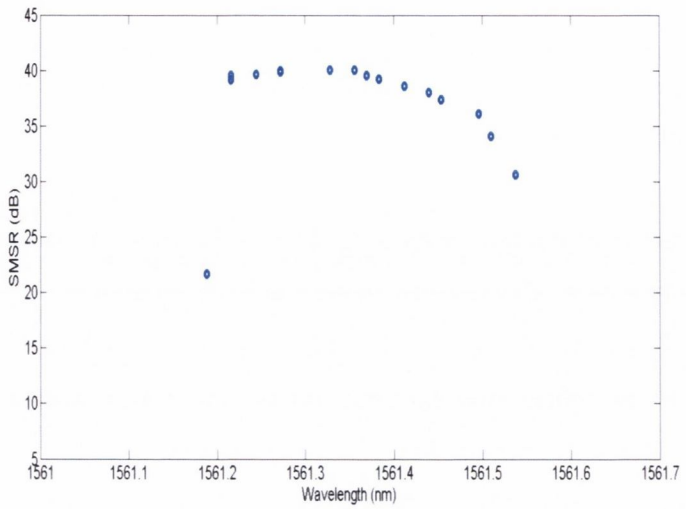

Figure 6.15. SMSR versus wavelength for the front current from 80mA to 120mA and the back current from 200mA to 240mA.

6.2. Thermal tuning

The lasing wavelength for semiconductor lasers is very dependent on the temperature of the device as both the bandgap energy and the refractive index change with temperature, the cavity length also changes due to thermal expansion however this is a small change over the temperatures range used in our experiment. For the current of 30 mA, with a device resistance of 4 Ω and the photon energy of 0.8 eV (~1550 nm) there can be found that a total of 19.6 mW of power supplied to the laser is lost giving a temperature increase of around 2 K. Due to the thermal dependence of the bandgap energy a thermal dependence of the gain curve and therefore the peak gain wavelength λ_p can be obtained. The dependence of λ_p on the temperature gives a Fabry- Perot type laser their typical peak gain wavelength temperature dependence of 0.5 nm/K which corresponds to $-2.5*10^{-4}$ eV/K. Due to the temperature dependence of the refractive index, the cavity modes and therefore the above- threshold lasing mode will tune as 0.1 nm/K. Any heating of the laser cavity will also increase the threshold current and decrease the differential efficiency of the laser. This can limit the tunability of a laser by temperature tuning [2].

Here the temperature tuning of the laser with the slot period of 70μm on the front mirror and 76 μm on the back mirror is investigated. Eleven channels were picked for the wavelength of 1525nm, 1529nm, 1534nm, 1538nm, 1543nm, 1549nm, 1553nm, 1558nm, 1563nm, 1567nm, 1572nm. The channels were set manually by changing the currents injected into the front and back mirror. The temperature of the heat sink was changing with a step of 5°C from 15°C to 40°C. The temperature tuning of all eleven channels is shown in Figure 6.16 below.

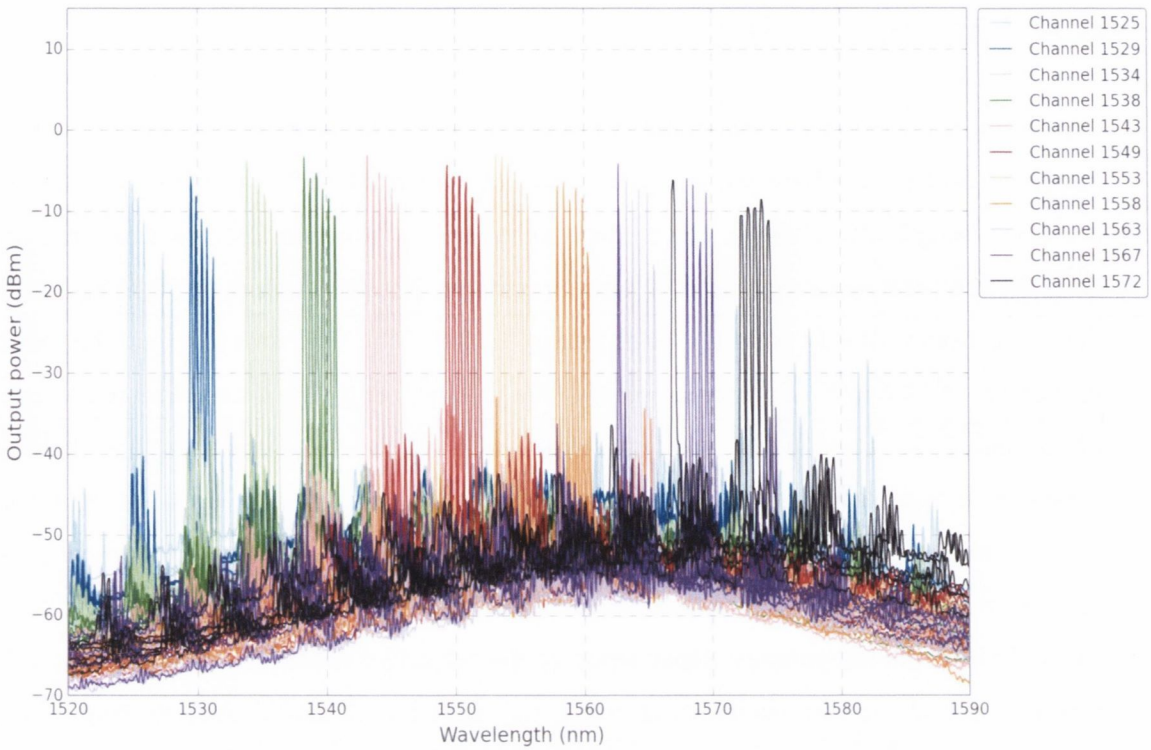

Figure 6.16. The temperature tuning of eleven channels of the laser with the slot period of 70 μm/76 μm. The temperature is changing from 15°C to 40°C with the step of 5°C.

The total range is 49.64nm from 1524.8nm to 1574.4 nm. It can be seen that for the first channel of 1525nm for the high temperatures of 35°C and 40°C, the mode competition is observed on the red side of the spectrum. For channels ten and eleven a big super-mode hop more than 0.5 nm is observed while changing the temperature of 5°C from 15°C to 20 °C. It can be also observed that the SMSR is decreasing with increasing temperature. The temperature tuning range is much smaller than the 4.6 nm super- mode spacing and therefore cannot be used to complete full wavelength coverage over the entire wavelength range accessible to the laser.

Figure 6.17. shows the change of the peak wavelength with increasing temperature for all eleven channels. The wavelength is red shifted with increasing temperature.

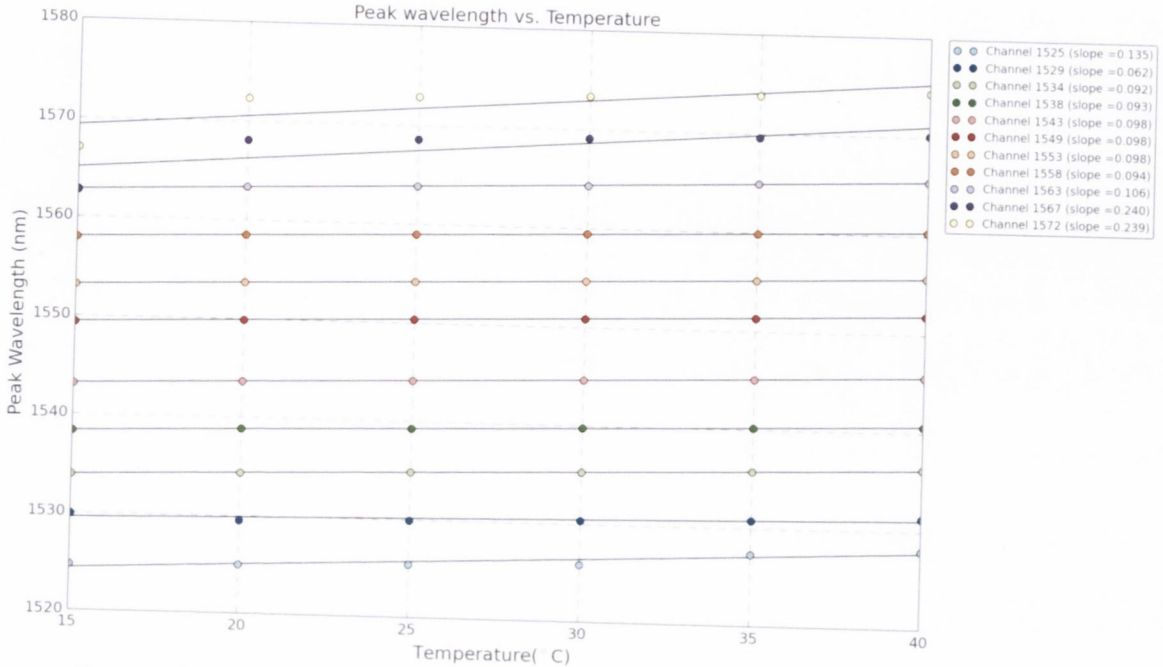

Figure 6.17. Peak wavelength for all eleven channels versus temperature from 15°C to 40°C.

The change in SMSR for eleven channels with increasing temperature is shown in Figure 6.18. SMSR values decrease with increasing temperature of the heat sink. The lowest SMSRs are observed for the highest temperature of 40 °C for all eleven channels.

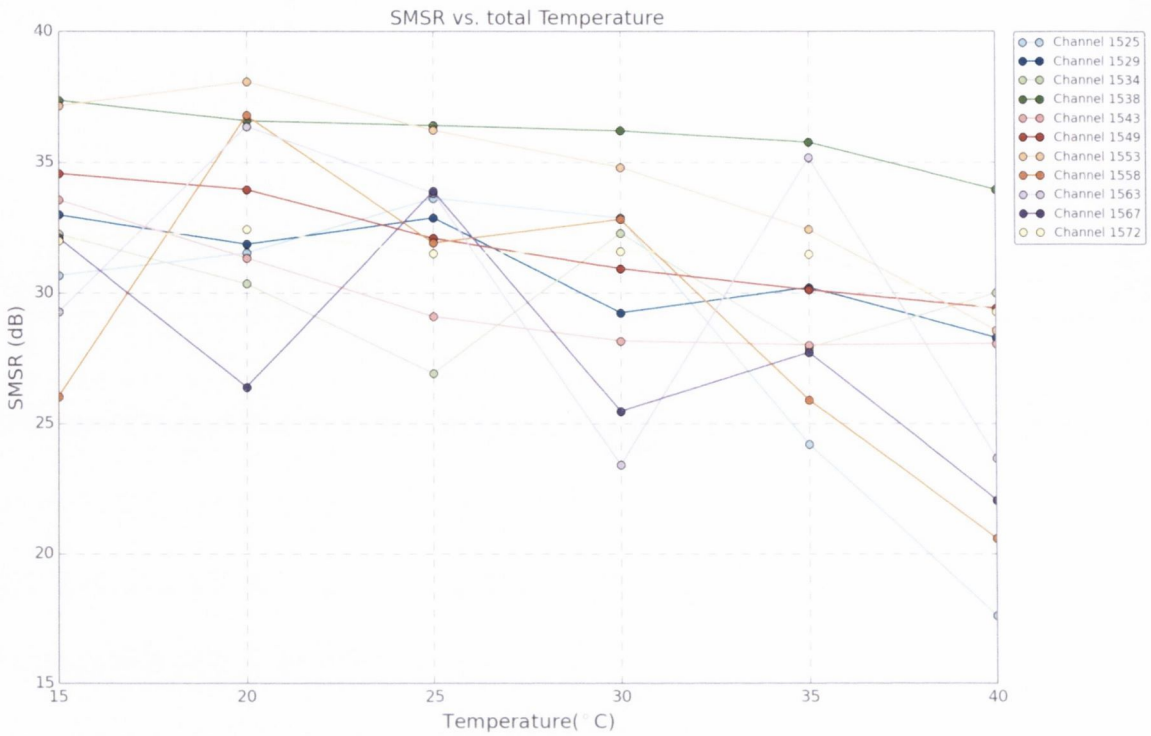

Figure 6.18. SMSR versus temperature change from 15 °C to 40 °C for eleven channels.

Combining figures 6.17 and 6.18 SMSR versus peak wavelength for different temperature can be plotted as shown in figure 6.19. For channel four with the wavelength of 1538nm, SMSR values are more than 30 dB during the temperature tuning.

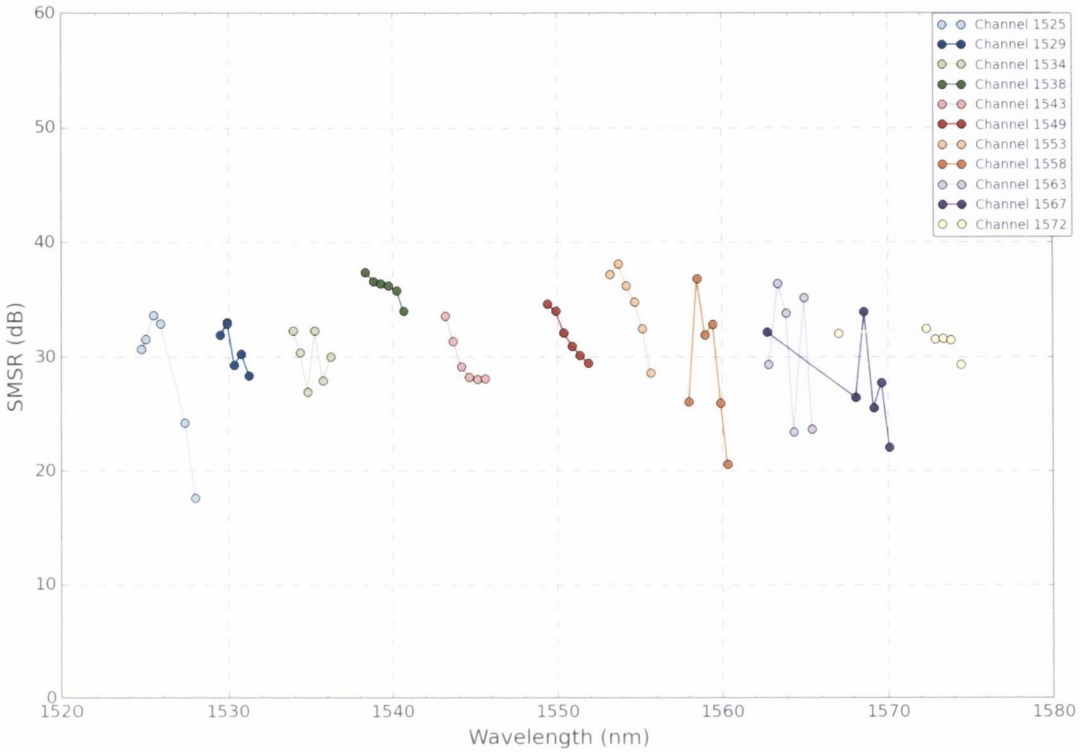

Figure 6.19. SMSR versus peak wavelength for all eleven channels.

6.3. Linewidth measurements

The laser linewidth is introduced and determined in this section. A good introduction to linewidth theory can be find in [2] [7]. The linewidth of a laser diode in an important parameter in optical communications as a broad linewidth will reduce the distance over which the pulses from the laser can be transmitted due to dispersion in the optical fibre. Single mode lasers have a finite linewidth caused by spontaneous emission entering into the lasing mode. The spontaneous emitted photons will have a random phase with respect to the coherent emission generated by stimulated emission within the laser structure. The optical power and the number of photons in the laser cavity depends on the laser structure therefore the linewidth depends on the laser structure. The number of photons in the laser is determined by:

$$S' = \frac{\overline{S} V_a}{\Gamma} \tag{6.1}$$

where $\overline{S}$ is the average photon density, V_a is the active volume and Γ is a confinement factor. The change in phase $\Delta\phi_i$ due to the addition of a photon with random phase is given by

$$\Delta\varphi_i = \frac{1}{\sqrt{S'}} \sin(\theta_i) \tag{6.2}$$

where θ_i is taken from figure 6.20 below showing the result of a spontaneously emitted photon. The filed can be represented by β - the field amplitude normalized so that the average intensity $I = \beta * \beta$ also equals the average number of photons in the cavity $\beta = I^2 \exp(i\varphi)$ where $I(t)$ and $\varphi(t)$ represent the intensity and the phase of the laser filed. A basic assumption is that the *i*th spontaneous emission event change β by $\Delta\beta_i$ where $\Delta\beta_i$ has a unit magnitude and a random phase of $\Delta\beta_i = \exp(i\varphi + \theta_i)$, where θ_i is a random angle.

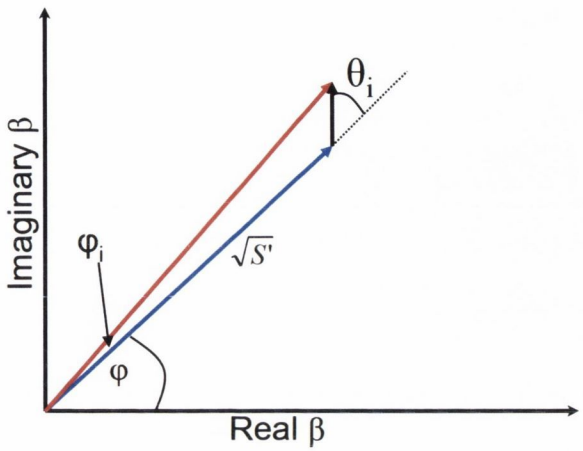

Figure 6.20. Phasor representation of the field in the laser. β – the filed amplitude $\beta=I^2\exp(i\varphi)$ increased by $\Delta\beta_i$ having amplitude of unity and phase $i\varphi+\theta_i$.

When the spontaneous emission rate is

$$\frac{R_{sp}V_a}{\Gamma} \tag{6.3}$$

the accumulated phase change over time t and then

$$\Delta\varphi_t = \sum_{i=1}^{R_{sp}V_a/\Gamma} \frac{1}{\sqrt{S'}}\sin(\theta_t) \tag{6.4}$$

By equating the variance per time of $\varphi(t)$to a change in angular frequency, an expression for the laser linewidth can be found as:

$$\Delta\upsilon = \frac{\Delta\omega}{2\pi} = \frac{R_{sp}V_a/\Gamma}{4\pi S''} \tag{6.5}$$

$$\text{var}\frac{[\Delta\varphi(t)]}{t} = \frac{\left\langle[\varphi(t)-\varphi(0)]^2\right\rangle}{t} = \frac{R_{sp}V_a/\Gamma}{2S'} = \Delta\omega \tag{6.6}$$

The distribution of $\Delta\varphi(t)$ is Gaussian which leads to a Lorentzian lineshape [2]. From Einstein's relations the spontaneous emission R_{sp} can be described as

$$R_{sp} = \frac{\Gamma v_g g_{eff} n_{sp}}{V_a} \tag{6.7}$$

where v_g is the group velocity, g_{eff} is the modal gain and n_{eff} is the spontaneous emission coefficient. The power out of each facet is

$$P = \frac{v_g \alpha_m \bar{S} V_a h\upsilon}{2\Gamma} \tag{6.8}$$

where P is the power out of each facet assuming that both facets are equal. The linewidth can be rewritten as

$$\Delta\upsilon = \frac{h\upsilon v_g^2 (\alpha_i + \alpha_m)\alpha_m n_{sp}}{8\pi P} \tag{6.9}$$

α_m is the mirror loss, α_i is the internal loss and $h\upsilon$ is the photon energy.This is the Schawlow-Townes expression for the linewidth.

It was realized by Henry [8] that for the diode lasers a significant correction factor is required in the linewidth expression. For a semiconductor laser there is an extra enhancement to the linewidth called the linewidth enhancement factor α_H due to the phase noise created when spontaneous emission from the laser cavity gain media changes the laser frequency. This effect occurs when a spontaneous emission event changes the photon density which changes the carrier density as the carrier and photon densities are related through the carrier and photon density equations. In [8] this enhancement of the linewidth is given and the linewidth can be written as

$$\Delta\upsilon = \frac{h\upsilon v_g (\alpha_i + \alpha_m)\alpha_m n_{sp}}{8\pi P}\left(1 + \alpha_H^2\right) \tag{6.10}$$

which is referred as Schawlow-Townes-Henry linewidth.

As the linewidth is of the order of few MHz [2] [9] [10]normal measuring equipment such as optical spectrum analyser OSA cannot determine it as an OSA has a its best resolution at ~0.01nm (~1^{-11}m)~1.25GHz. To determine the linewidth another method not relying on the OSA must be used. To determine the tunable laser linewidth the

delayed self-heterodyne (DS-H) method [11] is used providing very high resolution from about 10kHz to 1GHz. The basics of this method are presented below.

The laser needs to be operating in a single mode regime with SMSR > 30dB. In this method interference between two optical fields are used. The two optical fields come from the original beam and a time delayed portion of itself. Two beams must have spatial overlap and polarization alignment. The spatial overlap is obtained by sending both optical waves down the same single mode fiber which ensures good spatial overlap. The polarization alignment is obtained by including a polarization controller PA in the set- up to create a polarization overlap between the optical waves.

Here the delayed self- heterodyne DS-H method to obtain the optical linewidth of the semiconductor tunable laser is presented. More detailed analysis can be found in [11].

Considering an optical field and its delayed self- incident on a photodetector after being spatially combined, the optical fields take form of

$$E_1(t) = \sqrt{P_1(t)} \exp[i(2\pi\nu_1 + \varphi_1(t))] \tag{6.11}$$

and

$$E_1(t) = \sqrt{P_2(t)} \exp[i(2\pi\nu_2 + \varphi_2(t))] \tag{6.12}$$

where the delayed field is denoted with an index 2,where φ_i is the optical phase and ν_i is the frequency of the ith field. Optical powers are the fields amplitude squared:

$$P_i(t) = |E_i(t)|^2 \tag{6.13}$$

As the photodetector detects the power and not the optical field itself the detected power is

$$i(t) = \Re|E_i(t)|^2 = \Re|E_1(t) + E_2(t)|^2 \tag{6.14}$$

where $\Re$ is the detector responsivity

$$\Re = \frac{\eta_d q}{h\upsilon} \tag{6.15}$$

η_d is the detector quantum efficiency and q and $h\upsilon$ are the electronic charge and the photon

energy, respectively. For a wavelength of 1550nm $q/h\upsilon$ has a value of 1.24 eV.

The final power detected at the photodetector is

$$i(t) = \Re\left[P_1(t) + P_2(t) + 2\sqrt{P_1 P_2}\cos(2\pi\nu_0\tau_0 + \Delta\varphi(t,\tau_0))\right] \qquad (6.16)$$

where P_1 and P_2 are the powers measured by the photodetector from the optical field and delayed self, $2\pi\nu_0\tau_0$ is the average phase- setting of the interferometer used to where the delay between both optical fields is τ_0, and $\Delta\varphi(t,\tau)$ is the time varying phase difference caused by any phase or frequency modulation and the intereferometric delay τ_0.

The self- heterodyne experimental set up for the linewidth measurements is shown in figure 6.21 below.

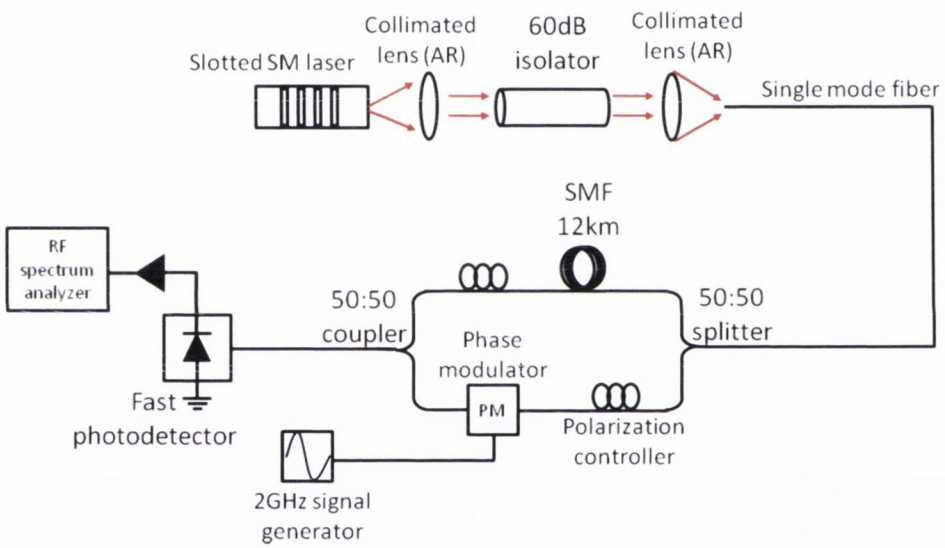

Figure 6.21. Self -heterodyne experimental set up for the linewidth measurements.

A free space optical isolator giving 60 dB isolation between forward and backward propagating light is included in the measurement system. This prevents backward reflections of light into the laser cavity. 1% of the emitted light is coupled to the optical spectrum analyser OSA to determine the wavelength of the super-mode. The 99% portion of the light is split again in the interferometer and one half is sent through 12 km of optical fiber to produce a delay of 60μs, the delay must be more than the coherence time of the laser. This means that the two beams will combine as if they originated from two different sources giving incoherent mixing. The other path goes through a polarization controller to ensure the polarization is closely matched to maximize the interference between the two beams. This process is equivalent to mixing two lasers with the same

linewidth and central frequency. The phase modulator shifts the signal to 2GHz to increase the accuracy. The 50:50 coupler combines the two beams together. Then the signal is sent to a fast photodetector. The linewidth spectrum was recorded using an electrical spectrum analyzer (ESA) with the resolution bandwidth set to 100 kHz. A Voigt function, which is a convolution of Lorentzian and Gaussian profiles, was used to fit the linewidth spectrum. The Lorentzian profile is a contribution of frequency noise spectra for spontaneous emission while the Gaussian profile is a contribution due to the technical noise such as temperature fluctuation, mechanical vibrations or injected current noise [12]. Due to measuring a bare device for high currents there is more temperature fluctuations and therefore the Gaussian contribution dominates as we shall see below.

The linewidth of the lasers with the slot period of 97μm/108μm and 70μm/76μm was measured.

Fig. 6.22 shows an example of the spectrum of the tunable laser with the slot period of 97μm/108μm for a wavelength of 1543.27 nm with the linewidth of 4 MHz.

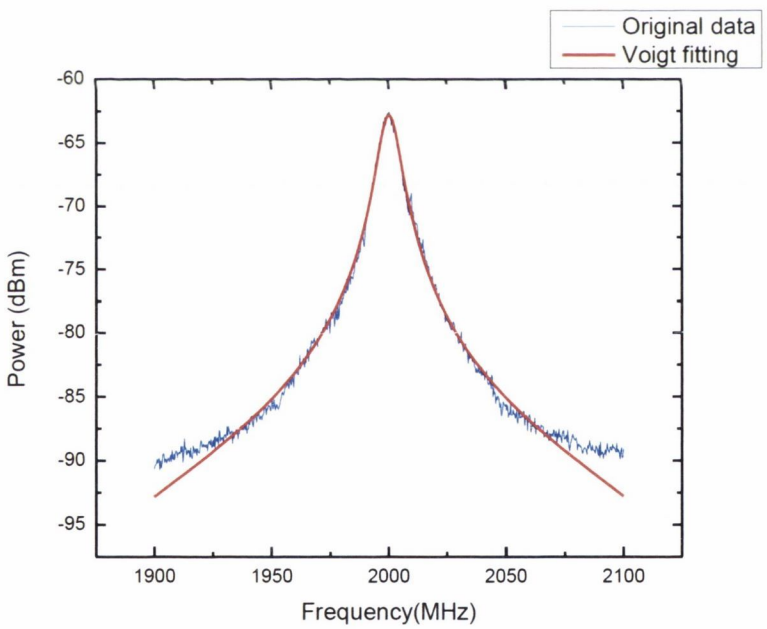

Figure 6.22. Example of a spectrum of the tunable laser for a wavelength of 1543.27 nm for the laser with slot period of 97μm/108μm

Figure 6.23 below shows the linewidth versus peak wavelength for the laser with slot period of 97μm/108μm.

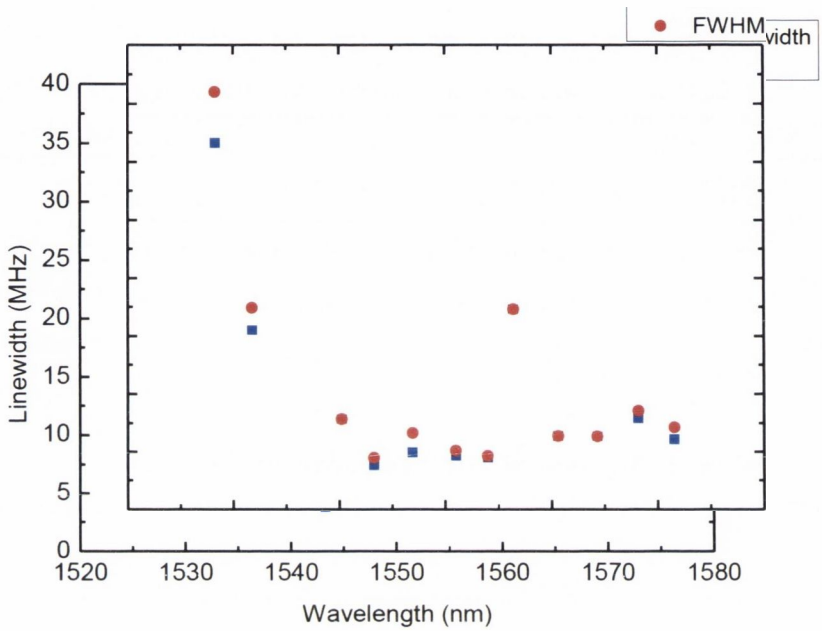

Figure 6.23. Linewidth versus wavelength for the laser with the slot period of 97μm/108μm.

From the Voigt fitting we extracted an FWHM which is the total linewidth and the Lorentzian part which is the intrinsic linewidth. FWHM shows how the Gaussian contribution affects the total linewidth as the Gaussian part is related to the noise coming from the current sources. A clear dependence of the spectral linewidth on wavelength is observed. The linewidth is large at short wavelengths and is nearly constant from 1540 nm to 1570 nm. In the range from 1520 nm to 1540 nm the laser shows a low SMSR and a large linewidth would be expected.

Figure 6.24 below shows an example of a spectrum for the wavelength of 1549.41nm for the laser with the slot period of 70μm for the front mirror and 76μm for the back mirror. The linewidth is 8.6 MHz.

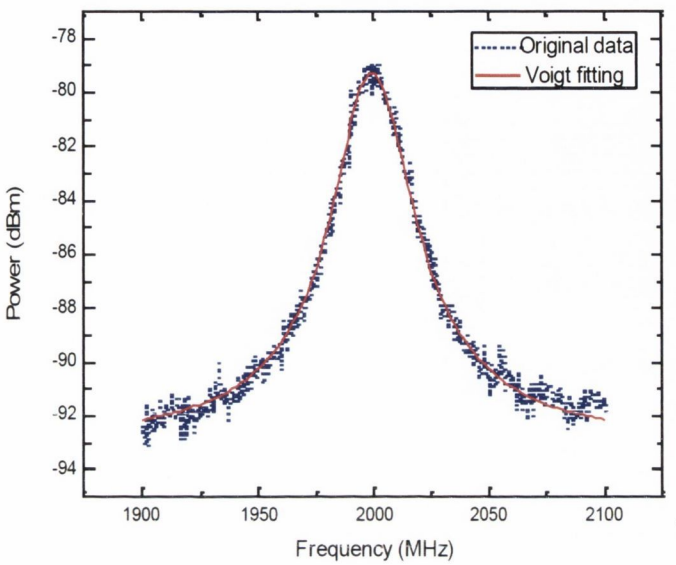

Figure 6.24. Example of a spectrum of the tunable laser for a wavelength of 1549.41 nm for the laser with slot period of 70μm for the front mirror and 76μm for the back mirror.

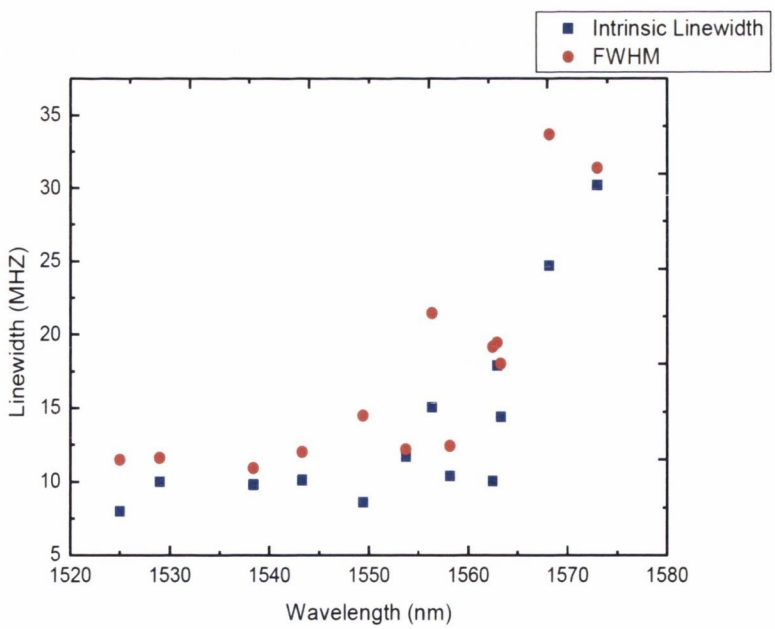

Figure 6.25. Linewidth versus wavelength for the laser with slot period of 70μm for the front mirror and 76μm for the back mirror.

As seen from figure 6.25 the linewidth depends on wavelength. The linewidth increases with increasing wavelength.

One limitation with this method is due to the current sources used to inject the currents into four laser sections. As with any current source some noise fluctuations will be present and the

laser was biased with four independent current sources, it was not possible to replace them with low noise current sources, therefore the values determined here are larger as seen by the difference in the Voigt and the Gaussian linewidths.

The spectral linewidth of a semiconductor laser should be increasing with increasing wavelength values due to the increase of the linewidth enhancement factor [2] [13]. The linewidth enhancement factor increases due to the fact that the density of states at the long wavelength (lower energy) end is mostly filled compared to the short wavelength (higher energy) end [14]. Therefore the change of gain with carrier density change at the long wavelength end will be smaller than the change of gain at the short wavelength end. Looking at the results for the laser with shorter slot period of 70μm for the front mirror and 76 μm for the back mirror we can see that the linewidth values increase with increasing wavelength. The lowest recorded linewidth is about 8.6MHz.

The laser with a longer slot period clearly exhibits lower linewidth value that for the laser with a shorter slot period. The difference is about ~4.6MHz.

Conclusion

The further characterization of the slotted tunable lasers was shown in this chapter. The continuous tuning, temperature tuning and linewidth measurements were investigated to provide more detailed laser characteristics. The tunable slotted laser exhibits the continuous tuning range of 0.6 nm (~75GHz). The laser with nine contacts has the contiuous tuning range only of 0.2nm (~25GHz) which is shorter by about 0.4 nm than for the laser with five contacts. The laser with nine slots on the front mirror and five slots on the back mirror exhibits a continuous tuning range of about 0.3 nm (~37.5GHz). The total temperature tuning range is about 49.64 nm for twelve modes. Each mode was tuned individually by about 2.5 nm(~313 GHz) while changing the temperature from 15°C to 40°C with a step of 5°C. The linewidth of two laser with the slot periods of 97μm/108μm and 70μm/76μm was measured. The laser with the longer slot period has a narrower linewidth of ~4MHz, while the linewidth for the laser with a shorter slot period was ~8.6MHz.

References

[1] C. A. Brackett, „Dense wavelength division multiplexing networks: Principles and applications," *IEEE Journal on Selected Areas in Communications,* vol 8, no 6, pp. 948- 964, 1990.

[2] J. Buus and M. Amann, Tunable laser diodes and related optical sources, Wiley-IEEE Press, 2005.

[3] G. Agrawal, Ligthwave Technology: Telecomminication Systems, Wiley, 2005.

[4] B. Mason, G. Fish, J. Barton, L. Coldren and S. DenBaas, „Characteristics of sampled grating DBR laser with integrated semiconductor optical amplifiers," *Otical Fiber Communication Conference,* vol 1, pp. 193-195, 2000.

[5] S.Oku, S. Kondo, N. Y, T. Hirono, M. Nakao and T. Tamamura, „Surface- grating Bragg reflector lasers using deeply etched groove formed by reactive beam etching," *Indium Phosphide and Related Materials, International conference on,* pp. 299-302, 1998.

[6] F. Delorme, „Widely tunable 1.55-μm lasers for wavelength-division-multiplexed optical fiber communications," *Quantum Electronics, IEEE Journal,* vol 34, no 9, pp. 1706-1716, 1998.

[7] L. Coldren, S. Corzine and M. Nasanovic, Diode lasers and photonics integrated circuits, Wiley, 2012.

[8] C. Henry, „Theory of the liewidth of semiconductor lasers," *IEEE Journal of Quantum Electronics,* vol 18, no 2, pp. 259-264, 1982.

[9] K. Shi, F. Smyth, P. M. Anandarajah, D. Reid, Y. Yui and L. P. Barry, „ Linewidth of SG-DBR laser and its effect on DPSK transmission," *Optics Communications,* vol 283, no 24, pp. 5040-5045, 2010.

[10] H. Joseph and D. Sadot, „A novel self-heterodyne method for combined temporal and spectral high resolution measurement of wavelength transients in tunable lasers," *IEEE In Conference on Lasers and Electro-Optics (CLEO),* vol 3, pp. 2031-2033, 2005.

[11] T. Okoshi, K. Kikuchi and A. Nakayama, „Novel method for high resolution measurement of laser output spectrum," *Electronics Letters,* vol 16, no 16, pp. 630-631, 1990.

[12] S. Spießberger, M. Schiemangk, A. Wicht, H. Wenzel, O. Brox and G. Erbert, „ Narrow linewidth DFB lasers emitting near a wavelength of 1064 nm," *Journal of*

Lightwave Technology, vol 28, no 17, pp. 2611-2616, 2010.

[13] S. Ogita, M. Yano, H. Ishikawa and H. Imai, „Linewidth reduction in DFB laser by detuning effect," *Electronics Letters,* vol 23, pp. 393-394, 1987.

[14] D. Byrne, W. Guo, R. Phelan, Q. Lu, J. Donegan and B. Corbett, „Measurement of linewidth enhancement factor for InGaAlAs laser diode by Fourier series expansion method," *Electronics Letters,* vol 43, no 21, pp. 1145-1146, 2007.

Chapter 7. Tunable lasers- second run.

Introduction

The design for the tunable lasers presented in this chapter was completed in February 2014 and the lasers were fabricated in May 2014. The purpose of this new design was to focus on shorter slot periods to determine the effects on the laser tuning range and SMSR. The lasers presented in this chapter have the same epitaxial structure as the lasers described in Chapter 5. They are five contact lasers where the first section is the semiconductor optical amplifier- SOA section, the second one in the front mirror section, the next one is the central gain section with the length of 500 μm, then the back mirror section and the last one the PD section. All the lasers have the same length to ease the fabrication process. From the previous design presented in Chapter 5, we concluded that the best laser was the one with the shortest slot period of 70μm for the front mirror and 76μm for the back mirror. The difference in the slot periods of both mirrors is 6μm and the difference in FSRs is 0.4μm. For the second run of the laser presented in this chapter we decided to keep the difference between the slot periods of around 5-6μm and the difference between the FSRs no less than 0.4μm.

Nine slots front mirror with the slot period of 66μm, nine slots back mirror with the slot period of 72 μm

Not all results we have taken for the tunable lasers from the second fabrication run are presented in this chapter. The results for the laser repeats from three other submounts with five contact lasers are not shown here as there are no significant differences between them. In this chapter the lasers with the shortest slot periods are presented. The mirror length for those lasers are comparable to the mirror lengths of SG-DBR laser [1] [2].

To complete the characterisation, four current sources were used independently to inject current to the SOA, gain and two mirror sections. The experimental set up is the same as the one shown in Figure 5.2 in Chapter 5. The devices was mounted on the heat sink which was held to a constant temperature of 20°C using a thermoelectric cooling. The current injected into the gain sections were kept constant and set to 120 mA. The PD section was left unbiased. The current injected into the SOA section was 30-40mA. The currents injected into the two mirror sections were scanned from 0 to 300 mA with a step of 5 mA. During these set of experiments a bigger scanning step was used to achieve faster tuning scan as there were many devices to study. The photodiode and picoammeter were used to record the coupled output power to determine if the coupling efficiency is stable. The output spectra, peak wavelength and side mode suppression ratio (SMSR) were recorded using an optical spectrum analyser with a resolution bandwidth of 0.1 nm and a sensitivity of -75dB.

The laser characterized here has a slot period of 66μm in the front mirror and 72 μm in the back mirror, which leads to FSR of 5.2 nm and 4.76 nm, respectively. The mirror lengths are 594nm for the front mirror and 648nm for the back mirror. The SOA current was set to 30mA.

The output power map is shown in figure 7.1 below. As can be seen the output power increases with increasing front current which suggests as previously found that the back mirror has very little influence in overall tuning effect.

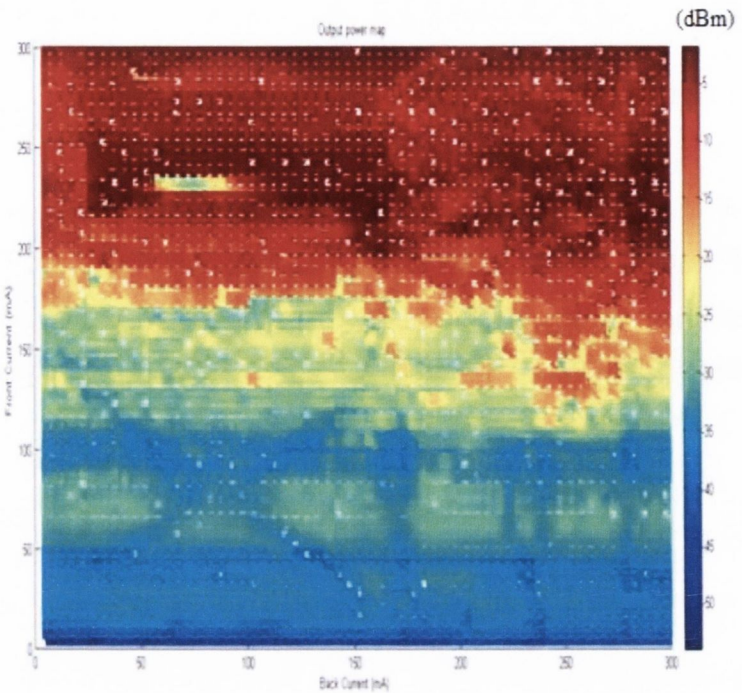

Figure 7.1. Output power map versus currents injected into two mirror sections for the laser with slot period of 66μm for the front mirror and 72μm for the back mirror.

The wavelength and the SMSR tuning maps are shown in figures 7.2 and 7.3, respectively.

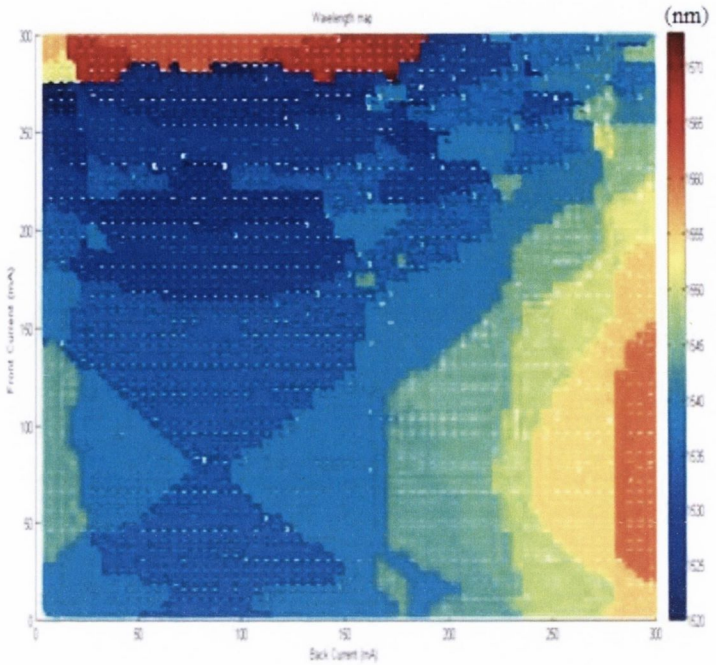

Figure 7.2. Wavelength tuning maps versus currents injected into the mirror sections for the laser with slot period of 66μm for the front mirror and 72μm for the back mirror.

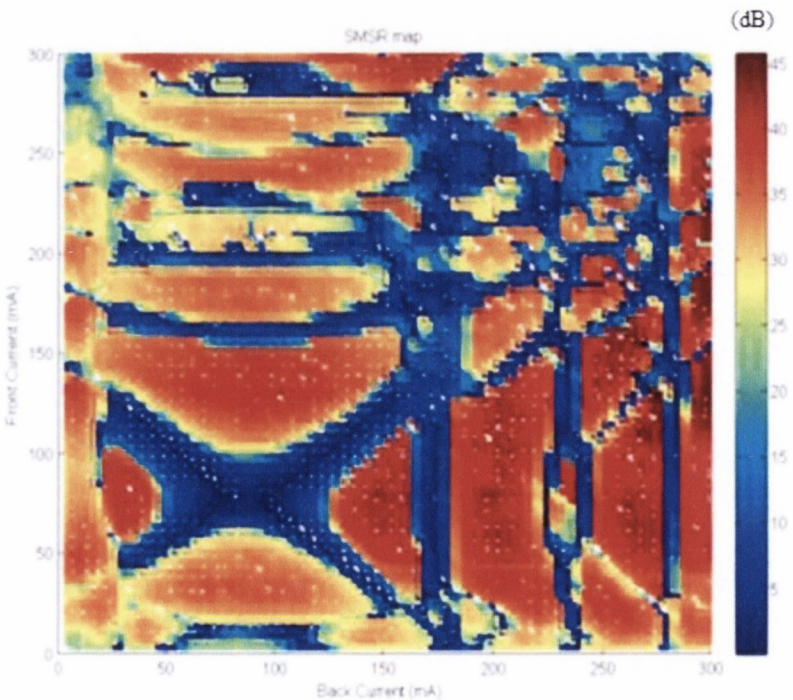

Figure 7.3. SMSR tuning map versus currents injected into the mirror sections for the laser with slot period of 66μm for the front mirror and 72μm for the back mirror.

The wavelength bands are clearly visible on the wavelength map for all currents injected into the front and back mirror sections. As shown in figure 7.3 there are big regions marked in red colour which indicate good SMSR values. Low SMSR occur at the boundaries of super-mode hops as well as for the region where the currents injected into the two mirror sections are quite high as for this region there is a lot of heating involved. Combining figures 7.2 and 7.3, the SMSR versus wavelength is plotted as shown in figure 7.4. Eleven super-modes are present for the tuning range of 48nm from 1520nm to 1568nm. The first mode at the edge of the gain spectrum for the wavelength of 1520nm has an SMSR value below 30dB. The next ten modes exhibit SMSR values more than 30dB. The highest observed SMSR is around 45dB for the wavelength of 1560nm.

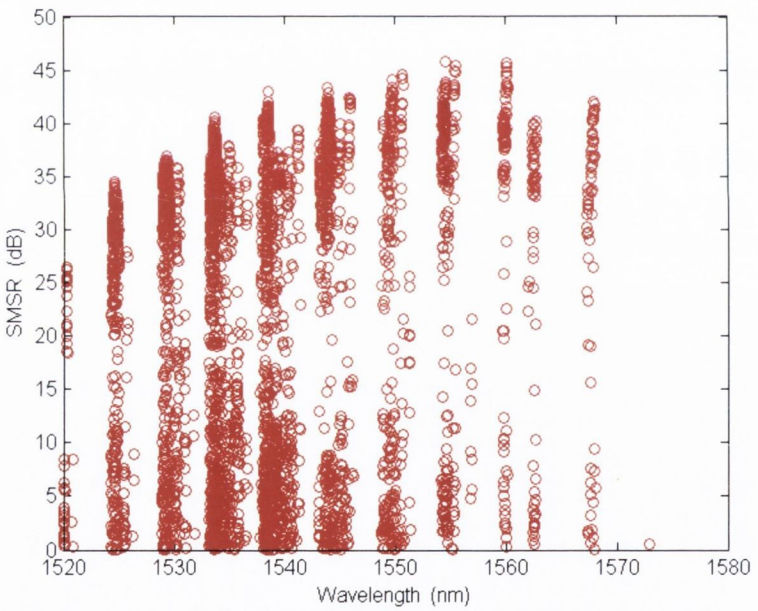

Figure 7.4. SMSR versus wavelength for the laser with slot period of 66μm for the front mirror and 72μm for the back mirror.

Combining figures 7.1 and 7.2, the output power versus wavelength can be plotted as shown in figure 7.5. below. As can be seen the output power is quite uniform for all super-modes with a variation within 5dBm.

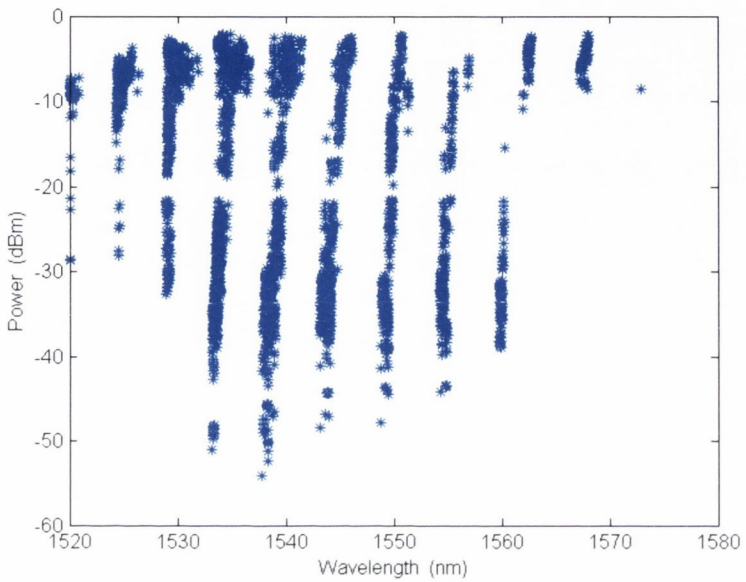

Figure 7.5. Output power versus peak wavelength for the laser with slot period 66μm for the front mirror and 72μm for the back mirror.

Nine slots front mirror with the slot period of 64μm, nine slots back mirror with the slot period of 70 μm

The laser described in this section has a slot period of 64μm for the front mirror and 70μm for the back mirror, which leads to an FSR of 5.36nm and 4.9nm, respectively. The front mirror length is 576μm and the back mirror length is 630μm. The current injected into the SOA section was set to 30mA.

The output power map is shown in figure 7.6 below. The super-mode bands are visible on the map. The output power decreases with increasing currents injected into the mirror sections. For relatively high values of the current injected into the front mirror section, there is a region where the power drops significantly.

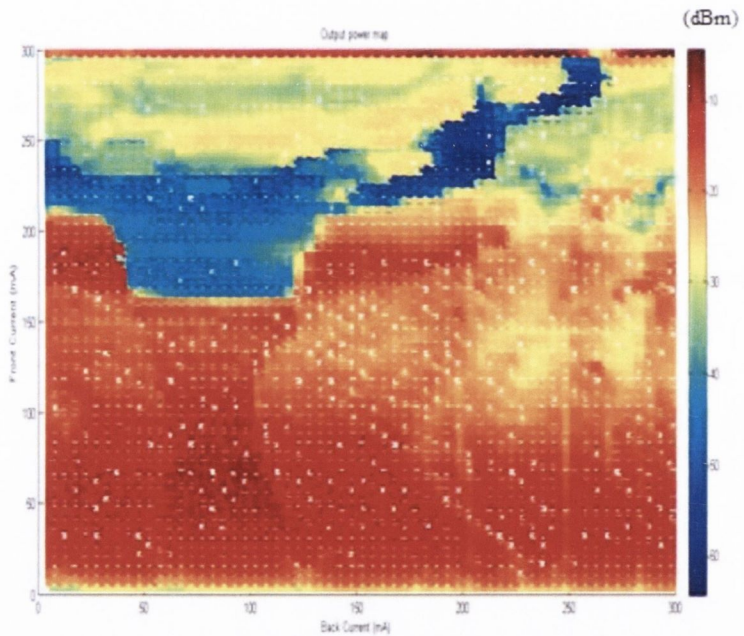

Figure 7.6. Output power map versus currents injected into the two mirror sections for the laser with slot period of 64μm for the front mirror and 70μm for the back mirror.

The wavelength tuning maps is shown in figure 7.7. The wavelength bands and wavelength islands are clearly visible within the map.

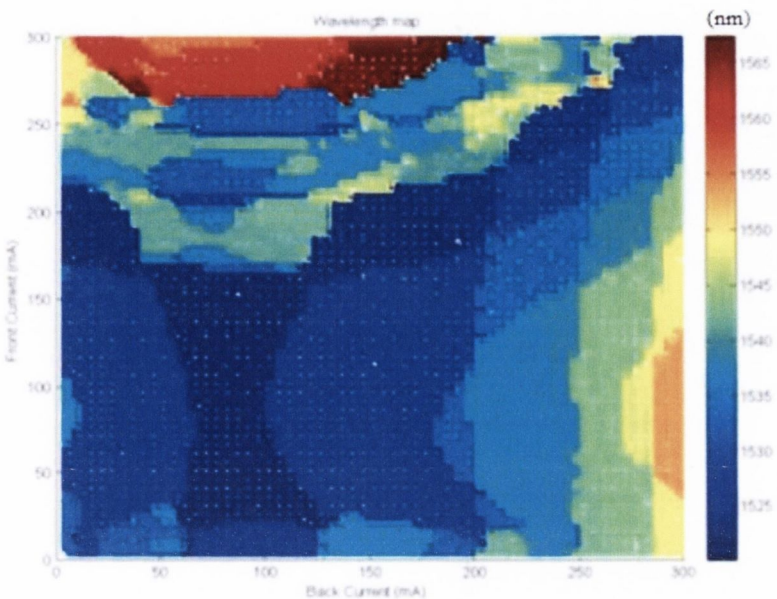

Figure 7.7. Wavelength tuning maps versus currents injected into two mirror sections for the laser with slot periods of 64μm for the front mirror and 70μm for the back mirror.

The SMSR tuning map is shown in Figure 7.8. below.

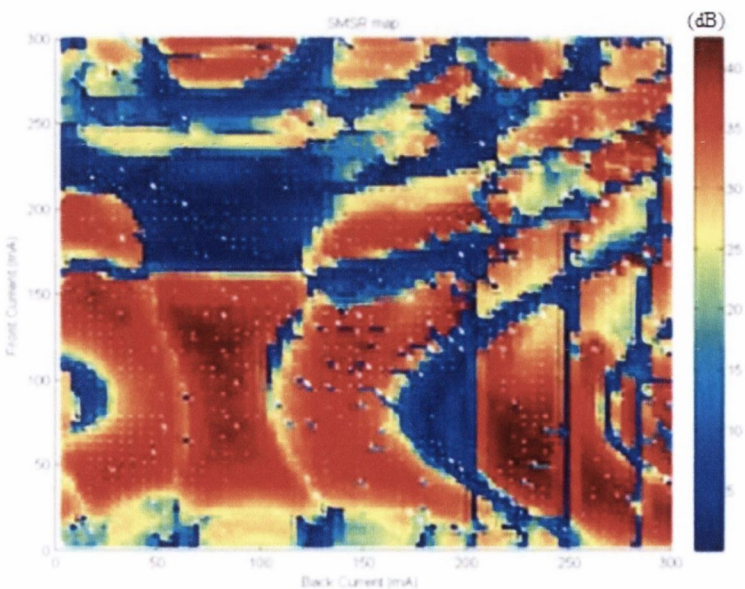

Figure 7.8. SMSR map versus currents injected into two mirror sections for the laser with slot period of 64μm for the front mirror and 70μm for the back mirror.

Comparing the output power map and the SMSR map it can be noticed that the sudden drop of the power corresponds to a region with low SMSR visible on the SMSR map. Looking at the wavelength map shown in figure 7.7, it is clear that the laser tuning in this particular region does not proceed smoothly. There are sudden jumps causing a competition between few different wavelengths. From figure 7.8 low SMSR values occur at the boundaries of the super-mode hops.

SMSR versus peak wavelength and the output power versus peak wavelength are plotted in figures 7.9 and 7.10, respectively. The wavelength tuning range is about 48nm from the wavelength of 1520nm to 1568nm. 10 super-modes are present, all of them with SMSR greater than 30dB. The SMSR is slightly decreasing with increasing wavelength.

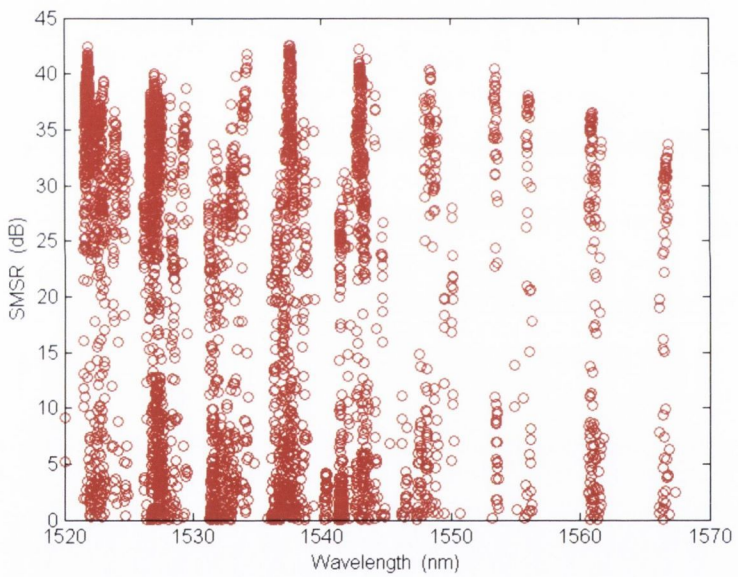

Figure 7.9. SMSR versus peak wavelength for the laser with slot period of 64μm for the front mirror and 70μm for the back mirror.

As seen in figure 7.10, the output power is uniform for all modes with variation within 2dBm.

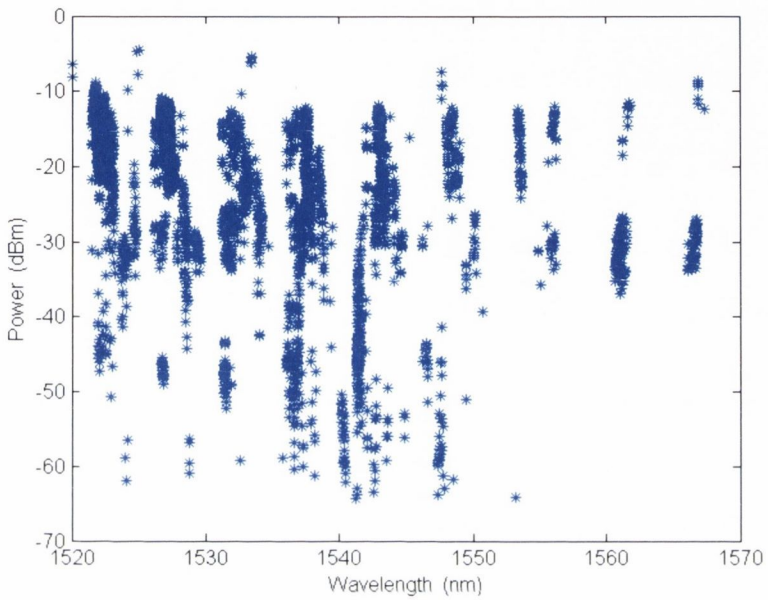

Figure 7.10. Output power versus peak wavelength for the laser with slot period of 64μm for the front mirror and 70μm for the back mirror.

Nine slots front mirror with the slot period of 57μm, nine slots back mirror with the slot period of 62 μm

The laser presented in this section has the slot period of 57μm for the front mirror and 62μm for the back mirror, which leads to FSRs of 6.02nm and 5.5nm, respectively. The front mirror length is 513nm and the back mirror length is 558nm which is comparable with an SG-DBR laser mirror length [1]. The current injected into the SOA section was set to 40mA. The currents injected into the front and back mirrors were scanned between 300mA and 0mA with a step of 5mA.

The output power tuning map, the wavelength tuning map and the SMSR tuning map versus currents injected into the front and back mirror sections are plotted in figures 7.11, 7.12 and 7.13, respectively.

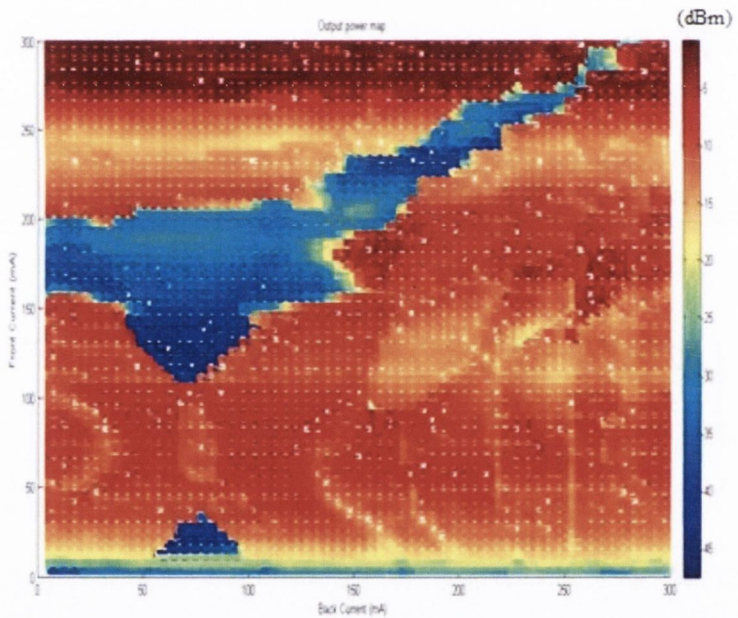

Figure 7.11. Output power map versus currents injected into the front and back mirror sections, for the laser with slot period of 57μm for the front mirror and 62μm for the back mirror.

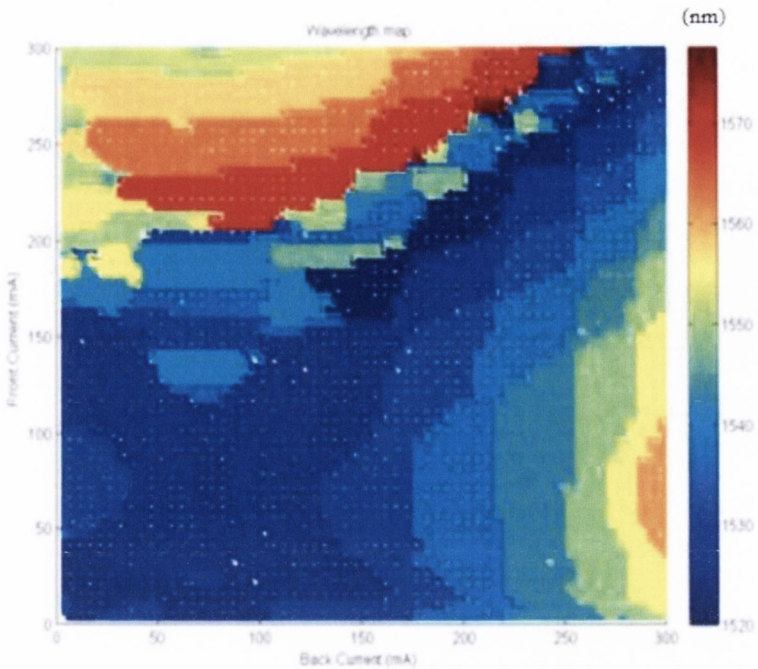

Figure 7.12. The wavelength tuning map versus currents injected into two mirror sections for the laser with slot period of 57μm for the front mirror and 62μm for the back mirror.

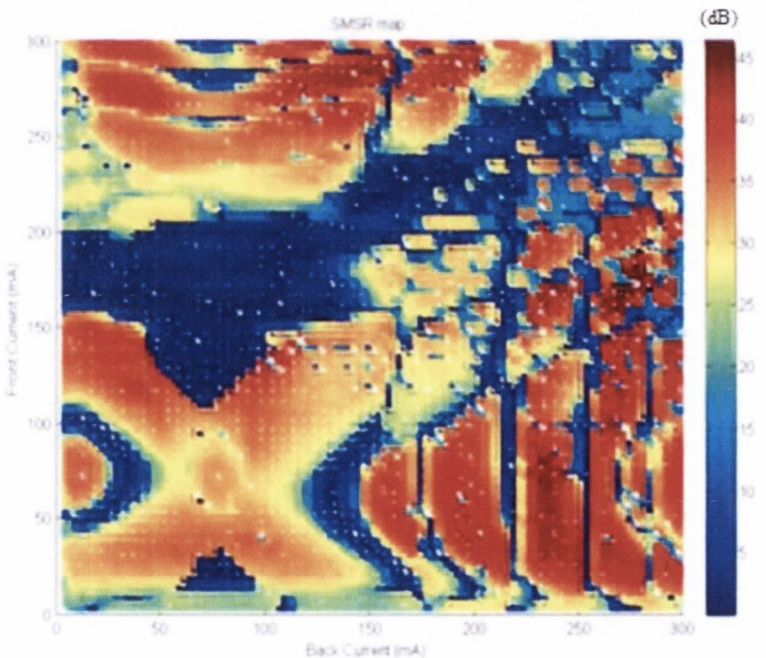

Figure 7.13. The SMSR tuning map versus currents injected into two mirror sections for the laser with slot period of 57μm for the front mirror and 62μm for the back mirror.

The super-mode band structure is clearly visible in the power map in figure 7.11 for the laser described in the previous section, again for relatively high front current there is a region of sudden power drop. Comparing with the wavelength and SMSR map, it can be seen that in this particular region of low output power, the wavelength does not change smoothly between the modes. A few different wavelengths that are competing are observed. Also as shown in the SMSR map in this region, the SMSR values are very low due to the mode competition.

The SMSR plotted versus peak wavelength is shown in figure 7.14, below. Fourteen distinct modes are present over the tuning range of 55nm for the wavelength from 1520nm to 1575nm. First thirteen modes have SMSR values above 30dB. The last super-mode for the wavelength of 1575nm placed at the edge of the gain spectrum shows the lowest SMSR. The highest SMSR is about 45dB for the wavelength of 1542nm.

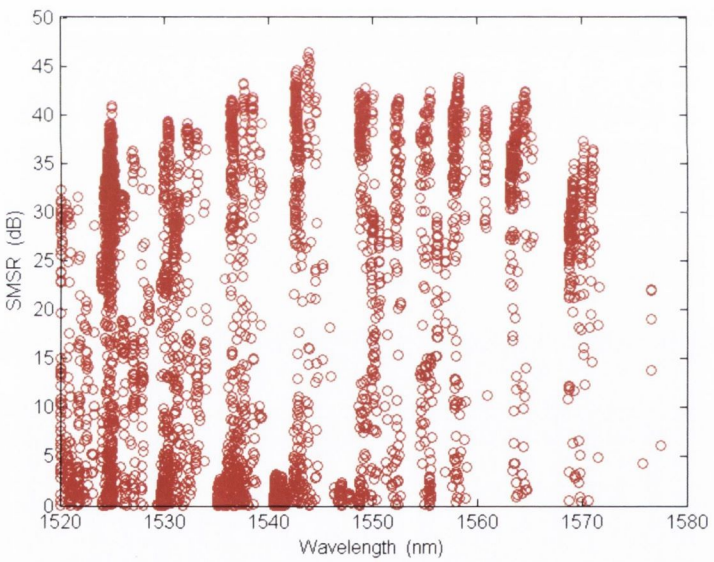

Figure 7.14. SMSR plotted versus peak wavelength for the laser with slot period of 57μm for the front mirror and 62μm for the back mirror.

The output power plotted versus peak wavelength is plotted in figure 7.15 below. The modes on the red side of the spectrum exhibit the highest output power, which does not correspond with the highest values of SMSR.

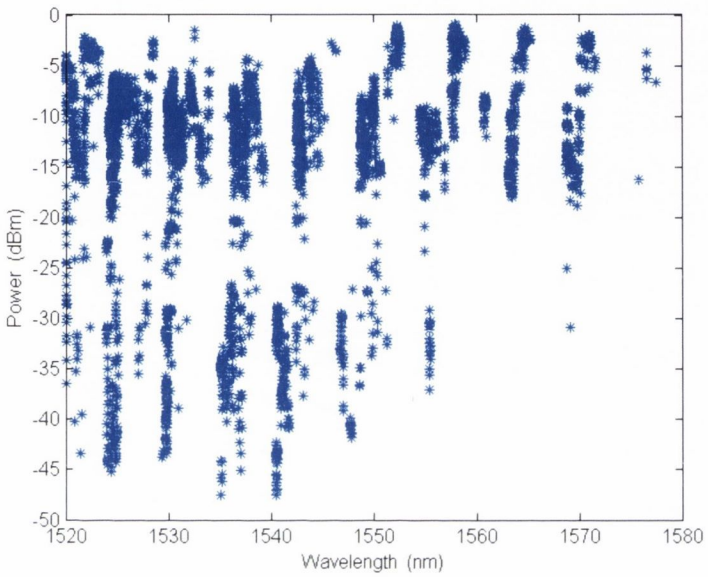

Figure 7.15. Output power plotted versus peak wavelength for the laser with slot period of 57μm for the front mirror and 62μm for the back mirror.

Nine slots front mirror with the slot period of 52μm, nine slots back mirror with the slot period of 57 μm

The laser presented in this section is the shortest laser in the current design. The slot period is 52μm for the front mirror and 57μm for the back mirror, which leads to FSRs of 6.6nm and 6.02nm, respectively. The mirror lengths are 468nm and 513 nm for the front and back mirror, respectively and the mirror length are comparable with an SG-DBR laser mirror lengths. The current injected into the SOA section was set to 30mA. The currents injected into the two mirror section were scanned between 300 and 0mA with the step of 5mA. From the simulations shown in chapter 4, six super- modes are expected.

The output power, wavelength and SMSR tuning maps are shown in figures 7.16, 7.17, 7.18, respectively.

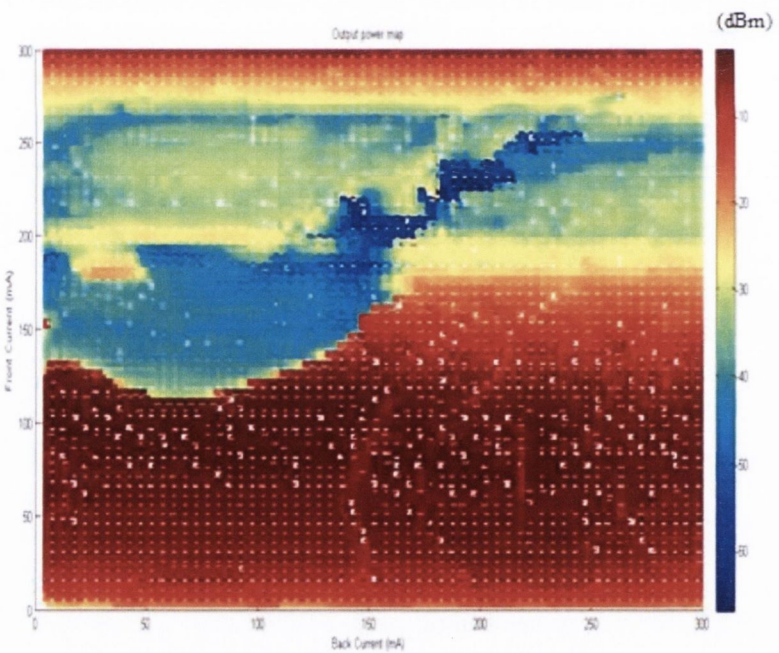

Figure 7.16. The output power maps versus currents injected into the two mirror sections for the laser with slot period of 52μm for the front mirror and 57μm for the back mirror.

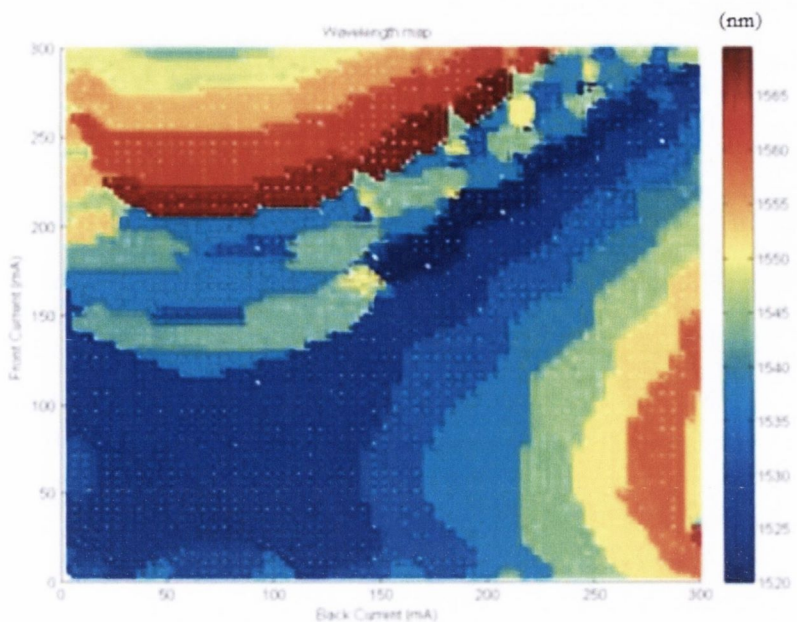

Figure 7.17. The wavelength tuning map versus currents injected into the two mirror sections for the laser with slot period of 52μm for the front mirror and 57μm for the back mirror.

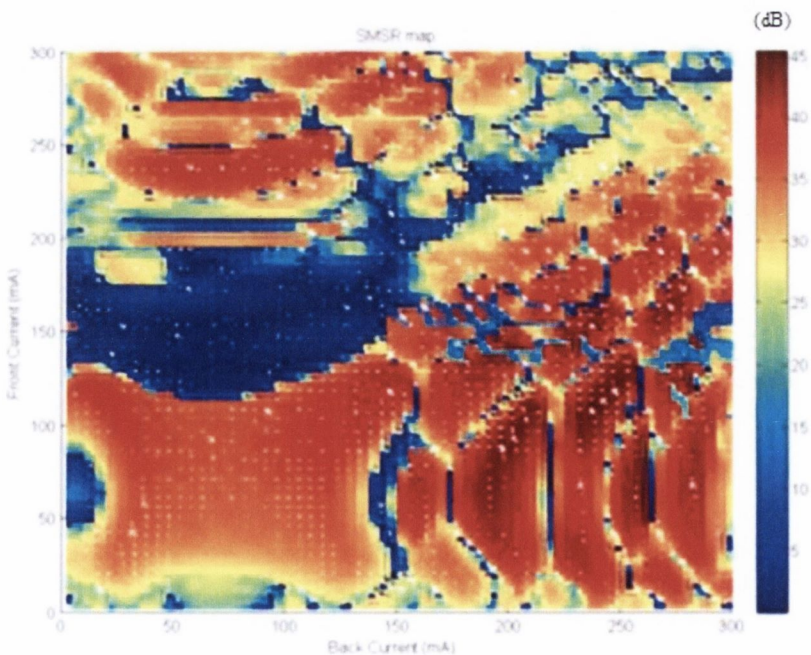

Figure 7.18. SMSR tuning map versus currents injected into the two mirror sections for the laser with slot period of 52μm for the front mirror and 57μm for the back mirror.

As was seen in two previous cases, again a significant drop of the power is observed for relatively high values of the current injected into the front mirror (Figure 7.16). Closer inspection of the wavelength map shows that again in this particular region there is mode competition resulting in low SMSR values. The wavelength bands and wavelength islands are clearly visible on the wavelength map. Looking at the SMSR map in figure 7.18 we observe that there is only one region with low SMSR values, corresponding to low output power and the mode competition. Decrease of the SMSR is also observed at the boundaries of the super-mode hops.

SMSR versus peak wavelength is plotted in figure 7.19 below. Eleven modes are present over the tuning range of 50nm for the wavelength from 1520nm to 1570nm. All eleven super-modes shows SMSR greater than 30dB. The modes on the edge of the blue and red side of the spectrum show lower SMSR.

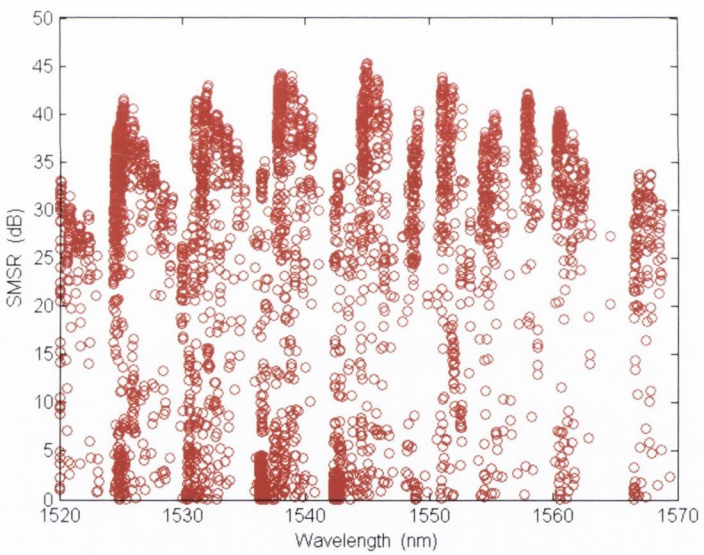

Figure 7.19. SMSR versus peak wavelength for the laser with the slot period of 52μm for the front mirror and 57μm for the back mirror.

The output power versus peak wavelength is shown in figure 7.20. The power for the modes on the edge of the spectrum is lower than for the modes in the centre. Lower output power corresponds to lower SMSR as shown in figure 7.19.

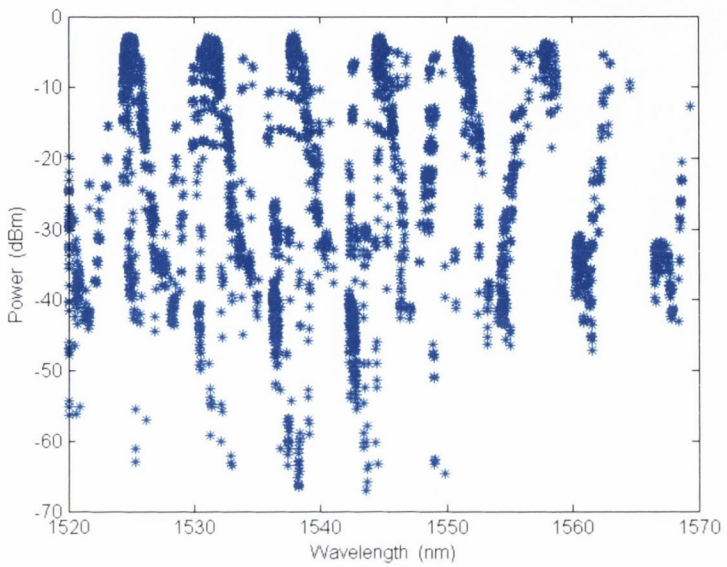

Figure 7.20. Output power versus peak wavelength for the laser with the slot period of 52μm for the front mirror and 57μm for the back mirror.

Table 7.1. below shows gathered tuning results for all laser from the new run presented in this chapter.

Slot period	66μm/72μm	64μm/70μm	57μm/62μm	52μm/57μm
FSR	5.2nm/4.76nm	5.36nm/4.9nm	6.02nm/5.5nm	6.6nm/6.02nm
Tuning range	48nm	48nm	55nm	50nm
Number of super-modes	11	10	14	11
Number of super-modes with SMSR > 30dB	10	10	13	11

Table 7.1. Tuning results for the tunable lasers from the new fabrication run.

Linewidth measurements of the laser with the slot period of 52μm for the front mirror and 57μm for the back mirror.

The delayed self- heterodyne technique [3] was used to measure the linewidth. The experimental set-up is the same as described and shown in Figure 6.16 in Chapter 6. A Voigt function, which is a convolution of Lorentzian and Gaussian profiles, was used to fit the spectrum. The Lorentzian profile is a contribution of frequency noise spectra for spontaneous emission while the Gaussian profile is a contribution due to the technical noise such as temperature fluctuation, mechanical vibrations or injected current noise [4]. Due to measuring a bare device for high currents there is more temperature fluctuations and therefore the Gaussian contribution dominates, especially for the wavelengths on the red side of the spectrum as we shall see in figure 7.22 below. Also in this case a higher current injected into the SOA and gain sections were needed to drive the laser therefore more temperature and noise fluctuations were involved during this set of measurements.

Again found in Chapter 5, the laser was biased with four independent current sources and it was not possible to replace them with low noise current sources therefore the values determined here are larger as seen by the difference in the Voigt and the Gaussian linewidths.

Figure 7.21. below shows an example of the spectrum of the tunable laser with the slot period of 52μm/57μm for a wavelength of 1525 nm with the linewidth of 4.95 MHz.

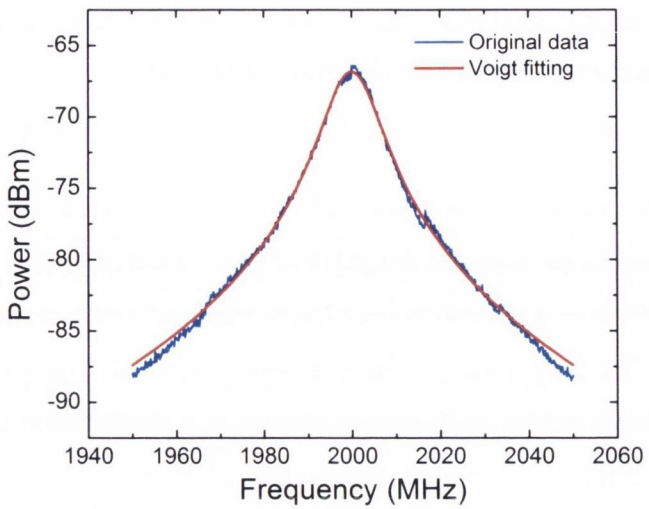

Figure 7.21. Example of a spectrum of the tunable laser for a wavelength of 1525 nm for the laser with slot period of 52μm/57μm.

Figure 7.22 below shows the linewidth versus peak wavelength for the laser with slot period of 52μm/57μm. It can be seen that for wavelength of 1562.04nm and 1568.4 nm there is a big difference between the intrinsic linewidth and FWHM. The intrinsic values of the linewidth are about 3MHz while the FWHM is about 17MHz. This suggests that Gaussian profile due to the technical noise is dominating for these particular wavelengths. For other points, the linewidth is increasing with increasing wavelength.

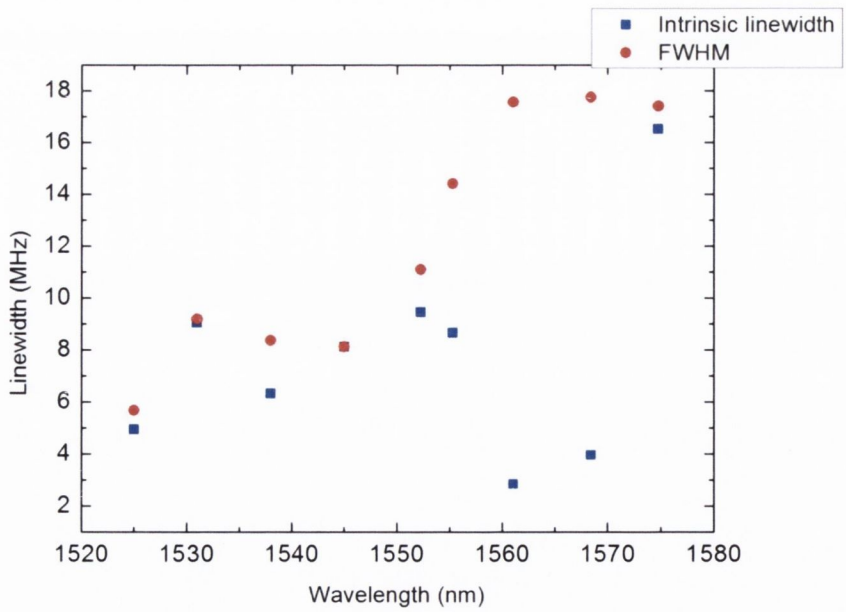

Figure 7.22. Linewidth versus wavelength for the laser with slot period of 52μm for the front mirror and 57μm for the back mirror.

Conclusion

The tunable lasers presented in this chapter were fabricated in May 2014. All devices shown here exhibit wide tuning range of about 50nm with good SMSR >30dB for all super-modes. Comparing with the lasers from Chapter 6, the spectrum for the new laser is blue shifted. It is now possible to access the wavelength of 1520nm. The tuning range for the new lasers is slightly shorter than for the laser from the first fabrication run. The widest tuning range for the lasers from Chapter 6 was 55nm for the device with the slot period of 70μm/76μm. For the lasers from the second run the widest tuning range is 50nm for the laser with the slot period of 57μm/62μm and 52μm/57μm. Lasers from both runs show similar trends in the tuning maps: characteristic symmetry lines and tuning islands going from big toward small as the currents injected into the both mirror section is increasing. Also the lasers from the second fabrication run have good SMSR values bigger than 30 dB for all super- modes. The SMSR maps for all lasers from the new run show a similar trend. The best wavelength and SMSR maps are from a device with the shortest slot period of 57/62μm. The linewidth of the shortest laser with the slot period of 52μm for the front mirror and 57μm for the back mirror was also measured. For two wavelength of 1562.04 nm and 1568.4 nm the intrinsic linewidth is low about 3MHz while FWHM have values about 17MHz. The Gaussian profile due to the technical noise dominates in these two cases.

References

[1] L. Schneider, M. Pfeiffer, J. Piprek, A. Witzig and B. Witzigmann, „Sampled-grating DBR lasers: calibrated 3D simulation of tuning characteristics," *In OPTO-Ireland, International Society for Optics and Photonics,* pp. 95-106, 2005.

[2] J. Buus i M. Amann, Tunable laser diodes and related optical sources, Wiley-IEEE Press, 2005.

[3] T. Okoshi, K. Kikuchi and A. Nakayama, „Novel method for high resolution measurement of laser output spectrum," *Electronics Letters,* vol 16, no 16, pp. 630-631, 1990.

[4] S. Spießberger, M. Schiemangk, A. Wicht, H. Wenzel, O. Brox and G. Erbert, „ Narrow linewidth DFB lasers emitting near a wavelength of 1064 nm," *Journal of Lightwave Technology,* vol 28, no 17, pp. 2611-2616, 2010.

Chapter 8. Conclusion and future work.

There is no doubt that semiconductor tunable lasers can offer a good number of key features in optical communications and have many applications there. In the work presented in this thesis, a new approach to semiconductor tunable lasers has been shown as an alternative to complex laser structures that exist in optical communication market.

In chapter 4, a design and fabrication process of slotted tunable laser have been presented. Using the Scattering matrix method (SMM), the laser parameters such as slot depth, slot number, slot width were optimized. Also different slot periods were chosen to get a various number of lasers and see how tuning parameters such as tuning range, number of super- modes, free spectral range (FSR), SMSR are influenced by this parameter. The optimized slot parameters were then incorporated into the MatLab program to simulate the wavelength and SMSR maps of the lasers. For the simulation a simple model of tunable laser was used to give an idea how the tuning of the laser will be changing depending on different slot period. The next step was to show how using CleWin 4 software, the tunable lasers mask can be prepared. On the laser mask three types of slotted lasers were designed: five section laser, six section laser and nine section lasers. Each laser bar consist of eleven lasers with different slot periods plus usually two or three repeats. The final step was to show step by step the fabrication process of the slotted tunable lasers.

In chapter 5 the laser from the first fabrication run were characterized. The wavelength and SMSR tuning maps for different types slotted lasers were presented there. Also the performance of a five section laser with nine slots on the front mirror and five slots on the back mirror was shown in this chapter. The phase tuning of the six section laser was also investigated. The nine section laser with an isolation contact was also characterized showing that its tuning maps are similar to the tuning maps of an SG-SBR laser. The laser

with the slot period of 70μm on the front mirror and 76μm on the back mirror was shown to be the best laser from the first fabrication run taking into account its tuning range, SMSR and number of super- modes.

In chapter 6 a further characterization of the tunable lasers was introduced by determining the continuous tuning of five contact laser with nine slots etched on both mirrors and with nine slots in the front mirror and five slots in the back mirror. A continuous tuning was also investigated for the nine contact laser. For the laser with nine slots in both mirrors the continuous tuning range is about 0.6 nm (~75GHz) and for the laser with nine/five slots is 0.3nm (~37.5GHz). The laser with nine contacts shows the continuous tuning of 0.2nm (25GHz). For the temperature tuning, the super- modes were shifted of about 0.5 nm for all eleven channels while changing the temperature from 15°C to 40°. Finally the linewidth of the laser with the slot period of 97μm/108μm and 70μm and 76μm was measured using self- heterodyne method. Both lasers have the linewidth in the range of MHz.

In chapter 7 a characterisation of the slotted laser from the second fabrication run was presented. The lasers shown in this chapter have short slot periods. The wavelength and SMSR maps and the linewidth measurements for the laser with the shortest slot period of 52μm/57μm were presented there. The lasers from the second fabrication run show very good performance and the best laser was shown to be the one with the slot period of 57μm/62μm. It has the widest tuning range and the biggest number of super- modes.

All the lasers presented in this thesis are integrated with semiconductor optical amplifier (SOA). The experimental results suggest that the slotted tunable laser can be used in optical communication systems. The big advantage of those lasers is that they can be integrated with other optical components and also they are easy to fabricate as was shown in chapter 4. All lasers exhibit a wide tuning range ~50nm and more with good SMSR > 30dB for almost all super- modes. The SMSR and output power can be easily boosted by increasing the current injected into the gain sections as was shown in chapter 5.

The future design could focus on decreasing the slot number on the mirrors which would decrease the laser length. Also a program for the simulated tuning maps could be further improved by incorporating the gain along the whole laser cavity and by incorporating the temperature effects. Having the gain included for whole laser cavity would allow to obtain more accurate tuning maps and use bigger current range during the simulations. Including the temperature effects would allow us to investigate more how the change of

the temperature of heat sink would affect the overall tuning performance of the laser such as tuning range, number of super- modes and SMSR. Also a study of how the slot period affects the laser linewidth and what is the best period to obtain the narrowest linewidth could be considered. A future design could also include three different slot depths in the laser mirrors to further improve a laser performance.

The laser should also be properly packaged which is essential for any possible commercial development. The packaging of the devices will allow to further improve their performance as then the laser will be isolated from the environment. Studies using these lasers at system level in optical networks are planned.